

VLBI and  $\gamma$ -ray studies of radio galaxies  
in the TANAMI monitoring program

INAUGURAL-DISSERTATION

ZUR

Erlangung des Doktorgrades  
der Mathematisch-Naturwissenschaftlichen Fakultät  
der Universität zu Köln



vorgelegt von

**Roberto Angioni**

aus

Carbonia, Italien

Köln 2019

Berichtersteller:

Prof. Dr. Andreas Eckart

Prof. Dr. J. Anton Zensus

Tag der letzten mündlichen Prüfung: 19.10.2018

# Abstract

Relativistic jets in Active Galactic Nuclei (AGN) are among the most extreme sources of radiation in the universe. They are launched and accelerated by accreting supermassive black holes found in the center of a fraction of galaxies. These jets emit strongly across the whole electromagnetic spectrum, and are especially bright in the radio and  $\gamma$ -ray bands, where they are among the most studied astrophysical sources. In the simplest models, the production of  $\gamma$ -rays in radio-loud AGN involves the same relativistic particles that give rise to the radio emission. Therefore, we expect to observe a close connection between the two bands. This has been well-established in studies of large AGN samples. However, such samples are dominated by AGN with well-aligned jets, a sub-class called *blazars*, where the observed emission is strongly beamed and amplified due to relativistic Doppler effects. While this makes blazars easier to detect, it also poses the challenge of disentangling orientation-dependent effects from the intrinsic physical properties. To this date, there has been no systematic study on the relation between parsec-scale radio emission and  $\gamma$ -ray properties of the misaligned parent population of blazars, i.e., *radio galaxies*.

In this thesis, I present the first systematic VLBI and  $\gamma$ -ray monitoring study of a representative sample of radio galaxies with strong compact radio emission, with the aim of exploring the intrinsic relationship between high-energy emission and pc-scale jet properties in AGN. I base the study on the decade(s)-long Very Long Baseline Interferometry (VLBI) monitoring provided by the TANAMI program, the largest multi-epoch observational campaign on radio-loud AGN in the Southern sky.

First, I introduce the basic properties of AGN (Chapter 1), and discuss the current understanding of the relation between radio and  $\gamma$ -ray emission in AGN (Chapter 2). I then introduce the instruments and the corresponding data reduction techniques relevant to this thesis work, i.e.,  $\gamma$ -ray telescopes (Chapter 3) and VLBI arrays (Chapter 4).

Chapter 5 presents the results on the evolution of the parsec-scale jet in TANAMI radio galaxies, including milliarcsecond resolution images at 8.4 GHz for several observing epochs, and a jet kinematic analysis to estimate the intrinsic jet speed, viewing angle, and overall evolution, at the highest resolution available for this sample.

The information from parsec-scale jet kinematics is combined with  $\gamma$ -ray flux variability results from the *Fermi*-LAT space telescope (presented in Chapter 6), and the observed properties in these two bands and their interplay are discussed in Chapter 7. I summarize the main results in Chapter 8.

I first discuss individual results on noteworthy TANAMI radio galaxies, such as the FR II radio galaxy Pictor A, the peculiar AGN PKS 0521–36, the TeV source PKS 0625–35, and the first  $\gamma$ -ray detected young radio galaxy, PKS 1718–649 (Section 7.1). I then combine the TANAMI radio galaxy sample with publicly available results from the MOJAVE survey, the largest VLBI monitoring program of AGN in the northern sky, to study the largest sample to date of radio galaxies with parsec-scale kinematics and  $\gamma$ -ray information (Section 7.2). Testing for possible correlations between the average radio and  $\gamma$ -ray properties of radio galaxies, I show that the high-energy emission from the compact jets of radio galaxies is not strongly driven by orientation-dependent Doppler boosting effects, much unlike the situation in their blazar counterparts. However, a significant correlation between  $\gamma$ -ray flux and radio flux still holds, suggesting a direct physical link between the intrinsic emission properties of AGN jets in the two wavebands.

# Zusammenfassung

Relativistische Jets in aktiven galaktischen Kernen (AGN) gehören zu den stärksten Quellen elektromagnetischer Strahlung im Universum. Sie werden angetrieben und beschleunigt durch supermassive schwarze Löcher, die sich im Zentrum einiger Galaxien befinden und Gas akkretieren. Diese Jets strahlen stark über das ganze elektromagnetische Spektrum, und sind besonders hell im Radio- und Gamma-Bereich, bei denen sie zu den am besten untersuchten astronomischen Quellen gehören. In den einfachsten Modellen wird die Gamma-Strahlung in radiolauten AGN von denselben relativistischen Teilchen emittiert, die auch für die Radio-Strahlung sorgen. Deshalb erwarten wir eine enge Verbindung zwischen diesen Frequenzbändern. In Untersuchungen mit vielen AGN wurde dies bestätigt. Allerdings weisen die meisten der AGN in diesen Stichproben mit der Sichtlinie ausgerichtete Jets auf; diese Unterklasse von AGN nennt man Blazare. In diesen ist die Emission stark in einem kleinen Abstrahlungswinkel kollimiert und verstärkt durch relativistische Doppler-Effekte. Auf der einen Seite sind diese Objekte dadurch leichter zu detektieren, auf der anderen Seite ist es schwieriger, zwischen Effekten der Ausrichtung der Quelle und intrinsischen physikalischen Eigenschaften zu unterscheiden. Bisher gab es keine systematische Studie zur Relation von Radio- und Gamma-Strahlung auf Parsec-Skalen in der übergeordneten Population von Blazaren, den Radiogalaxien.

In dieser Arbeit präsentiere ich die erste systematische Studie einer repräsentativen Stichprobe von Radiogalaxien mit starker, kompakter Radioemission mit VLBI- und Gamma-Beobachtungen. Ziel dieser Studie ist es, die intrinsische Relation zwischen hochenergetischer Emission und Eigenschaften der Jets auf Parsec-Skalen in AGN zu untersuchen. Für diese Studie verwende ich die jahrzehntelangen Beobachtungen mit Very Long Baseline Interferometry (VLBI) des TANAMI-Programms, der größten Beobachtungs-Kampagne zu radiolauten AGN am Südhimmel, die mehrere Epochen umfasst.

Zuerst führe ich in die grundlegenden Eigenschaften von AGN ein (Kapitel 1) und zeige die momentane Sicht auf die Beziehung zwischen Radio- und Gamma-Strahlung in AGN (Kapitel 2). Weiter präsentiere ich die Instrumente und die

Techniken der Datenreduktion, die für diese Arbeit relevant sind, d. h. Gamma-Teleskope (Kapitel 3) und VLBI-Teleskope (Kapitel 4).

In Kapitel 5 zeige ich die Ergebnisse bezüglich der Entwicklung der Jets auf Parsec-Skalen in TANAMI-Radiogalaxien. Dazu gehören Karten mit Millibogensekunden-Auflösung bei 8.4 GHz für verschiedene Beobachtungsepochen sowie eine Analyse der Kinematik der Jets bei der höchsten in dieser Studie möglichen Auflösung, um ihre intrinsischen Jet-Geschwindigkeiten, Beobachtungswinkel und ihre Gesamtentwicklung abzuschätzen.

Die aus der Kinematik der Jets auf Parsec-Skalen gewonnenen Informationen werden mit den Ergebnissen des Fermi-LAT Weltraumteleskops zur Flussdichte-Variabilität im Gamma-Bereich (Kapitel 6) kombiniert. In Kapitel 7 diskutiere ich die beobachteten Eigenschaften in den beiden Frequenzbändern und ihr Zusammenspiel. Kapitel 8 ist eine Zusammenfassung der wesentlichen Resultate.

Als erstes erörtere ich die einzelnen Ergebnisse beachtenswerter TANAMI-Radiogalaxien, wie der FR II Radiogalaxie Pictor A, des irregulären AGN PKS 0521-36, der TeV-Quelle PKS 0625-35, und der ersten Gamma-detektierten jungen Radiogalaxie, PKS 1718-649 (Abschnitt 7.1). Danach kombiniere ich die Stichprobe von TANAMI-Radiogalaxien mit den öffentlich zugänglichen Ergebnissen der MOJAVE-Studie, dem größten Programm zur kontinuierlichen Beobachtung von AGN am Nordhimmel, um die bisher größte Stichprobe von Radiogalaxien mit Informationen zur Kinematik auf Parsec-Skalen und zur Gamma-Strahlung zu erhalten (Abschnitt 7.2). Ich teste in dieser Stichprobe mögliche Korrelationen zwischen den durchschnittlichen Eigenschaften der Gamma- und Radiostrahlung. Dabei zeige ich, dass die hochenergetische Emission kompakter Jets in Radiogalaxien nicht stark von ausrichtungsabhängigen, strahlungsverstärkenden Doppler-Effekten beeinflusst wird, ganz anders als in den Blazaren. Trotzdem bleibt eine signifikante Korrelation zwischen Gamma- und Radiostrahlung, was auf einen direkten physikalischen Zusammenhang zwischen den intrinsischen Eigenschaften der Emission in AGN Jets in diesen beiden Wellenlängenbereichen hinweist.

# Contents

|          |   |           |
|----------|---|-----------|
| <b>1</b> | <b>Active Galactic Nuclei</b>   | <b>1</b>  |
| 1.1      | Anatomy of an AGN . . . . .   | 2         |
| 1.1.1    | The central engine . . . . .  | 2         |
| 1.1.2    | The emission-line regions . . . . .                                       | 5         |
| 1.1.3    | The dusty absorber . . . . .  | 6         |
| 1.2      | The unified model of AGN . . . . .  | 7         |
| 1.2.1    | Radio-quiet unification . . . . .   | 7         |
| 1.2.2    | Radio-loud unification . . . . .  | 9         |
| 1.3      | Properties of relativistic jets from supermassive black holes . . . . .   | 11        |
| 1.3.1    | Relativistic effects . . . . .  | 11        |
| 1.3.2    | Radiative processes . . . . .   | 14        |
| <b>2</b> | <b>The puzzle of <math>\gamma</math>-ray emission in radio galaxies</b>   | <b>19</b> |
| 2.1      | The <i>Fermi</i> -LAT view of radio galaxies . . . . .                    | 19        |
| 2.2      | The connection between radio and $\gamma$ -ray emission in radio-loud AGN | 21        |
| 2.3      | VLBI kinematics and $\gamma$ -ray variability . . . . .                   | 22        |
| <b>3</b> | <b><math>\gamma</math>-ray astronomy</b>                                  | <b>25</b> |
| 3.1      | Historical notes . . . . .  | 25        |
| 3.2      | The <i>Fermi</i> $\gamma$ -ray space telescope . . . . .                  | 25        |
| 3.2.1    | The Large Area Telescope . . . . .  | 27        |
| 3.2.2    | The Gamma-ray Burst Monitor . . . . .                                     | 29        |
| 3.3      | <i>Fermi</i> -LAT data reduction principles . . . . .                     | 31        |
| 3.3.1    | The likelihood and the Test Statistic . . . . .                           | 31        |
| 3.3.2    | The Region of Interest and the sky model . . . . .                        | 32        |
| 3.4      | <i>Fermi</i> -LAT data reduction steps . . . . .                          | 33        |
| 3.4.1    | Standard point-source detection analysis . . . . .                        | 33        |
| 3.4.2    | Source finding, localization and upper limit analysis . . . . .           | 35        |
| <b>4</b> | <b>Radio interferometry</b>   | <b>37</b> |
| 4.1      | Radio astronomy basics . . . . .  | 37        |
| 4.2      | Interferometry and VLBI . . . . .   | 39        |
| 4.3      | VLBI data reduction . . . . .   | 42        |
| 4.3.1    | Calibration . . . . .   | 42        |
| 4.3.2    | Imaging . . . . .   | 44        |
| 4.4      | The TANAMI monitoring program . . . . .                                   | 46        |

---

|          |  |            |
|----------|--|------------|
| <b>5</b> | <b>Radio VLBI data analysis and results</b>                                    | <b>51</b>  |
| 5.1      | The TANAMI radio galaxy sample . . . . .                                       | 51         |
| 5.2      | VLBI data analysis . . . . .   | 53         |
| 5.3      | Imaging results . . . . .  | 54         |
| 5.4      | Kinematics results . . . . .   | 66         |
| <b>6</b> | <b><i>Fermi</i>-LAT data analysis and results</b>                              | <b>89</b>  |
| 6.1      | $\gamma$ -ray data analysis . . . . .  | 89         |
| 6.2      | Results . . . . .  | 90         |
| <b>7</b> | <b>Parsec scale jet and <math>\gamma</math>-ray emission in radio galaxies</b> | <b>100</b> |
| 7.1      | Individual source discussion . . . . .   | 100        |
| 7.2      | Sample properties . . . . .  | 102        |
| 7.2.1    | Average radio and $\gamma$ -ray properties . . . . .                           | 104        |
| 7.2.2    | Correlations between radio and $\gamma$ -ray properties . . . . .              | 109        |
| <b>8</b> | <b>Conclusions</b>   | <b>113</b> |
| <b>A</b> | <b>Full-resolution VLBI images and parameters</b>                              | <b>115</b> |
| <b>B</b> | <b>Modelfit component parameters</b>   | <b>141</b> |
| <b>C</b> | <b><i>Fermi</i>-LAT results on full MOJAVE and TANAMI samples</b>              | <b>151</b> |
|          | <b>Bibliography</b>  | <b>163</b> |

# Chapter 1

## Active Galactic Nuclei

*Active Galactic Nuclei* (AGN) are among the most powerful steady sources of radiation in the universe. This radiation spans the entire electromagnetic spectrum, from radio wavelengths to  $\gamma$ -rays, with bolometric luminosities from  $10^{42}$  erg/s up to  $10^{49}$  erg/s. This exceptionally high luminosity, together with the compactness of the emission and its peculiar spectral properties such as the presence of strong broad emission lines and the bright and blue continua, is what set apart AGN as a new class of astronomical objects in the early days of this research field.

AGN were discovered for the first time by Seyfert (1943), who studied a sample of galaxies and noted their unusually bright central regions and strong broad and narrow emission lines. In the following decade, the newly born radio astronomy field produced the first complete source catalogs, such as the Third Cambridge Catalog (Edge et al. 1959; Bennett 1962). It was immediately noted that many of these strong radio sources had a bright, compact optical counterpart resembling a stellar object, but with an unusual spectrum, characterized by a strong blue continuum and bright emission lines (e.g., Baade & Minkowski 1954). Shortly after, Schmidt (1963) correctly interpreted the optical lines in the spectrum of the “radio star” 3C 273 as normal Balmer lines redshifted by  $z = 0.158$ . The distance implied by this measurement established these bright “radio stars” as extragalactic sources, at a distance scale much larger than any other known astronomical object at the time, and revealed their large intrinsic luminosity. Following several other large redshift measurements for similar objects, this class of sources was dubbed *quasars*, for Quasi-Stellar Radio Sources.

AGN research continued to expand in the following decades, revealing a host of different source types and observational flavors. The main focus of this thesis, i.e., radio galaxies, are indeed a subclass of AGN.

In the following, I will give a brief overview of the physical scenario which is most frequently invoked to explain the various observed AGN types. I will then focus on radio galaxies, the main subject of this study. For a much more extensive and complete reading on the subject, I refer the reader to the recent review by Padovani et al. (2017).

## 1.1 Anatomy of an AGN

There is now a widely accepted view of what are the main building blocks of all AGN. This is based on the idea that the different AGN flavors are a manifestation of the same basic processes and elements, with a variation in relatively few parameters, namely the accretion rate, the presence of a relativistic jet launched from the AGN core, and the viewing angle of the system. A schematic view of these concepts is illustrated in Fig. 1.1. I will now give a description of the main components depicted there, which are believed to be present in almost all AGN: a central accreting supermassive black hole, line emitting gas orbiting it, and a dusty absorber. The figure also shows that in some sources a narrow, well-collimated jet is produced by the central engine: this is actually the case only for a small fraction of AGN, called radio-loud AGN, which will be extensively discussed in Section 1.3.

### 1.1.1 The central engine

The combination of extreme compactness and large luminosity in these sources quickly led to the conclusion that the fueling mechanism of AGN could only be based on the conversion of gravitational energy into radiation, through accretion of large amounts of material onto a massive, compact central object (e.g., Salpeter 1964). It is now widely accepted that this central object can only be a supermassive black hole (SMBH), with mass exceeding  $10^6 M_\odot$ , reaching up to  $10^{10} M_\odot$  for the most extreme objects <sup>1</sup>. The linear scale associated to the SMBH is expressed by the *Schwarzschild radius*, i.e., the distance below which no information can escape the gravitational pull of the black hole, since the escape velocity exceeds the speed of light in vacuum. This quantity is solely determined by the black hole mass, and is given by

$$R_s = \frac{2GM_{\text{BH}}}{c^2} \sim 3 \times 10^5 \frac{M_{\text{BH}}}{M_\odot} \text{ cm} \quad (1.1)$$

<sup>1</sup>See e.g., Mezcuca (2017) and Ichikawa & Inayoshi (2017) for more information on these approximate lower and upper limits, respectively.

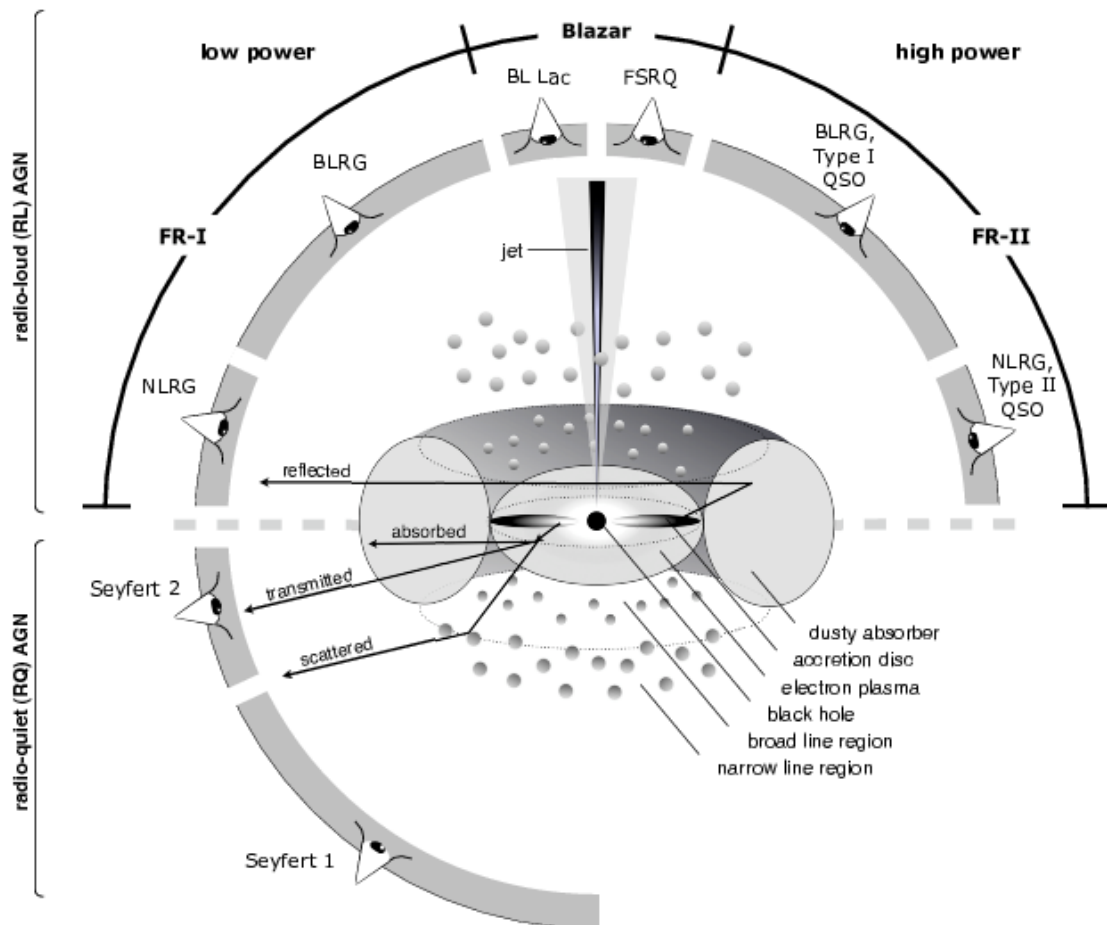


FIGURE 1.1: Schematic representation of the orientation based unified model. Image from Beckmann & Shrader (2012), page 132.

For the most extreme SMBHs in the most luminous AGN, this scale corresponds to  $\sim 10^{-3}$  pc.

The accretion flow on the SMBH can take the form of a geometrically thin, optically thick rotating disk (Shakura & Sunyaev 1973) or a geometrically thick, optically thin, spherically-symmetric flow (e.g., Begelman 1979). The latter family of models is usually referred to as Advection Dominated Accretion Flow (ADAF).

The transition between these two phases is believed to depend on the accretion rate onto the SMBH. This is characterized using the Eddington luminosity, a theoretical upper limit deriving from the balance between radiation pressure generated by the accretion and the gravitational pull of the accreting central object. It can be expressed as

$$L_{\text{Edd}} = \frac{4\pi G c m_p M_{\text{BH}}}{\sigma_T} = 1.26 \times 10^{38} \frac{M_{\text{BH}}}{M_{\odot}} \text{ erg s}^{-1} \quad (1.2)$$

where:

- $G$  is the gravitational constant;
- $c$  is the speed of light in vacuum;
- $m_p$  is the proton mass;
- $M_{\text{BH}}$  is the mass of the central black hole;
- $\sigma_T$  is the Thomson cross section.

Assuming that the accretion luminosity is directly proportional to the mass accretion rate, with efficiency  $\eta$ , this could be expressed as

$$L_{\text{Edd}} = \eta \dot{M}_{\text{Edd}} c^2 \quad (1.3)$$

from which the Eddington accretion rate can be derived as

$$\dot{M}_{\text{Edd}} = \frac{4\pi G m_p M_{\text{BH}}}{\eta c \sigma_T} \quad (1.4)$$

This is then the maximum sustainable accretion rate for a given black hole mass, in this simple description. For  $\dot{M} < 10^{-3} - 10^{-4} \dot{M}_{\text{Edd}}$ , the accretion flow takes the form of an ADAF system, while for  $\dot{M} > 10^{-3} - 10^{-4} \dot{M}_{\text{Edd}}$  it will form an accretion disk (see e.g., Ghisellini & Celotti 2001; Ghisellini et al. 2011, and references therein).

In the former case, the high density of the material in the disk, and its rotation, will cause the material to be heated by viscous friction up to high temperatures, in the range  $10^4 - 10^6$  K, and to emit bright radiation in the optical-UV band. Indeed the emission component associated with the accretion disk is called the “Big Blue Bump”, and it is often an easily recognizable feature in the spectral energy distribution (SED) of sources with efficient accretion flows (see the black solid line in Fig. 1.2). The conversion efficiency of accreted mass into radiation is of the order of  $\sim 10\%$  (Soltan 1982), making this one of the most radiatively efficient processes in nature.

On the other hand, ADAF systems are much less radiatively efficient and therefore less luminous, and do not contribute significantly to the overall emission observed from the system.

Finally, X-ray observations indicate the presence of an additional component in the inner region of AGN, i.e., a corona of low-density, high-temperature gas residing above the accretion disk, with  $T \sim 10^6 - 10^7$  K. The high-energy electrons

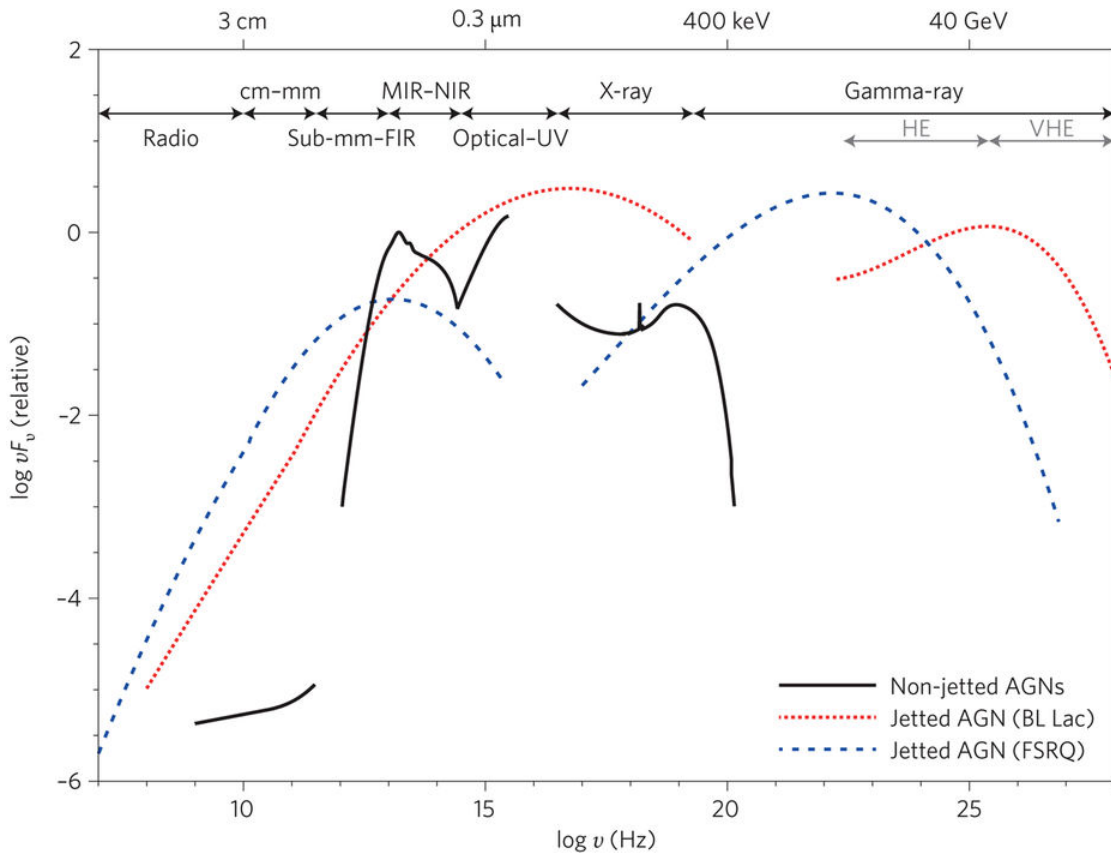


FIGURE 1.2: Spectral Energy Distributions (SEDs) of AGN belonging to different classes. Figure from Padovani (2017), adapted from Harrison (2014).

in the corona up-scatter the thermal photons from the accretion disk via the Inverse Compton process, producing hard X-ray emission with a power-law spectral shape (Haardt & Maraschi 1991). This radiation illuminates the accretion disk, and is partly reflected and partly absorbed, giving rise to fluorescent  $K\alpha$  lines, of which the most prominent is the iron line at 6.4 KeV (see black solid line in Fig. 1.2). When detected with sufficient spectral resolution, this emission line shows a distorted, asymmetrical shape, which has been interpreted as evidence of general relativistic effects, placing the emitting material in the innermost regions of the accretion disk (e.g., Tanaka et al. 1995; Nandra et al. 1997). Modeling the shape of the Fe  $K\alpha$  line can provide an estimate of the spin of the SMBH (e.g., Fabian et al. 2009).

### 1.1.2 The emission-line regions

The presence of strong emission lines in the optical spectrum was one of the telltale signs that AGN were a novel kind of astronomical source in the earlier studies. In some sources, some of the lines appeared as exceptionally broad, with

widths of the order of  $(10^3 - 10^4)$  km/s, while others showed narrow profiles with  $\Delta v \sim 10^2$  km/s. The lines are due to material orbiting the SMBH, ionized by the continuum emission from the accretion disk and corona (e.g., Peterson 1997, chapters 5 and 6, and references therein). Additionally, the narrow lines include several so-called “forbidden” transitions. These transition cannot be observed naturally on Earth since the particle density is high enough so that it is much more likely that particles in excited states will decay collisionally, and not radiatively. Because of this, the fact that we do observe a certain forbidden line implies an upper limit on the density of the line-emitting gas, which is usually of the order of  $n_e \sim 10^3 \text{ cm}^{-3}$ . On the other hand, the inferred densities for the gas producing the broad lines is estimated to be  $n_e > 10^9 \text{ cm}^{-3}$  (Peterson 1997). Due to the different inferred locations and physical properties, it was concluded that the broad and narrow lines come from distinct regions, which are called Broad Line Region (BLR) and Narrow Line Region (NLR). Indeed, assuming that the emission lines comes from clouds of gas in Keplerian motion around the SMBH, and that their width is given by Doppler broadening produced by their orbital speed, their different width translates into different orbital distances. The broad lines being produced closer to the AGN central engine, at distances smaller than one parsec, while the NLR gas is estimated to be  $\sim 10^2$  parsecs away.

### 1.1.3 The dusty absorber

Interestingly, sources which lack broad lines also show a much weaker, redder continuum, and appear less bright in X-rays. This suggests that radiation from the central engine and the BLR is being absorbed by an intervening structure of dense material along our line of sight, whose size should be smaller than the distance between the SMBH and the NLR (Antonucci & Miller 1985). The absorber would be heated by the radiation from the central engine, and emit thermal radiation in the mm-FIR band (Barvainis 1987). This component is indeed observed in the SED of AGN, and is the main contributor to the emission in this band in non-jetted AGN (see solid black line in Fig. 1.2). Since this obscuring structure only appears in some AGN, it was immediately assumed that this absorber should have a toroidal shape (Antonucci & Miller 1985). There is compelling evidence that the torus is not uniform, but has a clumpy morphology with different clouds of material, as testified by the observation of variable X-ray absorption (Markowitz et al. 2014). The scale of the torus may depend on the luminosity of the central engine (Lawrence 1991, but see also, e.g., Stalevski et al. 2016), and is usually of the order of one parsec.

The fact that a BLR is present also in sources which do not normally show broad lines is demonstrated by the observation of such lines in polarized light (Antonucci & Miller 1985). The BLR emission is scattered on the inner torus, and reflected with a preferred polarization due to the orientation of the dust grains. This observation confirms the hypothesis that AGN have the same basic components, and the different observed varieties are due to different viewing angles of the system, since the torus breaks the spherical symmetry (see Fig. 1.1).

## 1.2 The unified model of AGN

The idea that the anisotropy of the AGN central structure could explain and unify many of the various observed subclasses gained momentum in the 1980s, and found its full realization in the following decade, when it was formulated in a complete way most notably by Antonucci (1993) and Urry & Padovani (1995).

### 1.2.1 Radio-quiet unification

Considering only non-jetted AGN, the orientation with respect to the dusty torus and the intrinsic luminosity of the source were isolated as the only two parameters driving the different realizations of the AGN phenomenon.

Based on orientation, AGN can be divided into:

- **Type 1** - the central system is viewed in such a way that the accretion flow and the BLR are not obscured by the torus. As a result we observe bright X-ray emission and a blue optical continuum, with both narrow and broad spectral lines (see top panel of Fig. 1.3).
- **Type 2** - the dusty torus intersects our line of sight towards the SMBH, so that the emission from the central engine and the BLR is strongly absorbed. Therefore we observe much weaker X-ray emission, and a redder optical spectrum with only narrow lines (see bottom panel of Fig. 1.3). Broad lines can be observed in polarized emission.

On the other hand, non-jetted AGN can be divided based on luminosity:

- **Seyfert** - these are typically local sources. Due to the low AGN luminosity, it is still possible to observe the host galaxy, which is typically of spiral morphology.

- **QSO** - or Quasi-Stellar Objects, are luminous sources dominated by the compact emission from the AGN. They are typically found at high-redshift.

Therefore, a low-luminosity non-jetted AGN where the torus is viewed face-on, will be classified as Seyfert 1, while the same object with the torus viewed edge-on will appear as a Seyfert 2. The same is true for the high-power counterparts of these systems, which can be observed as Type 1 QSO or Type 2 QSO.

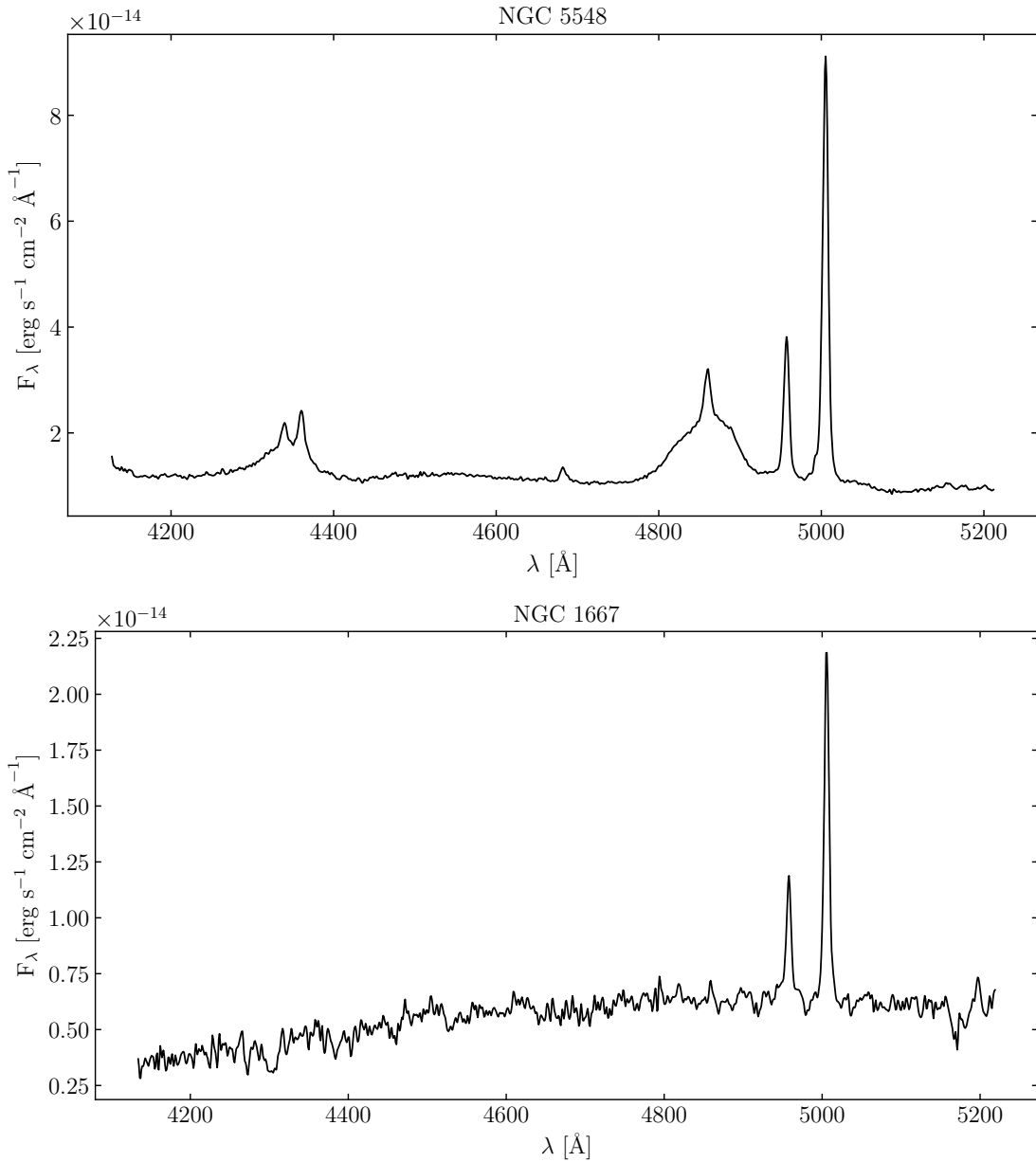


FIGURE 1.3: Optical nuclear spectrum of the Seyfert 1 galaxy NGC 5548 (top panel) and the Seyfert 2 galaxy NGC 1667 (bottom panel). Note the co-existence of broad and narrow lines in the former case, and only of narrow lines in the latter. Adapted from Ho et al. (1995). Data from the double spectrograph at the Palomar 5.1 meter telescope.

### 1.2.2 Radio-loud unification

The third, and probably most important parameter that allowed astronomers to distinguish between different AGN classes, is the presence or absence of a relativistic jet, produced in the vicinity of the SMBH. These jets, and the large scale structures they produce, completely change the look of the AGN SED, as can be seen in Fig. 1.2. The jet emission produces a characteristic double-peaked SED, with one peak occurring usually in the mm-IR band, and another in the  $\gamma$ -ray band. The first high-redshift AGN discovered, i.e., quasars, and the sources found in the first radio catalogs, belong to this class. Since they were first discovered in the radio band, they are usually referred to as *radio-loud* (RL) AGN, while non-jetted AGN are called *radio-quiet* (RQ). RQ AGN represent the vast majority of AGN ( $> 90\%$ , Padovani 2011). Historically, this division has been based on flux density ratios between the radio and optical (Kellermann et al. 1989) or X-ray bands (Terashima & Wilson 2003), since RL AGN are typically orders of magnitude brighter in the radio w.r.t. RQ sources (see Fig. 1.2). However, it has been noted that these criteria are not general enough, since the measured fluxes can be contaminated by emission components unrelated with the jet in some sources (Padovani 2017).

The presence of narrow, well-collimated relativistic jets adds another anisotropic component to the AGN picture. Since the emitting material has a relativistic velocity component towards the observer, the appearance of a source will change dramatically whether we are seeing the jet at a close angle with our line of sight, or in the plane of the sky. These effects will be discussed in depth in Section 1.3.1, while the emission processes occurring in the jets will be described in Section 1.3.2. Here I simply introduce the nomenclature associated with the unified model of jetted AGN.

- **Blazars** - when the jet is closely aligned with our line of sight, relativistic effects strongly boost the observed radiation and shorten its variability time scales. As a result, the SED of blazars is completely dominated by the non-thermal jet emission. These sources can be further divided into two subclasses:
  - **FSRQ** or Flat Spectrum Radio Quasars - the jet emission in these sources typically peaks in the mm-to-NIR band and at MeV-GeV  $\gamma$ -rays, respectively. FSRQs host highly efficient accretion disks, which emit brightly in the optical-UV band (see the red dotted line in Fig. 1.2), with strong broad line emission. They are typically high-redshift sources.

- **BL Lac** - the jet emission in these sources typically peaks in the optical-UV-soft X-rays band and at TeV  $\gamma$ -rays, respectively. The peculiarity of these sources, named after the prototype source BL Lac, is in their almost featureless optical spectrum. The absence of observed emission lines could be either intrinsic, or due to the position of the low-energy SED peak of the non-thermal jet emission, which could swamp any other contribution in the optical-UV band. BL Lacs are typically much more local sources than FSRQs.
- **Radio galaxies** - when the jet is oriented away from our line of sight, its radiation is much less affected by relativistic effects. Specifically, it is much fainter across the whole SED, allowing us to discern additional components such as the AGN host galaxy in the optical, and large scale radio structures formed when the jets interact with the interstellar medium (ISM). Radio galaxies can be divided in two classes based on the total radio power at 1.4 GHz (Fanaroff & Riley 1974), which also correspond to a different morphology of the large scale structure:
  - **FR I** or Fanaroff-Riley type 1 - the jet is bright and usually double-sided. It becomes non-relativistic between the pc and kpc scales, often showing an irregular structure. The jet is much brighter than the diffuse lobes created by its interaction with the ISM.
  - **FR II** or Fanaroff-Riley type 2 - the jet is fainter, often one sided and more collimated, and still relativistic up to kpc scales. The radio emission is dominated by bright, compact regions at the interface between the radio lobes and the ISM, called hot-spots.

It is believed that FR I and FR II radio galaxies represent the misaligned parent population of BL Lacs and FSRQs, respectively (Urry & Padovani 1995, see Fig. 1.1). Since the inner region of jetted AGN includes the same building blocks as RQ AGN, they also fall into the different classes determined by the other parameter of the unified models, i.e., the orientation w.r.t the obscuring torus. As described in the upper half of Fig. 1.1, a radio galaxy where the torus does not obscure the central engine is called a Broad Line Radio Galaxy (BLRG), while its obscured counterpart would be a Narrow Line Radio Galaxy (NLRG). With regard to the remaining unified model parameter, i.e., the luminosity of the central engine, it is believed that FR Is host inefficient, underluminous accretion flows, while FR IIs host highly efficient, luminous disks (Ghisellini & Celotti 2001). The complete picture of the orientation-based unified scheme is depicted in Fig. 1.1, for RL AGN in the top half and RQ AGN in the bottom half.

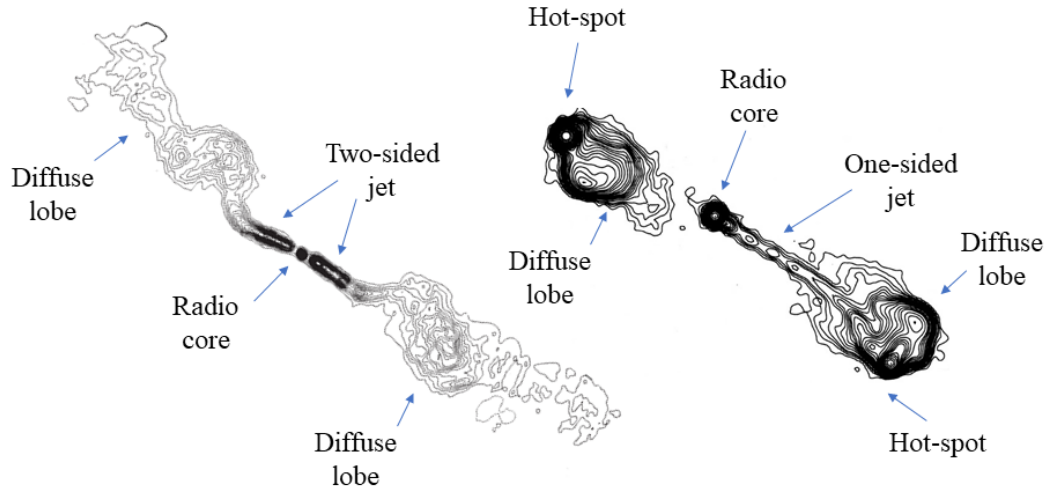


FIGURE 1.4: Schematic view of the large scale structure of classic radio galaxies. *Left side*: The FR I source 3C 449, with the characteristic symmetric jets, and irregular, faint diffuse lobes. Image adapted from Perley et al. (1979). *Right side*: the FR II source 3C 175, with the typical one sided jet and bright hot-spots. Image adapted from Bridle et al. (1994).

### 1.3 Properties of relativistic jets from supermassive black holes

In this section I will outline the basic properties of AGN jets which are relevant to this thesis work.

#### 1.3.1 Relativistic effects

##### Doppler boosting

In radio-loud AGN the observed non-thermal emission is produced by a population of particles residing in the jet, which moves with bulk relativistic speed. This implies two different effects. The emitted radiation is beamed in the direction of motion, with an angle given by  $\theta_b \sim 1/\Gamma$ , where  $\Gamma = (1 - \beta^2)^{-1/2}$  is the bulk jet Lorentz factor, with  $\beta = v/c$ . Moreover, the more the jet is aligned with the observer's line of sight (l.o.s.), the more the emitted radiation is boosted by relativistic Doppler effect.

To see this, we consider the specific intensity emitted by a single component moving with the jet's bulk velocity, i.e., the emitted flux per unit frequency and solid angle. In the observer's reference frame, this would be

$$I(\nu) = \frac{h\nu dN}{dt d\nu d\Omega dA} \quad (1.5)$$

Considering the relativistic transformation of frequencies, time, and solid angle, between the observer's frame and the jet rest frame, i.e. (Ghisellini 2013),

$$\begin{aligned} \nu &= \delta \nu' \\ d\nu &= \delta d\nu' \\ dt &= dt' / \delta \\ d\Omega &= d\Omega' / \delta^2 \\ &, \end{aligned} \quad (1.6)$$

we obtain the result

$$I(\nu) = \delta^3 I'(\nu'), \quad (1.7)$$

where  $\delta = \{\Gamma[1 - \beta \cos(\theta)]\}^{-1}$  is the Doppler factor, and  $\theta$  is the viewing angle. Integrating over frequencies we obtain the flux transformation

$$F = \delta^4 F'. \quad (1.8)$$

This orientation-dependent effect is the reason for the differences in the observed emission coming from blazars and radio galaxies, as mentioned above, since the dependency of the observed flux on the Doppler factor is so strong. As illustrated in the left panel of Fig. 1.5, the Doppler factor rises quite sharply for relativistic jets viewed at angles  $\lesssim 10^\circ$ . This value is therefore taken as an indicative transition point between the blazar and radio galaxy classes.

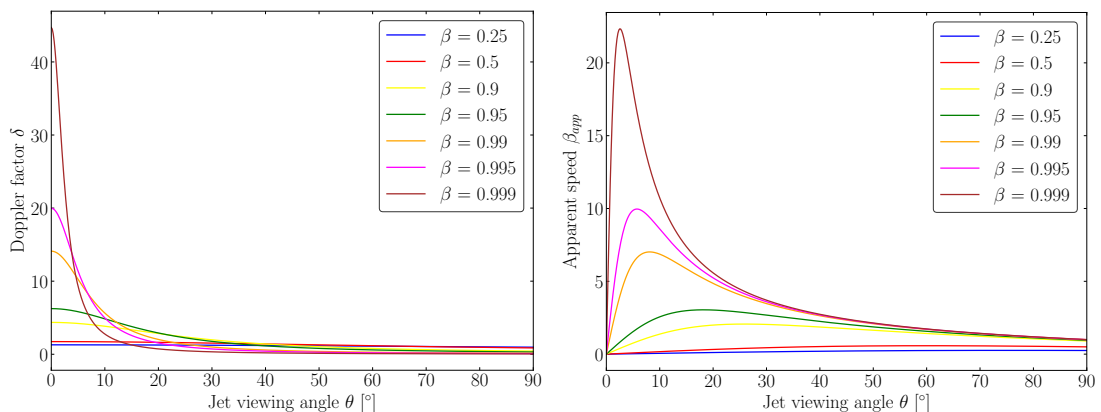


FIGURE 1.5: Jet Doppler factor  $\delta$  (left panel) and apparent speed  $\beta_{app}$  (right panel) as a function of jet viewing angle for different values of intrinsic jet speed  $\beta$ .

### Superluminal motion

Shortly after the identification of 3C 273 with a distant quasar, Rees (1966) predicted that if such a radio source expands with relativistic speed in the direction of the observer, it should be possible to measure speeds larger than the speed of light, simply because of the geometrical configuration under which the system is viewed. A few years after, Gubbay et al. (1969) reported the first detection of such superluminal apparent speeds using radio interferometric observations of 3C 273. This phenomenon was then observed in several other sources, and was established as one of the most common features observed in the pc-scale jets of strong radio sources (see e.g., Zensus 1997, and references therein).

The dependence of the measured apparent speed as a function of the intrinsic jet parameters can be easily derived. In the schematic representation of Fig. 1.6, suppose that  $O$  is the observer, while  $A$  is the jet core.

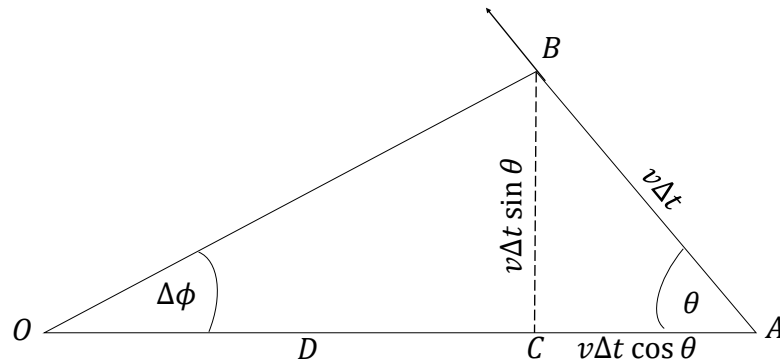


FIGURE 1.6: Schematic representation of the geometrical configuration leading to the effect of apparent superluminal speed.

Suppose a moving emission component is launched by the jet core with a speed  $v$  at an angle  $\theta$  with our line of sight, and in a time  $\Delta t$  reaches the position  $B$ . The observer can only measure the angular separation between  $A$  and  $B$ , and the time difference between the component ejection and the time it reaches the point  $B$ . Assuming the distance to the source ( $D$ ) is known, the angular separation is given by  $\Delta\phi = v\Delta t \sin(\theta)/D$ . For the observer, the component is emitted at time  $t_1 = [D + v\Delta t \cos(\theta)]/c$ , and is seen to reach  $B$  at  $t_2 = \Delta t + D/c$ , measuring a time difference  $\Delta t' = t_2 - t_1 = \Delta t + D/c - [D + v\Delta t \cos(\theta)]/c = \Delta t[1 - \beta \cos(\theta)]$ , where  $\beta = v/c$ . The apparent transverse velocity of the component, will therefore be  $\beta_{\text{app}} = D\Delta\phi/c\Delta t'$ , which results to be

$$\beta_{\text{app}} = \frac{\beta \sin(\theta)}{1 - \beta \cos(\theta)} \quad (1.9)$$

As can be seen in the right panel of Fig. 1.5, the apparent speed can reach values much larger than the speed of light, for a relativistic jet well-aligned with our line of sight.

### 1.3.2 Radiative processes

In this section we give a brief overview of the main physical processes responsible for the emission observed in radio-loud AGN, concentrating on the non-thermal ones. For a detailed discussion see Rybicki & Lightman (1979), or the recent review by Ghisellini (2013).

#### Synchrotron emission

The synchrotron emission process accounts for the low-energy component in the SED of radio-loud AGN, which for this reason is often referred to as the synchrotron component, or peak (see e.g. Fig. 1.2).

The synchrotron process occurs when a charged relativistic particle is accelerated in a magnetic field. When a particle with charge  $e$  and Lorentz factor  $\gamma$  travels through a uniform and static magnetic field  $B$ , it will experience a Lorentz force perpendicular to its direction, and therefore will travel with constant velocity in the direction of the field but with a circular motion in the perpendicular plane, i.e., will spiral around the direction of the field, with a frequency

$$\nu = \frac{eB}{2\pi\gamma mc}. \quad (1.10)$$

When a charged particle accelerates it radiates energy, and in this case the radiated luminosity is given by (Rybicki & Lightman 1979)

$$L_{\text{syn}} = \frac{4e^4 B^2 E^2}{9m^4 c^7} \propto B^2 E^2 \quad (1.11)$$

where  $E$  is the energy of the particle. An artistic representation of the synchrotron process is given in Fig. 1.7.

In radio-loud AGN, synchrotron emission is produced by an ensemble of relativistic electrons. The total emission can be calculated by integrating over the energy distribution of the electrons. Assuming that this distribution is a power-law of the form  $N(E) = N_0 E^{-\delta}$ <sup>2</sup>, the resulting emission spectrum is also a power-law, with a flux density  $S_{\text{syn}}(\nu) \propto \nu^{-\alpha}$ , where the spectral index is  $\alpha = (\delta - 1)/2$ , and has typical values of  $0.5 < \alpha < 1$ . This spectral form is valid if the

<sup>2</sup>This is supported by observations of the energy spectrum of cosmic rays, which are believed to be accelerated through similar processes.

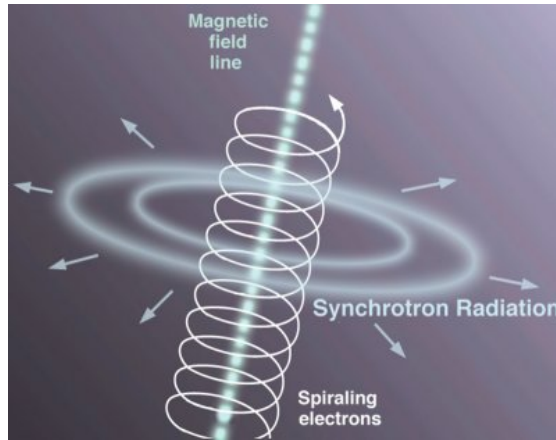


FIGURE 1.7: Artistic representation of the synchrotron emission process. Image: Jon Lomberg/Gemini Observatory.

electrons are optically thin with respect to their emitted photons. This is only true above a critical frequency  $\nu_{\max}$ . Below this frequency a significant fraction of the synchrotron photons is absorbed by interactions with the same emitting electrons (a process called *Synchrotron Self-Absorption*, or SSA). The overall spectrum is therefore given by

$$S_{\text{syn}}(\nu) \propto \begin{cases} \nu^{5/2}, & \text{for } \nu < \nu_{\max} \\ \nu^{-\alpha}, & \text{for } \nu > \nu_{\max} \end{cases} \quad (1.12)$$

Moreover, at still higher frequencies the most energetic electrons lose energy more rapidly, therefore there is a cutoff due to these radiative losses. Fig. 1.8 shows a typical synchrotron spectrum.

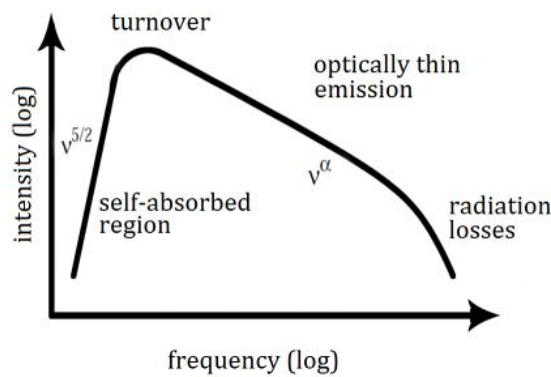


FIGURE 1.8: Schematic representation of a typical synchrotron spectrum. The spectral index  $\alpha$  is assumed to be negative in the figure. Credit: Special Astrophysical Observatory of the Russian Academy of Sciences (URL: <http://www.sao.ru/hq/giag/gps-en.html>).

### Inverse Compton emission

The Inverse Compton (IC) process takes place when a low-energy photon interacts with an ultra-relativistic particle, and is upscattered to higher energies. This process is the most popular and simple assumption which is made to explain high-energy emission from radio-loud AGN, although it has become clear that it cannot be the only relevant emission process at these energies.

The frequency of the observed photon after the scattering is related to its original frequency by a factor  $\nu' \sim \gamma^2\nu$ , so the photon's energy gain is  $E' \sim \gamma^2E$ , where  $\gamma$  is the electron Lorentz factor. For interactions with ultra-relativistic electrons, this factor can be large enough to upscatter a photon from the radio-IR band up to the X-ray and  $\gamma$ -ray band.

The luminosity produced at high energy via the IC process depends on the electron Lorentz factor, on the density of seed photons, and on the photon-electron cross section, therefore it is given by

$$L_{IC} = \frac{4}{3} \frac{v_e^2}{c} \sigma_T \gamma^2 U_{ph} \propto \gamma^2 U_{ph} \quad (1.13)$$

where  $U_{ph}$  is the energy density of the seed photon field and  $\sigma_T$  is the Thomson cross section. This expression is valid for photon energies  $h\nu \ll m_e c^2$ , and represents the so called Thomson scattering regime. For higher seed photon energies, the process occurs in the Klein-Nishina regime, where the cross section is reduced as the photon energy increases, thus decreasing the luminosity. The IC spectrum then cuts off quite sharply at high energies. Eventually, for very high seed photon energies the luminosity becomes negative and the photon loses energy to the electron, going back to the direct Compton scattering.

In radio-loud AGN, the seed photons for the IC process may come from two main sources. If these photons are the synchrotron photons emitted by the same relativistic particles responsible for the IC scattering, the process is called *Synchrotron Self Compton* (SSC). If, on the other hand, the low-energy seed photons come from an external source, such as the AGN accretion disc, the line-emitting regions, the torus or the Cosmic Microwave Background (CMB), then the process is called *External Compton* (EC).

In the case of SSC, it can be shown that the ratio of the IC luminosity to the synchrotron luminosity is simply given by the ratio of the energy densities of the seed photon field and of the magnetic field

$$\frac{L_{IC}}{L_{syn}} = \frac{U_{ph}}{U_B} \quad (1.14)$$

The peak frequencies of the two components of the SED (synchrotron and SSC), are related by the simple IC relation mentioned before, i.e.,  $\nu_{IC} \sim \gamma_{\max}^2 \nu_{\text{syn}}$ , where  $\gamma_{\max}$  is the maximum Lorentz factor in the electron distribution.

### Hadronic models

The emission processes discussed above have been used to explain the total non-thermal emission of radio-loud AGN, from radio to TeV energies. This radiation is therefore attributed to a population of relativistic electrons accelerated by the central engine of the AGN, and for this reason these models are called *leptonic* emission models. Although they have proven to be generally successful in explaining the SED of radio-loud AGN, there are now several cases of TeV detected AGN (mostly high-energy peaked BL Lacs, HBLs), in which they cannot account for the observed VHE radiation, without an unrealistic fine tuning of the model parameters (see e.g., Cerruti et al. 2015, and references therein).

For this reason, *hadronic* or *lepto-hadronic* models have been developed. In these models, a leptonic population is associated with the low-energy component of the SED, and to the MeV-GeV  $\gamma$ -ray portion of the high-energy component, via SSC processes. An ultra-relativistic hadronic (i.e., proton) component is also considered, which can interact with low-energy photons forming pions (both neutral and charged), or  $e^+e^-$  pairs. These particles can interact again with the low-energy photon field, giving rise to electromagnetic cascades. The resulting emission is then a combination of synchrotron emission from protons and from  $e^+e^-$  pairs produced either by  $p\gamma$  interactions,  $\gamma\gamma$  interactions or pion decay. These models have been proven to give an acceptable reproduction of the SED of blazars, particularly at high and very high energies (Cerruti et al. 2015).

Due to the much higher mass of hadronic particles, the presence of ultra-relativistic protons in AGN jets also implies very high jet powers, often exceeding the amount of energy produced in the accretion process (Ghisellini et al. 2014). This would favor models in which the jet power is provided not only by accretion, but also by the extraction of rotational energy from a highly spinning SMBH. This is possible if a large magnetic flux is accumulated in the vicinity of the SMBH, as predicted by the so called Magnetically Arrested Disk (MAD) models (Tchekhovskoy et al. 2011; Zamaninasab et al. 2014).

An interesting byproduct of considering an hadronic component in radio-loud AGN is the possibility to identify them as the sources of the Ultra-High-Energy Cosmic Rays (UHECRs) observed on Earth, which reach energies up to  $10^{20}$  eV (Kotera & Olinto 2011), and cannot be produced by galactic sources. Providing evidence

for the presence of protons accelerated at extreme energies would then constitute a plausible solution to this problem.

Additionally, hadronic processes in AGN could also provide plausible sources for the PeV neutrinos recently observed by the IceCube detector, which have been confirmed to be of astrophysical origin (Aartsen et al. 2013, 2016). Direct association of single neutrino detections with individual sources is extremely challenging, due to the poor neutrino localization. Such an association has been proposed by Kadler et al. (2016), who noted how the detection of a  $\sim 2$  PeV neutrino by IceCube in December 2012 (Aartsen et al. 2014) was coincident with a prolonged elevated  $\gamma$ -ray flux of the blazar source PKS B1424–418, as well as a factor  $\sim 3$  increase in its parsec-scale radio core flux. The long duration and luminosity of the outburst was found to be able to explain the neutrino flux inferred from the IceCube detection, and the chance coincidence of these coordinated events was estimated to be of the order of  $\sim 5\%$ . Previously, Krauß et al. (2014) showed how the observed high-energy flux from the six brightest blazars positionally consistent with the astrophysical IceCube neutrinos is sufficient to explain the inferred neutrino flux, if the X-ray to  $\gamma$ -ray emission of these sources is attributed to hadronic processes. Very recently, the association of PeV neutrinos with blazars has been definitively proven, thanks to the detection of an astrophysical neutrino detection with a relatively good localization, which was found to coincide with a GeV and TeV outburst of the blazar TXS 0506+056 (IceCube Collaboration et al. 2018, and companion papers).

## Chapter 2

# The puzzle of $\gamma$ -ray emission in radio galaxies

In this Chapter we will discuss the current understanding of high-energy  $\gamma$ -ray emission from radio galaxies.  $\gamma$ -ray instrumentation and data analysis will be discussed in detail in Chapter 3.

In our earliest view of the  $\gamma$ -ray sky, very few sources were associated with credible counterparts. For example, in the second COS-B catalog (2CG, Swanenburg et al. 1981), only four objects were proposed as counterpart to one or multiple  $\gamma$ -ray sources. One of these was the blazar 3C 273, the only AGN to appear in the catalog. It was with EGRET instrument, on board the Compton Gamma-ray Observatory (CGRO), that AGN started to populate the high-energy sky, with 67 detections in total. All of these sources belonged to the blazar class, except one, which provided the first detection of a radio galaxy above 100 MeV: unsurprisingly, this was the closest AGN to earth, i.e. Centaurus A (Sreekumar et al. 1999). Shortly after, another EGRET source was suggested to be associated with the radio galaxy NGC 6251 (Mukherjee et al. 2002). The third  $\gamma$ -ray detected radio galaxy was M 87, which was detected above 730 GeV by the HEGRA Cherenkov telescope (Aharonian et al. 2003), and then confirmed as VHE emitter by the H.E.S.S. array above 400 GeV (Aharonian et al. 2006). These first detections paved the way to more systematic studies of  $\gamma$ -ray emission in radio galaxies, that only started to become feasible with the launch of the *Fermi* space telescope.

### 2.1 The *Fermi*-LAT view of radio galaxies

The improved sensitivity of the *Fermi*-LAT with respect to EGRET quickly resulted in the detection of more radio galaxies in the MeV-GeV range, based on

the first few months of data, i.e. NGC 1275 (Abdo et al. 2009a) and M 87 (Abdo et al. 2009b). Additionally, not only the LAT confirmed the EGRET detection of  $\gamma$ -ray emission from Cen A (Abdo et al. 2010b), but also detected for the first time diffuse  $\gamma$ -ray emission from its giant radio lobes (Abdo et al. 2010c), contributing more than half of the total  $\gamma$ -ray flux from the radio galaxy.

In well-aligned blazar jets, the observed emission is strongly affected by relativistic Doppler boosting (see Section 1.3.1). In energy bands where the sensitivity of astronomical instruments is limited, such as the  $\gamma$ -ray range, these effects have a large impact on the population statistics of sources with different jet angles. In the latest *Fermi*-LAT source catalog (Acero et al. 2015), blazars are by far the most populous class among the associated extragalactic  $\gamma$ -ray sources <sup>1</sup>, with a total of more than 3000 objects. On the other hand, the LAT has detected only about 20 radio galaxies at the moment.

Abdo et al. (2010d) discussed the overall properties of misaligned AGN using the first 15 months of LAT data. They found that the average observed flux is low, of the order of  $F_{>100\text{MeV}} \sim 10^{-8}$  photons  $\text{cm}^{-2} \text{s}^{-1}$ , while the typical spectral shape is a relatively steep power-law, with seven sources having photon index larger than  $\sim 2.3$ . The FR I-FR II dichotomy is found to reflect in the  $\gamma$ -ray properties of radio galaxies as well, with FR IIs being typically brighter and with a steeper spectrum, and FR Is being fainter and with harder spectra. These features reproduce the dichotomy between BL Lacs and FSRQs, corroborating the orientatio-based unified model of jetted AGN (see Section 1.2.2).

Grandi et al. (2012a) pointed out that in this initial sample, FR I sources appeared to be significantly more numerous than FR IIs. This statistical feature becomes more evident by looking at the  $\gamma$ -ray-to-radio detection rate, which is much lower in FR II sources than in FR Is. The simplest interpretation of this statistical behavior is to associate the paucity of LAT-detected FR IIs with their larger redshift (on average) with respect to FR Is, but this hypothesis does not seem to be supported by the data. Another interpretation is based on the hypothesis that the main  $\gamma$ -ray emission mechanism is Synchrotron Self Compton (SSC) for FR Is and External Compton (EC) for FR IIs. In the latter case the Doppler boosting of the upscattered photons is stronger, and the beaming cone is narrower than in the case of SSC. Therefore, the beaming difference between these two processes could explain the lower  $\gamma$ -ray detection rate of FR IIs, because a narrower beaming cone implies stronger deboosting of radiation for a jet not aligned with the observer's line of sight. This hypothesis is supported by studies of the AGN environment of radio galaxies, that show a richer photon field for FR IIs, produced by e.g. an

---

<sup>1</sup>Most of the unassociated or unidentified sources at high galactic latitude ( $|b| > 10^\circ$ ) are also believed to be likely blazar candidates (e.g., Salvetti et al. 2017).

efficient accretion disk, the line-emitting regions or the torus, capable of providing abundant seed photons for the EC process, with FR Is characterized in turn by a poorer thermal photons environment, and thus more likely to emit at high energies via SSC (Torresi 2012).

## 2.2 The connection between radio and $\gamma$ -ray emission in radio-loud AGN

Since radio and  $\gamma$ -ray emission processes both involve non-thermal particles interacting with a magnetic field, or with each other, it is natural that the high-energy emission and the radio VLBI properties we observe should be related.

A significant relationship between  $\gamma$ -ray emission and VLBI jet properties was already found before the launch of *Fermi*, using Very Long Baseline Array (VLBA) and EGRET data. Taylor et al. (2007) found that EGRET-detected sources tended to have higher core brightness temperature and core dominance, two common indicators of high Doppler factors.

Less than a year after the launch of *Fermi*, Kovalev et al. (2009) investigated the connection between the VLBI properties of AGN monitored in the MOJAVE program and their  $\gamma$ -ray emission detected by the LAT in its first three months of survey. They found a positive correlation between between the total VLBI flux and the LAT flux, and that LAT-detected MOJAVE sources have higher total VLBI flux than non-detected sources. The same study also found that LAT-detected sources have preferentially high median core brightness temperature. The MOJAVE team also compared the early LAT detections with the measured apparent jet speed in Lister et al. (2009b), and found that LAT sources show faster jets on average, and also that variable  $\gamma$ -ray AGN show faster apparent motions.

These findings consistently suggest that Doppler boosting plays a key role in determining the  $\gamma$ -ray brightness and variability of blazars.

Ackermann et al. (2011) studied the correlation between the  $\gamma$ -ray properties of AGN after one year of LAT survey, and radio emission observed with the VLA, ATCA and the OVRO 40m telescope, testing any correlation against common dependencies on distance and the effects of limited flux and luminosity range. They found a moderate-to-high significance for correlations between radio emission and  $\gamma$ -ray emission. This study also found that the strength of the correlations increases when using concurrent radio and  $\gamma$ -ray measurements, rather than archival data, a fact that was expected due to the variable nature of AGN emission.

All the aforementioned studies deal with large, heavily blazar-dominated AGN samples, and do not discuss radio galaxies as a separate class of  $\gamma$ -ray emitters, due to their small number of detected sources.

### 2.3 VLBI kinematics and $\gamma$ -ray variability

There have been several studies linking the observed temporal behavior of  $\gamma$ -ray emission from radio galaxies to changes in their inner pc-scale jet, as revealed by milliarcsecond resolution VLBI observations in the radio band.

Grandi et al. (2012b) studied the  $\gamma$ -ray emission of the FR II radio galaxy 3C 111 on monthly time scales using the first two years of LAT data. 3C 111 is a faint  $\gamma$ -ray emitter, and therefore, as most radio galaxies, it was undetected in most of the months analyzed, except for one. Interestingly, the only month when the source was in a higher  $\gamma$ -ray state coincided with a multi-wavelength elevated state, as evidenced by mm-band radio, optical, and X-ray data (see Fig. 2.1), provided as part of a campaign by Chatterjee et al. (2011).

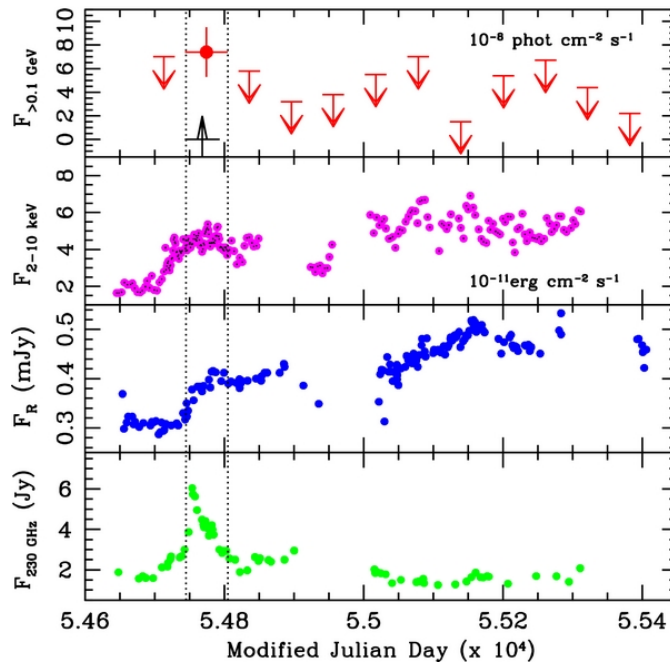


FIGURE 2.1: Fig. 2 from Grandi et al. (2012b). Multi-wavelength light curves of 3C 111. Top to bottom: *Fermi*-LAT ( $\gamma$ -rays), *RXTE* (X-rays), Liverpool/Perkins (optical), SMA (mm-band).

Moreover, high-resolution radio images at 43 GHz from the Boston University blazar monitoring program reveal that the multi-wavelength activity coincided

with the ejection of a new compact emission component from the radio core (Chatterjee et al. 2011). This, together with the time scale of the observed  $\gamma$ -ray variability, suggests that the  $\gamma$ -ray emission region is located within a distance of less than 0.3 pc from the central SMBH fueling the AGN.

Casadio et al. (2015) studied the evolution of the pc-scale radio jet of the peculiar radio galaxy 3C 120 during a period of elevated  $\gamma$ -ray activity between 2012 and 2014. While 3C 120 shows an FR I-like extended structure (Walker et al. 1987), its innermost jet and accretion flow are much more alike to an FR II source (Torresi 2012). They found that every period coincident with a  $\gamma$ -ray detection corresponds to the ejection of a new component from the radio core. However, the reverse is not true: not all component ejections coincide with a  $\gamma$ -ray elevated state. This seems to be true only for components ejected at smaller angles with our line of sight. Janiak et al. (2016) analyzed *Fermi*-LAT data from a second, much brighter flaring episode from 3C 120 in 2015, and they successfully modeled it as being due to the jet spine being temporarily aligned with our line of sight, an idea that goes along the same lines of the interpretation provided by Casadio et al. (2015).

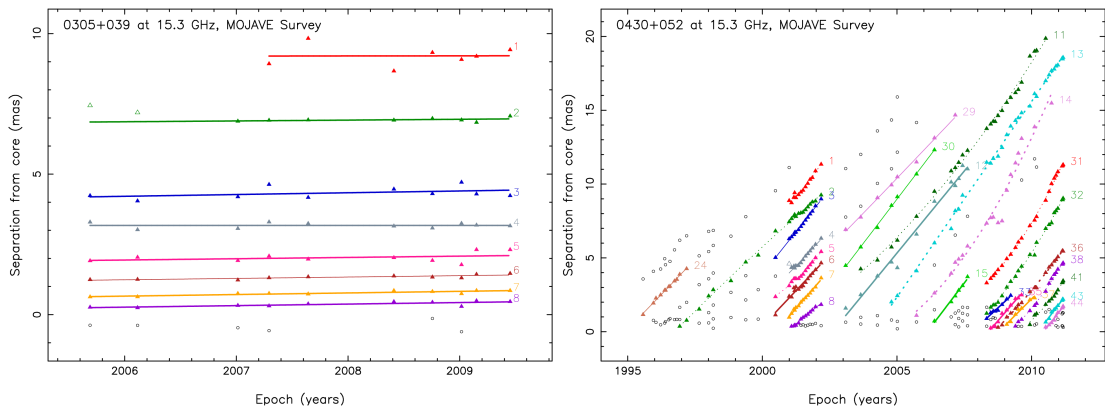


FIGURE 2.2: Core distance of fitted Gaussian components versus time, with linear fits, from MOJAVE 15 GHz VLBA observations (Lister et al. 2013). *Left panel:* the FR I radio galaxy 3C 78. *Right panel:* the FR II-like radio galaxy 3C 120. Both sources are detected by the *Fermi*-LAT.

At the moment, such a connection between VLBI kinematics and  $\gamma$ -ray variability hasn't been studied in any FR I source. The two radio galaxy classes exhibit distinct properties in both aspects.

For what concerns the pc-scale jet kinematics, FR I sources tend to show slow-moving jets with subluminal apparent speed, and few ejection of new compact components (see Lister et al. 2013, 2016, for the cases of 3C 78 and M87, respectively), while FR II sources often show apparent superluminal component motion and frequent ejections of new components (see Lister et al. 2013, for the cases of 3C 111 and 3C 120). An example for each source class is shown in Fig. 2.2, where

the different behavior is particularly evident. This pattern has also been identified in the VLBI kinematic properties of blazars, with BL Lacs showing slower jet speeds, and FSRQs showing fast moving components and frequent ejections (Hervet et al. 2016), a finding which supports the unified model of jetted AGN.

A different behavior in FR I and FR II radio galaxies has also been identified in the  $\gamma$ -ray variability. Grandi et al. (2013) studied the variability properties of *Fermi*-LAT detected radio galaxies using the first two years of LAT data, and found that FR I sources show stable emission, being detected for  $\sim 70\%$  of the given time range, while FR II sources were only detected during short-lived flaring states, with a duty cycle of less than  $\sim 30\%$ . Since FR I radio galaxies do not tend to show flaring episodes associated to VLBI component ejections, it hasn't been possible to establish a link between  $\gamma$ -ray emission and pc-scale jet properties in this sources, as it has been done for FR IIs. When FR I sources do show fast  $\gamma$ -ray variability, as in the case of the peculiar object IC 310 (Aleksić et al. 2014), this does not appear to be accompanied by changes in the pc-scale jet (Schulz 2016).

## Chapter 3

# $\gamma$ -ray astronomy

### 3.1 Historical notes

Since X-rays and  $\gamma$ -rays are strongly absorbed by the Earth's atmosphere, high-energy astronomy could only see its first light when it became possible to place detectors above all or most of the atmosphere, using balloons in the early days, and later with space telescopes.

The first  $\gamma$ -ray detector was carried on board of the *Explorer 11* satellite, in 1961. The detector measured a total of  $\sim 100$  photons, which were attributed to a uniform  $\gamma$ -ray background produced by the interaction of cosmic rays with the ISM (Kraushaar et al. 1965). About a decade later, the space telescope COS-B (1975-1982, Bignami et al. 1975) confirmed the detection of a  $\gamma$ -ray background and produced the first point source catalogs, including up to 25 objects (2CG Swanenburg et al. 1981). The first sensitive all-sky  $\gamma$ -ray survey at energies above 100 MeV came in the 90s, thanks to the *Compton Gamma-ray Observatory* (*CGRO*, 1991-2000), and especially its Energetic Gamma-Ray Experiment Telescope (EGRET, e.g. Thompson et al. 1993). *CGRO* contributed breakthrough observations of AGN, pulsars, Gamma-ray Bursts (GRBs), solar flares and diffuse  $\gamma$ -ray emission, increasing the number of  $\gamma$ -ray sources by an order of magnitude, with a total of 271 objects in the last EGRET source catalog (Hartman et al. 1999).

### 3.2 The *Fermi* $\gamma$ -ray space telescope

Our current view of the  $\gamma$ -ray sky is provided by the *Fermi*  $\gamma$ -ray space telescope <sup>1</sup>, an international mission funded by the space agencies of the USA (NASA), France,

---

<sup>1</sup>Previously known as *Gamma-ray Large Area Space Telescope* (*GLAST*), before launch.

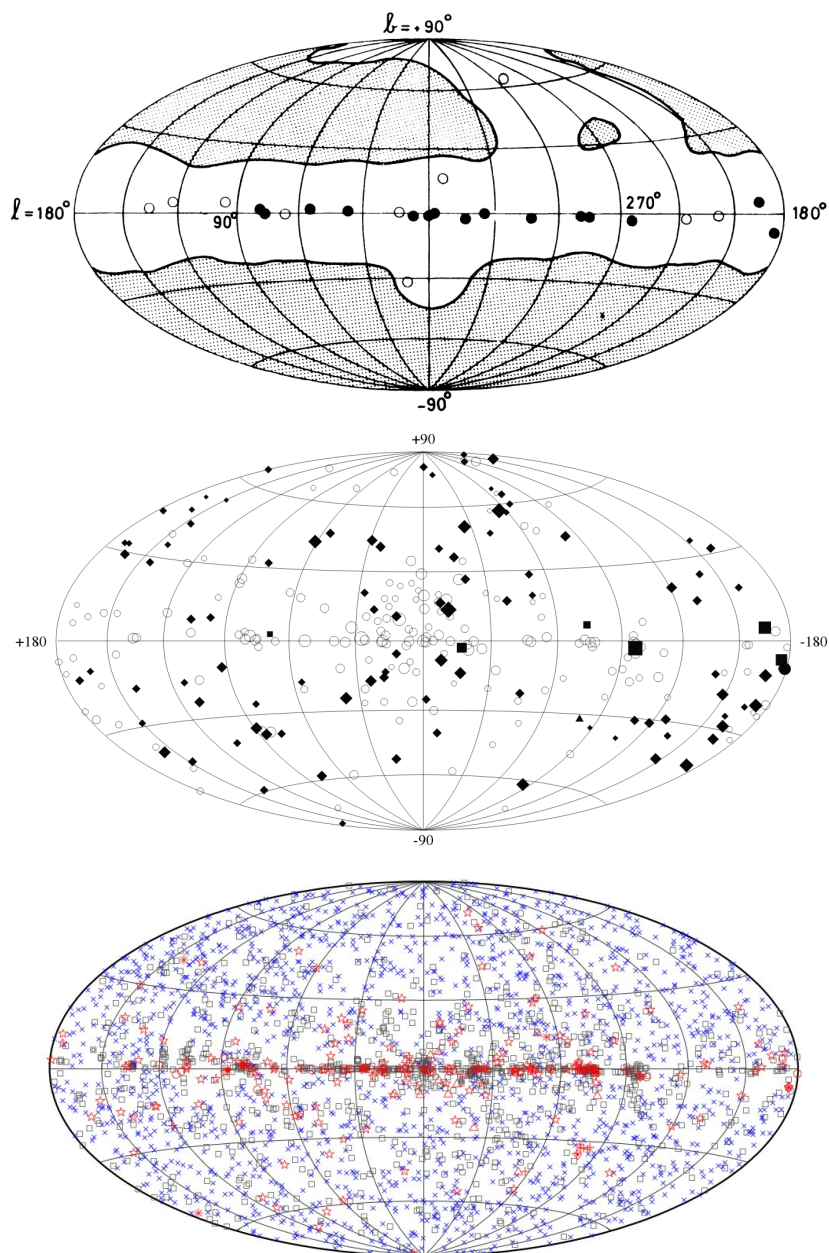


FIGURE 3.1: Sky maps from the source catalogs of the three major  $\gamma$ -ray telescopes from the birth of  $\gamma$ -ray astronomy to the present day. Top to bottom: COS-B (Swanenburg et al. 1981), EGRET (Hartman et al. 1999) and *Fermi-LAT* (Acero et al. 2015). All the maps are in galactic coordinates.

Germany, Italy, Japan, and Sweden. Launched on June 11, 2008, the spacecraft carries two instruments: the Large Area Telescope (LAT), and the Gamma-ray Burst Monitor (GBM). The improvement in our knowledge of the  $\gamma$ -ray sky provided by *Fermi* is exemplified in Fig. 3.1, where the sky maps from COS-B, EGRET and the *Fermi*-LAT are shown. Indeed, the latest *Fermi*-LAT source catalog contains over 3000 sources (Acero et al. 2015), over a factor of ten more with respect to the last EGRET source catalog.

### 3.2.1 The Large Area Telescope

The LAT is the main scientific instrument on board of the *Fermi* spacecraft. Here we provide a description of the instrument and its main performance parameters. For more details we refer the reader to Atwood et al. (2009).

Since  $\gamma$ -rays cannot be reflected or refracted due to their high energy, the best way to detect photons of energies above 100 MeV is through the process of pair-production. A  $\gamma$ -ray photon can interact with high- $Z$  material and be converted into an  $e^+e^-$  pair. The pair then travels with a kinetic energy given by  $E_{\text{ph}} - 2m_e c^2$ , and by tracking their position it is possible to reconstruct their arrival direction. The LAT is based exactly on these principles: it is made of a  $4 \times 4$  array of converter-tracker modules, each including 16 converter planes of high- $Z$  material (tungsten), interleaved with trackers made of 2 orthogonal layers of silicon strip detectors, to reconstruct the  $(x, y)$  position of the pair. Two additional tracker layers are present at the bottom of each module, which is completed with a calorimeter to measure the pair energy, and therefore reconstruct the original energy of the  $\gamma$ -ray photon. The calorimeter is made of 96 CsI(Tl) crystals, arranged in 8 layers of 12 crystals each, with each layer orthogonal to the previous one to provide a 2-D position. Fig. 3.2 shows the full  $4 \times 4$  array of converter/tracker and calorimeter modules which make up the LAT main detector, while Fig. 3.3 (left panel) shows a schematic structure of each converter/tracker module.

This core structure is fitted into an Anti-Coincidence Detector (ACD), which is necessary for background rejection. The spacecraft is subject to a high flux of cosmic rays, i.e., highly energetic charged particles, which can also interact with the detector forming a strong background signal, and therefore have to be discriminated against. To do this, the LAT is fully protected by a layer of material with a high interaction efficiency for charged particles (a plastic scintillator), so that if an event is measured both in the detector and in the ACD, it is rejected. A schematic view of the LAT fitted into the ACD is depicted in Fig. 3.3 (right panel).

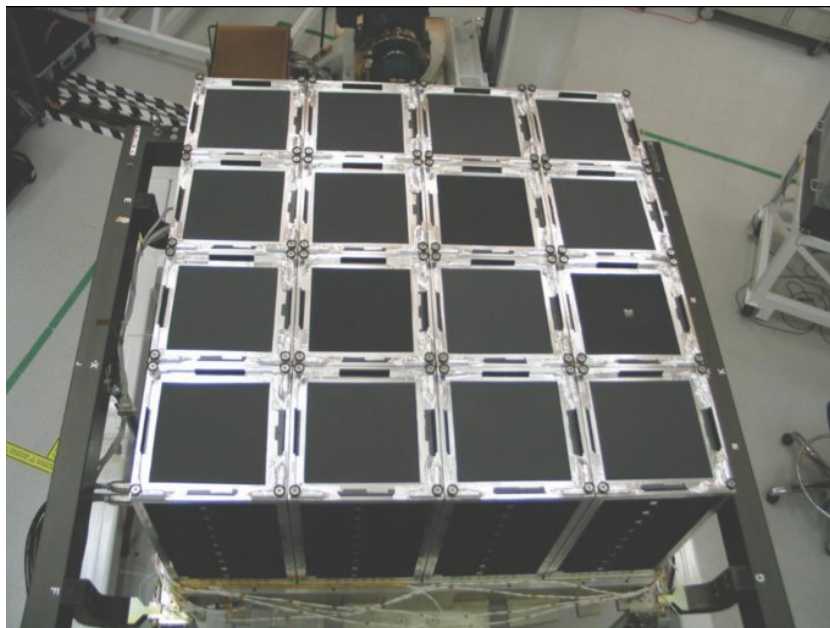


FIGURE 3.2: Completed 4×4 array of converter/tracker modules forming the LAT. Figure from Atwood et al. (2009).

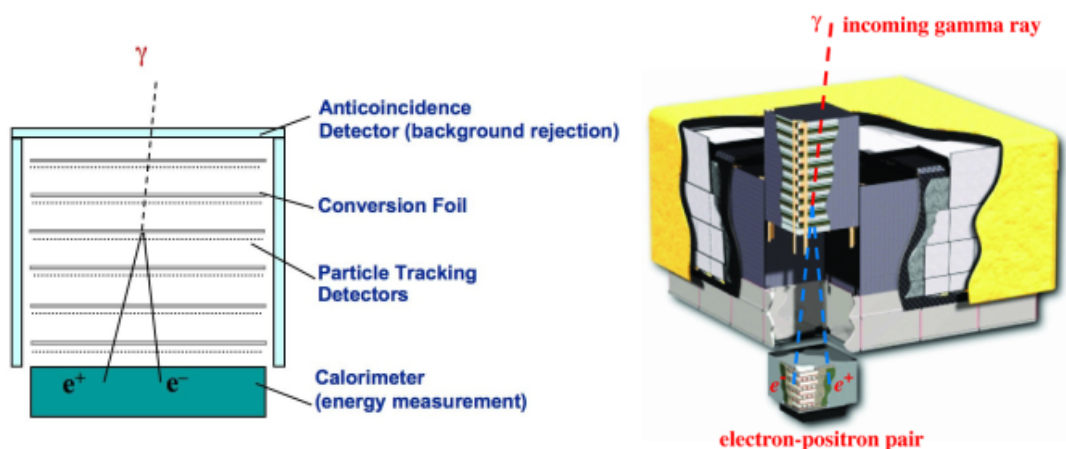


FIGURE 3.3: Schematic representations of the LAT and its measurement process, illustrated for one module (left) and for the whole detector (right). Figures from: <https://www-glast.stanford.edu/instrument.html>.

A summary of the LAT performance capabilities is given in Table 3.1. Since many of the main instrument parameters depend on energy and on the orientation of the telescope, the LAT performance is better understood by looking at the main parameters as a function of these variables.

As can be seen in Fig. 3.4, the core energy range of the LAT lies approximately between 1 GeV and 300 GeV, and its top performance energy range is between 1 GeV and 10 GeV. At energies below 1 GeV, the main drawbacks are the difficulty in reconstructing the direction of the photons, since the separation between the  $e^+e^-$  pair will be small, and energy dispersion (i.e, the fractional difference between

TABLE 3.1: Main LAT on-board performance capabilities. Adapted from Table 1 in Atwood et al. (2009).

| Energy range  | 20 MeV - 300 GeV  |
|---|---|
| Effective area <sup>a</sup>                           | 9,500 cm <sup>2</sup>   |
| Energy resolution (on-axis, equivalent Gaussian 1σ):  |   |
| 100 MeV - 1 GeV                                       | 9%-15%  |
| 1 GeV - 10 GeV  | 8%-9%   |
| 10 GeV - 300 GeV                                      | 8.5%-18%  |
| Angular resolution (on-axis, 68% containment radius): |   |
| > 10 GeV  | ≤ 0.15°   |
| 1 GeV   | 0.6°  |
| 100 MeV   | 3.5°  |
| Field of View (FoV)                                   | 2.4 sr  |
| Timing accuracy                                       | < 10 μs   |
| Point source location determination <sup>b</sup>      | < 0.5'  |
| Point source sensitivity <sup>b</sup>                 | 3 · 10 <sup>-9</sup> photons cm <sup>-2</sup> s <sup>-1</sup> |

<sup>a</sup> Maximum effective area (as a function of energy) for normal incident photons.

<sup>b</sup> For a steady source at high galactic latitude, with one year of integration.

the reconstructed energy and the true energy of the photon) increases with lower energies. At energies larger than 300 GeV, on the other hand, the main limitation is low photon statistics and the physical area of the detector. The dependence of the angular resolution on energy is illustrated in the bottom-right panel of Fig. 3.4. The 68% containment radius is several degrees large at ~ 100 MeV, but it drops quickly reaching a plateau at 0.1° after 10 GeV. The data can be divided into different event types based on the quality of the direction reconstructions, going from the worse reconstructed quartile, i.e., PSF0, to the best, PSF3. Restricting the analysis to the best reconstructed events implies a smaller number of photons, but it can be useful in order to obtain a good angular resolution at low energies, especially below 300 MeV, where the photon statistic is typically highest.

Another aspect to take into account when evaluating the LAT performance is the location of the target source, especially in Galactic coordinates, since the background diffuse model is much more uncertain for  $|b| < 10^\circ$ , due to the presence of diffuse emission from the galaxy. This is illustrated in Fig 3.5, where we can see how the point source sensitivity can change by almost an order of magnitude depending on the target's location with respect to the galactic plane.

### 3.2.2 The Gamma-ray Burst Monitor

The main purpose of the GBM is the spectral and temporal analysis of GRBs, but it also serves as a burst trigger for ground based follow-up observations, thanks to

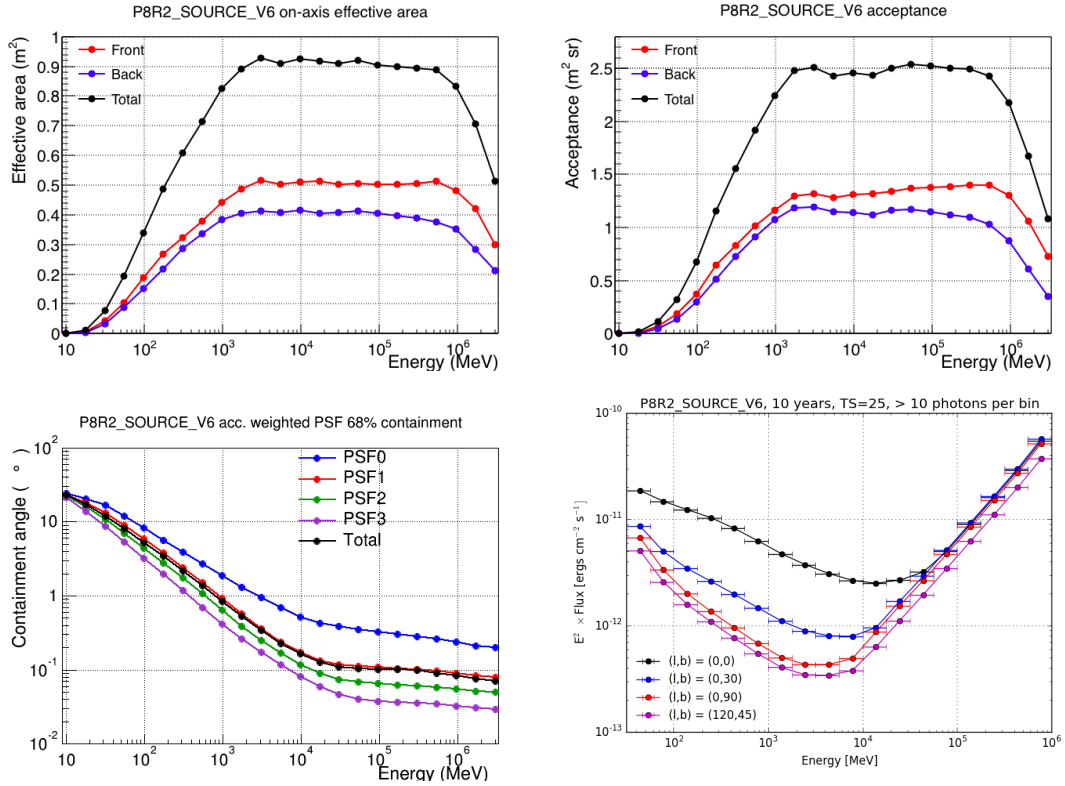


FIGURE 3.4: Main LAT performance capabilities as a function of different parameters. *Top left*: Effective area as a function of energy for a normal incident photon, for different event types and total. *Top right*: Acceptance, i.e., the effective area integrated over the solid angle, as a function of energy for different event types and total. *Bottom left*: Acceptance-weighted PSF as a function of energy for different PSF types (see main text) and total. *Bottom right*: Point source differential sensitivity for 10 years of integration on a steady source with uniform background, for four different sky positions (in Galactic coordinates). Images from: [http://www.slac.stanford.edu/exp/glast/groups/canda/lat\\_Performance.htm](http://www.slac.stanford.edu/exp/glast/groups/canda/lat_Performance.htm)

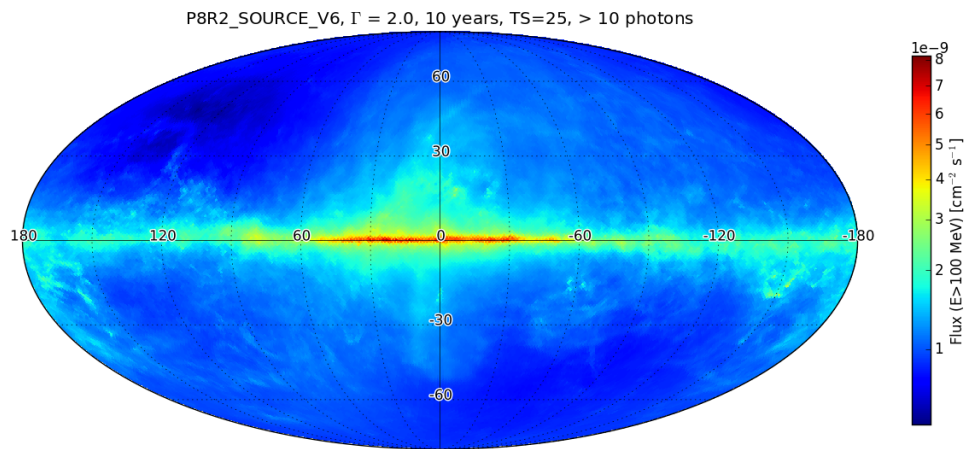


FIGURE 3.5: Map of the LAT 10-year integrated point-source sensitivity in Galactic coordinates, for an isolated source with a power-law spectrum with spectral index  $\Gamma = 2$ . This is defined as the lowest flux a point source can have in order to reach a  $5\sigma$  significance (with at least 10 detected photons) under the given conditions. Image from: [http://www.slac.stanford.edu/exp/glast/groups/canda/lat\\_Performance.htm](http://www.slac.stanford.edu/exp/glast/groups/canda/lat_Performance.htm)

its all-sky field-of-view. Recently, the importance of the GBM was highlighted by its fundamental role in the discovery of the first observed gravitational wave event with an electromagnetic counterpart, i.e., a neutron star merger that triggered a short GRB (Abbott et al. 2017; Abbott et al. 2017a,b).

The GBM consists of 12 NaI(Tl) and 2 BGO scintillation detectors, which cover the low-energy (8 keV - 1 MeV) and high-energy (200 keV - 40 MeV) portions of the energy range, respectively. The main GBM performance capabilities, as reported in Meegan et al. (2009), are listed in Table 3.2.

TABLE 3.2: Main *GBM* on-board performance capabilities.

|                          |   |
|--------------------------|---|
| Energy range             | 8 keV to 40 MeV                               |
| Energy resolution (FWHM) | $\sim 15\%$ at 100 keV; $\sim 10\%$ at 1 MeV  |
| Trigger threshold        | $0.74 \text{ photons cm}^{-2} \text{ s}^{-1}$ |
| Burst localization error | $< 15^\circ$                                  |
| Dead time per event      | $2.6 \mu\text{s}$                             |

### 3.3 *Fermi*-LAT data reduction principles

In this Section I will describe the general principles behind the processes through which *Fermi*-LAT data are analyzed. LAT data analysis poses several challenges, mainly due to the limited angular resolution, low photon statistics, and the energy-dependent detector performance.

#### 3.3.1 The likelihood and the Test Statistic

The analysis of LAT data basically consists in fitting a model of the sky to the data, including point sources and diffuse backgrounds. The detection significance for point sources is given in terms of a likelihood ratio.

The likelihood statistic  $L$  is defined as the probability of obtaining the observed data, given an input model.

If the data counts are binned, the likelihood is defined as the product of the probabilities of observing the detected counts in each bin. These probabilities, due to the small number of counts per bin, are given by the Poisson distribution

$$p_i = e^{-m_i} \frac{m_i^{n_i}}{n_i!}$$

This is the probability of detecting  $n_i$  counts in the  $i$ -th bin, where  $m_i$  is the predicted number of counts, given by the model. The product of these probabilities is the likelihood

$$L = e^{-N_{\text{exp}}} \prod_i \frac{m_i^{n_i}}{n_i!}$$

where  $e^{-N_{\text{exp}}}$  is the product of  $e^{-m_i}$  for all  $i$ , and  $N_{\text{exp}} = \sum_i m_i$  is the total expected number of counts predicted by the model. This definition is the basis of the binned likelihood analysis, and implies a certain trade-off between a smaller bin size (to give a better representation of the data) and an acceptable number of counts per bin (to obtain a statistically reliable fit).

When the bin size becomes infinitesimally small, so that  $n_i$  can only be 1 or 0, the likelihood becomes

$$L = e^{-N_{\text{exp}}} \prod_i m_i$$

where  $i$  is now the index over the counts. This definition is used in the unbinned likelihood analysis, which is more accurate since the counts are taken into account individually and not averaged over a bin, but is more computationally expensive, especially in the case of a large number of counts.

The detection significance for a source is given by the Test Statistic, defined as (Mattox et al. 1996):

$$\text{TS} = 2 \ln \frac{L_{\text{max},1}}{L_{\text{max},0}}$$

where  $L_{\text{max},1}$  is the maximum likelihood value for a model with the source at its given location, and  $L_{\text{max},0}$  is the maximum likelihood value for a model without the source. For an increasingly large number of counts, asymptotically the TS has the same distribution of the  $\chi^2$ , and therefore, as a rule of thumb, the square root of the TS is taken as the detection significance for a given source. This implies that, for example, a source can be considered detected at  $> 5\sigma$  significance if  $\text{TS} > 25$ . This is indeed the detection threshold used in the LAT source catalogs (Acero et al. 2015).

### 3.3.2 The Region of Interest and the sky model

Due to the limited angular resolution of the LAT (see Table 3.1), the sky model used for the likelihood analysis has to include a large sky area around the target source, in order to properly account for every photon observed around the source, and avoid contamination. This area has to encompass several PSF sizes, and is typically of the order of  $10^\circ - 15^\circ$ , and is called *Region of Interest*, or ROI.

The adopted sky model must describe the ROI as accurately as possible, taking into account all point sources, the Galactic diffuse component, and an isotropic diffuse background. The information contained in the model includes coordinates and spectral information for all its components, and it is based on the *Fermi*-LAT source catalogs. Possible spectral models include:

- Power Law

$$N(E) = N_0 \left( \frac{E}{E_0} \right)^\gamma$$

- Broken Power Law

$$N(E) = \begin{cases} N_0 \left( \frac{E}{E_b} \right)^{\gamma_1} & \text{for } E < E_b, \\ N_0 \left( \frac{E}{E_b} \right)^{\gamma_2} & \text{for } E > E_b. \end{cases}$$

- LogParabola

$$N(E) = N_0 \left( \frac{E}{E_0} \right)^{[\alpha + \beta \ln(\frac{E}{E_0})]}$$

- Power Law with exponential cutoff

$$N(E) = N_0 \left( \frac{E}{E_0} \right)^\gamma e^{-E/E_c}$$

The parameters above are the normalization  $N_0$ , calculated at the pivot energy  $E_0$ , the spectral index  $\gamma$  (or  $\alpha$  for the LogParabola), the break energy  $E_b$ , the curvature parameter  $\beta$ , and the cutoff energy  $E_c$ .

### 3.4 *Fermi*-LAT data reduction steps

I will now give an overview of the practical steps that constitute a typical binned analysis of LAT data, which is performed through the *Fermi* Science Tools. For additional information (e.g., on the unbinned analysis) I refer the reader to the official analysis documentation, provided at the *Fermi* Science Support Center (FSSC) <sup>2</sup>.

#### 3.4.1 Standard point-source detection analysis

The raw data are publicly available at the FSSC, and are provided in the form of an event file, also called FT1 file, and a spacecraft file, called FT2. The FT1

<sup>2</sup>URL: <https://fermi.gsfc.nasa.gov/ssc/data/analysis/documentation/>

file contains the raw photon data, while the FT2 file contains information of the telescope position and orientation during the selected time interval.

The first step of the analysis is to apply standard selection cuts to the raw data, selecting the ROI center coordinates and radius, and the desired time and energy range. Other standard cuts include a zenith angle cut to avoid contamination from the emission due to the Earth's limb (usually at  $\theta < 90^\circ - 100^\circ$ ), and a cut to exclude times when the ROI falls outside of the LAT field-of-view. This is done through the `gtselect` tool, which filters the event file based on the information present in the spacecraft file applying the chosen selection cuts. A further cut is necessary in order to select only so-called *Good Time Intervals* (GTI), by including only times when the LAT is in normal data-taking mode and no anomaly is corrupting the data. For example, this cut excludes times when the LAT is passing through the *South Atlantic Anomaly* (SSA), an area where orbiting satellites are subject to an increased flux of charged particles<sup>3</sup>. These additional cuts are performed using the `gtmktime` tool.

In the binned likelihood analysis, the counts are binned in energy, with a typical binning of ten logarithmically spaced energy bins per decade, and in space (although the analysis is less sensitive to the spatial binning). This is performed using the `gtbin` tool, which produces a 3-dimensional counts cube (sky position and energy).

The following step is to create a file including the sky model information. This is usually derived from the latest LAT source catalog, in our case the 3FGL (Acero et al. 2015), using a user-contributed tool called `make3FGLxml.py`<sup>4</sup>. The tool reads the ROI coordinates and size information from the FT1 file and adds all 3FGL sources included in the given area, plus the latest models for the galactic diffuse and isotropic diffuse components. Sources within an additional  $10^\circ$  are included in order to account for possible contributions of distant sources, especially at low energies where the LAT PSF reaches up to several degrees. The output of this tool is an XML file with the coordinates and spectral information for all the sources in the sky model.

It is now useful to pre-compute some computationally expensive quantities that are needed in order to calculate the likelihood, namely the livetime and the exposure map. This allows us to speed up the likelihood fitting, since they do not have to be recalculated every time a fit is performed. The livetime is the accumulated time during which the LAT is actively taking data for the given ROI. Since the LAT response functions depend on the photon off-axis angle, so will the number

---

<sup>3</sup>For more information see e.g. [https://heasarc.gsfc.nasa.gov/docs/rosat/gallery/misc\\_saad.html](https://heasarc.gsfc.nasa.gov/docs/rosat/gallery/misc_saad.html).

<sup>4</sup>Credit: T. Johnson. See [https://fermi.gsfc.nasa.gov/ssc/data/analysis/user/readme\\_make3FGLxml.txt](https://fermi.gsfc.nasa.gov/ssc/data/analysis/user/readme_make3FGLxml.txt) for the documentation.

of observed counts. Therefore the likelihood analysis requires the livetime as a function of sky position and off-axis angle. This is done through the `gtltcube` tool, which uses the information in the spacecraft file together with the selection cuts and GTIs in the filtered event file to produce a 3-dimensional quantity (sky position and inclination angle) called “livetime cube”. The exposure is defined as the effective area integrated over the entire ROI data space, i.e., time (as in the usual definition of exposure), but also energy and inclination angle, as the LAT response depends on these quantities as well. Due to its definition, the exposure map calculation requires the livetime cube as a prerequisite, in addition to the FT1 and FT2 files.

The binned likelihood analysis also requires model counts maps for each source present in the adopted sky model. In order to do this, the `gtsrcmaps` tool takes the spectral information for each source, multiplies it by the exposure at its position, and then convolves it with the instrument PSF.

Once all these quantities have been computed, it is possible to perform the actual maximum likelihood fit, using the `gtlike` tool. This will provide a TS and fitted parameter values with statistical errors for all sources (and spectral parameters) in the model that have been left free to vary in the fit. Typically, the target source and the galactic and isotropic diffuse components are left completely free, and the normalization of sources within  $5^\circ$  from the ROI center is also fitted, while the parameters of more peripheral sources are fixed to the catalog values, since they will have a much smaller influence on the result for the target source.

### 3.4.2 Source finding, localization and upper limit analysis

The initial sky model that is created starting from the latest LAT catalog is not always the most complete representation of the given ROI. This may happen especially when the current LAT data set has greatly exceeded the integration time used to build the latest source catalog, in the case of new, transient sources, but also in the case of upper limit analysis. In such cases, it is necessary to evaluate if the data shows excess emission with respect to the adopted sky model, after a successful first-order fit of the ROI. One of the most practical ways to do this is by producing a TS map. This procedure consists in inserting a test source with first-guess parameters through a grid of locations in the map, making a maximum likelihood fit, taking into account the existing sources in the model, and producing a TS for each grid point. This will result in a map of excess TS, and is performed using the `gttsmap` tool. New sources would then correspond to local maxima in the TS map, with a given threshold, e.g. the standard  $TS > 25$ . It is then possible

to add a new source to the model at the position of this maximum, and obtain an actual detection significance.

A similar concept, relying on the same idea, is source localization. If the detection significance is robust ( $TS > 25$ ), it is good practice to refine the position of the new source, since TS map maxima are just a first guess. This is done through the `gtfindsrc` tool, which uses a multidimensional minimization routine to find the optimal TS for a grid of positions around the initial guess. Naturally, this procedure works best for bright sources at high galactic latitude and with no other nearby bright sources, while on the other hand its results are not reliable for borderline-significant sources ( $TS \lesssim 25$ ), or for  $TS > 25$  sources close ( $\lesssim 0.5 - 1^\circ$ ) to a brighter source.

In the case when a source is not detected, it is possible to place an upper limit on its flux. This is typically done by integrating the likelihood profile as a function of flux, from its maximum down to the point where it decreases by the desired confidence level, typically 95%. The corresponding flux will then be the upper limit at the chosen level of confidence. For new sources, the threshold at which an upper limit is quoted instead of a flux measurement is usually set at  $TS < 25$ . For spectra or light curve bins of a known source, when it is robustly detected over the full range of time and energy, the threshold is commonly lowered to  $\sim 3\sigma$ , i.e.  $TS > 10$ .

## Chapter 4

# Radio interferometry

### 4.1 Radio astronomy basics

The radio band is the widest frequency window which is fully observable from the ground, with almost null absorption from the Earth's atmosphere. At high frequencies, this window is limited by absorption by water molecules in the atmosphere, which becomes dominant in the sub-mm range, at frequencies  $\gtrsim 300$  GHz. At low frequencies, the band is limited by the ionosphere, which reflects incoming radiation, preventing ground-based observations at frequencies  $\lesssim 30$  MHz.

In this frequency range, photons are not energetic enough to be detected via the photoelectric effect, as in the optical or X-ray bands. Radio emission is detected by focusing incoming waves on a dipole and measuring its electric field, which is then converted into an electric signal. In practice, this is done through an antenna (usually parabolic), with receivers installed in one of the foci of the optical system.

The response of the antenna is not uniform across its field of view, and its angular resolution is limited. The power measured from a point source as a function of off-axis angle is called *beam pattern*, and it has a characteristic shape given by the diffraction pattern associated with the antenna aperture. This function can be described with a sinc (see Fig. 4.1), where the absolute maximum is called *beam* or *main lobe* and the secondary maxima are called *side-lobes*. The Full-Width Half-Maximum (FWHM) of the main lobe indicates the angular resolution of the antenna, and is given by  $\theta = 1.22 \lambda/D$ , where  $\lambda$  is the wavelength of the observed radiation, and  $D$  is the antenna diameter.

For a typical radio wavelength of 3.6 cm, and a telescope diameter of 100 m, the resolution is of the order of 1 arcminute. Such a resolution is similar to the one of the human eye, and is therefore not suited to investigate the relevant

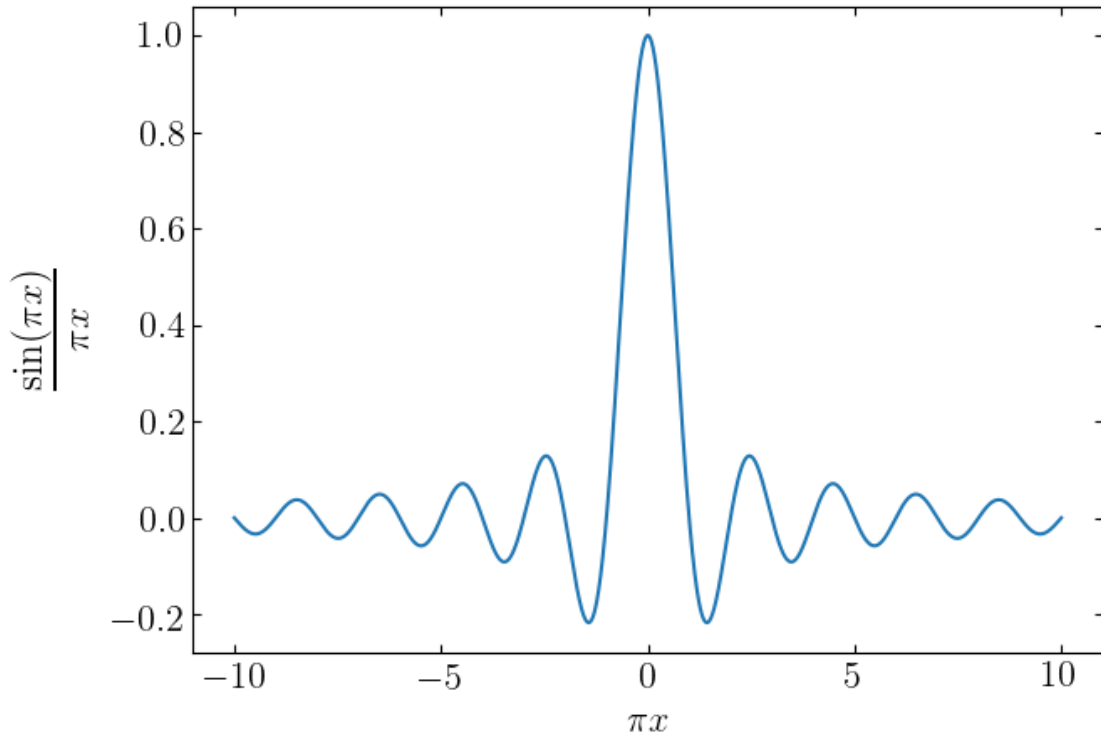


FIGURE 4.1: Sinc function, which is at the base of the antenna beam pattern.

physical scales of astronomical objects. For example, even for a relatively nearby radio galaxy such as the radio galaxy Pictor A (see Section 5.1), at a luminosity distance  $D_L \sim 150$  Mpc, one arcminute corresponds to  $\sim 40$  kpc in physical scale. The physical processes associated with jet formation, acceleration and collimation take place on scales ranging down to sub-parsec. At the redshift of Pictor A, one parsec corresponds to an angular scale of  $\sim 1.5$  milliarcseconds. In order to reach such an angular resolution, a single radio telescope would need to have a diameter of the same order of magnitude as the Earth's radius. These scales can only be probed by combining observations from many radio telescopes distributed around the globe, a technique known as Very Long Baseline Interferometry (VLBI).

As a comparison, moving into the optical band, where the resolution benefits from the much shorter wavelength, a single telescope would need to have a diameter larger than 80 m to reach these angular scales. For a comparison, the largest single-mirror optical telescope today is the Gran Telescopio Canarias (GTC), with a diameter of 10.4 m. The largest planned single-dish telescope is the European Extremely Large Telescope (E-ELT), with a diameter of 39.3 m, which is expected to achieve first light in 2024. Therefore, VLBI remains the only astronomical technique capable of achieving sub-milliarcsecond scale resolution for the foreseeable future.

## 4.2 Interferometry and VLBI

The basic idea of interferometry can be exemplified by a system with two antennas acting as a double slit interferometer (see Fig. 4.2). When the antennas point at the same source, at a direction defined by the vector  $\mathbf{s}$ , the second antenna will receive the signal with a geometrical delay determined by the distance from the first, which we call *baseline* ( $\mathbf{B}$ ), i.e.,  $\tau_g = \mathbf{s} \cdot \mathbf{B}/c$ .

The antenna outputs can then be expressed in terms of  $\tau_g$  as:

$$V_1 = V \cos [\omega(t - \tau_g)] \quad (4.1)$$

$$V_2 = V \cos (\omega t) \quad (4.2)$$

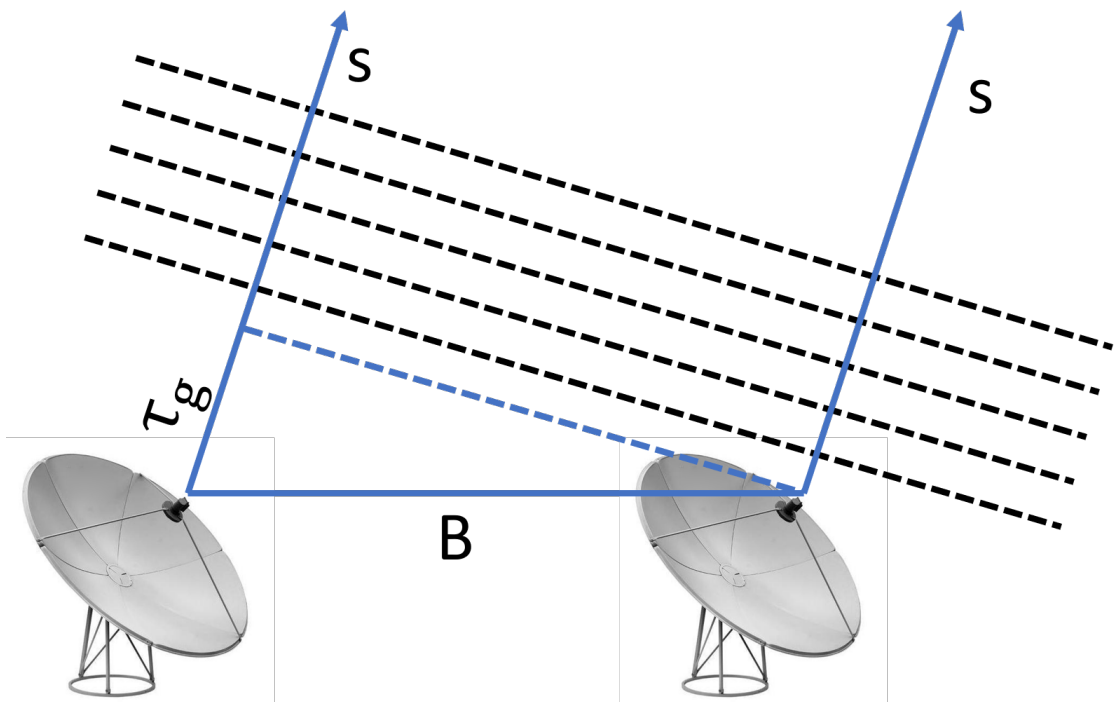


FIGURE 4.2: Schematic representation of a two element interferometer, with two antennas separated by a baseline distance  $B$ , looking at a target source defined by the direction  $s$ , leading to a geometrical delay  $\tau_g$  between the two elements.

The signals are then correlated, i.e., combined coherently, which requires a very precise determination of  $\tau_g$ . The product of the signals from the two antennas yields:

$$V_1 V_2 = V^2 [\cos (2\omega t - \omega\tau_g) + \cos \omega\tau_g]/2. \quad (4.3)$$

The term  $2\omega t - \omega\tau_g$  is variable on short timescales, and can therefore be made negligible through averaging. This simplifies the product, in the form:

$$R_{\cos} = \langle V_1 V_2 \rangle = (V^2 \cos \omega\tau_g)/2. \quad (4.4)$$

To recover the full information on the source distribution, this cosinusoidal response is combined with a sinusoidal term, obtained by shifting the phase of one of the signals by  $\pi/2$ . This term takes the form:

$$R_{\sin} = \langle V_1 V_2 \rangle = (V^2 \sin \omega\tau_g)/2. \quad (4.5)$$

The information from these terms can be combined in a complex quantity, called *visibility function*, which is defined as:

$$v = R_{\cos} - iR_{\sin} = Ae^{-i\phi}. \quad (4.6)$$

where  $A = \sqrt{R_{\cos}^2 + R_{\sin}^2}$  is the visibility amplitude and  $\phi = \tan^{-1}(R_{\sin}/R_{\cos})$  is the visibility phase.

It can be shown (see Thompson et al. 1986) that the Fourier transform of the visibility function is the intrinsic brightness distribution of the observed source

$$v_\nu(\mathbf{B}) = \int \int I_\nu(\mathbf{s}) e^{-2\pi i \nu \mathbf{B} \cdot \mathbf{s}/c} d\Omega \quad (4.7)$$

Typically, the distribution of the visibility function is expressed in a 2D plane perpendicular to the direction of the source, called  $(u, v)$ -plane, where  $u$  represents the E-W direction and  $v$  the N-S direction, in units of the observed wavelength. Each baseline as seen by the source provides a visibility point in the  $(u, v)$ -plane. Thanks to this, radio interferometry takes advantage of the Earth's rotation to maximize the sampling of the  $(u, v)$ -plane, also called *uv-coverage*. For each scan, the Earth's rotation will imply that the vector distance between antennas as seen by the source will be different, providing a new point in the  $(u, v)$ -plane. This effect creates circular tracks in the  $(u, v)$ -plane as the integration time of the observation increases, reaching a full circle for a 12 hours integration. A typical uv-coverage of the VLBI observations which provided the data used in this thesis is shown in Fig. 4.3.

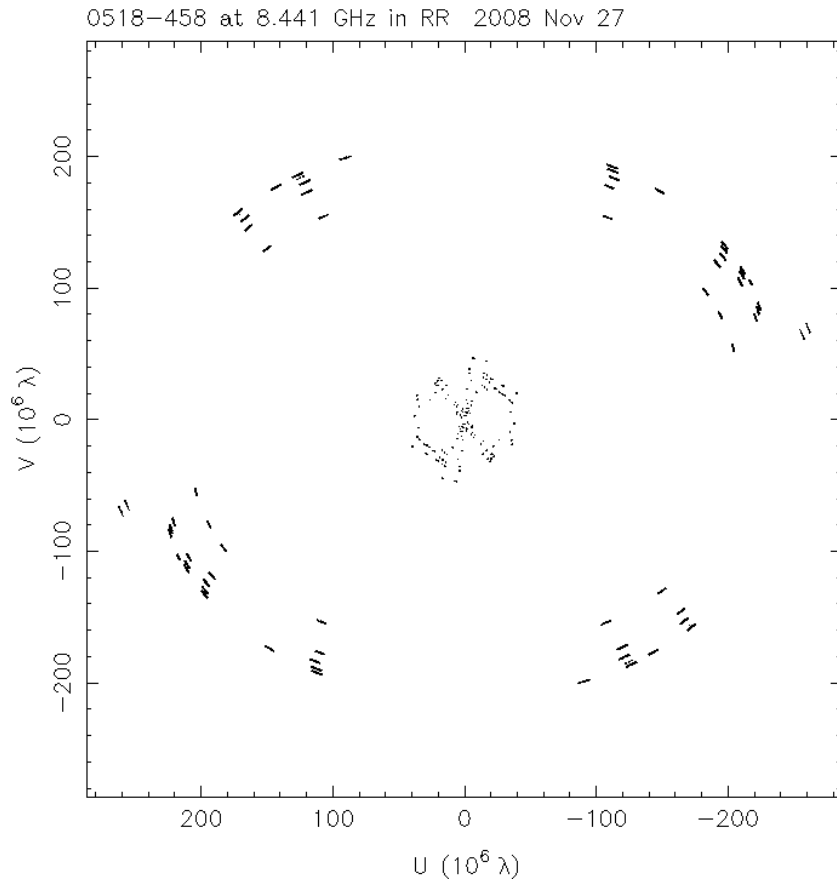


FIGURE 4.3:  $uv$ -coverage for a TANAMI observation of the FR II radio galaxy Pictor A at a frequency of 8.4 GHz. The coordinates are expressed in units of  $M\lambda$ .

Ideally, in order to recover unambiguously the true brightness distribution of the source, the  $(u, v)$ -plane should have perfect sampling. Obviously this is not feasible, given the finite number of antennas available in a VLBI array, and it is quite common to have large gaps in the  $uv$ -coverage. This can lead to large degeneracies in recovering the source brightness distribution, making the imaging process quite challenging.

Since the fringe pattern of a two-element interferometer is oriented perpendicularly to the baseline direction, the best resolution is achieved in the direction perpendicular to the longest baselines. Therefore, it is desirable to have an array configuration such as to provide the most symmetric  $uv$ -coverage possible. Additionally, the fringe distance depends on  $\lambda/B$ , and therefore each baseline is sensitive to a different angular scale. In particular, long baselines probe the smaller scales, while the short baselines probe large scales. When designing a VLBI array, it is vital to ensure that all scales are properly sampled, in order to recover a high-fidelity image of the source, and therefore the array should include relatively close antennas, as well as very long baselines. If, for example, only long baselines are

sampled, then the resulting array will only be sensitive to very compact emission, and be effectively blind to diffuse components.

Radio interferometry is a technique performed on a variety of scales and frequencies, as exemplified in Fig. 4.4, pushing the resolution limit both in terms of wavelength and baseline length. A typical example is the Karl G. Jansky Very Large Array (VLA) in Socorro (NM), USA (Perley et al. 2011), where 27 antennas of 25 m diameter are arranged in a “Y” shape, and can be moved on tracks to form different configurations. The most extended configuration reaches a maximum baseline of  $\sim 36$  km, for a resolution reaching down to the sub-arcsecond scales, and a sensitivity down to the  $\sim \mu\text{Jy}$  level. This makes the VLA an excellent tool for imaging the large scale structure of radio galaxies at high resolution (see the top image of Fig. 4.4), especially at cm wavelengths.

At the other end of the frequency and angular resolution parameter space, the most extreme spatial accuracy is achieved through global VLBI in the mm-submm band, which is performed using the Event Horizon Telescope (EHT) array. Thanks to a global array of submm telescopes observing at the frequency of 230 GHz, the EHT can achieve an angular resolution of the order of  $50 \mu\text{as}$  (see e.g. Doeleman et al. 2012).

### 4.3 VLBI data reduction

I will now describe the procedure used to reduce radio VLBI data.

#### 4.3.1 Calibration

As per the definition in Equation 4.6, interferometric visibilities are a complex quantity, described by an amplitude and a phase. The output of the antenna’s receivers is in arbitrary units, and therefore has to be converted into a physical flux through a correction factor. This is done through *amplitude calibration*. Additional corrections also need to be applied to the phases, due to e.g. imperfect knowledge of the antennas’ positions, time stamps, and most importantly due to variable atmospheric effects. These effects introduce a spurious dependence of the phase on frequency and time, which is corrected through *phase calibration*.

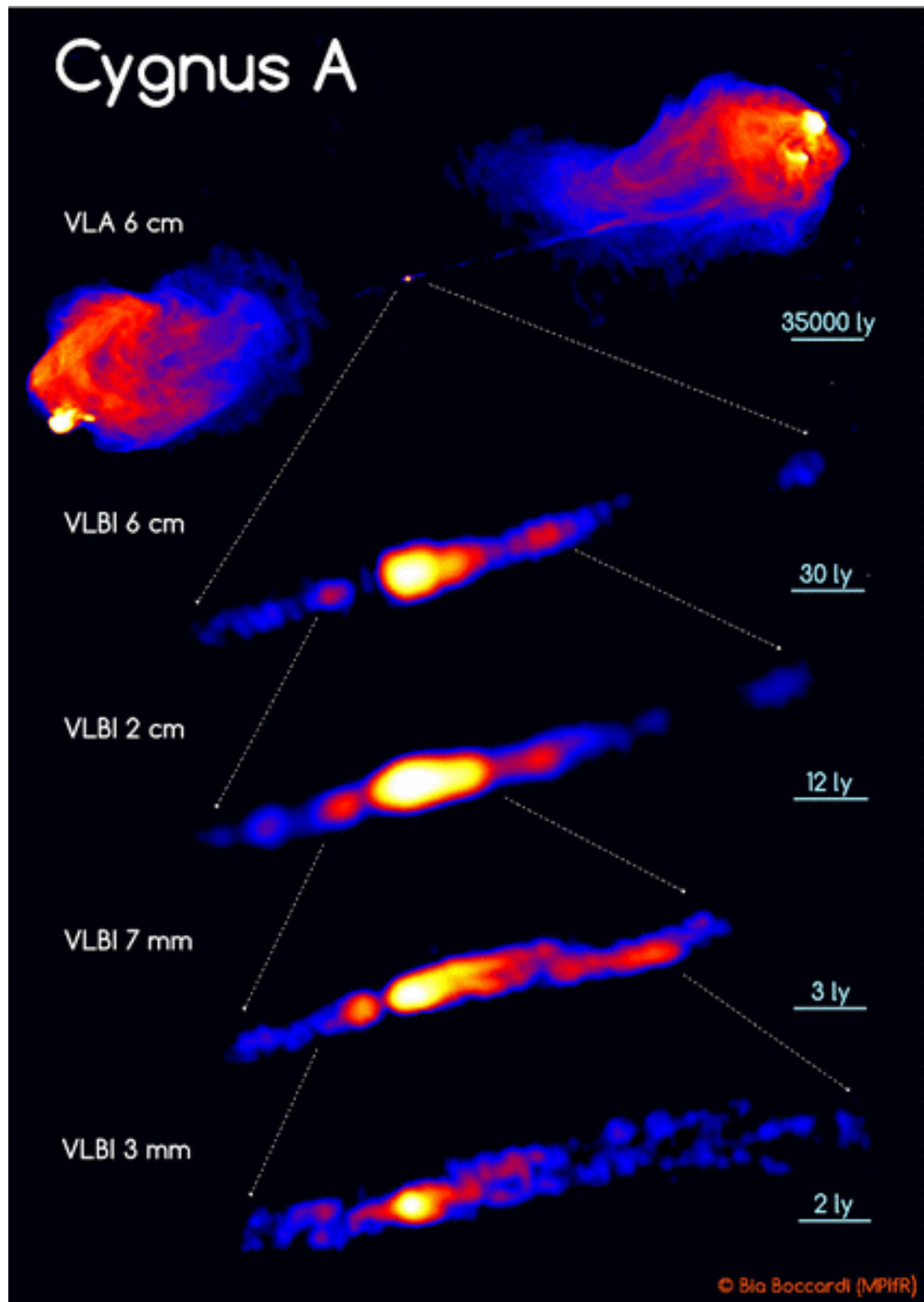


FIGURE 4.4: Radio interferometric images of the FR II radio galaxy Cygnus A from VLA scales to mm-VLBI. From Boccardi et al. (2017).

### 4.3.2 Imaging

The imaging of VLBI data is typically performed using the hybrid mapping technique, implemented in the software Difmap (Shepherd et al. 1994). As mentioned in Section 4.2, the visibility function is the Fourier transform of the true source brightness on the sky, convolved with the instrumental response. The latter is the so called *dirty map*.

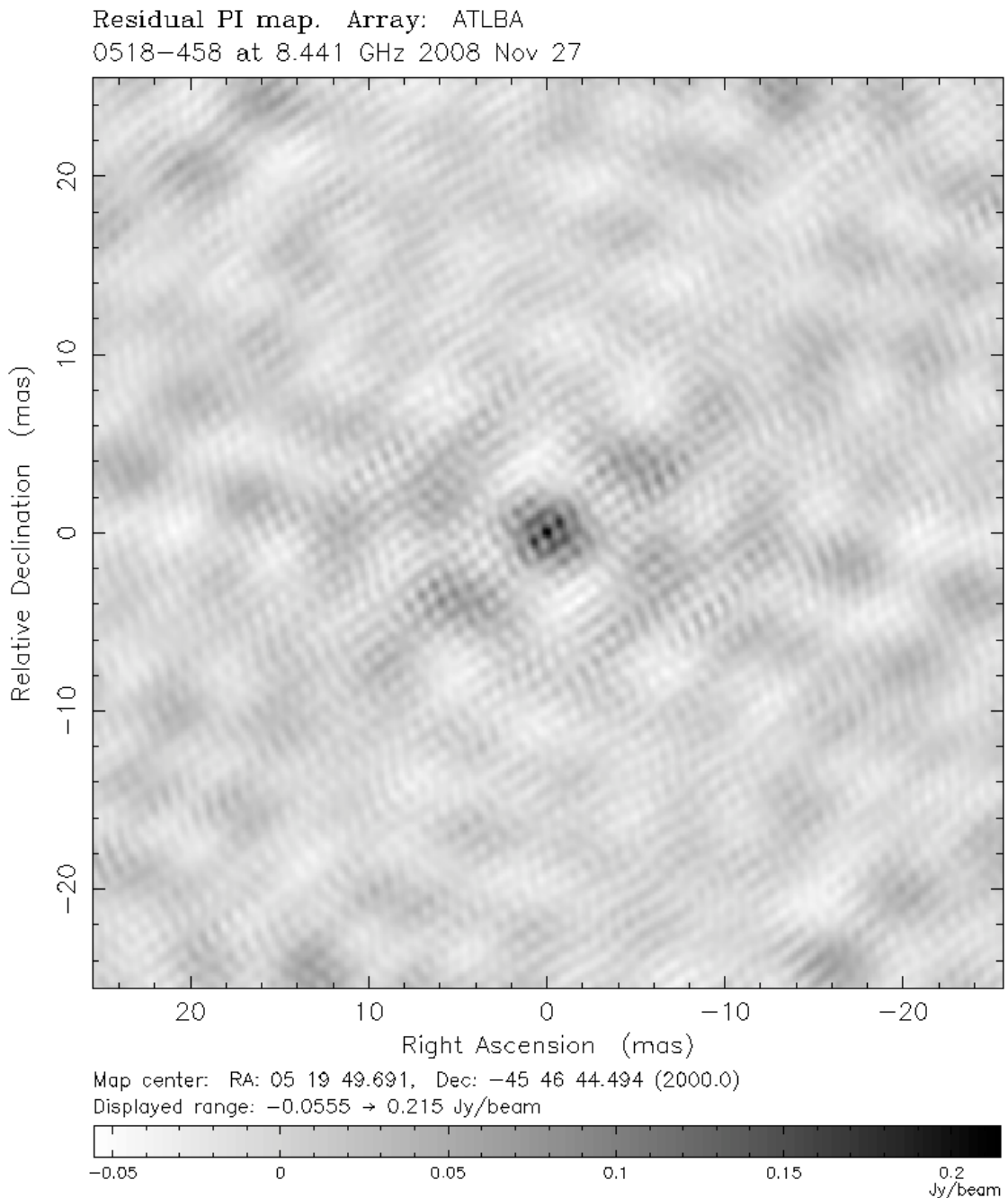


FIGURE 4.5: Dirty map for a TANAMI observation of the FR II radio galaxy Pictor A at a frequency of 8.4 GHz, corresponding to the same epoch as Fig. 4.3.

In order to recover the true brightness distribution of the source, removing the contamination provided by the instrumental response, the data has to be deconvolved. Specifically, the footprint of the so called *dirty beam* has to be removed, i.e., the instrumental response to a point source. This corresponds to the Fourier transform of the uv-coverage, and therefore carries all the effects given by its incompleteness, in-homogeneity or asymmetry. These effects manifest themselves in the form of side-lobes, i.e., spurious bright structures in the dirty map following the pattern given by the uv-coverage. It can be challenging to disentangle such structures from the real source brightness distribution, especially when imaging faint emission, and especially when the uv-coverage is highly incomplete.

In Difmap, the core of the imaging process is the CLEAN algorithm (Högbom 1974). This procedure consists in finding the map peak, subtracting a given fraction of it (typically 1-3%) from the map convolved with the dirty beam, and storing it in a model in the form of several point-like components, called *clean components*. This procedure is iterated, as fainter structures of the source emerge and are cleaned out, until only noise is left in the dirty map. To improve the convergence of the process, each clean iteration is followed by a phase *self-calibration* step, where the visibility phases are calibrated against the model itself. After obtaining a reasonable starting model for the source's brightness distribution through clean and phase self-calibration iterations, the visibilities can also be self-calibrated in amplitude, on increasingly small integration time scales. This procedure can greatly improve the dynamic range of the final image, but is also a delicate one: if the initial model is incorrect, this will imprint the associated error on the data, making spurious structures more permanent in the final image. This is particularly true for complex sources for which the structure is not well-known, and for arrays with few antennas and/or low SNR data.

The model resulting from this iterative process is finally convolved with a *clean beam*, i.e., a Gaussian fit to the main lobe of the dirty beam, to produce the clean map.

It is worth noting that when the data quality is not ideal, it is often necessary to have an initial guess of the true source structure, in order to produce a good quality image. With this, it is possible to guide the CLEAN algorithm so that clean flux is extracted from the dirty map only in certain areas, defined through rectangular windows. Naturally, this introduces a bias in the imaging process, which is especially relevant for highly incomplete uv-coverage data. A good way to test the robustness of a specific feature in the source brightness distribution is to image multi-epoch data of the same source, and check that such a feature can be imaged consistently in all epochs.

#### 4.4 The TANAMI monitoring program

Since AGN are highly variable sources, it is vital to study them in a time-resolved manner. Radio VLBI monitoring, in particular, can provide the highest-resolution view of the jet evolution at parsec-scales, and can constitute a fundamental tool in our understanding of high-energy processes in AGN (see Section 2.3). For this reason, several large VLBI monitoring programs have been established in the last decade. The largest is the MOJAVE survey (Monitoring Of Jets in Active galactic nuclei with VLBA Experiments, e.g., Lister et al. 2016, and references therein), which has been monitoring a large sample of AGN jets for  $\sim 20$  years using the NRAO Very Long Baseline Array (VLBA) at 15 GHz. Due to the array coordinates, the MOJAVE sample has a declination limit  $> -30^\circ$ , preventing observations of many noteworthy sources in the southern sky. The TANAMI program (Tracking Active galactic Nuclei with Austral Milliarcsecond Interferometry, Kadler et al. 2007) is the only large VLBI monitoring program of AGN in the southern hemisphere, and has been monitoring a large sample of jets since 2007, at 8.4 GHz and 22.3 GHz. The core of the VLBI array is the Australian Long Baseline Array (LBA), supported by antennas in New Zealand, South Africa, South America, and Antarctica. A full list of the participating antennas is presented in Table 4.1, while their distribution is depicted in Fig. 4.6

TABLE 4.1: List of radio telescopes forming the TANAMI array.

| Antenna                     | Diameter (m) | Location                                  |
|-----------------------------|--------------|---|
| Parkes                      | 64           | Parkes, New South Wales, Australia        |
| ATCA                        | 5×22         | Narrabri, New South Wales, Australia      |
| Mopra                       | 22           | Coonabarabran, New South Wales, Australia |
| Hobart                      | 26           | Mt. Pleasant, Tasmania, Australia         |
| Ceduna                      | 30           | Ceduna, South Australia, Australia        |
| Hartebeesthoek <sup>a</sup> | 26           | Hartebeesthoek, South Africa              |
| DSS 43 <sup>b</sup>         | 70           | Tidbinbilla, ACT, Australia               |
| DSS 45 <sup>b</sup>         | 34           | Tidbinbilla, ACT, Australia               |
| O’Higgins <sup>c</sup>      | 9            | O’Higgins, Antarctica                     |
| TIGO <sup>c,d</sup>         | 6            | Concepcion, Chile                         |
| Warkworth                   | 12           | Auckland, New Zealand                     |
| Katherine                   | 12           | Northern Territory, Australia             |
| Yarragadee                  | 12           | Western Australia                         |
| ASKAP <sup>e</sup>          | 12           | Murchinson, Western Australia             |

<sup>a</sup> Unavailable between Sept. 2008 and Sept. 2010.

<sup>b</sup> Operated by the Deep Space Network of the USA National Aeronautics and Space Administration (NASA).

<sup>c</sup> Operated by the German Bundesamt für Kartographie und Geodesie (BKG).

<sup>d</sup> Now in La Plata, Argentina.

<sup>e</sup> Contributing with a single antenna of the 36-element array.

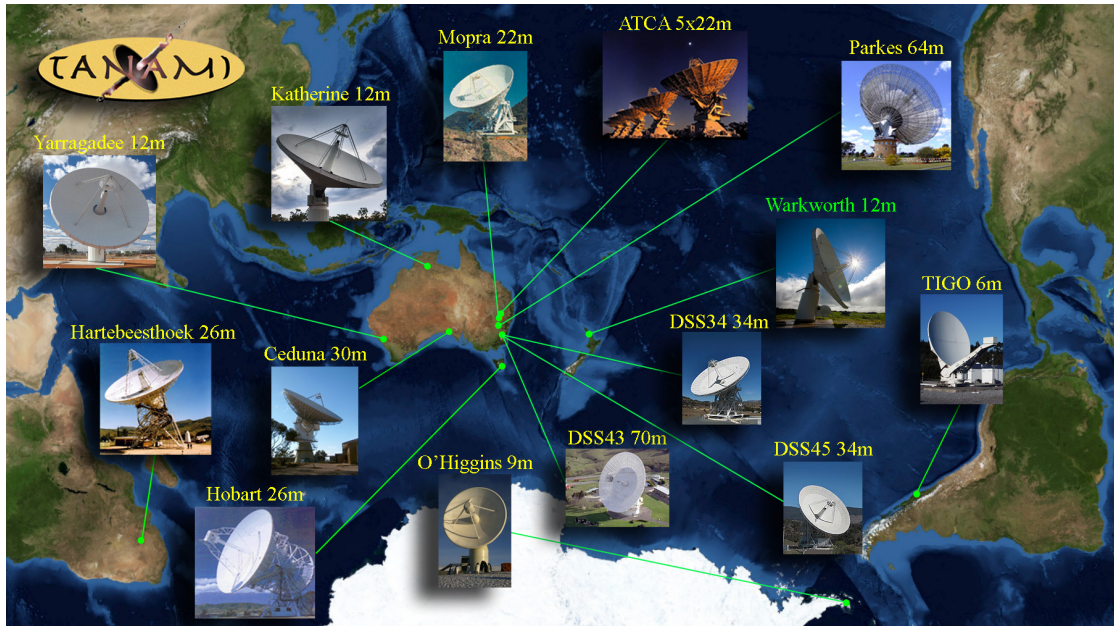


FIGURE 4.6: Geographic distribution of the antennas forming the TANAMI array.

The TANAMI sample was defined starting from two sub-samples, for sources south of  $\delta = -30^\circ$ . The radio-selected sub-sample was based on the catalogue of Stickel et al. (1994)<sup>1</sup>, with a flux density cut at  $S_{5\text{GHz}} > 2$  Jy and a spectral index cut at  $\alpha > -0.5$  ( $S \propto \nu^{+\alpha}$ ) between 2.7 and 5 GHz. The  $\gamma$ -ray selected sub-sample included all EGRET blazars in the given declination range. The sample also includes a few additional sources of interest which did not satisfy this selection, and were added manually to the monitoring program. First-epoch images of the initial sample of 43 sources were presented in Ojha et al. (2010). Additional sources were added over the years, mostly due to new  $\gamma$ -ray detections by *Fermi*-LAT, and the VLBI maps were presented in Müller et al. (2018), bringing the total number of monitored sources to  $\sim 100$ .

Among the most relevant results produced by the TANAMI VLBI monitoring is the complex jet evolution of the closest AGN, i.e., the FR I radio galaxy Centaurus A. Using the first  $\sim 3.5$  years of TANAMI data, Müller et al. (2014b) studied the jet kinematics of Cen A on sub-pc scales (see Fig. 4.7). They found apparent component motion with speeds in between  $0.1c$  and  $0.3c$ , with possible downstream acceleration, and constrained the jet viewing angle to be in the range  $12^\circ - 45^\circ$ . They also noticed the presence of a persistent local decrease in jet surface brightness, which can be explained with a star crossing the jet, and the subsequent interaction.

From its beginning, TANAMI has always had a strong multi-wavelength component, combining the VLBI data with  $\gamma$ -ray, X-ray, optical and multi-messenger

<sup>1</sup>In turn, this catalogue is based on Kuehr et al. (1981).

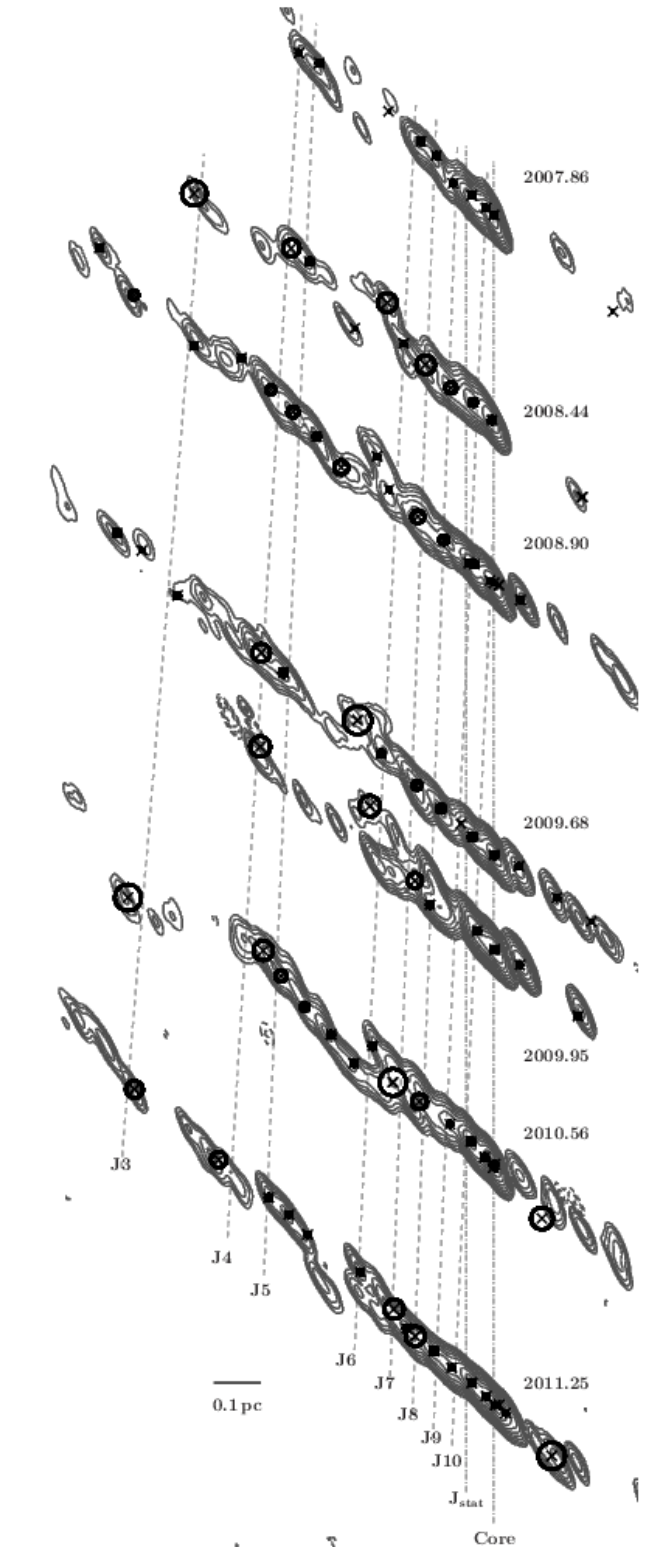


FIGURE 4.7: Fig. 5 from Müller et al. (2014b). Time evolution of the Cen A jet from TANAMI 8.4 GHz images, with fitted Gaussian components and their identification and tracking.

data (see e.g., Kadler et al. 2015). An example of this is a study of time-resolved SEDs of the brightest TANAMI  $\gamma$ -ray blazars (Krauß et al. 2016), where the *Fermi*-LAT light curves were divided in different activity states, and a quasi-simultaneous SED was built for each of the states. The authors found that the so called “blazar sequence” (see e.g., Ghisellini et al. 2017, and references therein), i.e., the fact that more luminous sources tend to have SEDs peaking at lower frequencies, is indeed observed during low and intermediate activity states, but not during active states.

Another example of the multi-wavelength nature of the TANAMI program is the study by Böck et al. (2016), who presented a comparison of the radio and  $\gamma$ -ray properties of 75 TANAMI sources, and found that the  $\gamma$ -ray luminosity correlates with radio core luminosity and brightness temperature, suggesting a link with the source Doppler factor.



## Chapter 5

# Radio VLBI data analysis and results

*This Chapter will be partially reproduced in Angioni et al. a,b, to be submitted to Astronomy & Astrophysics*

### 5.1 The TANAMI radio galaxy sample

This study is focused on the radio galaxies in the TANAMI sample, i.e. all non-blazar sources, whose optical spectrum is dominated by the host galaxy and not by the non-thermal jet emission (as is the case for blazars). Our sample includes well-known sources for which TANAMI provides the highest-resolution data available. The full list of TANAMI radio galaxies can be found in Table 5.1. Several radio galaxy subclasses are present, from classic FR I (e.g. Centaurus A) and FR II (e.g. Pictor A) to young radio sources (e.g. PKS 1718–649) and peculiar or misclassified AGN (e.g. PKS 0521–36). Only half of the sample has been detected by *Fermi*-LAT so far. This is not surprising, given that radio galaxies are faint  $\gamma$ -ray emitters.

Since TANAMI is the first major monitoring program for southern-hemisphere sources at milliarcsecond resolution, including a considerable number of radio galaxies, it provides the first data set suitable for kinematic studies on these scales. The most notable member of the TANAMI radio galaxy sample is the closest radio-loud AGN, Centaurus A, which has been studied extensively using TANAMI data (see Section 4.4). The peculiar source PMN J1603–4904 has also been extensively studied within the TANAMI collaboration before (Müller et al. 2014a, 2015, 2016). Therefore these two sources are not included in this study.

We investigated whether the resulting radio galaxy sample in TANAMI is representative of a complete sample of radio galaxies in our declination range. To do this, we cross-matched the Véron-Véron 13th edition AGN catalog (Véron-Cetty & Véron 2010) with the Parkes radio catalog (Wright & Otrupcek 1990). While the Véron-Véron catalog is not complete in a statistical sense, it is a comprehensive compendium of known AGN. The Parkes catalog on the other hand provides extensive information on the radio properties of the sources.

TABLE 5.1: TANAMI radio galaxies.

| B1950 name | Catalog name   | Class <sup>a</sup> | Redshift          | RA(J2000) | Dec(J2000) | LAT <sup>b</sup> |
|------------|----------------|--------------------|-------------------|-----------|------------|------------------|
| 0518–458   | Pictor A       | FR II              | 0.035             | 79.957    | –45.779    | yes              |
| 0521–365   | PKS 0521–36    | RG/SSRQ            | 0.057             | 80.742    | –36.459    | yes              |
| 0625–354   | PKS 0625–35    | FR I/BLL           | 0.055             | 96.778    | –35.487    | yes              |
| 0825–500   | PKS 0823–500   | RG                 | -                 | 126.362   | –50.178    | no               |
| 1258–321   | PKS 1258–321   | FR I               | 0.017             | 195.253   | –32.441    | no               |
| 1322–428   | Centaurus A    | FR I               | 0.0018            | 201.365   | –43.019    | yes              |
| 1333–337   | IC 4296        | FR I               | 0.013             | 204.162   | –33.966    | no               |
| 1343–601   | Centaurus B    | FR I               | 0.013             | 206.704   | –60.408    | yes              |
| 1549–790   | PKS 1549–79    | RG/CFS             | 0.15              | 239.245   | –79.234    | no               |
| 1600–489   | PMN J1603–4904 | MSO <sup>c</sup>   | 0.23 <sup>d</sup> | 240.961   | –49.068    | yes              |
| 1718–649   | PKS 1718–649   | GPS/CSO            | 0.014             | 260.921   | –65.010    | yes <sup>e</sup> |
| 1733–565   | PKS 1733–56    | FR II              | 0.098             | 264.399   | –56.567    | no               |
| 1814–637   | PKS 1814–63    | CSS/CSO            | 0.065             | 274.896   | –63.763    | no               |
| 2027–308   | PKS 2027–308   | RG                 | 0.54              | 307.741   | –30.657    | no               |
| 2152–699   | PKS 2153–69    | FR II              | 0.028             | 329.275   | –69.690    | no               |

<sup>a</sup> FR I: Fanaroff-Riley type 1; FR II: Fanaroff-Riley type 2; BLL: BL Lac; RG: Radio galaxy; SSRQ: Steep Spectrum Radio Quasar; CFS: Compact Flat Spectrum; MSO: Medium-size Symmetric Object; GPS: Gigahertz Peaked Spectrum; CSO: Compact Symmetric Object; CSS: Compact Steep Spectrum.

<sup>b</sup> Associated with a LAT  $\gamma$ -ray source from the 3FGL (Acero et al. 2015), unless otherwise indicated.

<sup>c</sup> Originally misclassified as BL Lac, this source has been classified as a young radio galaxy based on multi-wavelength studies (Müller et al. 2014a, 2015, 2016).

<sup>d</sup> Goldoni et al. (2016).

<sup>e</sup> First  $\gamma$ -ray detection reported by Migliori et al. (2016).

Since we are only interested in radio galaxies for the purpose of this study, we had to clean the sample by excluding known BL Lacs and QSOs. Physically, the only criterion distinguishing radio galaxies from blazars should be the jet viewing angle. However, it can be challenging to obtain this information, and estimates often suffer from a large uncertainty. We therefore made this selection based on the classification provided in the Véron-Véron catalog.

This left us with a total of 83 sources south of  $\delta = -30^\circ$ . Thirteen out of seventeen TANAMI radio galaxies are included in this sample. The missing sources are Centaurus A, which is misclassified as BL Lac in the Véron-Véron catalog; Centaurus B, and PMN J1603–4904 which are not included in the catalog probably due to their location in the galactic plane; as well as PKS 1258–321 which is also missing from the Véron-Véron catalog.

We looked manually for existing VLBI measurements for all these 83 sources on the NASA/IPAC Extragalactic Database (NED), and found existing data for six non-TANAMI radio galaxies, from the VLBA at 8.6 GHz (Petrov et al. 2005) or the LBA at 8.4 GHz or 4.8 GHz (Fey et al. 2004; Hancock et al. 2009). The resulting list is a complete sample of 21 southern radio galaxies with compact radio emission on VLBI scales, and the TANAMI radio galaxy sample of 15 sources can be considered representative of this complete sample.

## 5.2 VLBI data analysis

Many more antennas are available at 8.4 GHz (than at 22.3 GHz), yielding better angular resolution in this band, despite the lower frequency. Observations in this band are also more frequent. Hence, 8.4 GHz data are used for the kinematic analysis.

The data were calibrated using the National Radio Astronomy Observatory's Astronomical Image Processing System (AIPS) and imaged in Difmap (Shepherd et al. 1994) with the same procedures described in Ojha et al. (2010), and summarized in Chapter 4.

We have used selected epochs at 22.3 GHz, simultaneous with the 8.4 GHz ones, to produce spectral index maps of our targets. The spectral information is crucial in order to identify the VLBI core component, which usually presents a flat spectral index, and as an input for estimating the jet viewing angle. Since the absolute position information is lost in the imaging process due to the phase self-calibration, it is necessary to properly align the maps before computing the spectral index. This is done through a 2D cross-correlation procedure (Fromm et al. 2013), referenced on an optically thin region of the jet, whose position should not vary with frequency. After aligning the maps and convolving them with the same beam (typically the one of the map with lowest resolution), the spectral index is calculated for each point as

$$\alpha = \frac{\log(S_1/S_2)}{\log(\nu_1/\nu_2)}, \quad (5.1)$$

where we have assumed the convention  $S \propto \nu^{+\alpha}$ .

In order to study the evolution of the jet, we fit the clean, self-calibrated maps with circular Gaussian components using the `Modelfit` task in Difmap. We then cross identify them in the different epochs by selecting a component in the first epoch, and searching for the closest component in the following epochs. This selection was then corroborated by visual inspection of the maps and the component properties, e.g., the evolution of their flux density. We then fit the motion of the components which are robustly detected in at least 5 epochs, separately in RA and Dec, to derive the two components of the velocity vector, following Lister et al. (2009a):

$$\begin{aligned} x(t) &= \mu_x(t - t_{0x}) \\ y(t) &= \mu_y(t - t_{0y}) \\ \mu &= \sqrt{\mu_x^2 + \mu_y^2} \\ \beta_{\text{app}} &= \mu D_L / c(1 + z) \end{aligned} \quad (5.2)$$

where  $\mu_x$  and  $\mu_y$  are the angular speeds in RA and Dec,  $\mu$  is the resulting vector modulus, and  $\beta_{\text{app}}$  is the apparent speed in units of speed of light, obtained using the luminosity distance  $D_L$  and the redshift  $z$ . We do not fit accelerations since second-order terms are difficult to constrain without a long enough monitoring. Lister et al. (2009a) require a component to be detected in at least 10 epochs in order to fit an acceleration, and the maximum number of TANAMI epochs for the sources in our sample is 9. Therefore, we use a simple linear fit via  $\chi^2$  minimization.

For the uncertainty on the component position, we adopt the approach described in Lico et al. (2012). The error is calculated as the component size divided by its signal-to-noise ratio (SNR). The latter is calculated as the ratio between the flux of the component and the map noise. For

bright components, this estimate can yield unrealistically small uncertainties. As a lower limit for this case, we take the largest value between half the component size and  $1/5$  of the beam major axis. These procedures were implemented and executed using a novel GUI-based Python code co-developed with Laura Vega García, `kinepy`.

Since the TANAMI array composition can vary significantly across epochs, the uv-coverage, and consequently the beam will also be inhomogeneous across the epochs for a single source. This complicates the identification of components across the epochs, since one component detected in a low-resolution epoch may be resolved into multiple components in another epoch. To overcome this problem, we re-imaged the sources applying a Gaussian taper to the highest-resolution maps in order to downweight the visibilities from the longest baselines, and approximately match the beam size of the epoch with lowest resolution along the jet direction. The images were then convolved with the same circular beam.

Using the apparent speed measured from kinematics ( $\beta_{\text{app}}$ ) together with the jet-to-counterjet flux ratio  $R = S_{\text{jet}}/S_{\text{counterjet}}$ , it is possible to set some limits on the intrinsic jet speed  $\beta = v/c$  and viewing angle  $\theta$ .

$R$  and  $\beta_{\text{app}}$  can be expressed as a function of these two parameters:

$$\beta_{\text{app}} = \frac{\beta \sin \theta}{1 - \beta \cos \theta} ; R = \left( \frac{1 + \beta \cos \theta}{1 - \beta \cos \theta} \right)^{c-\alpha} \quad (5.3)$$

where the index  $c$  is 2 or 3 depending on whether  $R$  is calculated integrating the flux over the jet or using a single component, respectively. In our case we use  $c = 2$ .  $\alpha$  is the jet spectral index. In the cases where no counter-jet emission is detected, we place a lower limit on  $R$  by taking the maximum observed flux on the counter-jet side of the image.

The spectral and kinematic analysis were performed using two GUI-based Python programs developed by L. Vega García, implementing the procedures described above.

### 5.3 Imaging results

#### 0518–458 (Pictor A)

Pictor A is a classical powerful FR II radio galaxy. In a previous kinematic study Tingay et al. (2000) characterized the pc-scale jet of the source with three components, with a fastest apparent motion of  $\beta_{\text{app}} = (1.1 \pm 0.5)$ . They did not detect any counter-jet at this scale, and additionally they found an apparent bend in the jet at  $\sim 10$  mas from the core.

TANAMI monitoring has provided 5 epochs for this source. The full-resolution images are presented in Fig. A.1, and the corresponding image parameters are listed in Table A.1. The first epoch map was already presented in Ojha et al. (2010).

The jet extends for  $\sim 30$  mas westward from the brightest component, and several knots can be identified and tracked. We consistently detect emission upstream of the brightest component (assumed to be the core), in all epochs. This feature is not present in the first epoch map of Ojha et al. (2010), but its detection in multiple epochs in this work indicate that it is real.

To test if this can be considered as counter-jet emission, we produce a spectral index map of the source between the quasi-simultaneous X band (epoch 2008-11-27) and K band (epoch 2008-11-29) images. The resulting map is presented in Fig. 5.1. We see that the spectrum flattens around the brightest component, and becomes optically thin again in the upstream region. This indicates that this is counter-jet emission, and should therefore be taken into account when computing jet-to-counter-jet flux ratios.

We investigated the significance of a putative jet bending by plotting the position angle of the Gaussian components versus the radial distance. This is shown in Fig. 5.2. There is no obvious break in the distribution around  $\sim 10$  mas, in contrast with the findings of Tingay et al. (2000).

### 0521–365

This is a nearby AGN with uncertain classification. Leon et al. (2016) classify it as a BL Lac, and derive limits on the jet viewing angle, speed, and Doppler factor using the Atacama Large Millimeter Array (ALMA). Their results suggest a jet viewing angle in the range  $16^\circ \leq \theta \leq 38^\circ$ , from the jet sidedness. Their detection of a large scale double structure already suggests that Doppler boosting effects in this source are not dominant. D’Ammando et al. (2015) constrain the same parameters using SED modeling including  $\gamma$ -ray data, obtaining a more aligned jet viewing angle of  $6^\circ \leq \theta \leq 15^\circ$ . These results point to an intermediate jet viewing angle between a blazar and a steep spectrum radio quasar (SSRQ) or radio galaxy.

Previous VLBI observations performed with the VLBA and with the Southern Hemisphere VLBI Experiment (SHEVE) at 4.9 GHz and 8.4 GHz provided an upper limit on the apparent speed of jet components  $\beta_{app} < 1.2$  (Tingay & Edwards 2002). This is also consistent with the hypothesis that the jet of PKS 0521–36 is not strongly beamed.

Due to its known variability at  $\gamma$ -ray energies, PKS 0521–36 is one of the more densely monitored sources in the sample, with nine TANAMI epochs, which provide an excellent data set for a kinematic analysis. The full resolution maps are presented in Fig. A.2 and A.3, and the corresponding map parameters are listed in Table A.2.

The first epoch image was already presented in Ojha et al. (2010), and is consistent with the one we obtained for this work. The most sensitive and highest-resolution epoch is the second, which shows a faint jet flow extending out to  $\sim 60$  mas from the core to the north-west. There is a drop in the jet brightness around 10-15 mas from the core, which is seen consistently in all epochs. The jet structure is remarkably consistent across the epochs, hinting at a slow speed. The extended jet is not detected in the last epoch due to the lack of the shortest baseline ATCA-Mopra which provides the necessary sensitivity to the larger scale emission.

We produced a spectral index map between the quasi-simultaneous X band (epoch 2008-03-28) and K band (epoch 2008-03-26) images, which is presented in Fig. 5.3.

### 0625–354

This is an FR I radio galaxy, but shows an optical spectrum similar to a BL Lac object (Wills et al. 2004). Its  $\gamma$ -ray properties also suggest a moderately aligned jet, similar (but less extreme) to the case of IC 310 (Aleksić et al. 2014).

TANAMI is the first multi-epoch VLBI data set for this source, providing 9 epochs. A previous single-epoch observation with the LBA by Venturi et al. (2000) provided constraints on the jet angle to the line of sight and intrinsic jet speed using a lower limit on the jet-to-counterjet ratio and an estimate of the core dominance. The latter method gives the most constraining estimates of  $\theta \leq 43^\circ$  and  $\beta \geq 0.74$ .

The full resolution TANAMI maps are presented in Fig. A.4 and A.5, and the corresponding map parameters are listed in Table A.3. The first epoch map was already presented in Ojha et al. (2010), and is consistent with the one presented here.

We produce a spectral index map between X band (epoch 2008-11-27) and K band (epoch 2008-11-29), which is presented in Fig. 5.4. The index is relatively steep even in the brightest region.

### 0823–500

This source with unknown redshift is included in the PKS catalog (Wright & Otrupcek 1990), but not in the Verón-Verón AGN catalog (Véron-Cetty & Véron 2010), most likely due to its low galactic latitude ( $b = -7.0603194$ ). It is unclassified in the PKS catalog as well as in an optical identification of radio sources from the AT20G survey (Mahony et al. 2011, AT20G J082526–501039). It is classified as a galaxy on the NASA/IPAC Extragalactic Database (NED). This source is a relatively recent addition to the TANAMI sample, with only one available epoch. The TANAMI 8.4 GHz map (see Fig. A.6 and Tab. A.4 for the corresponding map parameters) shows a double-sided structure, with a core, jet and counterjet extending along the NE-SW direction. There is a gap of emission on the counter-jet side that extends for  $\sim 4$  mas from the core. The estimated jet-to-counterjet ratio is  $R = 1.25$ , which leads to a maximum viewing angle  $\theta < 87^\circ$ , suggesting a largely misaligned jet orientation.

### 1258–321

The source shows a faint one-sided jet extending to the north-west, aligned with the kpc-scale structure (Marshall et al. 2005). This source was not included in the first TANAMI paper, but its first-epoch image was presented for the first time in Müller et al. (2018). The TANAMI maps are presented in Fig. A.7 and the corresponding map parameters are listed in Table A.5.

### 1333–337

This FR I source shows a symmetric double-sided morphology on parsec scales, as showed by the full-resolution maps in Figg. A.8, A.9. The TANAMI spectral index maps, presented in Fig. 5.5, show an unresolved component with a spectral index  $\alpha \sim 0.8$ .

### 1343-601 (Centaurus B)

This classic FR I radio galaxy was added to the TANAMI sample after being detected by *Fermi*-LAT in the second source catalog (Nolan et al. 2012). Because of this, there are only two calibrated epochs at the moment, which are not sufficient to perform a robust kinematic analysis. Using one well-defined jet component, we can obtain a rough upper limit on the jet apparent speed, which results to be lower than  $0.89c$ . The two full-resolution maps are presented in Fig. A.10, and the corresponding map parameters are listed in Table A.7. The first epoch map was already presented in Müller et al. (2018).

**1549–790**

This Compact Flat-Spectrum (CFS) source exhibits a classic double-sided structure at milliarc-second resolution, suggesting that its viewing angle is large. The multi-epoch full-resolution images are presented in Figures A.11 and A.12.

**1718–649**

This is one of the most classic examples of the Compact Symmetric Object (CSO) and Gigahertz-Peaked Spectrum (GPS) source classes (see O’Dea 1998, for a review), i.e. a young radio galaxy. These sources are typically compact (linear size  $< 1$  kpc), and the radio emission is dominated by symmetric mini-lobes which can show hot-spots similarly to the large scale lobes of FR II radio galaxies. The advance speed of these hot-spots provides a kinematical age estimate for these sources, which is typically  $t_{age} < 10^3$  yr.

TANAMI provides the first multi-epoch data set for this well-studied source, and therefore the first opportunity for a measurement of its kinematical age. The full resolution maps are presented in Fig. A.13 and A.14, and the corresponding map parameters are listed in Table A.9. The first epoch map was already presented in Ojha et al. (2010), and is consistent with the one presented here. The main structure of two components separated by  $\sim 8$  mas is consistent across the epochs.

We present a spectral index map between 8.4 GHz and 22.3 GHz in Fig. 5.7. The spectral morphology suggests that the core of the young radio source is strongly absorbed at these frequencies, and should be located between the two emission components, corresponding to the region of highly inverted spectral index.

**1733–565**

This FR II radio galaxy shows a double-sided structure, with jets extending in the northeast-southwest direction, up to  $\sim 5$  mas from the core. The multi-epoch maps at 8.4 GHz and 22.3 GHz are presented in Figs. A.15, A.16. The jet structure appears to be consistent across the epochs. Spectral index maps were created using the first three epochs, and are presented in Fig. 5.8. The source is practically unresolved in the spectral maps, with an overall spectral index in the range  $-0.8 \lesssim \alpha \lesssim -0.3$ . We therefore do not detect a flat-spectrum core in this source.

**1814–637**

This CSS source has been proposed as a putative young radio source (Ojha et al. 2010, and references therein). At full resolution, it shows a compact, marginally resolved component. Using tapering in order to recover larger scale structures, we detect a symmetric structure in the N-S direction, reminiscent of classic CSOs. The full-resolution maps are presented in Fig. A.17, while the tapered maps are shown in Fig. A.18. The corresponding image parameters are listed in Tab. A.11.

**2027–308**

This is the most distant radio galaxy in the sample, with a redshift  $z = 0.539$ . Our full-resolution TANAMI images are presented in Figs. A.19, A.20. Interestingly, the source shows

an asymmetric double-sided structure, with one jet extending west-south-west and a counterjet which seems to bend north.

### 2152–699

This FR II source shows a relatively elongated jet, extending  $\sim 50$  mas from the core to the north-east. The jet is best seen in the first two TANAMI epochs (see Fig. A.21). The spectral index maps are shown in Fig. 5.9, and show a relatively steep core with a spectral index around  $-0.5 < \alpha < -0.7$ .

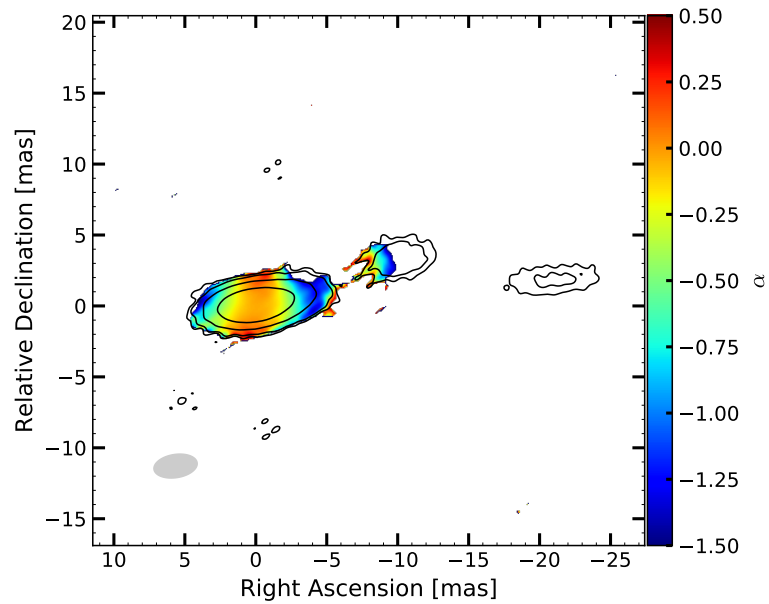


FIGURE 5.1: Spectral index map of Pictor A between 8.4 GHz and 22.3 GHz for epoch 2008-11-27. Black contours from the 8.4 GHz image. The convolving beam is represented in grey in the lower-left corner.

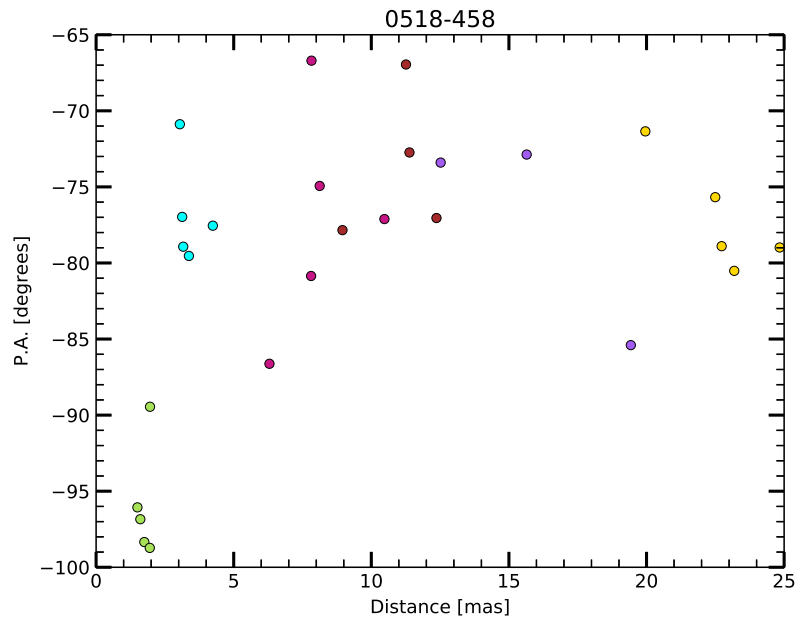


FIGURE 5.2: Position angle of Gaussian jet components for Pictor A versus radial distance from the core. The color coding indicates different components, and is the same as the upper left panel of Fig. 5.22.

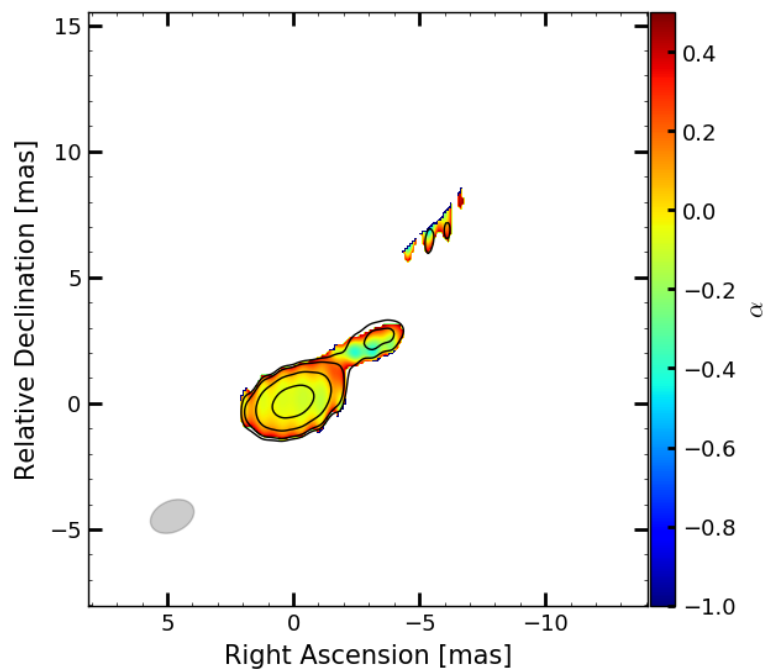


FIGURE 5.3: Spectral index map of PKS 0521–36 between 8.4 GHz and 22.3 GHz for epoch 2008-03-28. Black contours from the 8.4 GHz image. The beam with which both maps have been convolved with is represented in grey in the lower-left corner.

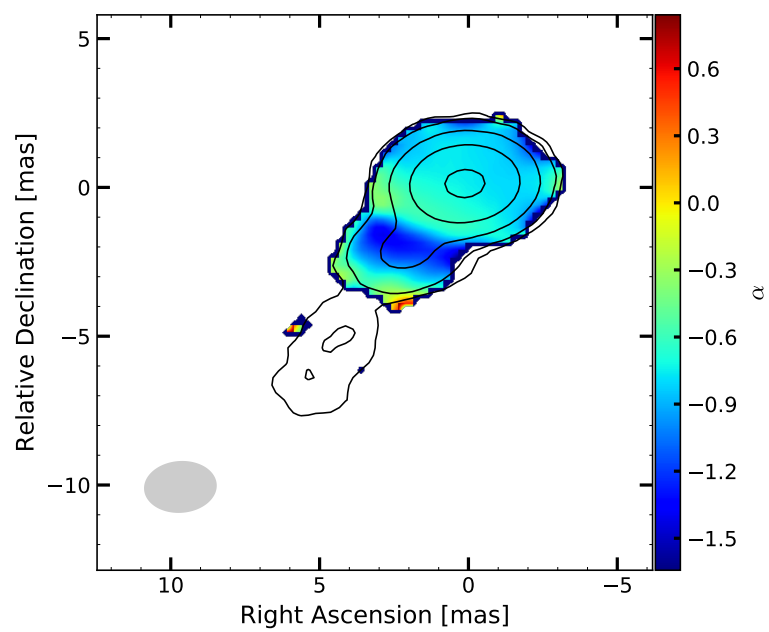


FIGURE 5.4: Spectral index map of PKS 0625–35 between 8.4 GHz and 22.3 GHz for epoch 2008-11-27. The black contours are from the 8.4 GHz image. The beam with which both maps have been convolved with, is represented in grey in the lower-left corner.

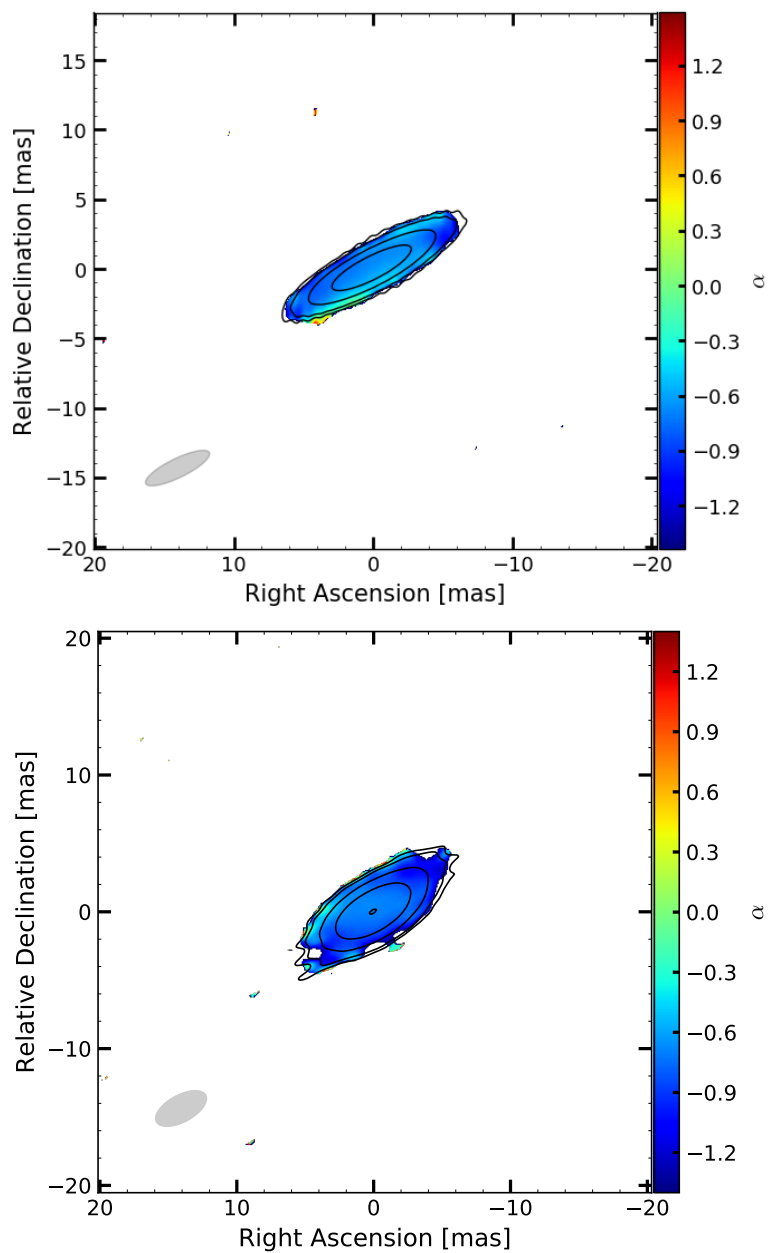


FIGURE 5.5: Spectral index map of IC 4296 between 8.4 GHz and 22.3 GHz for epochs 2008-02-07 and 2008-11-27. The black contours are from the 8.4 GHz image. The beam with which both maps have been convolved with, is represented in grey in the lower-left corner.

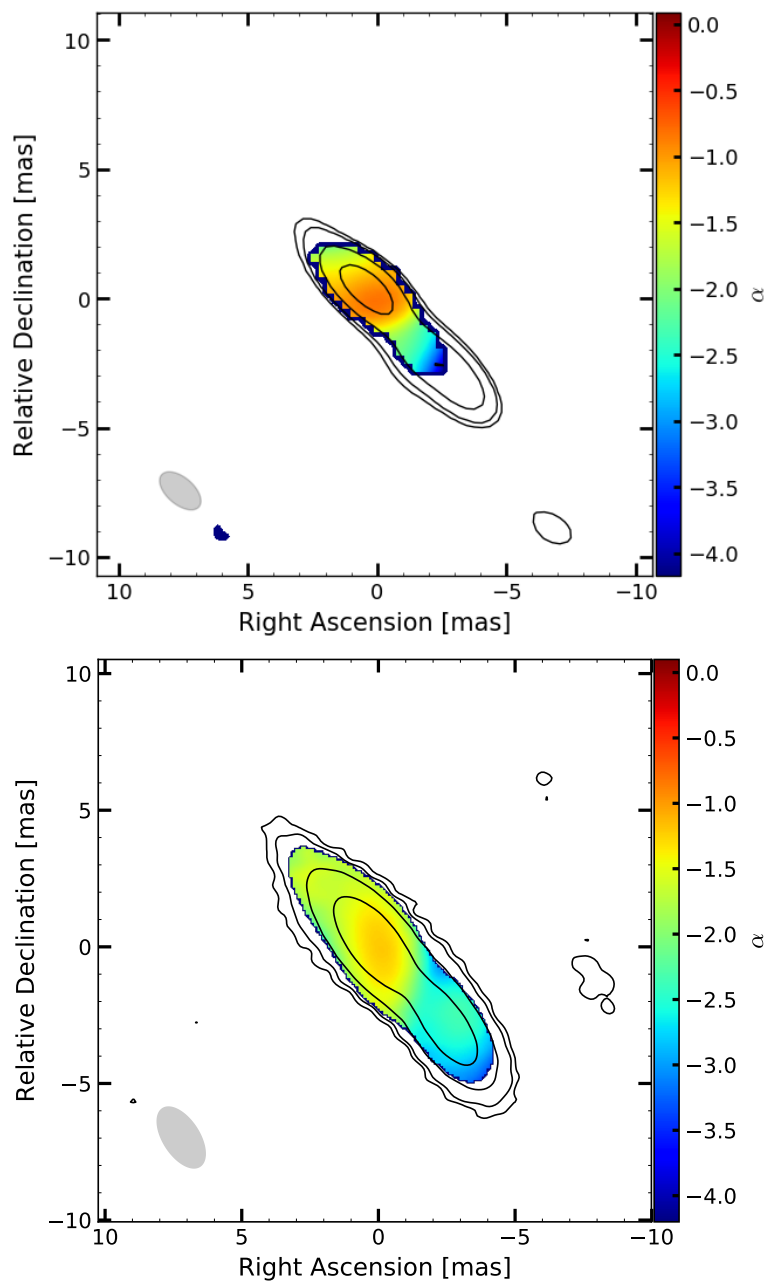


FIGURE 5.6: Spectral index map of PKS 1549–79 between 8.4 GHz and 22.3 GHz for epochs 2008-02-07 and 2008-11-27. The black contours are from the 8.4 GHz image. The beam with which both maps have been convolved with, is represented in grey in the lower-left corner.

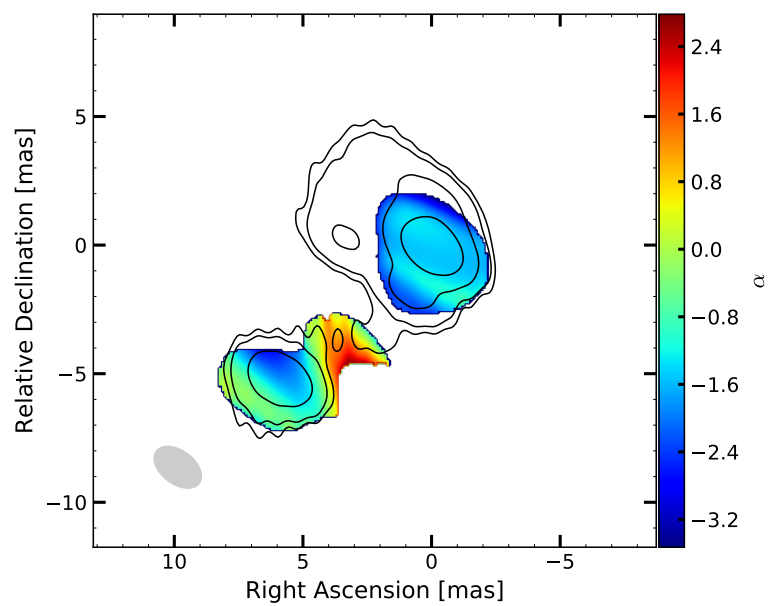


FIGURE 5.7: Spectral index map of PKS 1718–649 between 8.4 GHz and 22.3 GHz for epoch 2008-02-07. The black contours are from the 8.4 GHz image. The beam with which both maps have been convolved with, is represented in grey in the lower-left corner.

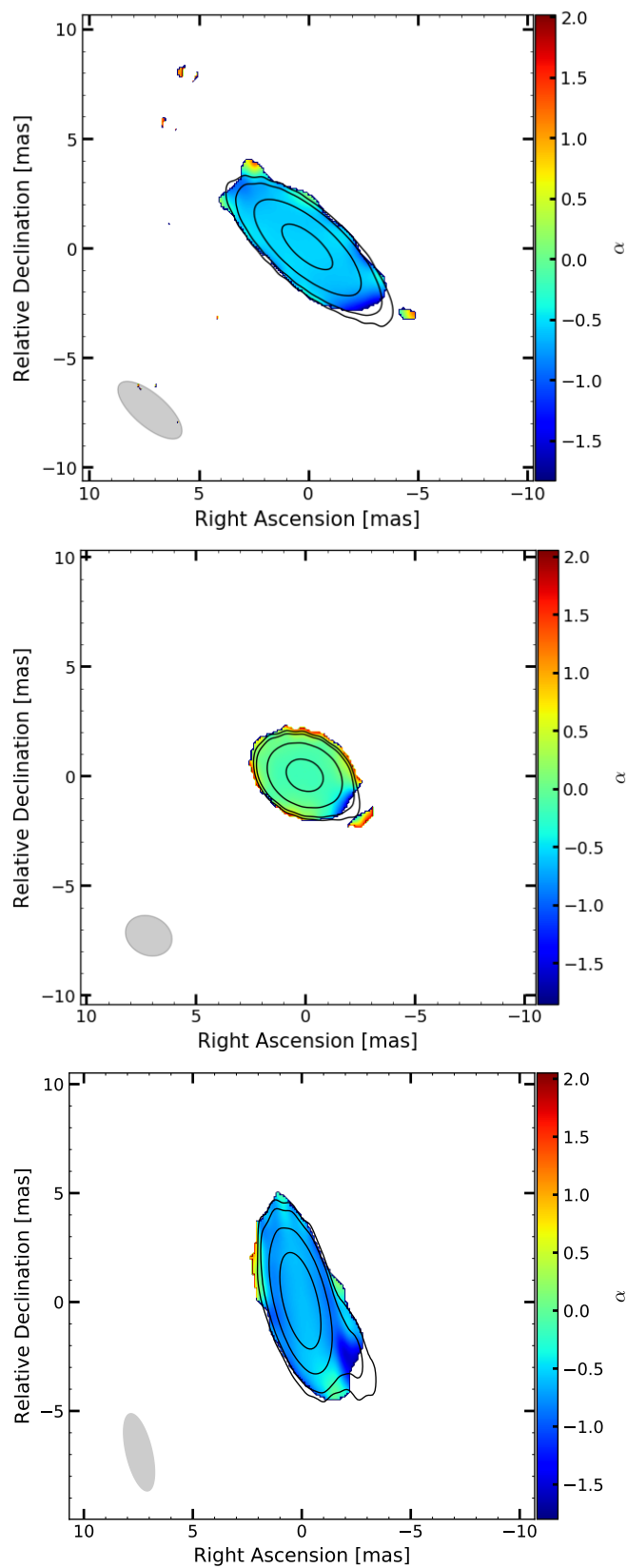


FIGURE 5.8: Spectral index map of PKS 1733–565 between 8.4 GHz and 22.3 GHz for epochs 2008-02-07, 2008-03-28 and 2008-08-08. The black contours are from the 8.4 GHz image. The beam with which both maps have been convolved with, is represented in grey in the lower-left corner.

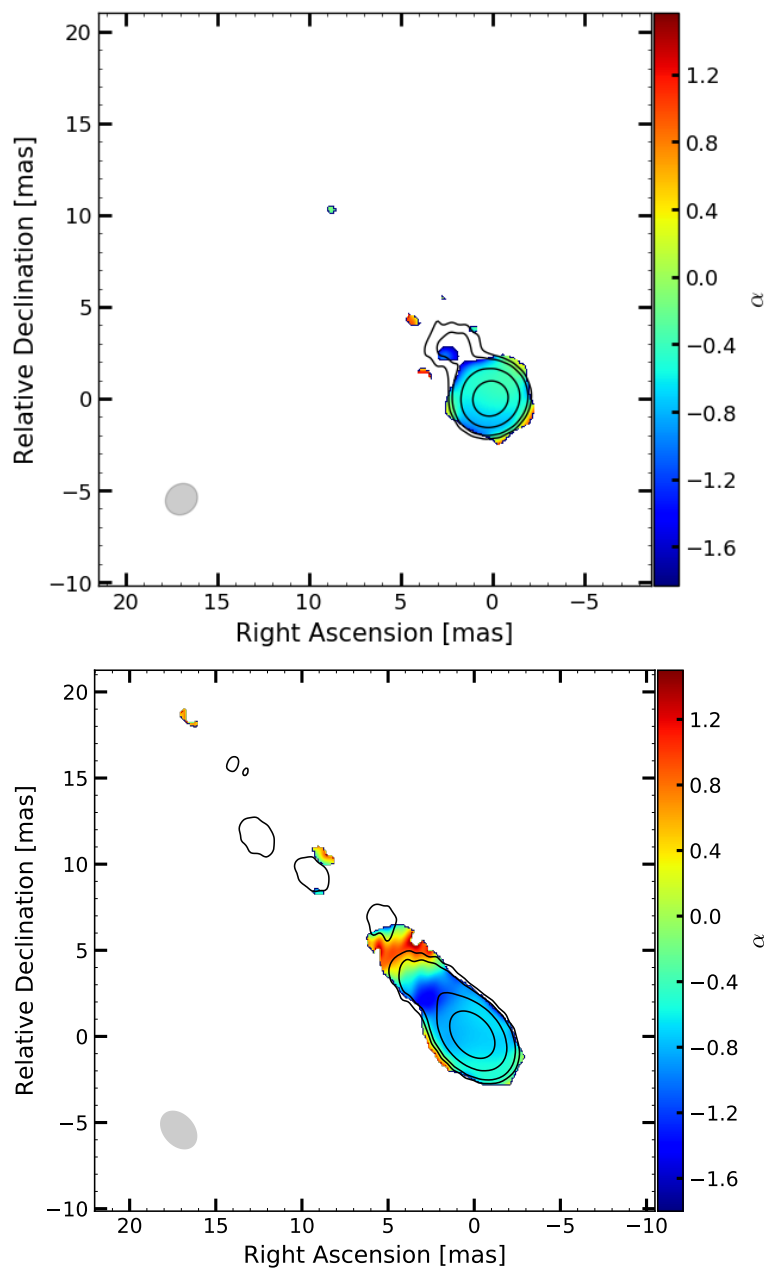


FIGURE 5.9: Spectral index map of PKS 2153–69 between 8.4 GHz and 22.3 GHz for epochs 2008-02-07 and 2008-11-27. The black contours are from the 8.4 GHz image. The beam with which both maps have been convolved with, is represented in grey in the lower-left corner.

## 5.4 Kinematics results

In this section we present the results of the kinematic analysis of our TANAMI radio galaxies on a source-by-source basis. The values describing the component motions for each source, i.e., angular speed and apparent linear speed, are listed in Tables 5.2 through 5.11. The results can be visualized with the plots of the identified Gaussian components and their identification and tracking (Figures 5.12 through 5.21), of their core separation versus time (Fig. 5.22, 5.23, 5.24) and of their flux versus time (Fig. 5.25, 5.26). Finally, the limits on the intrinsic jet speed and viewing angle resulting from our kinematic analysis are illustrated in Fig. 5.27, 5.28.

### 0518–458 (Pictor A)

We re-imaged the source applying a Gaussian taper in order to match the resolution of epoch 2010-07-24 (see Fig. A.1).

We find at least mildly relativistic apparent speeds with a minimum significant value of  $0.1c$  (J1) and a maximum of  $2.6c$  (J2), as allowed within the  $1\sigma$  errors (see Table 5.2). The lower limits are consistent with the estimates in Tingay et al. (2000), while the increased number of epochs allows us to reveal one component which is consistent with mild superluminal motion in the jet of Pictor A.

The top left panel of Fig. 5.27 shows the resulting limits on the intrinsic jet speed and viewing angle for Pictor A obtained via the combination of the apparent speed information with the jet-to-counterjet ratio. The estimates for  $R$  represent the minimum (dashed blue line), mean (continuous blue line) and maximum (dot-dashed blue line) values. The central estimate for  $\beta_{app}$  is the one for the fastest component, while the minimum and maximum values represent its error. The relatively small value of the jet ratio combined with the mildly superluminal apparent speed results in a tight constrain on the viewing angle, which lies in the range  $76^\circ < \theta < 80^\circ$ . To account for the observed apparent speed with such a large jet angle, the intrinsic jet speed should be  $\beta > 0.96$ .

### 0521–365

We re-imaged all epochs applying a Gaussian taper, in order to approximately match the resolution of epoch 2010-03-12 (see Fig. A.2).

The resulting apparent speed shows very slow motions for most components, as suggested by the consistent jet structure across the epochs (see Table 5.3).

Since we obtain slow jet speeds, we attempted to fit our TANAMI jet model together with the previous 8.4 GHz VLBI dataset from Tingay & Edwards (2002). It is possible to cross-identify and fit four components between the two datasets. This is shown in Fig. 5.23. The inclusion of additional epochs confirms that the fastest robustly detected motions in this jet are subluminal (see Table 5.4).

The middle panel of Fig. 5.27 shows the resulting limits on the intrinsic jet speed and viewing angle for PKS 0521–36. Since there is no counter-jet, we assume the lowest observed value of  $R$  as lower limit. For  $\beta_{app}$  the values adopted are the minimum and maximum observed values, considering the four components that are cross-identified with the Tingay & Edwards (2002) data set. We obtain a range of  $\beta > 0.67$  and  $\theta < 26^\circ$ , respectively.

**0625–354**

The outer jet of this source is too faint to be modeled reliably with Gaussian components, therefore we re-imaged only the inner  $\sim 20$  mas for the kinematic analysis, using a taper to obtain matching resolution between the epochs.

Our results show, for the first time, robust superluminal component motion in the pc-scale jet of PKS 0625–35, up to  $2.9c$  (see Table 5.5). Mueller et al. (2012) presented a preliminary kinematic analysis of the TANAMI data on PKS 0625–35, using the first six epochs. They found a highest apparent speed of  $\beta_{app} = 3.0 \pm 0.5$ , which is consistent with our result for component J3.

The lower panel of Fig. 5.27 shows the limits on the intrinsic jet speed and viewing angle for PKS 0625–35 resulting from our observations. In this case, again, we don't detect a counterjet, therefore we assume the minimum measured value of  $R$  as lower limit. The estimates for  $\beta_{app}$  are given by the fastest observed speed and its uncertainty. Our observations limit the intrinsic jet parameters to  $\beta > 0.89$  and  $\theta < 53^\circ$ .

**1258–321**

In this source, only one jet component can be tracked for at least five epochs. The corresponding apparent speed is subluminal (see Table 5.6). Fig. 5.27 shows the limits on the intrinsic jet speed and viewing angle for PKS 1258–321 resulting from our observations. In this case, again, we don't detect a counterjet, therefore we assume the minimum measured value of  $R$  as lower limit. The estimates for  $\beta_{app}$  are given by the measured speed of the only component with at least five epochs, and its error.

**1333–337**

We find that the two symmetric jet components show almost no motion during our monitoring period (see Table 5.7). Although we do find a non-zero separation speed for component CJ1, the uncertainty on this value is higher than 50%. In Fig. 5.28, we adopt the only non-zero apparent speed value as central estimate, and use its uncertainty to define the minimum and maximum estimates while constraining the intrinsic jet parameters of IC 4296.

**1343–601 (Centaurus B)**

As mentioned above, there are only two available TANAMI epochs for Cen B. Although it is not possible to perform a detailed kinematic analysis, as for the other sources, the data can give some indications regarding the presence or absence of superluminal motions in the source. We tentatively identify a local maximum in the brightness distribution of the Cen B VLBI jet at a distance of  $\sim 25$  mas downstream of the core in both our images, which were taken approximately nine months apart (see Fig. 5.10). If this association is correct, which will be tested by forthcoming TANAMI epochs, the apparent jet speed is likely subluminal or at most mildly superluminal.

**1549–790**

We find that the symmetric structure in this source is remarkably stable, with no measured jet motions, and an upper limit on the apparent speed of  $\beta_{app} < 1.7$  (see Table 5.8). We use this value to define the allowed intrinsic jet parameter space in Fig. 5.28.

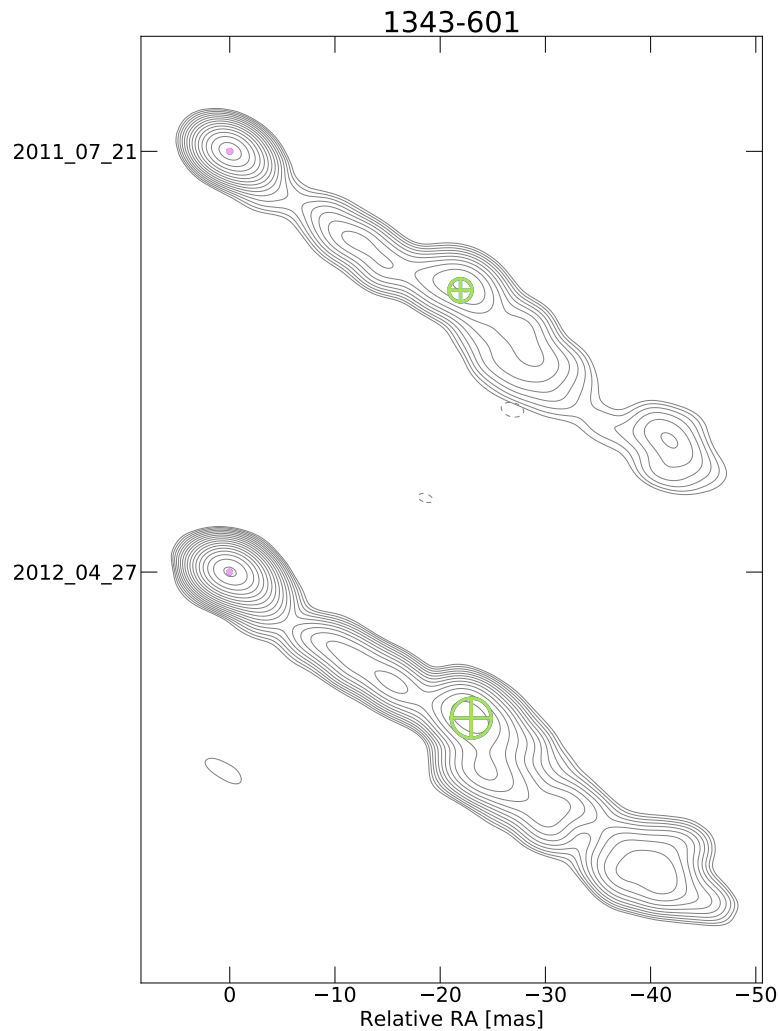


FIGURE 5.10: Multi-epoch images of Centaurus B. The colored crossed circles represent the circular Gaussian components that have been fitted to the clean maps.

### 1718–649

In this case the source is more complex than the classic core-jet morphology seen in the other radio galaxies presented here. We reference the kinematic analysis at the position of the brightest component (C1), even though it is not the core of the radio source in this case (see Section 5.3). The resulting kinematic values represent the evolution of the distance between the two components seen in the maps. In the lower-right panel of Fig. 5.22 we plot the distance between the two components (referenced to the brightest one) as a function of time, and the corresponding linear fit. The angular separation speed is  $\mu = (0.13 \pm 0.06)$  mas/yr, and the corresponding apparent linear speed is  $\beta_{app} = 0.13 \pm 0.06$ . We are therefore able to estimate when the young radio source first ejected its two symmetric component, and find a zero-separation epoch of  $1963 \pm 22$ .

### 1733–565

We do not detect any statistically significant motion in this double-sided jet (see Table 5.9). We once again use the maximum apparent speed value allowed by our measurements, i.e.,  $\beta_{app} < 0.24$ , to constrain the intrinsic jet parameter space (see Fig. 5.28).

**2027–308**

In this case as well, we do not measure any significant jet motion (see Table 5.10). The uncertainty of the component positions is very large, due to their faint flux. Therefore, we do not attempt to estimate the jet viewing angle and intrinsic speed for PKS 2027–308, as such estimates would be extremely uncertain and therefore not meaningful.

**2152–699**

This source shows the fastest apparent motions in this sample, up to  $\beta_{app} = 3.6 \pm 0.8$  (see Table 5.11). Interestingly, there is a clear trend of increasing apparent component speed with increasing core distance. This can be seen in Fig. 5.11, where this effect has been quantified by means of a simple linear fit. This behavior is strikingly similar to the one revealed by TANAMI data for the pc-scale jet of Centaurus A (Müller et al. 2014b), although the scales of both quantities are significantly larger in this case.

The high apparent speed and the absence of a detected counter-jet allow us to place a constrain of the viewing angle, which has to be  $\theta < 39^\circ$  (see lower-right panel of Fig. 5.28).

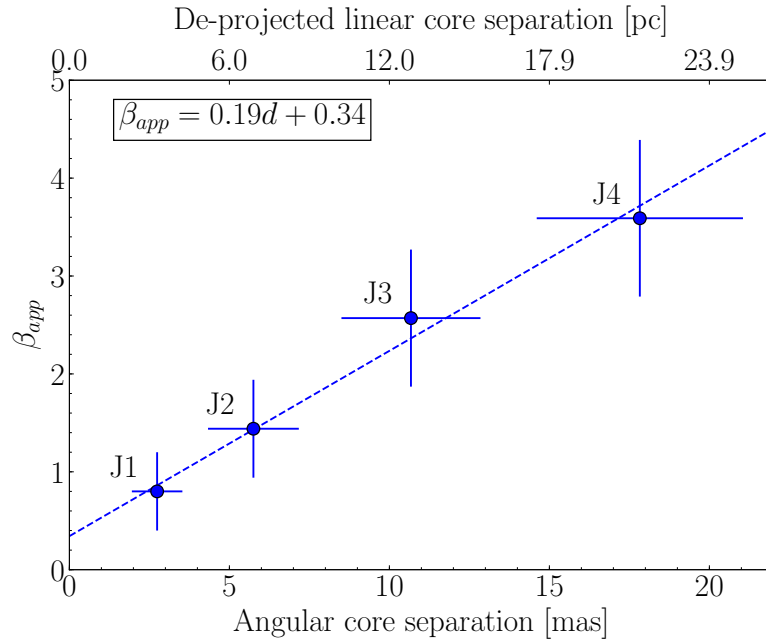


FIGURE 5.11: Apparent velocity of components in the jet of PKS 2153–69 as a function of average core distance. A clear linear increasing trend is seen, indicating downstream acceleration. The de-projected linear core distance has been calculated assuming the maximum possible viewing angle of  $\sim 27^\circ$  (see Fig. 5.27).

TABLE 5.2: Results of the kinematic analysis of Pictor A.

| ID  | $\mu$ (mas/yr) | $\beta_{app}$ | Ej. date     | # ep. |
|-----|----------------|---------------|--------------|-------|
| CJ1 | $0.1 \pm 0.2$  | $0.2 \pm 0.4$ | *            | 5     |
| J1  | $0.3 \pm 0.2$  | $0.6 \pm 0.5$ | $1997 \pm 9$ | 5     |
| J2  | $0.8 \pm 0.3$  | $1.9 \pm 0.7$ | $2000 \pm 3$ | 5     |

TABLE 5.3: Results of the kinematic analysis of PKS 0521–36.

| ID | $\mu$ (mas/yr)     | $\beta_{\text{app}}$ | Ej. date     | # ep. |
|----|--------------------|----------------------|--------------|-------|
| J1 | $0.003\pm 0.006$   | $0.01\pm 0.02$       | *            | 9     |
| J2 | $0.01\pm 0.005$    | $0.04\pm 0.02$       | *            | 9     |
| J3 | $0.020\pm 0.009$   | $0.07\pm 0.03$       | *            | 6     |
| J4 | $0.03\pm 0.02$     | $0.11\pm 0.06$       | *            | 8     |
| J5 | $0.5\pm 0.2$       | $1.9\pm 0.9$         | $1950\pm 23$ | 8     |
| J6 | $0.0665\pm 0.0009$ | $0.242\pm 0.003$     | *            | 8     |

TABLE 5.4: Results of the kinematic analysis of PKS 0521–36 for the components cross-identified with the Tingay &amp; Edwards (2002) dataset.

| ID | $\mu$ (mas/yr) | $\beta_{\text{app}}$ | # ep. |
|----|----------------|----------------------|-------|
| J1 | $0.04\pm 0.05$ | $0.16\pm 0.16$       | 15    |
| J2 | $0.04\pm 0.04$ | $0.13\pm 0.16$       | 15    |
| J3 | $0.11\pm 0.07$ | $0.4\pm 0.3$         | 8     |
| J4 | $0.25\pm 0.07$ | $0.9\pm 0.3$         | 12    |

TABLE 5.5: Results of the kinematic analysis of PKS 0625–35.

| ID | $\mu$ (mas/yr) | $\beta_{\text{app}}$ | Ej. date     | # ep. |
|----|----------------|----------------------|--------------|-------|
| J1 | $0.01\pm 0.18$ | $0.0\pm 0.6$         | *            | 9     |
| J2 | $0.4\pm 0.2$   | $1.4\pm 0.7$         | $1991\pm 8$  | 9     |
| J3 | $0.8\pm 0.3$   | $2.9\pm 0.9$         | $1989\pm 5$  | 9     |
| J4 | $0.6\pm 0.3$   | $2.0\pm 1.1$         | $1971\pm 14$ | 5     |

TABLE 5.6: Results of the kinematic analysis of PKS 1258–321.

| ID | $\mu$ (mas/yr) | $\beta_{\text{app}}$ | Ej. date    | # ep. |
|----|----------------|----------------------|-------------|-------|
| J1 | $0.7\pm 0.5$   | $0.8\pm 0.5$         | $2003\pm 3$ | 5     |

TABLE 5.7: Results of the kinematic analysis of IC 4296.

| ID  | $\mu$ (mas/yr) | $\beta_{\text{app}}$ | Ej. date        | # ep. |
|-----|----------------|----------------------|-----------------|-------|
| J1  | $0.16\pm 0.35$ | $0.14\pm 0.30$       | *               | 5     |
| CJ1 | $0.51\pm 0.36$ | $0.44\pm 0.32$       | $2004.4\pm 7.9$ | 5     |

TABLE 5.8: Results of the kinematic analysis of PKS 1549–79.

| ID  | $\mu$ (mas/yr)  | $\beta_{\text{app}}$ | Ej. date | # ep. |
|-----|-----------------|----------------------|----------|-------|
| J1  | $0.07 \pm 0.09$ | $0.7 \pm 0.8$        | *        | 5     |
| CJ1 | $0.06 \pm 0.11$ | $0.6 \pm 1.1$        | *        | 5     |

TABLE 5.9: Results of the kinematic analysis of PKS 1733–56.

| ID  | $\mu$ (mas/yr)    | $\beta_{\text{app}}$ | Ej. date | # ep. |
|-----|-------------------|----------------------|----------|-------|
| J1  | $0.008 \pm 0.030$ | $0.05 \pm 0.19$      | *        | 8     |
| CJ1 | $0.002 \pm 0.003$ | $0.01 \pm 0.02$      | *        | 8     |

TABLE 5.10: Results of the kinematic analysis of PKS 2027–308.

| ID  | $\mu$ (mas/yr)  | $\beta_{\text{app}}$ | Ej. date | # ep. |
|-----|-----------------|----------------------|----------|-------|
| J1  | $0.06 \pm 0.09$ | $1.7 \pm 2.7$        | *        | 6     |
| CJ1 | $0.2 \pm 0.3$   | $5.6 \pm 8.6$        | *        | 6     |
| CJ2 | $0.01 \pm 0.25$ | $0.3 \pm 7.9$        | *        | 6     |

TABLE 5.11: Results of the kinematic analysis of PKS 2153–69.

| ID | $\mu$ (mas/yr) | $\beta_{\text{app}}$ | Ej. date     | # ep. |
|----|----------------|----------------------|--------------|-------|
| J1 | $0.4 \pm 0.2$  | $0.8 \pm 0.4$        | $2005 \pm 2$ | 6     |
| J2 | $0.8 \pm 0.3$  | $1.4 \pm 0.5$        | $2004 \pm 2$ | 5     |
| J3 | $1.4 \pm 0.4$  | $2.6 \pm 0.7$        | $2003 \pm 1$ | 5     |
| J4 | $2.0 \pm 0.4$  | $3.6 \pm 0.8$        | $2002 \pm 1$ | 5     |

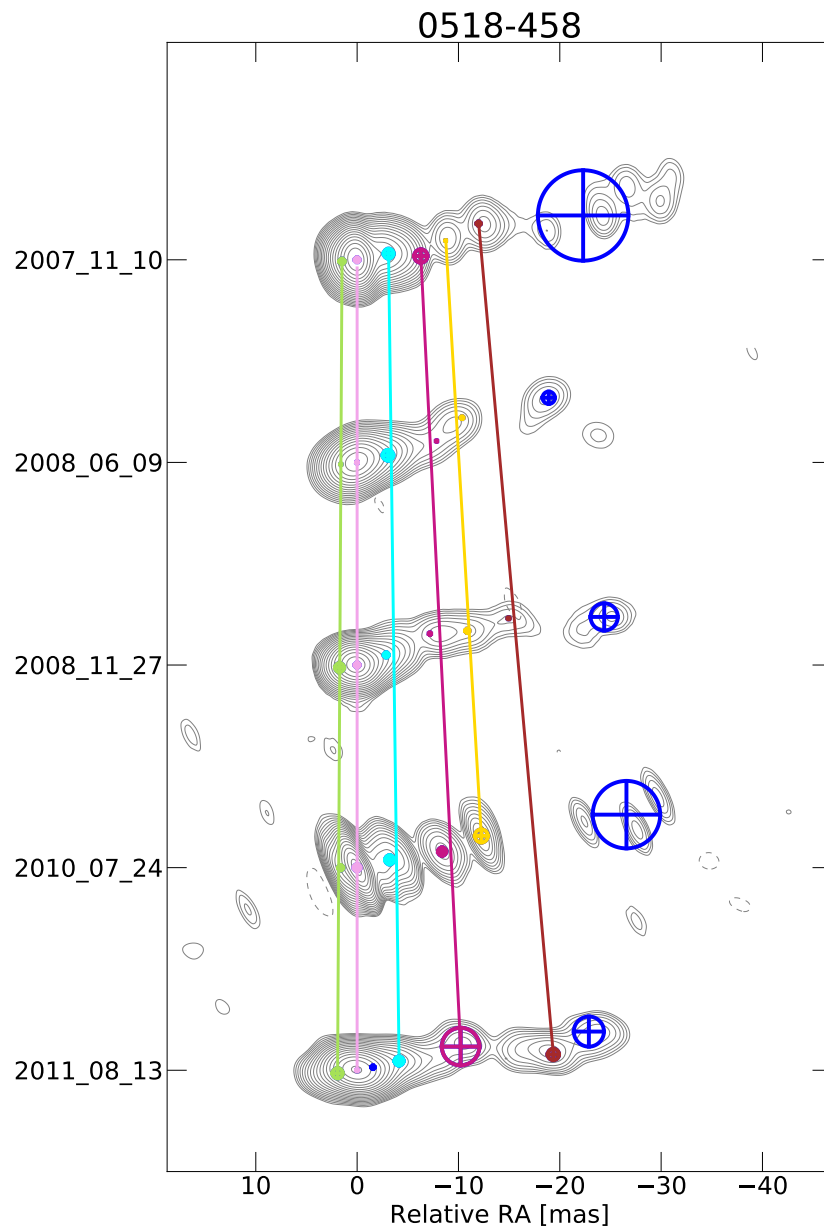


FIGURE 5.12: Multi-epoch tapered images of Pictor A. The colored crossed circles represent the circular Gaussian components that have been fitted to the clean maps. The distance between the images at different epochs is not to scale. The colored lines are not fits to the displayed component positions, but simple interpolations meant to guide the eye.

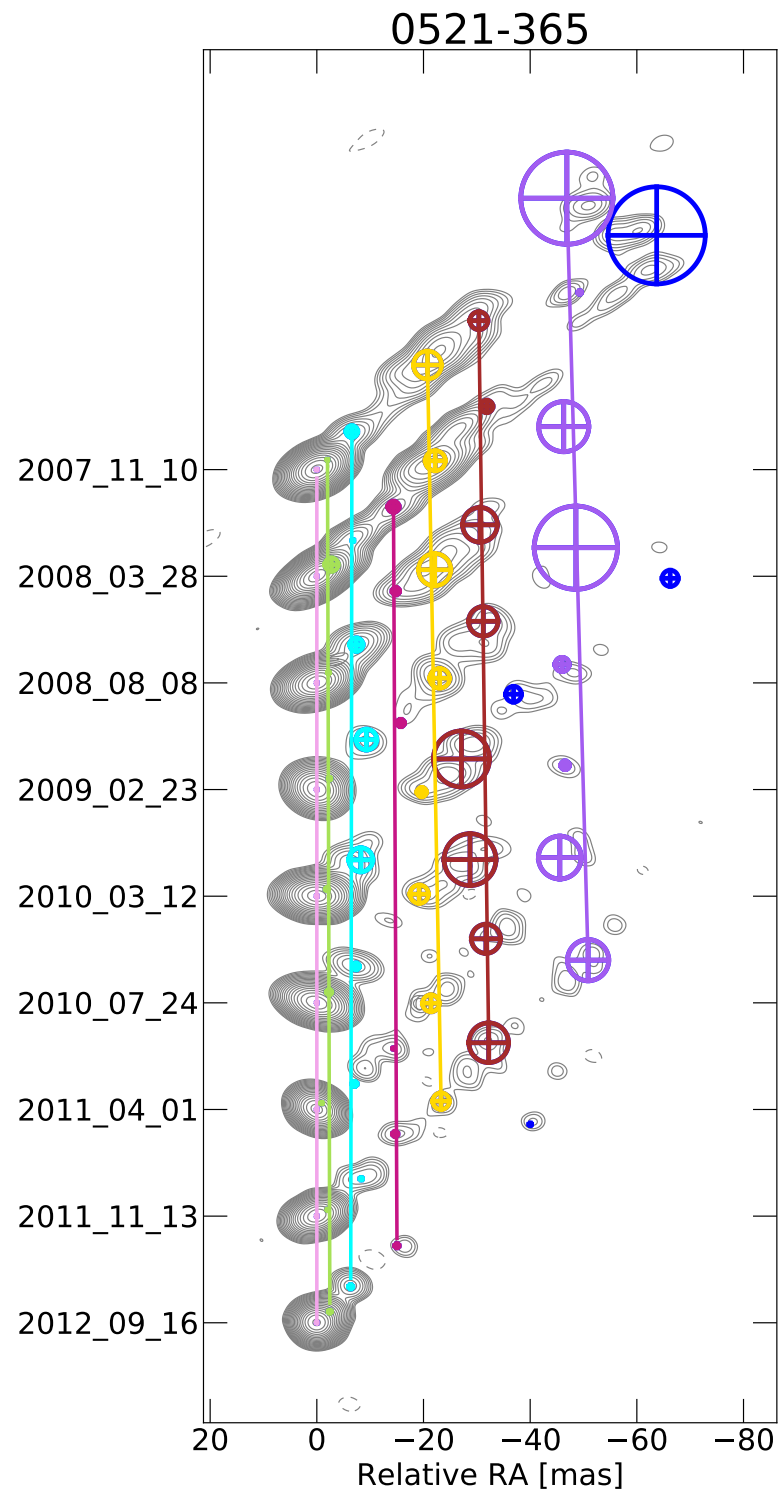


FIGURE 5.13: Multi-epoch tapered images of PKS 0521–36. The colored crossed circles represent the circular Gaussian components that have been fitted to the clean maps. The distance between the images at different epochs is not to scale. The colored lines are not fits to the displayed component positions, but simple interpolations meant to guide the eye.

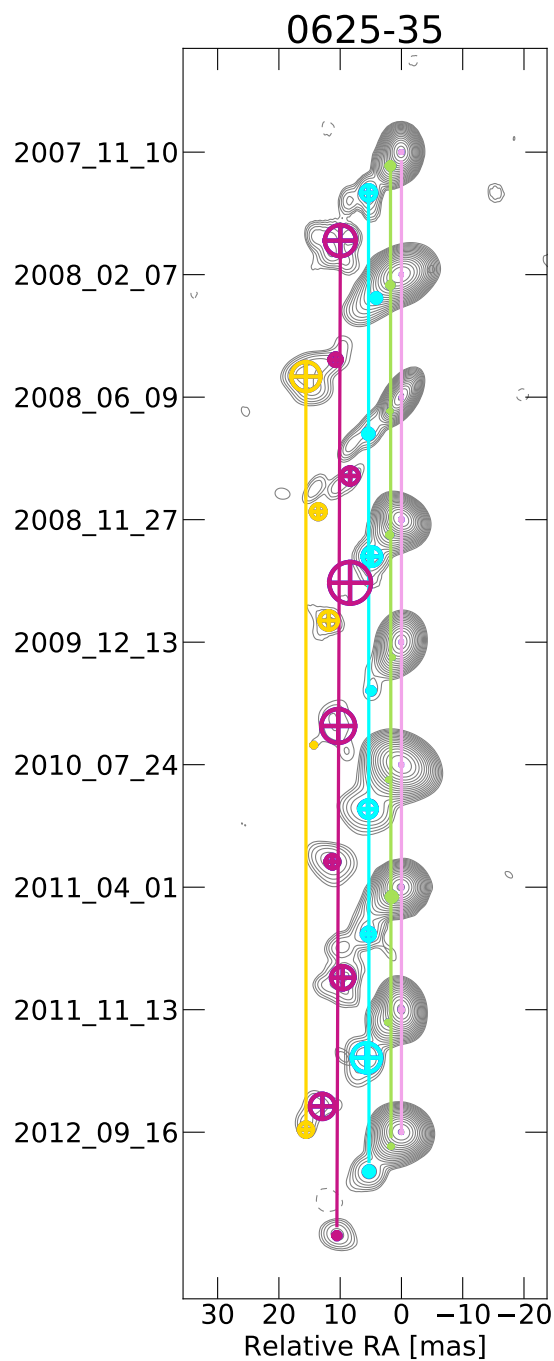


FIGURE 5.14: Multi-epoch images of PKS 0625–35. The colored crossed circles represent the circular Gaussian components that have been fitted to the clean maps. The distance between the images at different epochs is not to scale. The colored lines are not fits to the displayed component positions, but simple interpolations meant to guide the eye.

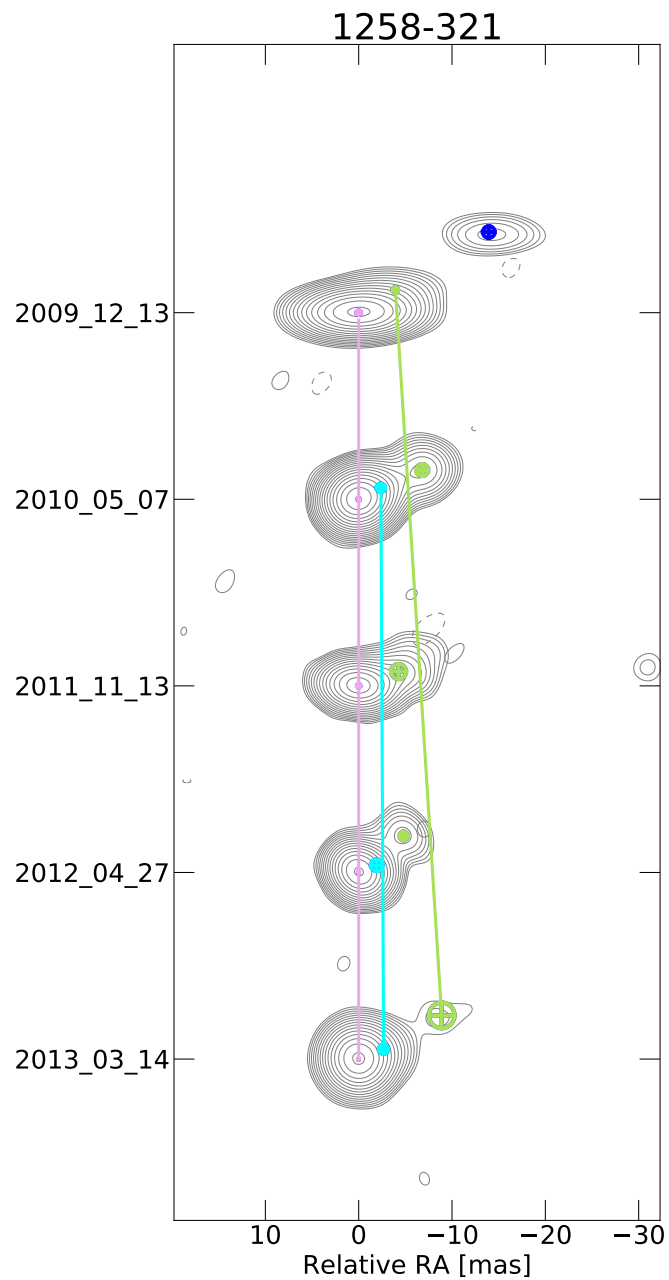


FIGURE 5.15: Multi-epoch tapered images of PKS 1258-321. The colored crossed circles represent the circular Gaussian components that have been fitted to the clean maps. The distance between the images at different epochs is not to scale. The colored lines are not fits to the displayed component positions, but simple interpolations meant to guide the eye.

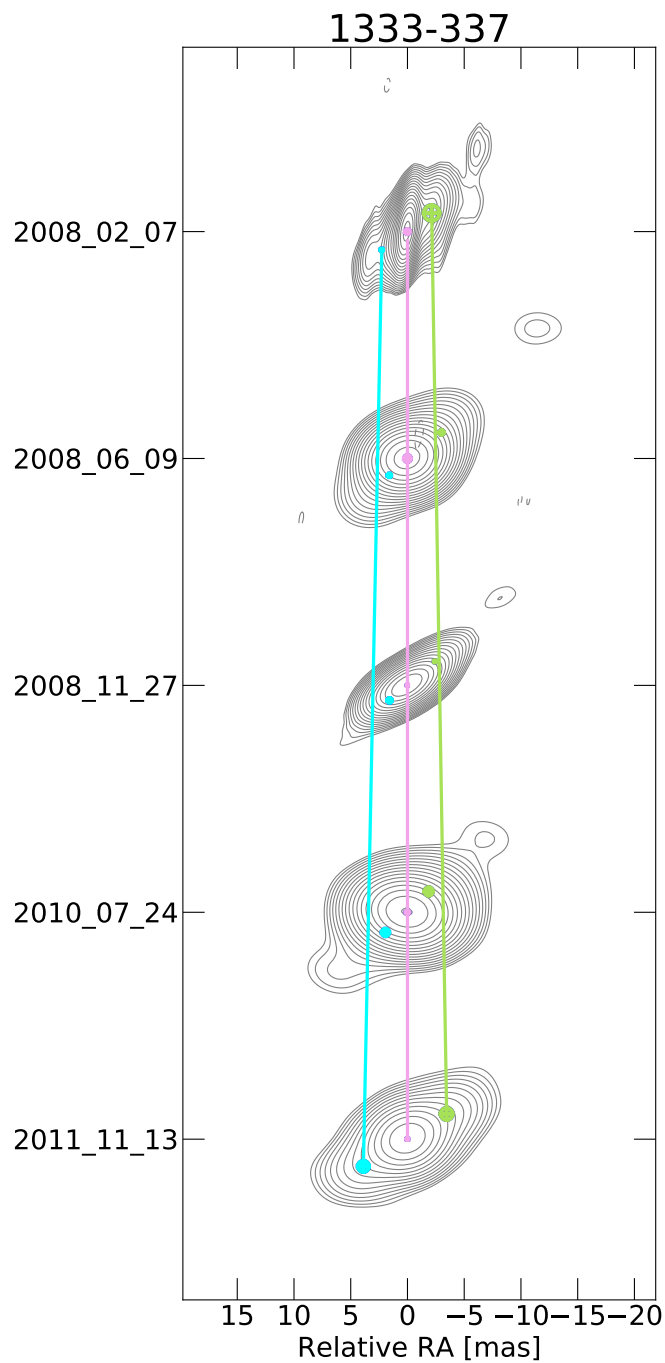


FIGURE 5.16: Multi-epoch tapered images of IC 4296. The colored crossed circles represent the circular Gaussian components that have been fitted to the clean maps. The distance between the images at different epochs is not to scale. The colored lines are not fits to the displayed component positions, but simple interpolations meant to guide the eye.

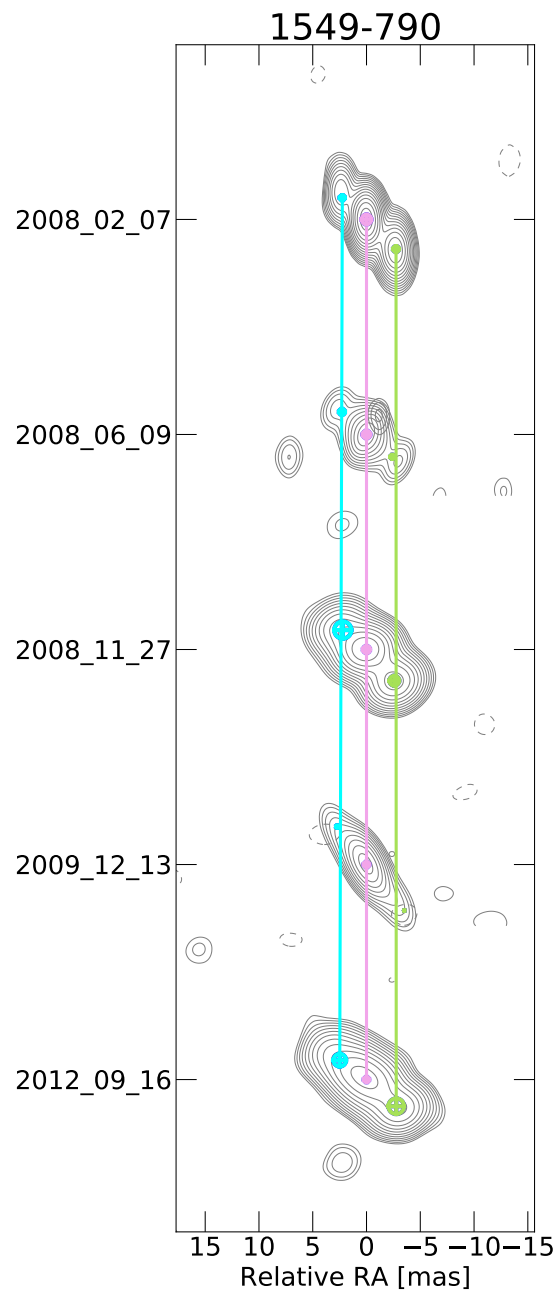


FIGURE 5.17: Multi-epoch tapered images of PKS 1549–79. The colored crossed circles represent the circular Gaussian components that have been fitted to the clean maps. The distance between the images at different epochs is not to scale. The colored lines are not fits to the displayed component positions, but simple interpolations meant to guide the eye.

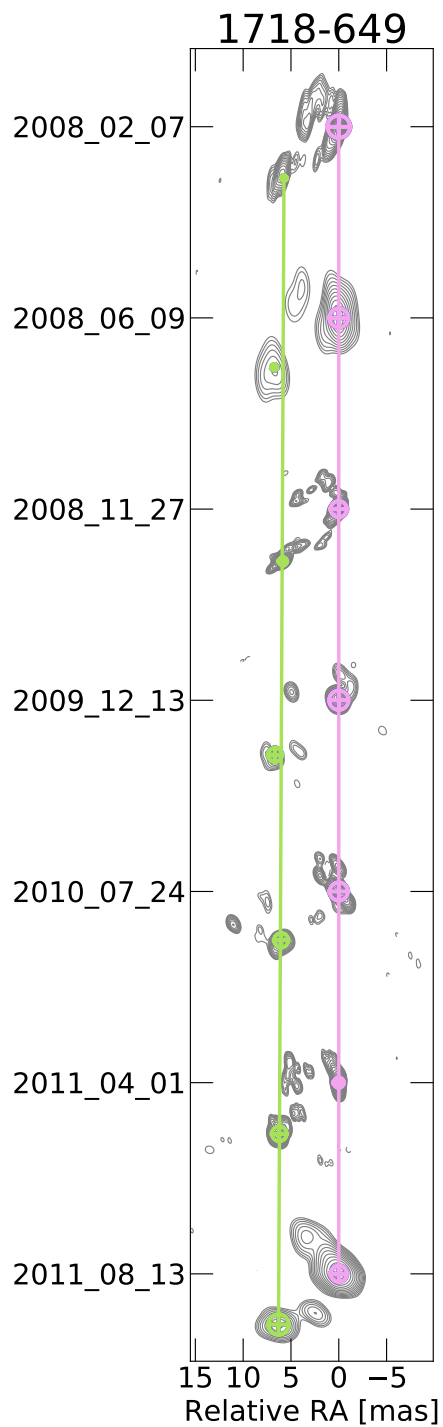


FIGURE 5.18: Multi-epoch images of PKS 1718–649. The colored crossed circles represent the circular Gaussian components that have been fitted to the clean maps. The distance between the images at different epochs is not to scale. The colored lines are not fits to the displayed component positions, but simple interpolations meant to guide the eye.

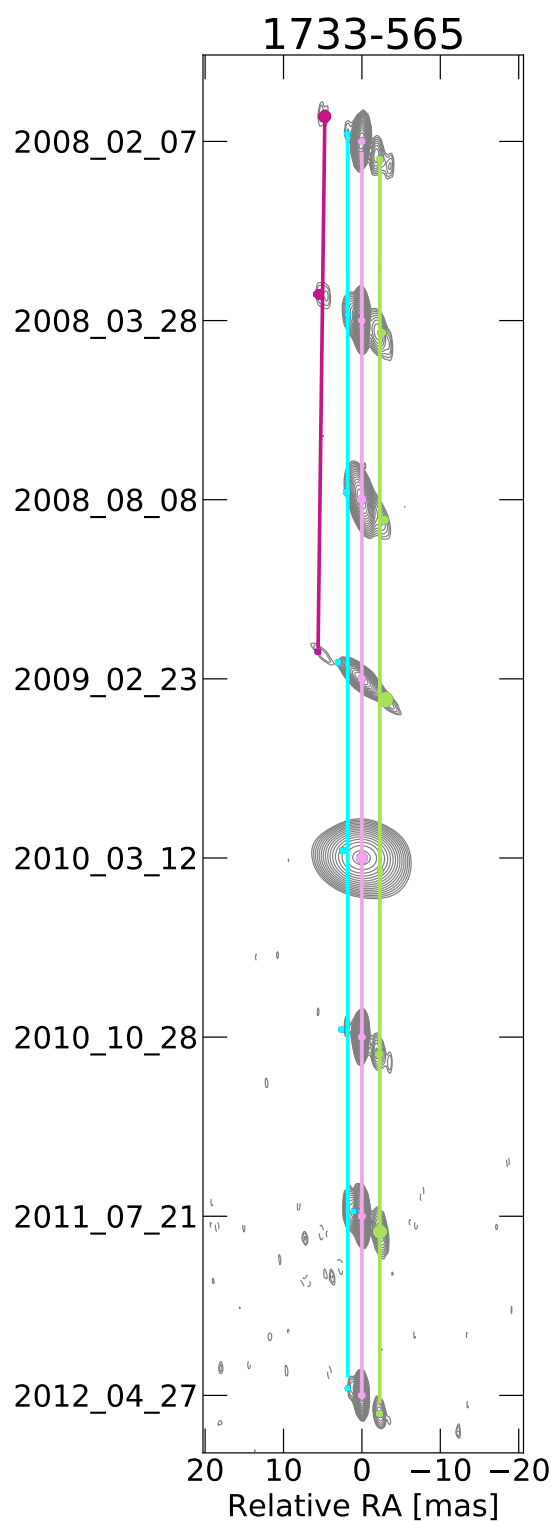


FIGURE 5.19: Multi-epoch tapered images of PKS 1733–56. The colored crossed circles represent the circular Gaussian components that have been fitted to the clean maps. The distance between the images at different epochs is not to scale. The colored lines are not fits to the displayed component positions, but simple interpolations meant to guide the eye.

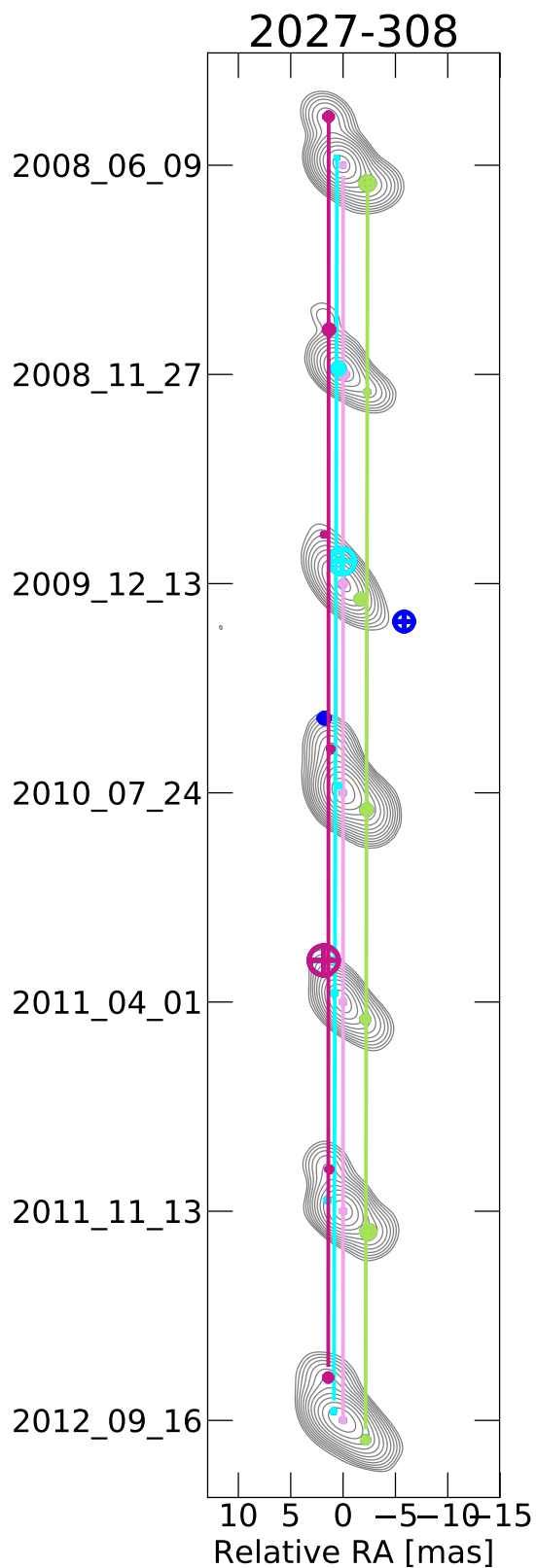


FIGURE 5.20: Multi-epoch tapered images of PKS 2027–308. The colored crossed circles represent the circular Gaussian components that have been fitted to the clean maps. The distance between the images at different epochs is not to scale. The colored lines are not fits to the displayed component positions, but simple interpolations meant to guide the eye.

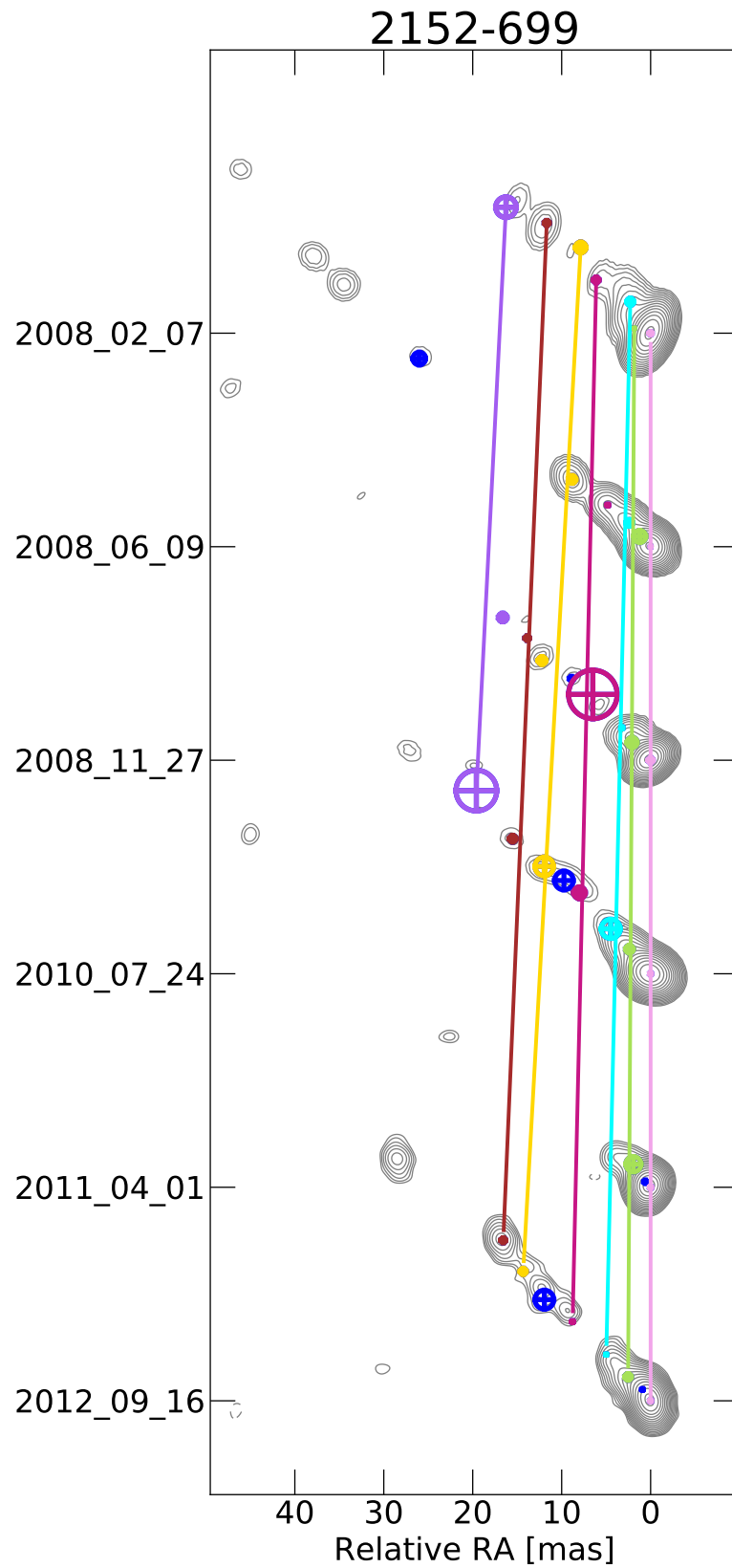


FIGURE 5.21: Multi-epoch tapered images of PKS 2152–69. The colored crossed circles represent the circular Gaussian components that have been fitted to the clean maps. The distance between the images at different epochs is not to scale. The colored lines are not fits to the displayed component positions, but simple interpolations meant to guide the eye.

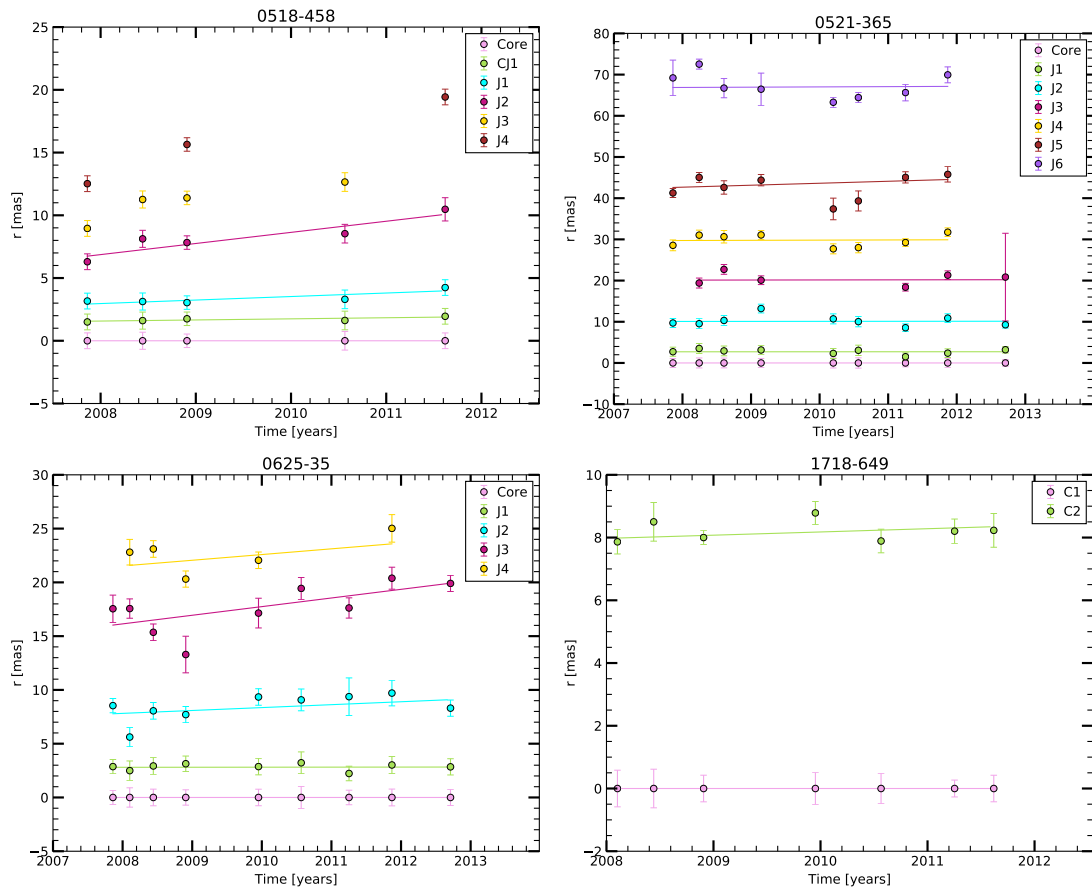


FIGURE 5.22: Jet kinematics of our radio galaxies: core distance of jet features as a function of time. The solid lines represent a least squares fit to their positions (the slope is the apparent speed). Top left to bottom right: Pictor A, PKS 0521–36, PKS 0625–35, PKS 1718–649.

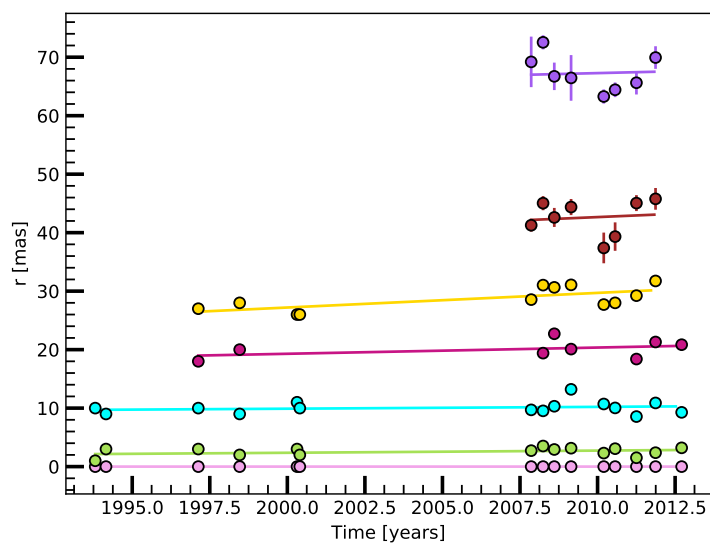


FIGURE 5.23: Jet kinematics of PKS 0521–36: core distance of jet features as a function of time, including the previous VLBI data set of Tingay & Edwards (2002). The solid lines represent a least squares fit to their positions (the slope is the apparent speed). Compare with top-right panel of Fig. 5.22.

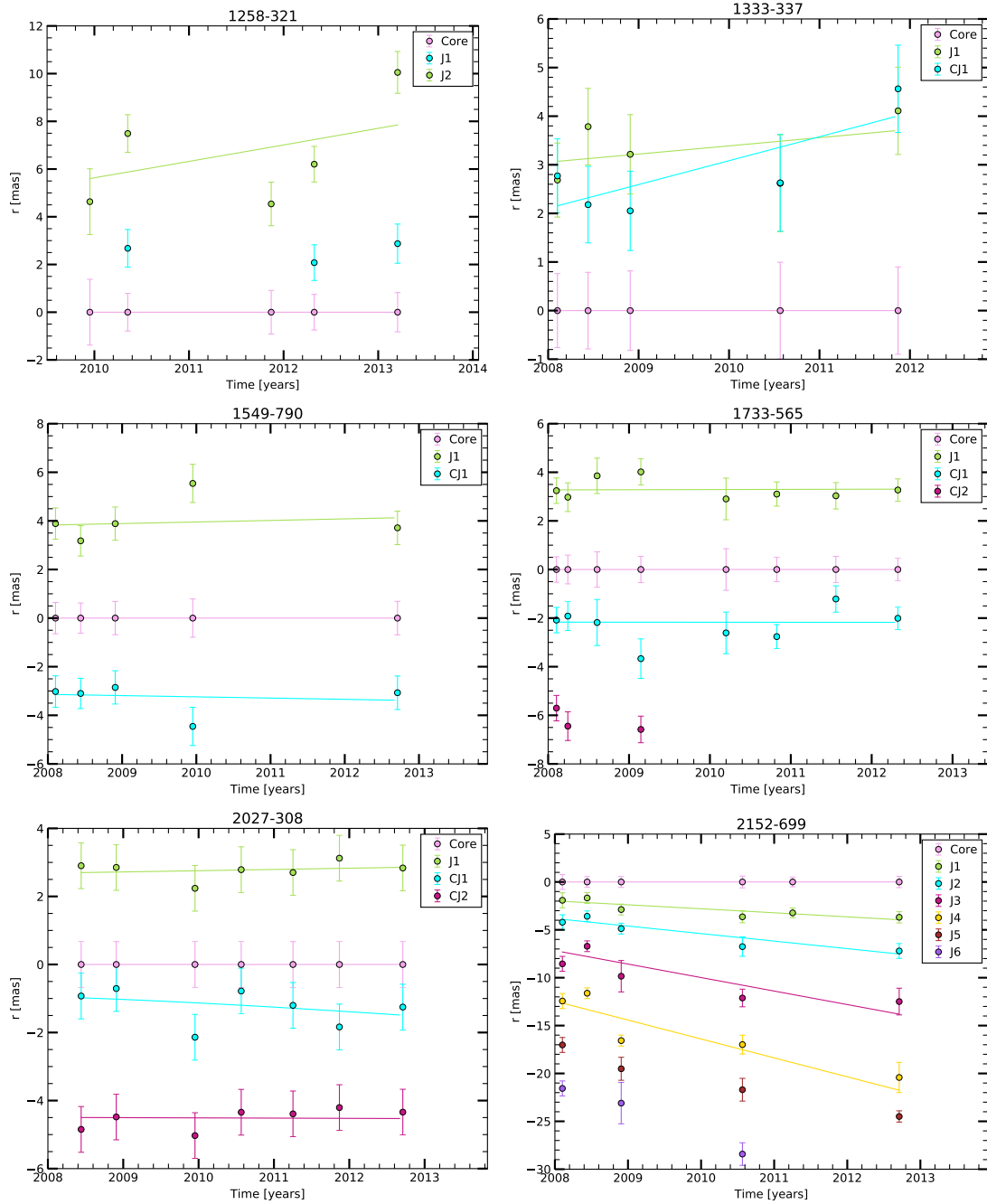


FIGURE 5.24: Jet kinematics of our radio galaxies: core distance of jet features as a function of time. The solid lines represent a least squares fit to their positions (the slope is the apparent speed). Top left to bottom right: PKS 1258–321, IC 4296, PKS 1549–79, PKS 1733–565, PKS 2027–308, PKS 2153–69.

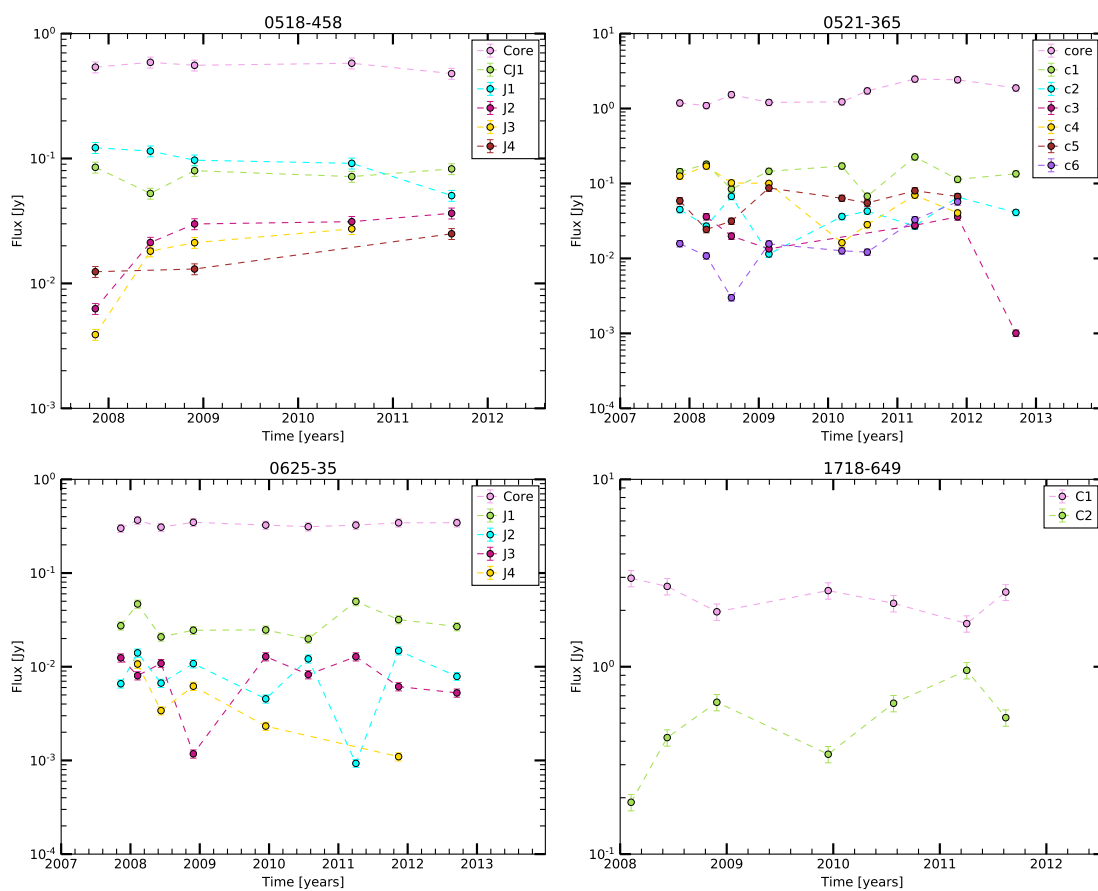


FIGURE 5.25: Flux density evolution of the modelled jet features with time. Top left to bottom right: Pictor A, PKS 0521–36, PKS 0625–35, PKS 1718–649.

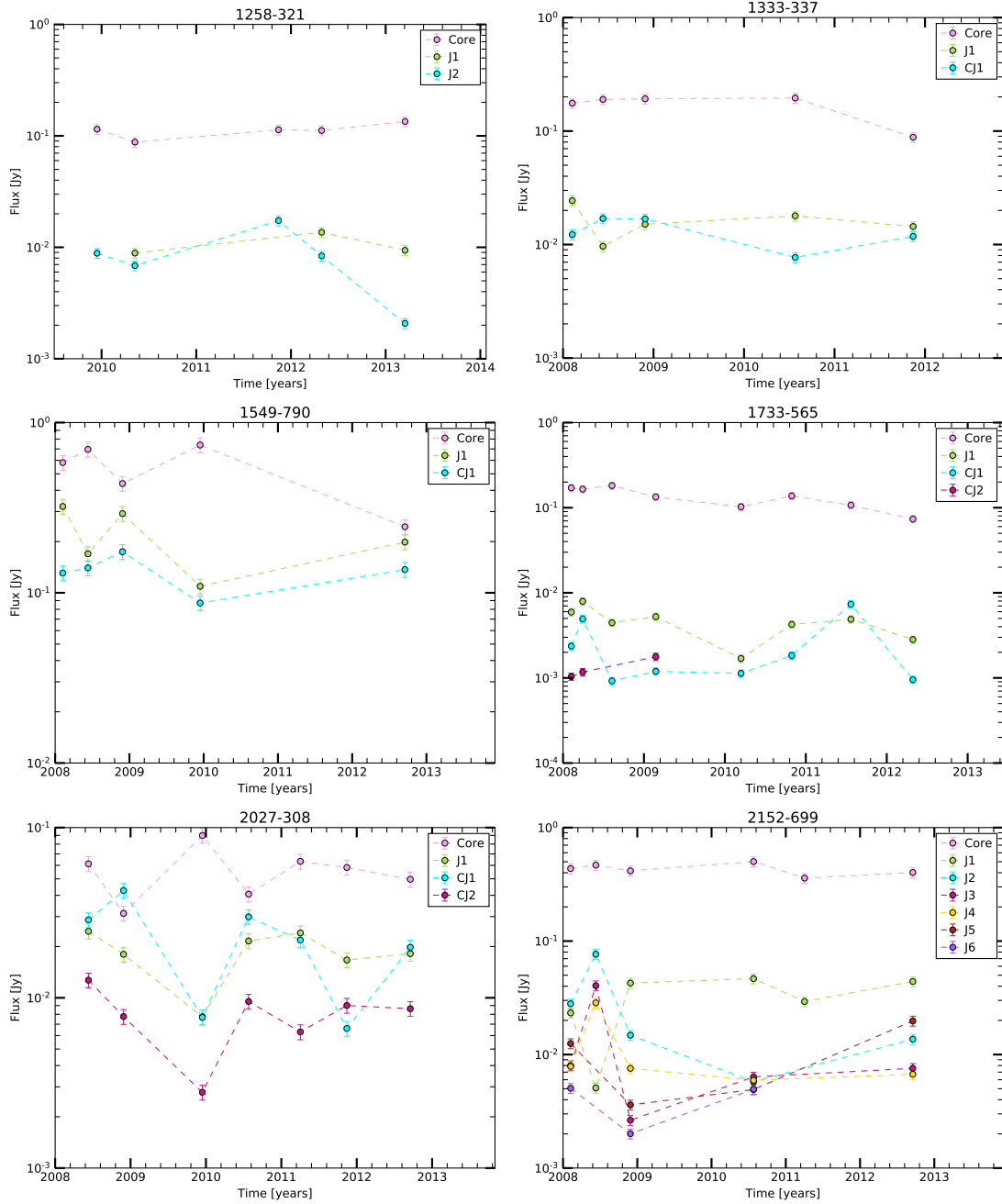


FIGURE 5.26: Flux density evolution of the modelled jet features with time. Top left to bottom right: PKS 1258–321, IC 4296, PKS 1549–79, PKS 1733–565, PKS 2027–308, PKS 2153–69.

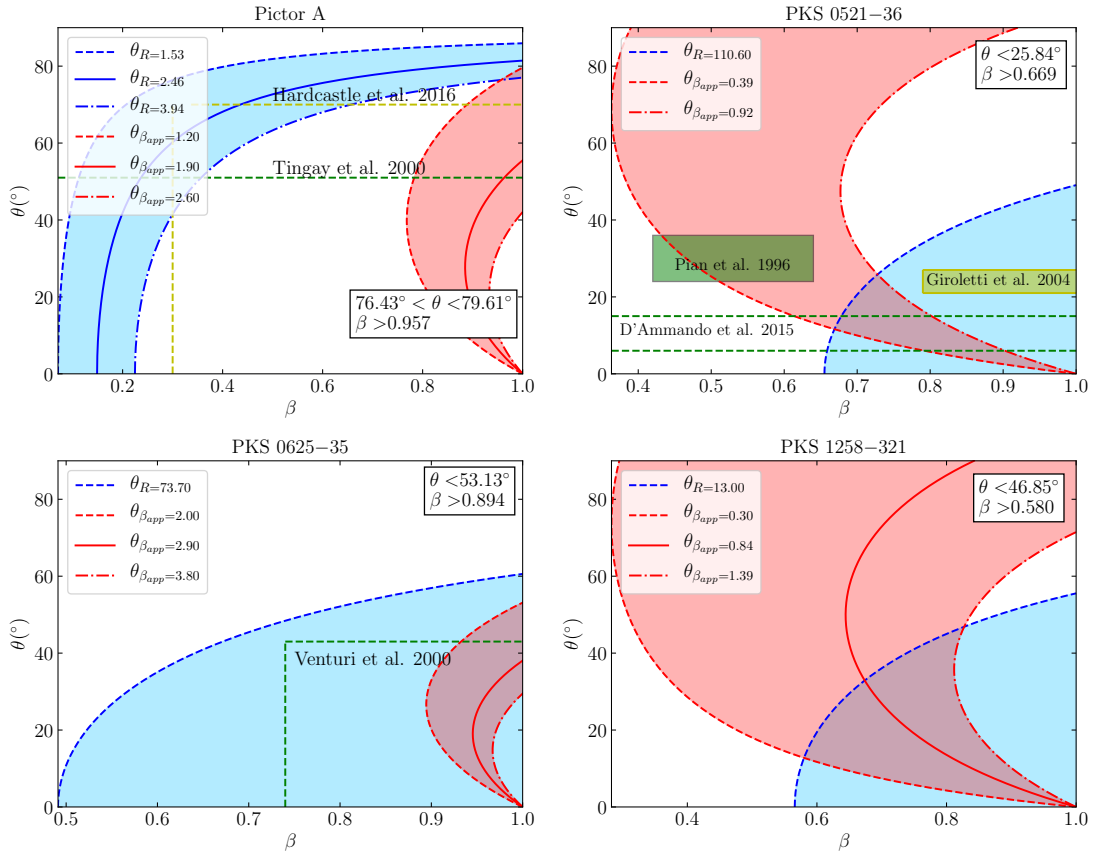


FIGURE 5.27: Parameter space of intrinsic jet speed  $\beta$  and viewing angle  $\theta$  allowed by our observations. The blue shaded area is the one allowed by the measurement of  $R$ , while the red shaded area is the one allowed by the observed  $\beta_{\text{app}}$ . For each source we provide a minimum, maximum and (except for PKS 0521–36) a central estimate of  $R$  and  $\beta_{\text{app}}$ . The top-right legend reports the resulting limits on  $\theta$  and  $\beta$ . The dashed colored lines and boxes indicate constraints from previous works, namely Hardcastle et al. (2016); Tingay et al. (2000) for Pictor A, Pian et al. (1996); Giroletti et al. (2004); D’Ammando et al. (2015) for PKS 0521–36, and Venturi et al. (2000) for PKS 0625–35.

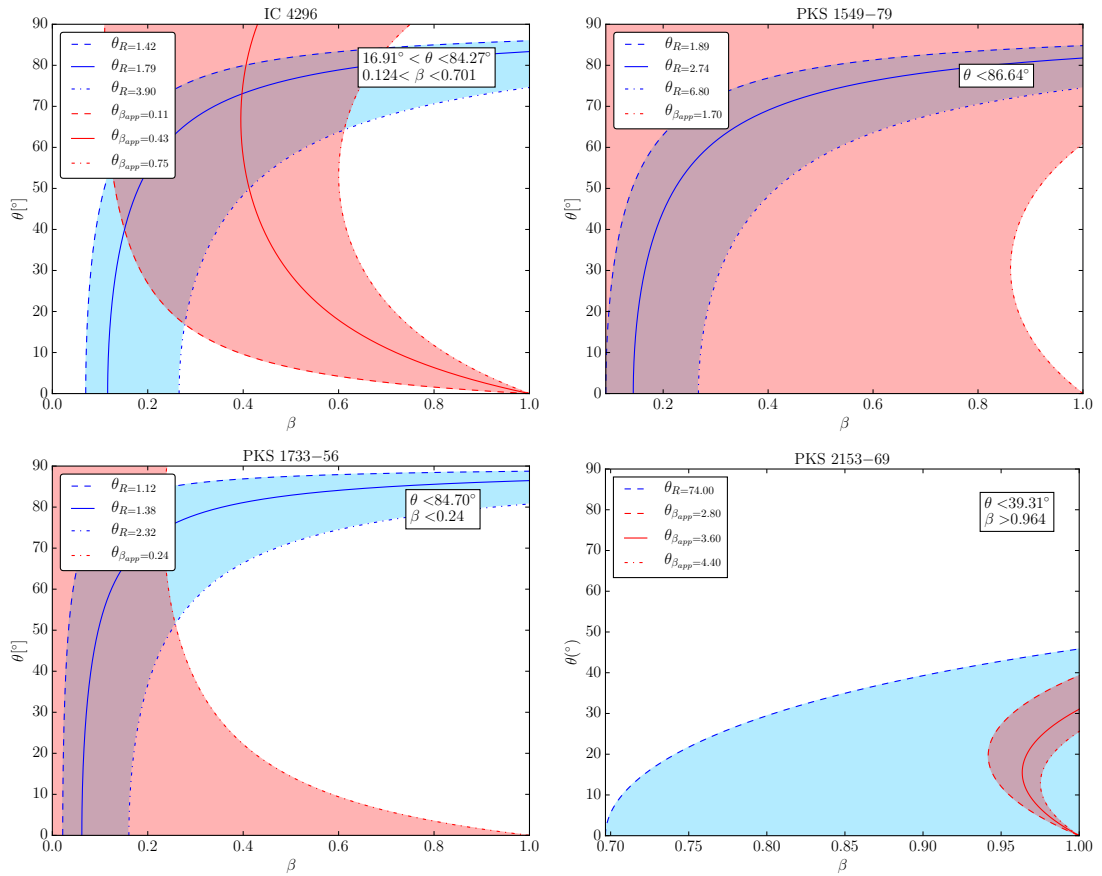


FIGURE 5.28: Parameter space of intrinsic jet speed  $\beta$  and viewing angle  $\theta$  allowed by our observations. The blue shaded area is the one allowed by the measurement of  $R$ , while the red shaded area is the one allowed by the observed  $\beta_{\text{app}}$ . When possible, we provide a minimum, maximum and a central estimate of  $R$  and  $\beta_{\text{app}}$ . The top-right legend reports the resulting limits on  $\theta$  and  $\beta$ .

## Chapter 6

# *Fermi*-LAT data analysis and results

*This Chapter will be partially reproduced in Angioni et al. a,b, to be submitted to Astronomy & Astrophysics*

### 6.1 $\gamma$ -ray data analysis

We perform a standard *Fermi*-LAT analysis as described in Section 3.4. We use the Python package `Fermipy` throughout the analysis. `Fermipy` is a wrapper that greatly simplifies the usage of the standard *Fermi* science tools (Wood et al. 2017).

We assume as starting model the latest *Fermi*-LAT source catalog, i.e. the third source catalog (3FGL, Acero et al. 2015) . We take a Region of Interest (ROI) of  $10^\circ$  around the target position, and include in the model all sources from 3FGL within  $15^\circ$  from the ROI center, together with the latest model for the galactic and isotropic diffuse (`gll_iem_v06.fits` and `iso_P8R2_SOURCE_V6_v06.txt`, respectively). We perform a binned analysis with 10 bins per decade in energy and  $0.1^\circ$  binning in space. We use the source event class, and the latest Pass 8 response function `P8R2_SOURCE_V6`. We enable an energy dispersion correction to take into account the degradation in energy resolution at low energies. We select only times when the zenith angle of the telescopes is smaller than  $100^\circ$ , to avoid contamination by the Earth's limb. We take advantage of the new Pass 8 characterization of events in different PSF quartiles, based on the quality of the direction reconstruction, from the worse quartile (PSF0) to the best (PSF3). We model each type separately and combine the resulting likelihood using the summed-likelihood method. Since the angular resolution of the LAT degrades at low energy, we progressively increase the low-energy cut for the worse PSF quartiles. The details of the selection of the different components are listed in Table 6.1.

We fit the ROI with the initial 3FGL model, freeing all the parameters of the target source and the normalization of all sources within  $5^\circ$  of the ROI center. Since our data set more than doubles the integration time with respect to the 3FGL catalog, we look for new sources with an iterative procedure. We produce a map of excess Test Statistic (TS). We look for  $TS > 9$  peaks

TABLE 6.1: Details of the selection cuts for different components in the LAT analysis.

| $E_{\min}$ | $E_{\max}$ | PSF quartile | Event type |
|------------|------------|--------------|------------|
| 100 MeV    | 100 GeV    | PSF3         | 32         |
| 400 MeV    | 100 GeV    | PSF2         | 16         |
| 500 MeV    | 100 GeV    | PSF1         | 8          |
| 800 MeV    | 100 GeV    | PSF0         | 4          |

in the TS map, with a minimum separation of  $0.3^\circ$ , and add a new point source to the model for each peak, assuming a power-law spectrum. We then fit again the ROI, and produce a new TS map. This process is iterated until all significant excesses are modeled out. We also perform a localization analysis on the target source and all new sources with  $TS > 25$  found in the ROI.

As listed in Table 5.1, roughly half of the TANAMI radio galaxies are detected in the 3FGL catalog. For 3FGL sources, we center the ROI on the catalog position of the  $\gamma$ -ray source, and derive an SED and light curve.

For the variability analysis, we look at the energy range 0.1-300 GeV. All the other parameters of the multi-component analysis are the same as those described above. We first perform a standard analysis over the whole time range, then we perform a dedicated analysis in each time bin, adopting the average model with only the parameters of the source of interest free to vary. When the statistics in each bin do not allow to fit the spectral shape ( $TS < 25$ ), we fix it to the average value, and fit only the normalization. We consider the source detected in each bin if  $TS > 10$  and the signal to noise ratio (i.e., flux over flux error) is higher than 2, otherwise we place a 95% confidence upper limit.

For sources not included in the 3FGL, we center the ROI on the radio position of the target. If a new source consistent with the target position is not found by the source-finding iterative procedure, we place a test source at the ROI center and derive an upper limit.

## 6.2 Results

Here we present the results of the LAT analysis described in the previous section, on a source-by-source basis. The results on the whole TANAMI radio galaxy sample are summarized in Table 6.2.

### 0518–458

Pictor A was reported as *Fermi*-LAT detection for the first time by Brown & Adams (2012) based on three years of data, and confirmed in the latest *Fermi*-LAT catalog, i.e. the 3FGL, which includes four years of data (Acero et al. 2015). It is the faintest source among the 3FGL TANAMI radio galaxies. While it has been established that diffuse structures such as lobes and hot spots may give a significant or even dominant contribution to  $\gamma$ -ray emission in radio galaxies (Abdo et al. 2010c; Ackermann et al. 2016), Brown & Adams (2012) found that this is not the case for Pictor A. Through SED modeling of the western hot-spot, the authors found that

Synchrotron Self-Compton (SSC) and Inverse Compton with CMB photons (IC/CMB) models failed to reproduce the X-ray and  $\gamma$ -ray data at the same time, and therefore concluded that the  $\gamma$ -ray emission must be dominated by the AGN jet. This is also supported by the indications of variability observed in the LAT data.

Our analysis over  $\sim 8.5$  years results in a higher significance w.r.t. the 3FGL, and the source properties are consistent with the catalog results within the errors. The SED of the source between 100 MeV and 100 GeV is presented in the upper left panel of Fig. 6.4.

We produced a monthly light curve over the whole  $\sim 8.5$  years time period, as described in Section 6 (Fig. 6.5). Pictor A is a relatively faint  $\gamma$ -ray source, therefore it is not detected on monthly timescales for most of this time range. The high state in September 2010 provided the statistics to allow a detection integrating over the first three years of *Fermi*-LAT data, with a monthly significance of  $TS \sim 40$ .

### 0521–365

This source is a very bright  $\gamma$ -ray emitter, showing significant variability. A monthly and weekly light curve over  $\sim 8.5$  years of data is shown in Fig. 6.6. The flaring activity in 2010-2011 has been studied by D’Ammando et al. (2015) down to 12-hour time scales. We find a second period of activity of comparable magnitude at the end of 2012. We investigated the short variability in this period by producing daily and 6-hours time scales light curves, which are presented in Fig. 6.7. The source is especially variable on these time scales in December 2012, with a maximum peak on 6-hours time scales observed on 2012-12-12, with an energy flux of  $(4.3 \pm 1.3) \times 10^{-3}$  MeV  $\text{cm}^{-2} \text{s}^{-1}$ , corresponding to an isotropic  $\gamma$ -ray luminosity of  $4.7 \times 10^{46}$  erg  $\text{s}^{-1}$ . The sharpest flux change is the decrease from this peak flux to the next 6-hours bin, with a variation of a factor  $\sim 6$ .

### 0625–354

This source has been detected by *Fermi*-LAT since the first source catalog (Abdo et al. 2010a). It is a recent addition to the small sample of six radio galaxies which have been detected by Cherenkov Telescopes in the TeV range (Abdalla et al. 2018). This is mostly due to its notably hard spectrum, as can be seen in our SED (Fig. 6.4). The source properties in the 3FGL energy range are consistent with the catalog values, and the significance is increased.

A monthly-binned light curve of the source over 8 years is presented in Fig. 6.8. No significant variability is detected.

### 1258–321

This FR I radio galaxy is not listed as a  $\gamma$ -ray source in any *Fermi*-LAT catalog, but it lies close to the unidentified source 3FGL J1259.5–3231. To test a possible association, we removed the catalog source from the model, and produced a map of the excess significance (TS) in the region (see Fig. 6.1, top panel). We ran a source-finding algorithm which adds new sources to the model starting from  $TS > 25$  peaks in the TS map. This found a new source PS J1259.8–3224, which after localization appears to be consistent with the catalog position of 3FGL J1259.5–3231, and does not include the radio position of PKS 1258–321.

A possible association for the  $\gamma$ -ray source is the radio source NVSS J125949–322329 (RA: 194.957542, Dec:  $-32.391361$ ,  $z = 0.013750$ ), which lies at an angular distance of  $\sim 54''$  from the  $\gamma$ -ray source's best fit position. This source has been indicated as a candidate  $\gamma$ -ray emitter based on its *WISE* colors by D'Abrusco et al. (2014).

There is no significant residual excess after modeling this source (see Fig 6.1, bottom panel). By placing a test source at the radio position of the PKS 1258–321, we derive an upper limit, which is listed in Table 6.2.

### 1343–601

Centaurus B was first reported as  $\gamma$ -ray source by the *Fermi*-LAT team in the 2FGL (Nolan et al. 2012). Its SED between 100 MeV and 100 GeV is presented in Fig. 6.4. Our analysis over  $\sim 8.5$  years yields results consistent with the catalog values within the error. It is interesting to note that in spite of its relatively steep spectral index, Cen B has been indicated as a good candidate for a TeV detection (Angioni et al. 2017). This is probably favored by its very low redshift (see Tab. 5.1).

The analysis of this source is particularly challenging due to its location behind the galactic plane ( $b = 1.73$ ), which contains rich diffuse emission structures, complicating point-source analysis. This ROI required the addition of many sources in excess of the 3FGL (we are using more than double the data with respect to the catalog), some of which may actually be due to contribution from improperly modeled galactic diffuse emission.

A monthly light curve of Cen B is presented in Fig. 6.9. The source is undetected for most of the time range, and does not show any significant variability.

### 1718–649

This source has recently become the first  $\gamma$ -ray detected young radio galaxy. Migliori et al. (2016) reported its detection using seven years of LAT data, with a significance of  $TS \sim 36$ , confirming it as the counterpart of the unidentified catalog source 3FGL J1728.0–6446. We double-checked this result using  $\sim 8.5$  years of data, and confirmed the association. Fig. 6.2 shows a TS excess map after subtracting 3FGL J1728.0–6446. The excess is nicely coincident with the position of PKS 1718–649. A new source is found by the source-finding algorithm (dubbed PS J1724.2–6459), and after localization we found that the source coincides with the position of the target within the errors.

### 2152–699

This source is close to the unidentified catalog source 3FGL J2200.0–6930. We analyzed the region with the same procedure as for PKS 1258–321 and PKS 1718–649, and found that the newly modeled  $\gamma$ -ray source is consistent with the position of 3FGL J2200.0-6930, and not with PKS 2153–69. There is no likely counterpart to the new  $\gamma$ -ray source PS J2200.5–6929 within the 95% error circle (see Fig. 6.3, top panel). Lowering the threshold of the source-finding algorithm to  $TS > 9$ , we find a significant source (PS J2152.0–6956) that lies  $\sim 0.5^\circ$  from the target position. Upon localization, we find that the 95% confidence uncertainty region for this source does not include PKS 2153–69. There is no significant residual excess after modeling the latter source (see Fig. 6.3, bottom panel), therefore we derive an upper limit at the target position, which is reported in Table 6.2.

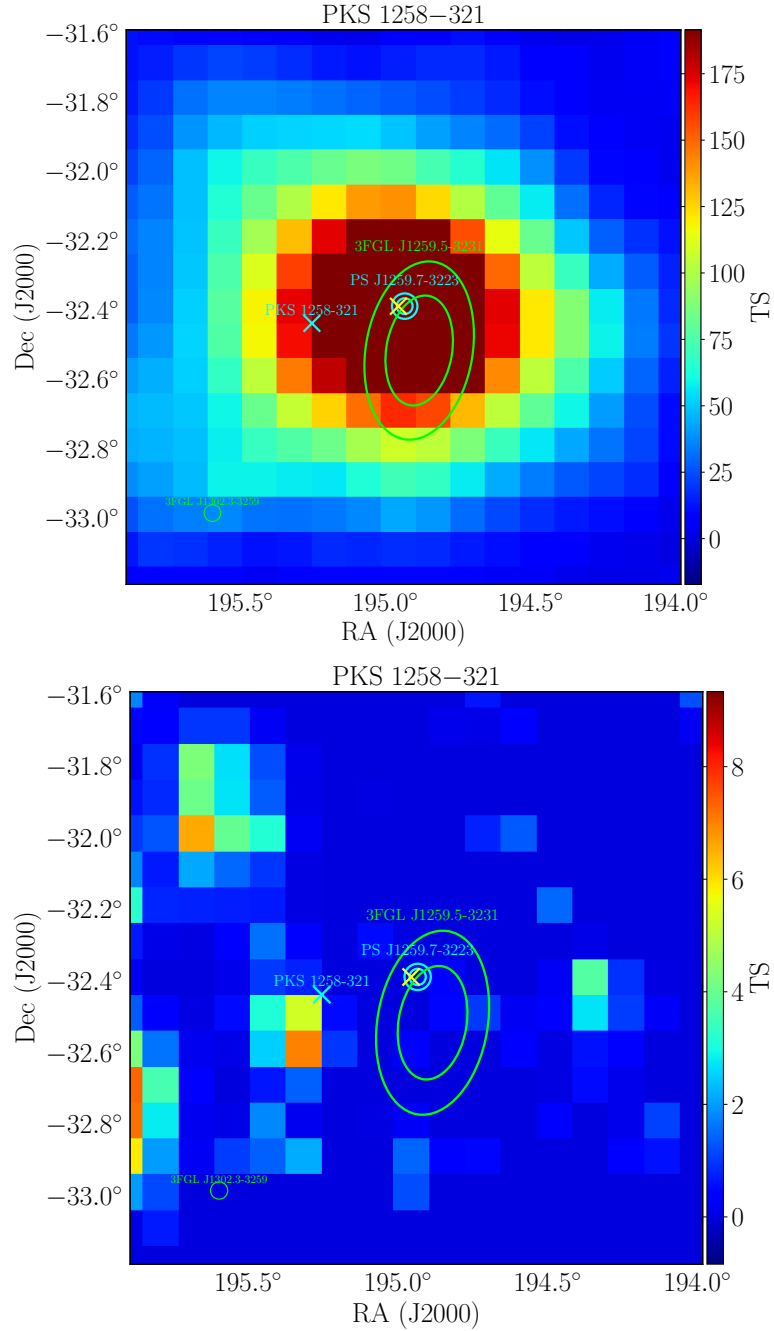


FIGURE 6.1: *Top panel:* Map of excess TS in the inner region of the ROI centered on PKS 1258-321, after removing the unidentified catalog source 3FGL J1259.5-3231. *Bottom panel:* residual excess TS map after modeling and localizing the new source PS J1259.7-3223. *Both panels:* The white cross represents the radio position of PKS 1258-321. The yellow cross represents the position of NVSS J125949-322329. The yellow ellipses represent the 68% and 95% positional uncertainties from the catalog for 3FGL J1259.5-3231. The circles (blue and red in the top and bottom panel respectively) represent the 68% and 95% positional uncertainties for the new source PS J1259.7-3223. The map radius is  $0.8^\circ$ . Each pixel corresponds to  $0.1^\circ$ .

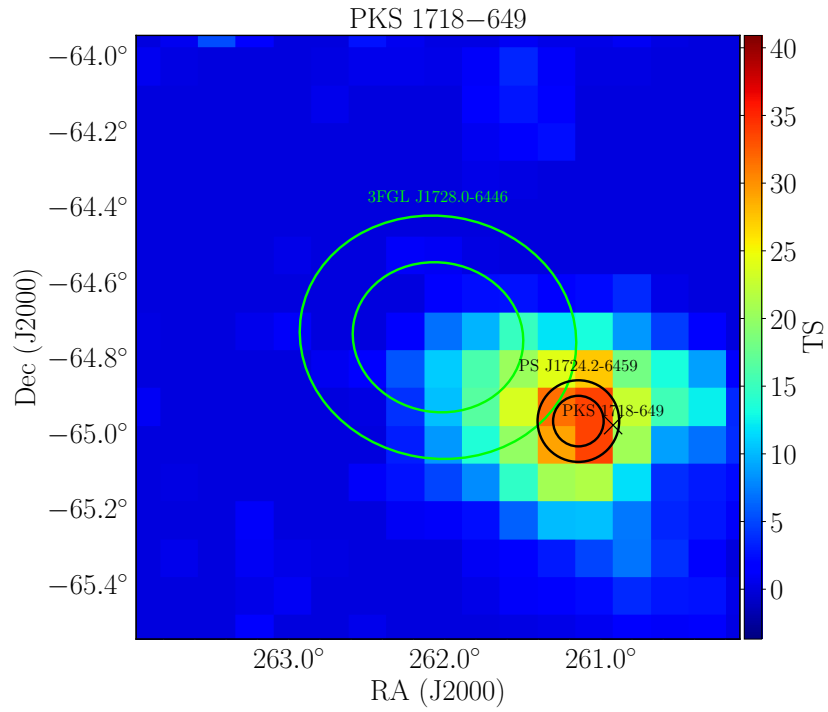


FIGURE 6.2: Map of excess TS in the inner region of the ROI centered on PKS 1718-649, after removing the unidentified catalog source 3FGL J1728.0-6446. The ellipses represent the 68% and 95% confidence positional errors on the catalog source, while the black circles represent the same errors for the new source PS J1724.2-6459. The map radius is  $0.8^\circ$ . Each pixel corresponds to  $0.1^\circ$ .

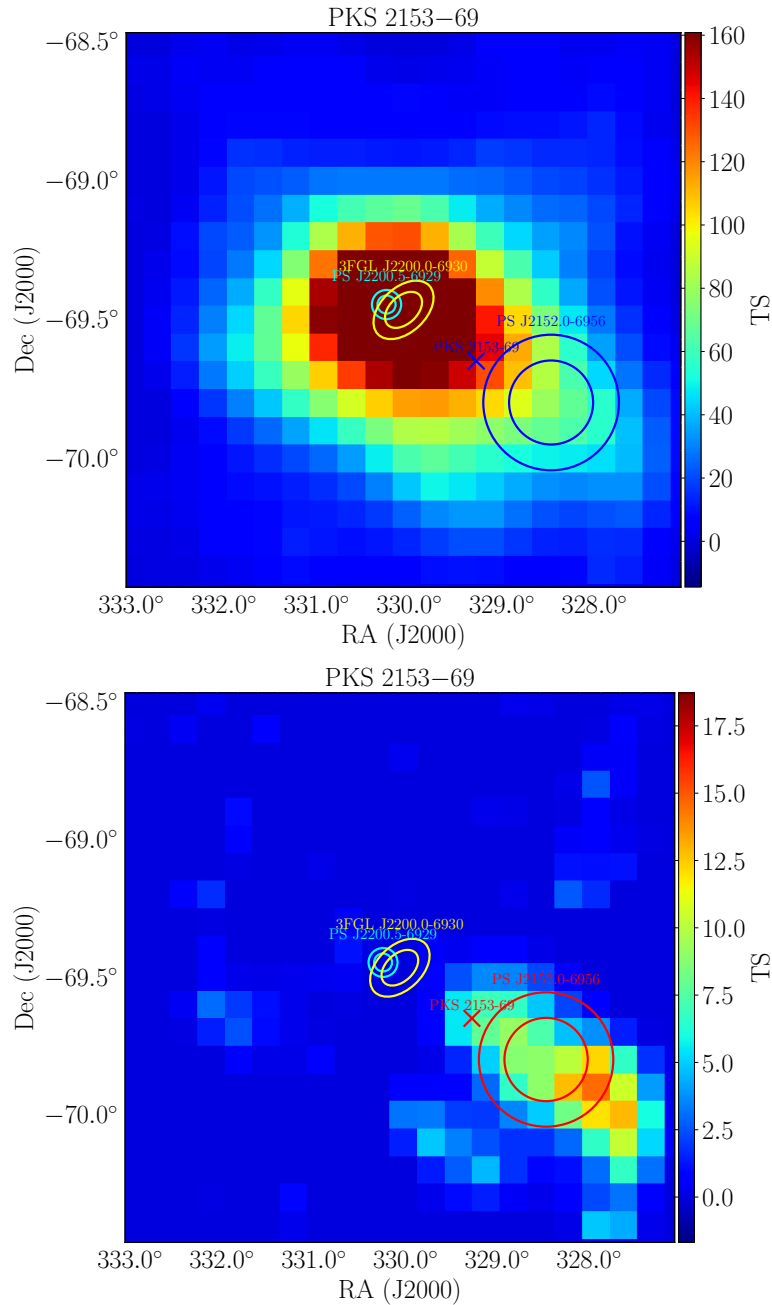


FIGURE 6.3: *Top panel:* Map of excess TS in the inner region of the ROI centered on PKS 2153-69, after removing the unidentified catalog source 3FGL J2200.0-6930. *Bottom panel:* residual excess TS map after modeling and localizing the new source PS J2200.5-6930. *Both panels:* The cross represents the radio position of PKS 2153-69. The yellow ellipses represent the 68% and 95% positional uncertainties from the catalog for 3FGL J2200.0-6930. The cyan circles represent the 68% and 95% positional uncertainties for the new source PS J2200.5-6930. The blue (top) and red (bottom) circles represent the 68% and 95% positional uncertainties for the new source PS J2152.0-6956. The map radius is  $1^\circ$ . Each pixel corresponds to  $0.1^\circ$ .

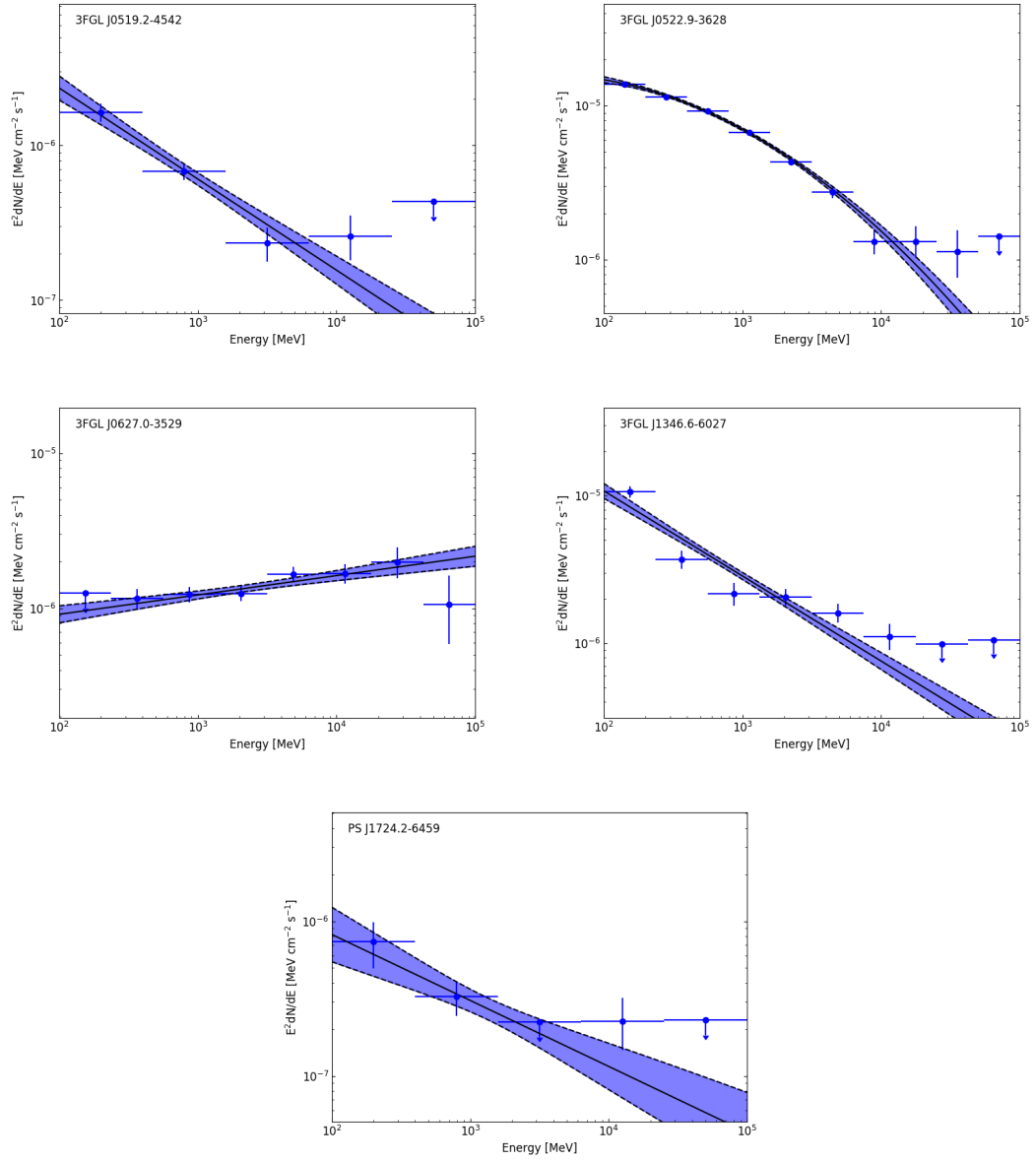


FIGURE 6.4: SED of the  $\gamma$ -ray detected TANAMI radio galaxies) over the full 103 months time period. An upper limit is placed for bins where  $TS < 9$ . The shaded region represents the fitted spectrum and its uncertainty.

TABLE 6.2: 0.1-100 GeV *Fermi*-LAT results on TANAMI radio galaxies

| B1950 name | Flux <sup>a</sup>                | Spectral index <sup>b</sup> | Curvature <sup>c</sup> | TS      |
|------------|----------------------------------|-----------------------------|------------------------|---------|
| 0518–458   | $(1.63 \pm 0.19) \times 10^{-8}$ | $2.63 \pm 0.08$             | -                      | 225.5   |
| 0521–365   | $(1.17 \pm 0.03) \times 10^{-7}$ | $2.33 \pm 0.02$             | $-0.074 \pm 0.011$     | 11313.2 |
| 0625–354   | $(1.07 \pm 0.10) \times 10^{-8}$ | $1.88 \pm 0.04$             | -                      | 1150.4  |
| 0823–500   | $< 1.84 \times 10^{-9}$          | -                           | -                      | 0.06    |
| 1258–321   | $< 4.68 \times 10^{-9}$          | -                           | -                      | 4.58    |
| 1322–428   | $(1.73 \pm 0.04) \times 10^{-7}$ | $2.68 \pm 0.02$             | -                      | 7500.0  |
| 1333–337   | $< 1.15 \times 10^{-8}$          | -                           | -                      | 14.18   |
| 1343–601   | $(6.85 \pm 0.66) \times 10^{-8}$ | $2.58 \pm 0.05$             | -                      | 416.0   |
| 1600–489   | $(6.8 \pm 0.4) \times 10^{-8}$   | $2.06 \pm 0.02$             | -                      | 2771.4  |
| 1549–790   | $< 5.07 \times 10^{-9}$          | -                           | -                      | 2.98    |
| 1718–649   | $(5.8 \pm 2.2) \times 10^{-9}$   | $2.43 \pm 0.18$             | -                      | 44.3    |
| 1733–565   | $< 1.37 \times 10^{-8}$          | -                           | -                      | 14.16   |
| 1814–637   | $< 1.89 \times 10^{-9}$          | -                           | -                      | 0.90    |
| 1934–638   | $< 2.61 \times 10^{-10}$         | -                           | -                      | 0.0     |
| 2027–308   | $< 6.51 \times 10^{-10}$         | -                           | -                      | 2.62    |
| 2152–699   | $< 3.44 \times 10^{-9}$          | -                           | -                      | 7.72    |

<sup>a</sup> *Fermi*-LAT flux between 0.1-100 GeV in photons  $\text{cm}^{-2} \text{s}^{-1}$ .

<sup>b</sup> *Fermi*-LAT spectral index  $\Gamma$ , in case of power-law spectrum  $dN/dE = N_0 \times (E/E_0)^{-\Gamma}$ , or  $\alpha$  in case of logParabola spectrum  $dN/dE = N_0 \times (E/E_b)^{-[\alpha + \beta \log(E/E_b)]}$ .

<sup>c</sup> Curvature parameter of logParabola spectrum  $\beta$ .

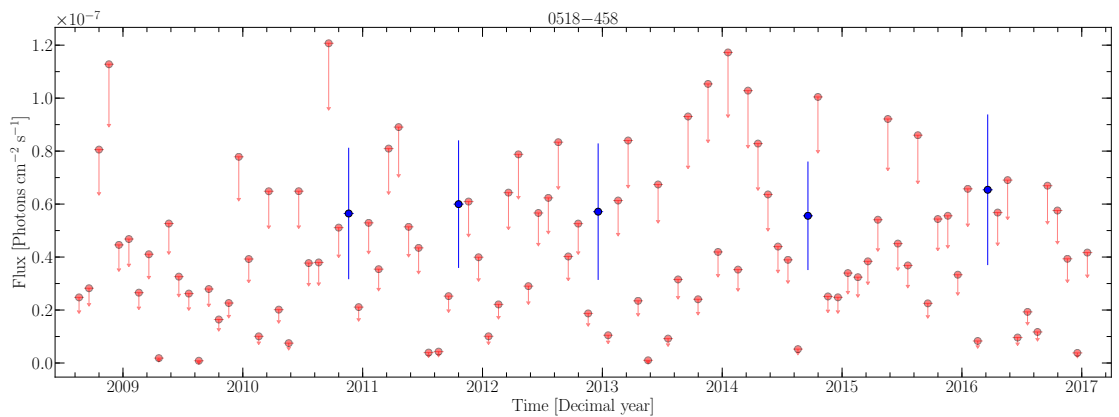


FIGURE 6.5: Light curve of Pictor A between 0.1-300 GeV over 103 months of *Fermi*-LAT data, with monthly binning. Blue points are detections, red arrows are upper limits.

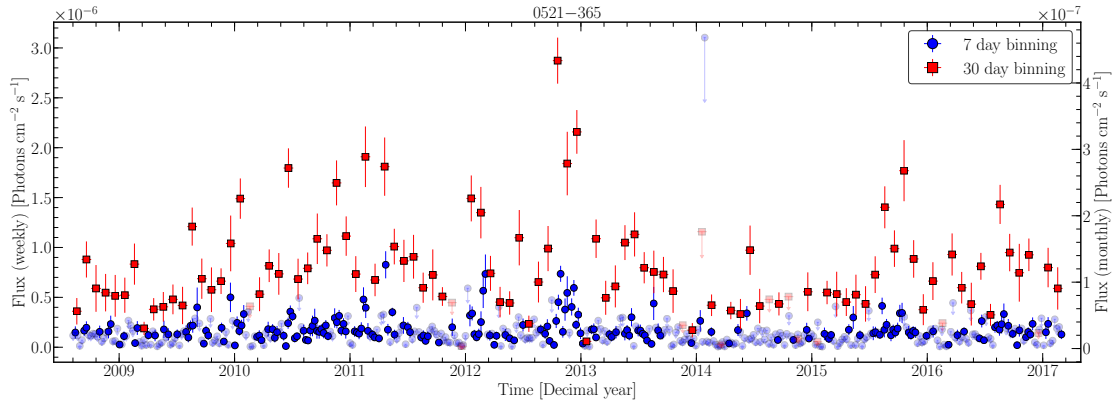


FIGURE 6.6: Light curve of PKS 0521–36 between 0.1-300 GeV over 103 months of *Fermi*-LAT data, with weekly (blue points) and monthly (red points) binning. Upper limits are indicated by arrows of the respective colors. The left y-axis reports the weekly flux values, the right one reports the monthly flux values.

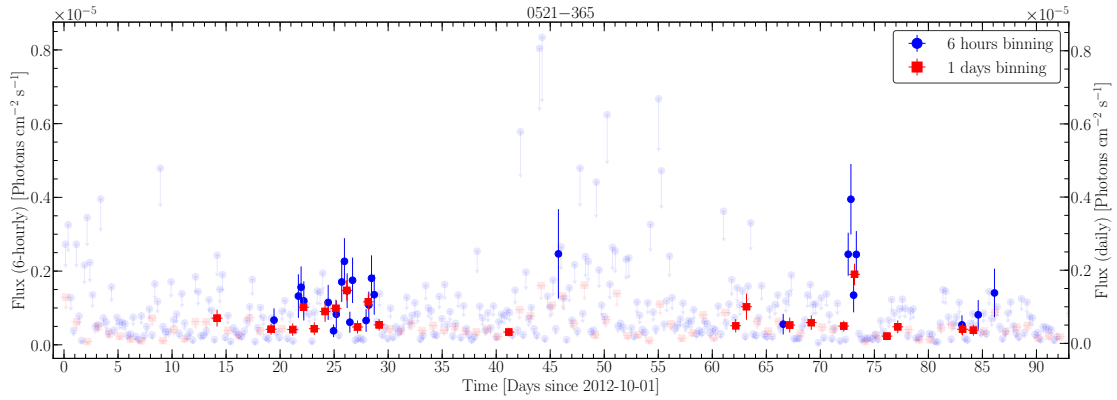


FIGURE 6.7: Light curve of PKS 0521–36 between 0.1-300 GeV over 103 months of *Fermi*-LAT data, with 6-hours (blue points) and daily (red points) binning. Upper limits are indicated by arrows of the respective colors. The left y-axis reports the 6-hours flux values, the right one reports the daily flux values.

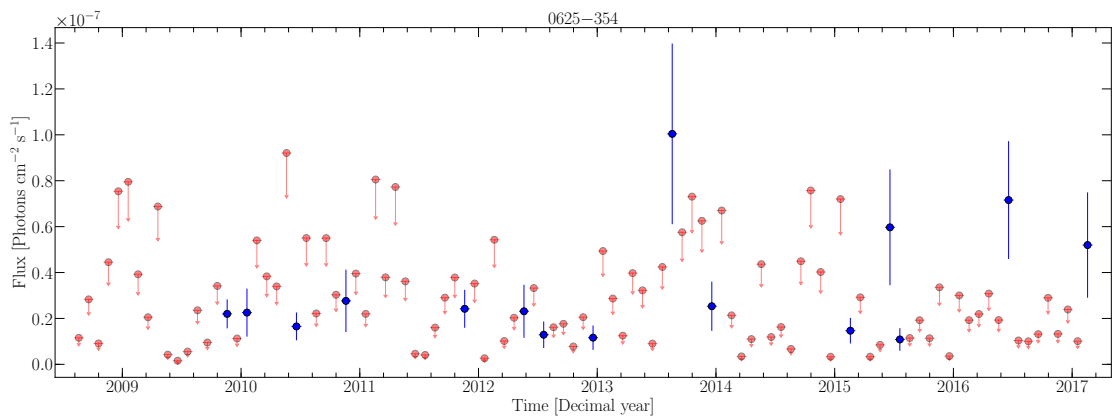


FIGURE 6.8: Light curve of PKS 0625–35 between 0.1-300 GeV over 103 months of *Fermi*-LAT data, with monthly binning. Blue points are detections, red arrows are upper limits..

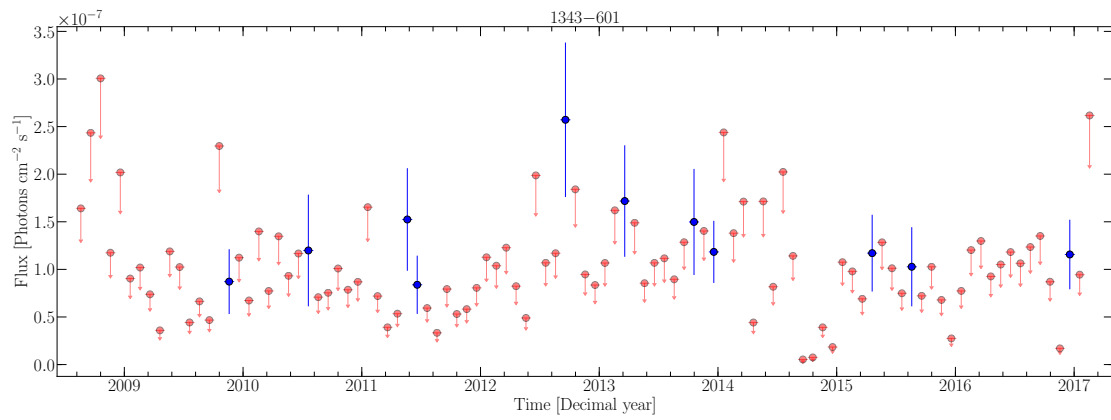


FIGURE 6.9: Light curve of Centaurus B between 0.1-300 GeV over 103 months of *Fermi*-LAT data, with monthly binning. Blue points are detections, red arrows are upper limits.

## Chapter 7

# Parsec scale jet and $\gamma$ -ray emission in radio galaxies

*This Chapter will be partially reproduced in Angioni et al. a,b, to be submitted to Astronomy & Astrophysics*

In this Chapter we discuss the relationship between the observed parsec-scale jet properties and  $\gamma$ -ray emission in radio galaxies, as revealed by our VLBI kinematic analysis and  $\gamma$ -ray data from *Fermi*-LAT, first on a source-by-source basis, than focusing on the properties of radio galaxies as a whole.

### 7.1 Individual source discussion

#### 0518–458 (Pictor A)

Based on their VLBI data, Tingay et al. (2000) place an upper limit on the jet viewing angle of  $\theta < 51^\circ$ . This is not consistent with the allowed range of parameters from our TANAMI observations, i.e.,  $76^\circ < \theta < 80^\circ$  and  $\beta > 0.96$ .

Hardcastle et al. (2016) observed the jet of Pictor A in X-rays using *Chandra* observations, combined with ATCA images of the large scale radio structure. They detect an X-ray counterjet, and place an upper limit on the viewing angle of  $\theta < 70^\circ$  and a lower limit on the intrinsic jet speed of  $\beta > 0.3$  from the jet sidedness. The authors noted that at the time there was no direct evidence of bulk relativistic motion in the jet of Pictor A, and pointed out the value of future VLBI studies on the source in order to investigate this. Our results provide the first robust measurement of component motion in the pc-scale jet of Pictor A. Our lower limit on the intrinsic jet speed does not constrain the jet to be highly relativistic, but significantly reduces the parameter space with respect to the estimate by Hardcastle et al. (2016) (see Fig. 5.27). Our lower limit on the viewing angle of  $\sim 40^\circ$  confirms that the X-ray emission mechanism cannot be Inverse Compton on CMB photons (IC/CMB), since this would require  $\theta$  smaller than a few degrees and  $\beta \sim 1$ .

The  $\gamma$ -ray light curve of Pictor A shows that the source is often undetected on monthly time scales. In a variability study of 12 radio galaxies using four years of *Fermi*-LAT data Grandi et al. (2013) found that FR II sources were detected only during short periods of activity (e.g. 3C 111, Grandi et al. 2012b), while FR I sources were detected for a larger fraction of the investigated time range. This seems to be consistent with our results on Pictor A, a classic FR II radio galaxy, which is detected in  $\gamma$ -rays  $\sim 5\%$  of the time over 103 months.

Our TANAMI data combined with the  $\gamma$ -ray variability allows us to shed some light on the nature of the high-energy emission in Pictor A. It is worth noting that a new VLBI component emerged from the radio core of Pictor A between 2010-07-24 and 2011-08-13. Since the elevated  $\gamma$ -ray state that allowed the first *Fermi*-LAT detection was within this time range, it is plausible that it was caused by the passage of a new shock through the radio core, corresponding to the ejection of this new VLBI component. This hypothesis is in agreement with the results of Brown & Adams (2012), who modeled the SED of the western hot-spot of Pictor A, and found that it cannot reproduce the observed X-ray and  $\gamma$ -ray emission at the same time, and therefore the LAT detection is probably due to emission from the innermost part of the jet.

It is worth speculating whether the association with pc-scale jet activity is a defining feature of  $\gamma$ -ray emitting FR II radio galaxies. If our inference is correct, Pictor A would be yet another example of this kind of behavior, after 3C 111 (Grandi et al. 2012b) and 3C 120<sup>1</sup> (Casadio et al. 2015). This would nicely fit with the findings of Grandi et al. (2013), if we assume that FR II sources can only be detected when there is significant activity in their innermost jet, and/or when the inner jet is temporarily well-aligned with our line-of-sight (see Casadio et al. 2015; Janiak et al. 2016, for the case of 3C 120). The presence of jet spine “wiggling” and precession is suggested by numerical simulations such as e.g. Liska et al. (2018). This would naturally lead to a low duty cycle for  $\gamma$ -ray activity, and consequently to fewer detected FR IIs, exactly as observed (e.g. Grandi et al. 2016, and references therein).

### 0521–365

Our VLBI results complete the multi-wavelength picture provided by Tingay & Edwards (2002), D’Ammando et al. (2015) and Leon et al. (2016), confirming that the jet of PKS 0521–36 is not highly beamed, with viewing angles larger than  $10^\circ$  still allowed by our observations.

Pian et al. (1996) used multi-wavelength data to model the broadband SED of PKS 0521–36, and found that the source is likely not Doppler-boosting dominated, with an estimated viewing angle of  $\theta = 30^\circ \pm 6^\circ$  and a Doppler factor  $\delta \sim 1.5$ . This range of parameters, which would point towards a classification as typical radio galaxy, is completely ruled out by our kinematic analysis, as can be seen in Fig.5.27.

The observed fast  $\gamma$ -ray variability is typical of blazar jets, where the time scales are strongly reduced by the large Doppler factors. However, as shown by the VLBI results presented here, and by previous multi-wavelength studies, it is unlikely that the jet of PKS 0521–36 is strongly affected by Doppler boosting. Therefore the jet does not seem to respond to the strong  $\gamma$ -ray activity. On the other hand, we observe a doubling of the VLBI core flux density during the first  $\gamma$ -ray flaring periods of 2010-2011 (see Fig. 5.25), which suggests that the  $\gamma$ -ray emission region is located inside the radio core, and not in the jet.

<sup>1</sup>While 3C 120 shows an FR I-like extended structure (Walker et al. 1987), its innermost jet and accretion flow are much more alike to an FR II source (Torresi 2012).

This combination of slow pc-scale jet and fast  $\gamma$ -ray variability bears some resemblance to the case of IC 310, a transitional FR I-BL Lac object which shows minute-timescale variability at VHE (Aleksić et al. 2014), but no fast jet motion in VLBI images (Schulz 2016, Schulz et al. in prep.). For this source, Aleksić et al. (2014) favor a model where the fast  $\gamma$ -ray variability is produced by charge depletion in the supermassive black hole magnetosphere due to low accretion rate phases.

### 0625–354

The estimated viewing angle and jet speed ranges from VLBI data allow for the scenario of PKS 0625–35 as a highly relativistic jet seen at an angle at the edge between the radio galaxy and blazar classifications. This is also supported by the indications of a hard X-ray nuclear component in the source and by the source’s position in the parameter space of radio core luminosity at 5 GHz and X-ray non-thermal luminosity, which places it exactly in the region between FR Is and BL Lacs (Trussoni et al. 1999).

### 1718–649

Our kinematic analysis allows us to obtain a rough estimate on the age of this young radio source, albeit with a large relative error, as  $t_{\text{age}} = d_{\text{max}}/\mu = (70 \pm 30)$  years. This limit is consistent with a quite small age for the source, compared to usual estimates for young sources ( $t_{\text{age}} \sim 10^5$  yr, Tingay et al. 1997, and references therein). This is mostly due to the notably small linear size of  $\sim 2.5$  pc, compared with the bulk of the young radio sources population (e.g. Orienti & Dallacasa 2014). Our estimates are also in broad agreement with the one reported in Giroletti & Polatidis (2009).

## 7.2 Sample properties

In this section, we investigate the radio and  $\gamma$ -ray properties of the radio galaxies in the TANAMI program as a sample. To increase the sample size, we added all radio galaxies with published VLBI results from the MOJAVE survey <sup>2</sup>, and performed the same LAT analysis described in Section 6. The resulting  $\gamma$ -ray properties of the sources are listed in Table 7.1. We detect (TS>25) three sources not previously published in any *Fermi*-LAT catalog, i.e., NGC 315, NRAO 128, and PKS 1514+00, in addition to the well-known  $\gamma$ -ray source 3C 120. PKS 1128–047 is not classified as radio galaxy in the *Fermi*-LAT catalogs, but it is according to the NASA/IPAC Extragalactic Database (NED) and MOJAVE. We exclude NGC 1052 due to its lack of a clear VLBI core in the MOJAVE data, although we are aware that at higher frequencies the absorption by the surrounding torus is not present and a clear core is detected at 86 GHz (Baczko et al. 2016). The MOJAVE kinematics results were taken from Lister et al. (2013) and Lister et al. (2016). The exact reference for each source is given in Table 7.1.

The resulting sample includes a total of 35 objects. This is the largest radio galaxy sample with combined  $\gamma$ -ray and VLBI measurements ever studied so far.

The radio and  $\gamma$ -ray luminosity is calculated as follows:

<sup>2</sup>We have used the combined sample from Lister et al. (2013) and Lister et al. (2016), including a total of 21 radio galaxies with measured apparent speed.

$$L_r = S_r \times 4\pi D_L^2 \quad (7.1)$$

and

$$L_\gamma = S_\gamma \times 4\pi D_L^2 \times \frac{1-\Gamma}{2-\Gamma} \times \frac{E_{\max}^{2-\Gamma} - E_{\min}^{2-\Gamma}}{E_{\max}^{1-\Gamma} - E_{\min}^{1-\Gamma}} \quad (7.2)$$

respectively, where

$D_L$  is the luminosity distance,

$S_r$  is the radio flux density,

$S_\gamma$  is the LAT flux,

$\Gamma$  is the LAT photon index,

$[E_{\min}, E_{\max}]$  is the energy range of the LAT analysis.

TABLE 7.1: 0.1-100 GeV *Fermi*-LAT results on MOJAVE radio galaxies. Sources reported as LAT detections here for the first time are highlighted in italic.

| B1950           | Common name        | Redshift | Flux <sup>a</sup>                | Spectral index <sup>b</sup> | Curvature <sup>c</sup> | TS                   | Ref. <sup>d</sup> |
|-----------------|--------------------|----------|----------------------------------|-----------------------------|------------------------|----------------------|-------------------|
| 0007+106        | Mrk 1501           | 0.0893   | $< 4 \times 10^{-9}$             | -                           | -                      | 1.87                 | [2]               |
| 0026+346        | B2 0026+34         | 0.517    | $< 3 \times 10^{-9}$             | -                           | -                      | 6.76                 | [2]               |
| <i>0055+300</i> | <i>NGC 315</i>     | 0.0165   | $(5.5 \pm 1.3) \times 10^{-9}$   | 2.29±0.11                   | -                      | 77.3                 | [2]               |
| 0108+388        | GB6 J0111+3906     | 0.668    | $< 5 \times 10^{-9}$             | -                           | -                      | 2.95                 | [2]               |
| 0305+039        | 3C 78              | 0.0287   | $(7.0 \pm 1.0) \times 10^{-9}$   | 1.96±0.07                   | -                      | 385                  | [1]               |
| <i>0309+411</i> | <i>NRAO 128</i>    | 0.136    | $(5.7 \pm 1.7) \times 10^{-9}$   | 2.29±0.13                   | -                      | 53.6                 | [2]               |
| 0316+413        | 3C 84              | 0.018    | $(3.36 \pm 0.04) \times 10^{-7}$ | 2.006±0.008                 | 0.060±0.004            | 9.63×10 <sup>4</sup> | [1]               |
| 0415+379        | 3C 111             | 0.0491   | $(3.4 \pm 0.3) \times 10^{-8}$   | 2.75±0.07                   | -                      | 186                  | [1]               |
| 0430+052        | 3C 120             | 0.033    | $(2.8 \pm 0.3) \times 10^{-8}$   | 2.70±0.06                   | -                      | 226                  | [1]               |
| 0710+439        | B3 0710+439        | 0.518    | $< 6 \times 10^{-10}$            | -                           | -                      | 0.0                  | [2]               |
| 1128-047        | PKS 1128-047       | 0.27     | $(7.6 \pm 1.3) \times 10^{-9}$   | 2.46±0.10                   | -                      | 58.9                 | [2]               |
| 1228+126        | M87                | 0.00436  | $(1.9 \pm 0.2) \times 10^{-8}$   | 2.08±0.04                   | -                      | 1410                 | [2]               |
| 1345+125        | 4C +12.50          | 0.121    | $< 1 \times 10^{-9}$             | -                           | -                      | 0.97                 | [2]               |
| 1509+054        | PMN J1511+0518     | 0.084    | $< 2 \times 10^{-9}$             | -                           | -                      | 0.35                 | [2]               |
| <i>1514+004</i> | <i>PKS 1514+00</i> | 0.052    | $(8.8 \pm 1.6) \times 10^{-9}$   | 2.46±0.10                   | -                      | 82.3                 | [2]               |
| 1607+268        | CTD 93             | 0.473    | $< 7 \times 10^{-9}$             | -                           | -                      | 5.88                 | [2]               |
| 1637+826        | NGC 6251           | 0.0247   | $(2.2 \pm 0.2) \times 10^{-8}$   | 2.28±0.04                   | 0.09±0.02              | 1610                 | [2]               |
| 1845+797        | 3C 390.3           | 0.0555   | $< 2 \times 10^{-9}$             | -                           | -                      | 5.35                 | [2]               |
| 1957+405        | Cygnus A           | 0.0561   | $< 4 \times 10^{-9}$             | -                           | -                      | 2.76                 | [2]               |
| 2021+614        | OW 637             | 0.227    | $< 1 \times 10^{-8}$             | -                           | -                      | 18.6                 | [2]               |
| 2128+048        | PKS 2127+04        | 0.99     | $< 2 \times 10^{-9}$             | -                           | -                      | 0.2                  | [2]               |

<sup>a</sup> *Fermi*-LAT flux between 0.1-100 GeV in photons cm<sup>-2</sup> s<sup>-1</sup>.

<sup>b</sup> *Fermi*-LAT spectral index  $\Gamma$ , in case of power-law spectrum  $dN/dE = N_0 \times (E/E_0)^{-\Gamma}$ , or  $\alpha$  in case of logParabola spectrum  $dN/dE = N_0 \times (E/E_b)^{-[\alpha+\beta \log(E/E_b)]}$ .

<sup>c</sup> Curvature parameter of logParabola spectrum  $\beta$ .

<sup>d</sup> MOJAVE reference paper for the VLBI results: [1] Lister et al. (2013); [2] Lister et al. (2016)

### 7.2.1 Average radio and $\gamma$ -ray properties

We first consider the distribution of measured VLBI luminosity and maximum apparent speed, which is illustrated in Fig. 7.1. It can be seen that there is a lack of low-luminosity sources ( $\lesssim 10^{24}$  W/Hz) with superluminal speed. This was already found to be true for blazars (e.g. Cohen et al. 2007; Lister et al. 2013), but this is the first time that it is observed in radio galaxies. On the other hand, while for blazars a population of high-luminosity, low-speed sources is observed (Cohen et al. 2007), this is not the case in our radio galaxy sample. Cohen et al. (2007) interpreted this sub-population, mostly composed of BL Lac blazars, as sources where the VLBI apparent speed measured at 15 GHz is not representative of the jet bulk Lorentz factor. This is now a well-established fact for high-energy peaked BL Lacs (HBLs, see e.g. Piner & Edwards 2018, and references therein). Our data show no evidence for an obvious misaligned parent population of these intrinsically luminous, low-speed blazars.

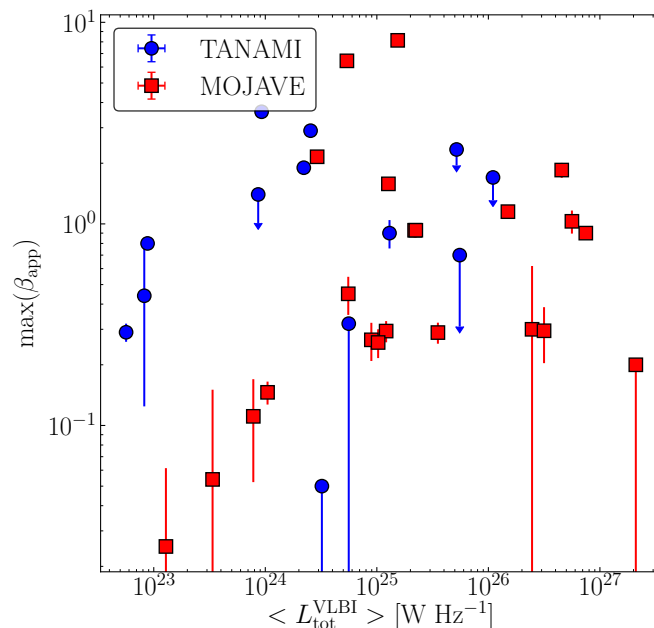


FIGURE 7.1: Maximum observed apparent speed as a function of total VLBI luminosity.

In order to compare the radio properties of  $\gamma$ -ray detected and undetected radio galaxies, we visualize their distribution with histograms, shown in Fig. 7.2. We test whether there is a statistically significant difference in the distribution of LAT detected and undetected radio galaxies using the Kolmogorov-Smirnov statistic (KS). The results of this test are listed in Table 7.2. In terms of apparent speed (top left panel of Fig. 7.2) the distributions of LAT detected and undetected sources do not appear to differ substantially, although it can be seen that the highest bin includes mostly  $\gamma$ -ray detected sources. The distribution of median core flux density (top right panel of Fig. 7.2) shows a quite clear dichotomy between the two subsamples, with the LAT-undetected sources occupying the lower end, and the LAT-detected sources dominating the upper end of the distribution. This is visible to a smaller extent for the median jet flux density (i.e., total minus core) as well (middle left panel of Fig. 7.2, shown in logarithmic scale for ease of visualization). On the other hand, the distribution of median core luminosity (middle right

panel of Fig. 7.2) shows no clear separation based on  $\gamma$ -ray detections. We have also explored the distribution of core brightness temperature, defined as

$$T_b = \frac{2 \ln 2 S_r \lambda^2 (1+z)}{\pi k_b \theta^2} \quad (7.3)$$

where  $k_b$  is Boltzmann's constant,  $S_r$  is the radio flux,  $\lambda$  is the observing wavelength,  $z$  is the source redshift, and  $\theta$  is the FWHM of the circular Gaussian model fitted to the core component. Since the component sizes resulting from modeling can result to be much smaller than the actual resolution, we have calculated an upper limit on the component size based on its signal-to-noise ratio (SNR), following Kovalev et al. (2005):

$$\theta_{\text{lim}} = b \sqrt{\frac{4 \ln 2}{\pi} \ln \left( \frac{\text{SNR}}{\text{SNR} - 1} \right)} \quad (7.4)$$

where  $b$  is the beam size. The signal-to-noise ratio (SNR) was calculated as the ratio between the peak flux of the residual map after subtracting the gaussian component, in an area defined by the component size, and the post-fit rms in the same residual map area. When the fitted component size was  $\theta < \theta_{\text{lim}}$ , we have used  $\theta_{\text{lim}}$  as an upper limit, and therefore the obtained  $T_b$  is a lower limit estimate. We did not compute the resolution limit for the MOJAVE sources, since we only made use of publicly available data. Looking at the distribution in the bottom left panel of Fig. 7.2, there is a hint of higher  $\langle T_b \rangle$  for LAT detected sources, which occupy the majority of the highest bins, while LAT-undetected sources populate most of the lowest bins. Finally, we see no clear distinction in the distribution of VLBI core dominance (bottom right panel of Fig. 7.2). We define this parameter as a ratio between VLBI core flux density and total flux density, i.e.,  $CD = S_{\text{core}}^{\text{VLBI}}/S_{\text{tot}}^{\text{VLBI}}$ . Quantitatively, the KS test shows that LAT detected and undetected sources differ most significantly ( $p$ -value < 5%, significance  $> 2.5\sigma$ ) in their distribution of median VLBI core flux density. Additionally, there is a hint of statistically significant separation between the two sub-population in terms of their median core  $T_b$ .

TABLE 7.2: Results of a KS test to assess whether the LAT detected and undetected subsample are drawn from the same parent population, according to their average radio properties as illustrated in Fig. 7.2. We report the value of the KS statistic, the associated two-tailed  $p$ -value and corresponding significance.

| Variable  | KS statistic | $p$ -value | Significance ( $\sigma$ ) |
|---|--------------|------------|---------------------------|
| $\langle S_{\text{core}}^{\text{VLBI}} \rangle$ | 0.53         | 0.009      | 2.61                      |
| $\langle T_b^{\text{core}} \rangle$             | 0.50         | 0.017      | 2.39                      |
| $\langle L_{\text{core}}^{\text{VLBI}} \rangle$ | 0.41         | 0.073      | 1.79                      |
| $\langle S_{\text{jet}}^{\text{VLBI}} \rangle$  | 0.38         | 0.13       | 1.51                      |
| $\max(\beta_{\text{app}})$                      | 0.23         | 0.70       | 0.64                      |
| $\langle CD_{\text{VLBI}} \rangle$              | 0.18         | 0.91       | 0.11                      |

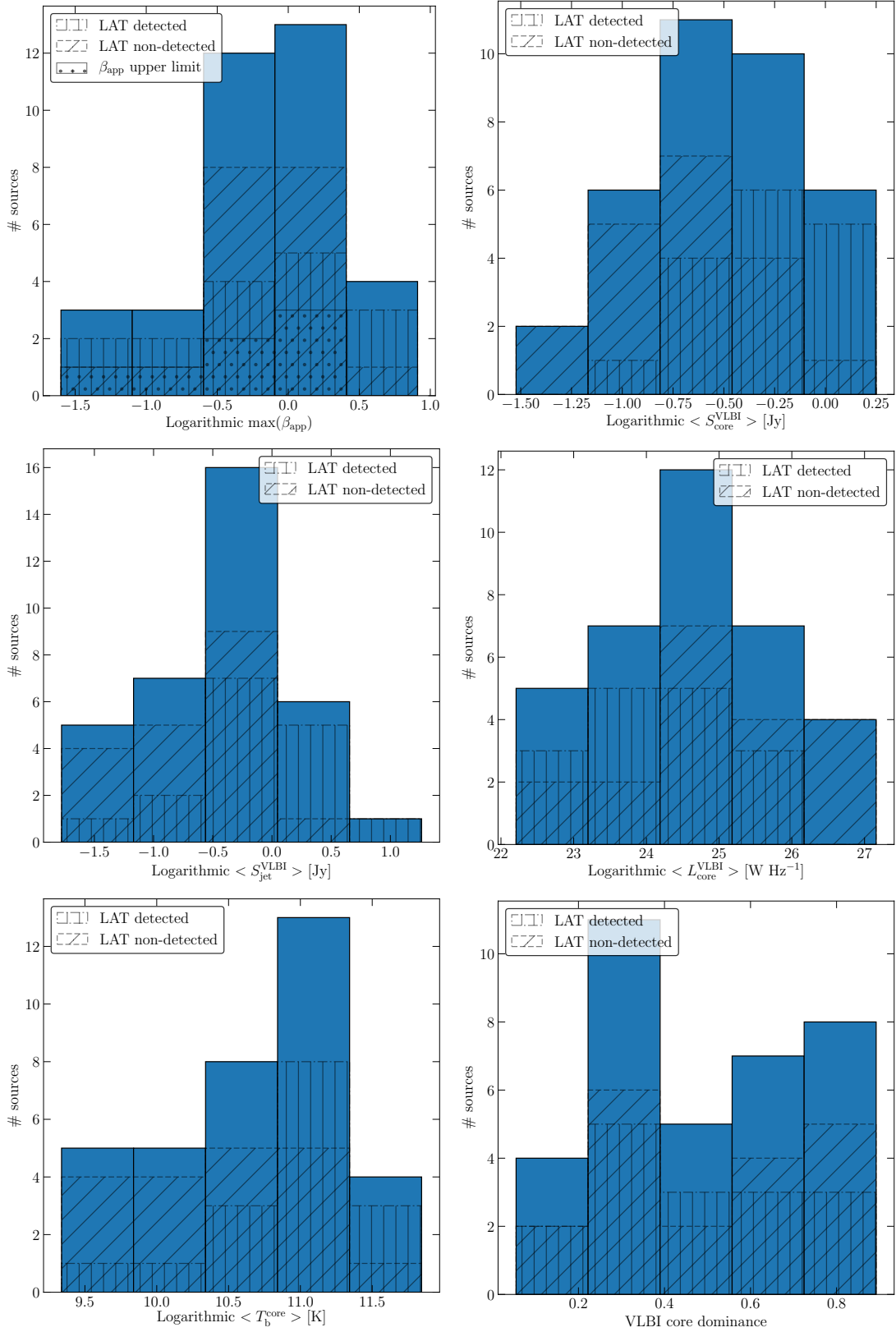


FIGURE 7.2: Histograms of radio VLBI properties for radio galaxies from the MOJAVE and TANAMI monitoring programs. The filled blue area represents the total sample, while the hatched areas indicate the LAT-detected and LAT-undetected subsamples. *Top left:* maximum measured apparent speed. *Top right:* median VLBI core flux density. *Center left:* median VLBI jet flux density. *Center right:* median VLBI core luminosity. *Bottom left:* median core brightness temperature. *Bottom right:* median VLBI core dominance.

We then compare the  $\gamma$ -ray properties of our radio galaxy sample with other source classes, namely with blazars. In order to do this, we performed a consistent LAT analysis on the whole MOJAVE and TANAMI samples, as described in Section 6.1. The resulting merged sample includes 460 sources, and the resulting  $\gamma$ -ray properties are listed in Tables C.1 through C.11. We then looked at the distribution of  $\gamma$ -ray flux, spectral shape and luminosity<sup>3</sup> in the different source classes.

It is worth noting that as the  $\gamma$ -ray luminosity depends on the photon index (see Eq. 7.2), it is necessary to assume a spectrum for undetected sources. We have chosen to assume a typical value of  $\Gamma = 2.2$ . In order to evaluate the effect of this assumption on the calculated values, we compute the dependence of  $\gamma$ -ray luminosity on the photon index assuming a flux of  $1 \times 10^{-8}$  photons  $\text{cm}^{-2} \text{s}^{-1}$  and a luminosity distance of 100 Mpc. The result is illustrated in Fig. 7.3. It can be seen that the dependence appears to be negligible for indices  $\Gamma > 2.0$ , a range that includes  $\sim 87\%$  of detected sources in the combined TANAMI+MOJAVE sample, and is still within a factor  $\sim 2.5$  for indices  $\Gamma > 1.8$ , i.e., for  $\sim 95\%$  of the detected sample (see top right panel of Fig. 7.4). We therefore conclude that assuming a spectral index value to calculate the LAT luminosity of undetected sources does not constitute a significant source of bias.

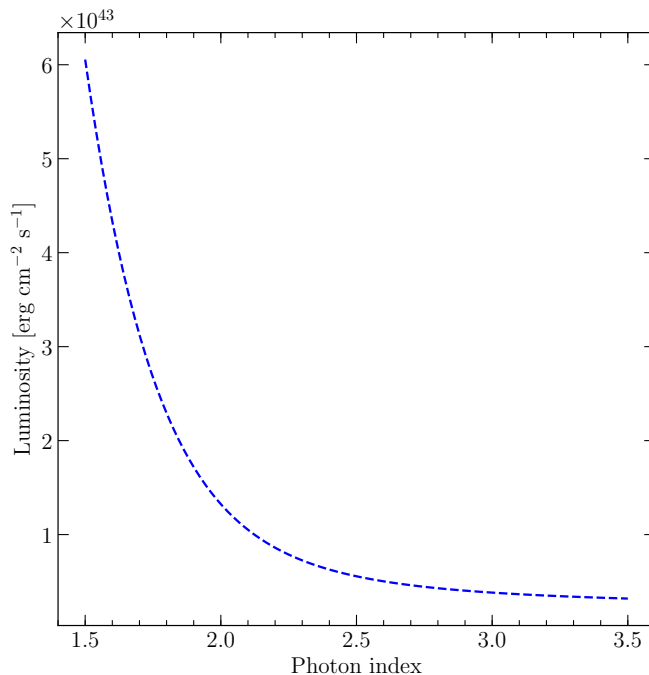


FIGURE 7.3: Calculated  $\gamma$ -ray luminosity as a function of the assumed photon index for a source with flux  $1 \times 10^{-8}$  photons  $\text{cm}^{-2} \text{s}^{-1}$  and a luminosity distance of 100 Mpc.

The distribution of  $\gamma$ -ray fluxes (see upper left panel of Fig. 7.4) shows that radio galaxies populate the low-brightness part of the distribution, while blazars (FSRQs and BL Lacs) are typically an order of magnitude brighter. In terms of photon index (see upper right panel of Fig. 7.4), there is no clear separation between aligned and misaligned jets. This is consistent with

<sup>3</sup>Note that  $\sim 0.3\%$  of FSRQs,  $\sim 2\%$  of radio galaxies,  $\sim 36\%$  of BL Lacs and  $\sim 84\%$  of unclassified sources in the sample do not have a redshift, therefore it was not possible to calculate the luminosity for these sources.

the unified model of radio-loud AGN (see Section 1.2.2), as the spectral differences between blazar subclasses are expected to reflect in their misaligned counterparts. However, it is worth noting that there are no radio galaxies with photon index larger than  $\sim 2.7$ , while there is a significant population of steep-spectrum FSRQs covering this range of the distribution. This might be due to the fact that the LAT radio galaxy sample includes more FR I sources (see Section 2.1), which are considered the misaligned counterpart of BL Lacs (see Section 1.2.2), that tend to have flatter spectra, as can be easily seen in the histogram. Finally, we take into account the effect of redshift by calculating the  $\gamma$ -ray luminosity, whose distribution is represented in the bottom panel of Fig. 7.4. Eliminating the effects related to source redshift, we can see even more clearly that radio galaxies populate the low-luminosity end of the distribution.

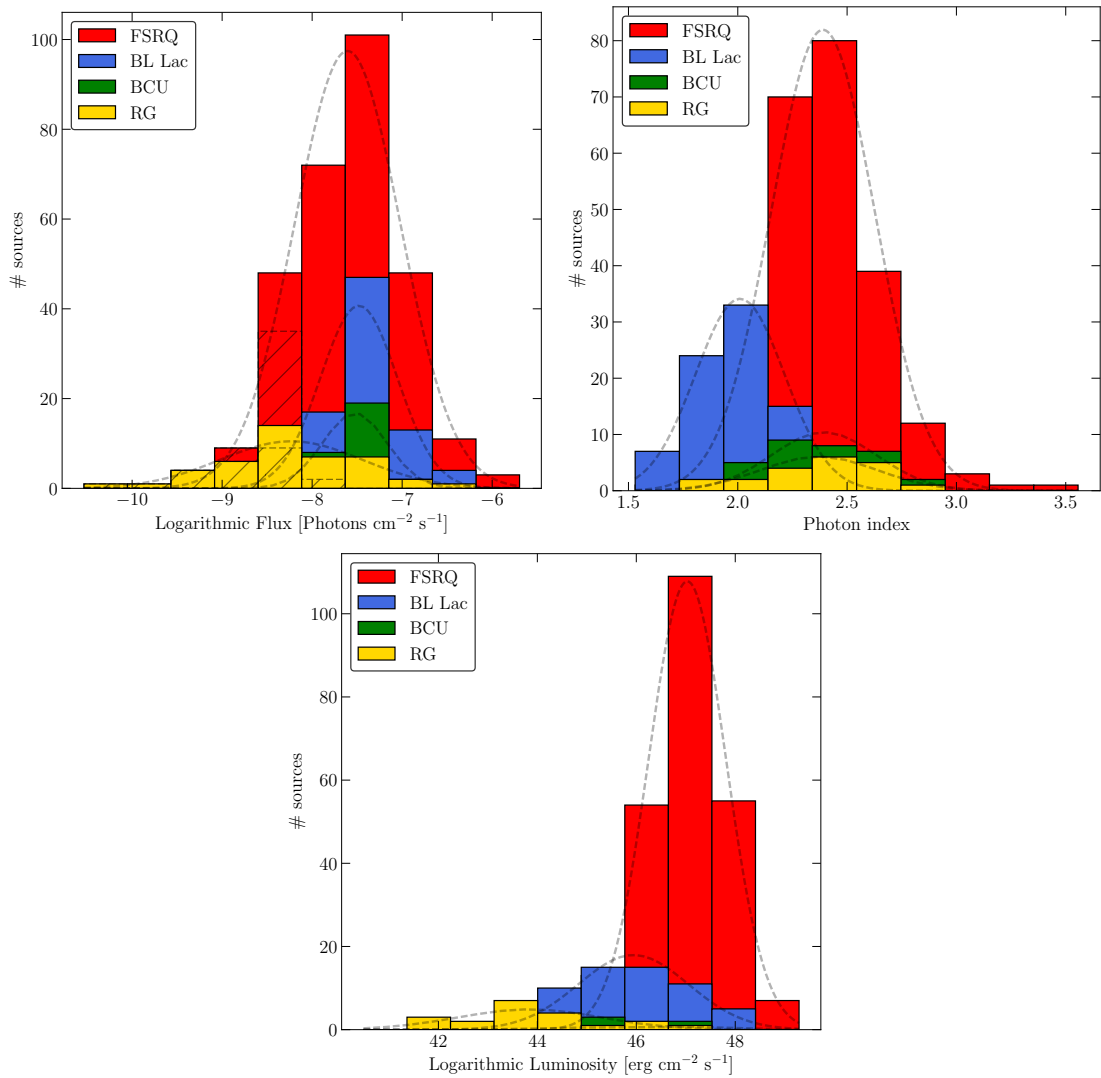


FIGURE 7.4: Histograms of  $\gamma$ -ray properties of AGN in the MOJAVE and TANAMI combined sample for different source classes (red: FSRQs, blue: BL Lacs, green: unclassified sources, yellow: radio galaxies). *Top left*: logarithmic 0.1-100 GeV flux. Hatched regions indicate flux upper limits ( $TS < 25$ ). *Top right*:  $\gamma$ -ray photon index for detected sources. *Bottom*: logarithmic 0.1-100 GeV luminosity for detected sources with measured redshift. The dashed faded black lines represent Gaussian fits to the distribution of each source class, meant to guide the eye.

### 7.2.2 Correlations between radio and $\gamma$ -ray properties

In order to investigate possible correlations between the radio and  $\gamma$ -ray properties of the sources in this sample, we have used the Kendall's correlation coefficient ( $\tau$ ) adapted to take into account the presence of upper limits, following Akritas & Siebert (1996). The correlation coefficient is equal to zero in the case of uncorrelated data, one in case of maximum correlation, and minus one in case of maximum anti-correlation. The resulting correlation coefficients with errors and the relative significance are listed in Table 7.3, and the corresponding scatter plots are included in Fig. 7.5.

TABLE 7.3: Correlation coefficients between radio and  $\gamma$ -ray properties of our radio galaxy sample, related  $p$ -values and corresponding significance.

| Variables  | Kendall's $\tau$ | $p$ -value | Significance ( $\sigma$ ) |
|--|------------------|------------|---------------------------|
| $\langle S_{\text{core}}^{\text{VLBI}} \rangle$ vs. $F_{\gamma}$ | $0.32 \pm 0.11$  | 0.006      | 2.75                      |
| $\langle S_{\text{jet}}^{\text{VLBI}} \rangle$ vs. $F_{\gamma}$  | $0.19 \pm 0.11$  | 0.1        | 1.65                      |
| $\langle CD_{\text{VLBI}} \rangle$ vs. $L_{\gamma}$              | $0.16 \pm 0.11$  | 0.17       | 1.37                      |
| $L_{\gamma}$ vs. $\langle T_{\text{b}}^{\text{core}} \rangle$    | $0.08 \pm 0.11$  | 0.5        | 0.67                      |

We find a significant correlation ( $p$ -value  $< 5\%$ , significance  $> 2.5\sigma$ ) between median VLBI core flux density and *Fermi*-LAT flux (top left panel of Fig. 7.5). This result appears to indicate that in radio galaxies, the observed  $\gamma$ -ray flux is related to the radio flux density of the innermost pc-scale jet. Such a correlation was already highlighted for large, blazar-dominated AGN samples (see e.g. Kovalev et al. 2009; Ackermann et al. 2011; Böck et al. 2016; Lico et al. 2017). We can confirm that a similar dependence of  $\gamma$ -ray flux on the radio core flux density holds for misaligned AGN jets as well. We do not find a significant correlation between median VLBI jet flux density and *Fermi*-LAT flux (top right panel of Fig. 7.5). This suggests that the dominant contribution to the  $\gamma$ -ray emission is the innermost radio core. To take into account the different distance scale for each source, we calculated the luminosity in both the radio and  $\gamma$ -ray bands. The resulting values are illustrated in the center left panel of Fig. 7.5. Since both quantities are directly proportional to the flux in the respective band, they share the same correlation results. Additionally, the common dependence on the square of the luminosity distance induces a 1:1 linear relationship which is not intrinsic, as revealed by a partial correlation test taking into account redshift. In the center right panel of Fig. 7.5 we show the median VLBI core brightness temperature as a function of  $\gamma$ -ray luminosity. As can be readily seen, there is no correlation between the core brightness temperature and the  $\gamma$ -ray luminosity. Böck et al. (2016) found, for the full TANAMI sample, an indication of increasing core brightness temperature with increasing  $\gamma$ -ray luminosity. Interestingly, our results focused on  $\gamma$ -ray radio galaxies show that the  $\gamma$ -ray luminosity appears to be completely uncorrelated with the core brightness temperature for misaligned jets. Since the core brightness temperature is often considered as an indicator of Doppler boosting (e.g., Kovalev et al. 2005), this indicates that while the core flux density does reflect higher  $\gamma$ -ray fluxes, high-energy emission in radio galaxies is not Doppler boosting dominated. Further support to this inference comes from the VLBI core dominance, another indicator of Doppler boosting. As can be seen in the bottom panel of Fig. 7.5, the observed  $\gamma$ -ray luminosity is not correlated with the core dominance, supporting the finding that it is not driven by Doppler boosting.

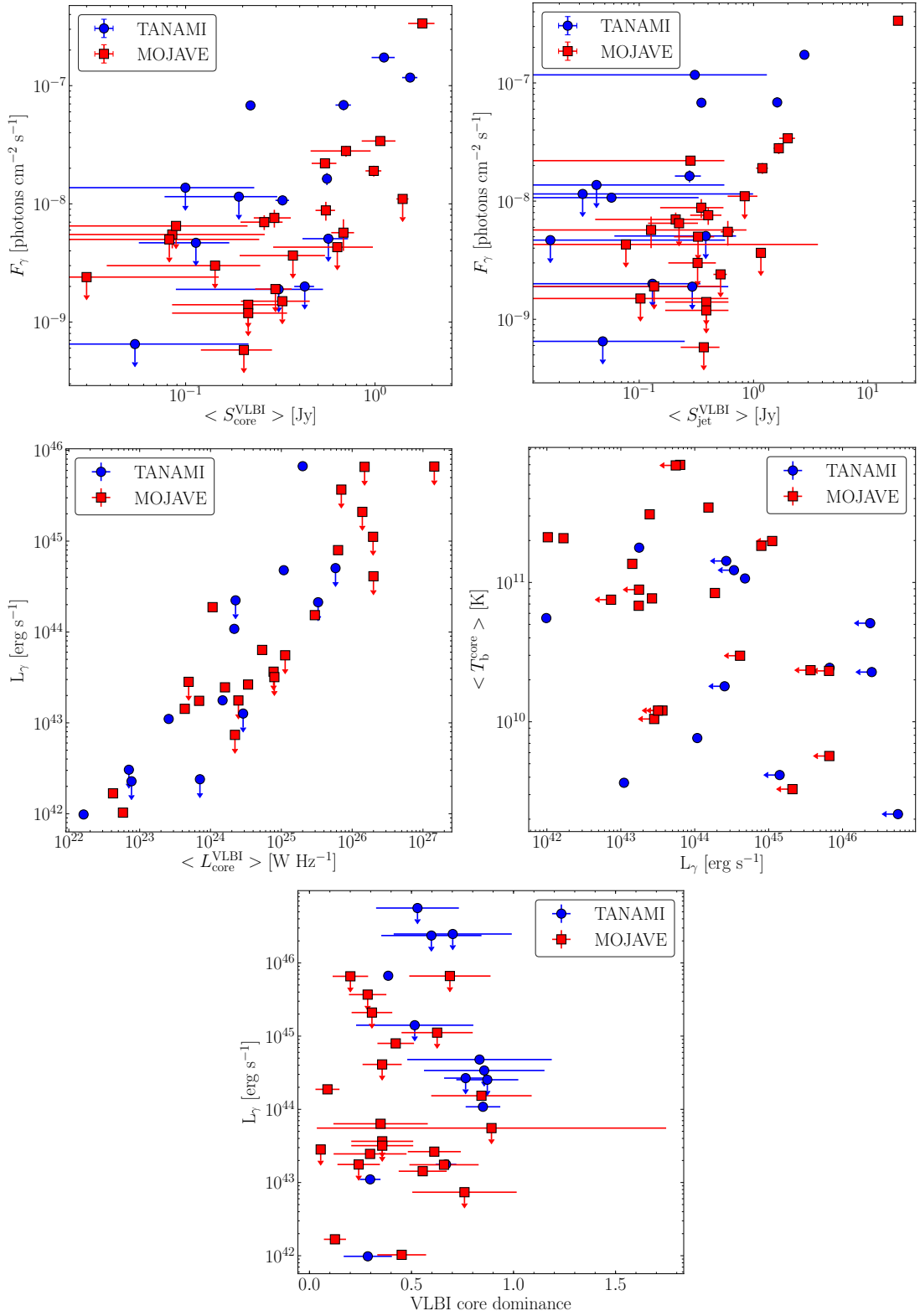


FIGURE 7.5: *Top left:* *Fermi*-LAT flux as a function of average VLBI core flux density. *Top right:* *Fermi*-LAT flux as a function of average VLBI jet flux density. *Center left:* *Fermi*-LAT luminosity as a function of average VLBI core luminosity. *Center right:* Average VLBI core brightness temperature as a function of *Fermi*-LAT luminosity. *Bottom center:* *Fermi*-LAT luminosity as a function of average VLBI core dominance.

Overall, the comparison of several VLBI and *Fermi*-LAT properties of radio galaxies consistently suggests that high-energy emission in misaligned jets is not driven by orientation-dependent Doppler boosting effects, in agreement with the unified model of jetted AGN.

In all the correlations discussed above, we have implicitly assumed that the radio spectral index is zero, and therefore for each source the flux density at 8.4 GHz (the frequency of the TANAMI observations) is the same as the one at 15 GHz (the frequency of the MOJAVE observations). Naturally, this may not always be the case, and it is therefore relevant to investigate the presence of a possible bias related to this effect. To test this, we assumed a common spectral index value  $\alpha = -0.5$ , and back-extrapolated the MOJAVE flux densities to 8.4 GHz. As a result, the flux densities increase on average by  $\sim 36\%$ , the Kendall's correlation coefficient decreases by  $\sim 2\%$ , and the p-value increases by  $\sim 20\%$ , but it remains below the 1% threshold. We therefore conclude that the different frequency of the two VLBI monitoring programs does not influence our results significantly.



# Chapter 8

## Conclusions

*This Chapter will be partially reproduced in Angioni et al. a,b, to be submitted to Astronomy & Astrophysics*

In this thesis, we have presented the first systematic study of the relationship between parsec-scale radio jets and high-energy  $\gamma$ -ray emission in radio galaxies. A relationship between parsec-scale radio emission and  $\gamma$ -ray properties has been firmly established for large AGN samples. However, such samples are heavily dominated by blazars, i.e. radio-loud sources with aligned jets, whose emission is strongly affected by Doppler boosting. Such effects allow us to detect high-energy emission more easily in blazars, but they also mask the intrinsic properties of jets with orientation-dependent effects. Therefore, it is necessary to extend the characterization of the relationship between the innermost jet and high-energy emission to the AGN population which is less affected by extrinsic effects, i.e., radio galaxies, the misaligned counterpart of blazars.

In the framework of the TANAMI monitoring program, we have studied the jet evolution of a representative sample of radio galaxies in the southern hemisphere, deriving their kinematic properties and providing estimates on their intrinsic jet viewing angle and speed. We have complemented this with  $\gamma$ -ray light curves from *Fermi*-LAT data, and investigated the interplay between pc-scale jet evolution and high-energy variability.

Our main results on individual, noteworthy TANAMI radio galaxies can be summarized as follows:

- **Pictor A:** we find that the first  $\gamma$ -ray detection of this source was coincident with the passage of a new VLBI component through the compact core, an association that appears to be a defining feature of  $\gamma$ -ray FR II radio galaxies. Additionally, we detect a pc-scale counter-jet for the first time in this source, which allows us to estimate a lower limit on the viewing angle. We conclude that the jet of Pictor A should lie between  $76^\circ$  and  $80^\circ$  from our line of sight.
- **PKS 0521–36:** our VLBI results show subluminal motions on a  $\sim 20$  years time range, while the *Fermi*-LAT light curve shows fast variability down to 6-hours time scales. On the other hand, the doubling of the VLBI core flux during  $\gamma$ -ray flaring activity in 2010–2011 suggests the location of the high-energy emission region should be within the compact radio core. Such a combination of fast high-energy flaring activity and slow jet motions

bears some resemblance to the case of the hybrid FR I/BL Lac object IC 310 (Aleksić et al. 2014).

- **PKS 0625–35:** our TANAMI monitoring confirms the presence of superluminal motion in this jet, up to  $\beta_{\text{app}} = 2.9$ . We place an upper limit on the viewing angle at  $\theta < 53^\circ$ . This is consistent with the  $\gamma$ -ray properties of the source, i.e., a hard *Fermi*-LAT spectrum and the observed TeV emission.
- **Centaurus B:** The small number of epochs does not allow a full kinematic analysis. However, using the two available images, we tentatively constrain the jet speed to be likely subluminal or at most mildly superluminal.
- **PKS 1718–649:** TANAMI provides the first multi-epoch pc-scale maps of this archetypal CSO, which is also the first young radio galaxy to have been detected in  $\gamma$ -ray. Our kinematic analysis yields a rough estimate of the age of this young radio object, which is of the order of 70 years. Moreover, a spectral index map between 8.4 GHz and 22.3 GHz suggests that the core of this young radio source is strongly absorbed at these frequencies.
- **PKS 2153–69:** this FR II radio galaxy is, together with PKS 0625–35, the only source to show clear superluminal motion in its jet, up to  $\beta_{\text{app}} = 3.6$ . Interestingly, there is a clear trend of higher apparent speed as a function of distance along the jet, suggesting that the flow is still being accelerated on physical scales of the order of a few tens of pc.

In order to study the connection between pc-scale properties and high-energy emission in radio galaxies in a more general fashion, we included public results from the MOJAVE program, which provided us with a total sample of 35 sources with VLBI monitoring and high-energy data from *Fermi*-LAT, the largest sample of  $\gamma$ -ray detected radio galaxies studied with VLBI techniques so far. We find that the VLBI core flux density correlates with the observed  $\gamma$ -ray flux, as observed in blazars, while the  $\gamma$ -ray luminosity does not correlate with typical Doppler boosting indicators such as core brightness temperature and core dominance. This indicates that while the compact pc-scale emission does drive the observed high-energy flux, the observed  $\gamma$ -ray luminosity is not driven by Doppler boosting effects, as is observed in blazars. This difference reinforces the orientation-based unified model of jetted AGN, since radio galaxies are not expected to be Doppler boosting-dominated, having misaligned jets w.r.t. our line of sight.

## Appendix A

# Full-resolution VLBI images and parameters

Here we present all the multi-epoch VLBI images of TANAMI radio galaxies at full resolution (Fig. A.1 through A.22) and list the corresponding image parameters in Tables A.1 through A.13. These images were discussed in Section 5.3, and were used to obtain the kinematic analysis presented in Section 5.4, in some cases after applying a taper to obtain a uniform resolution across the epochs.

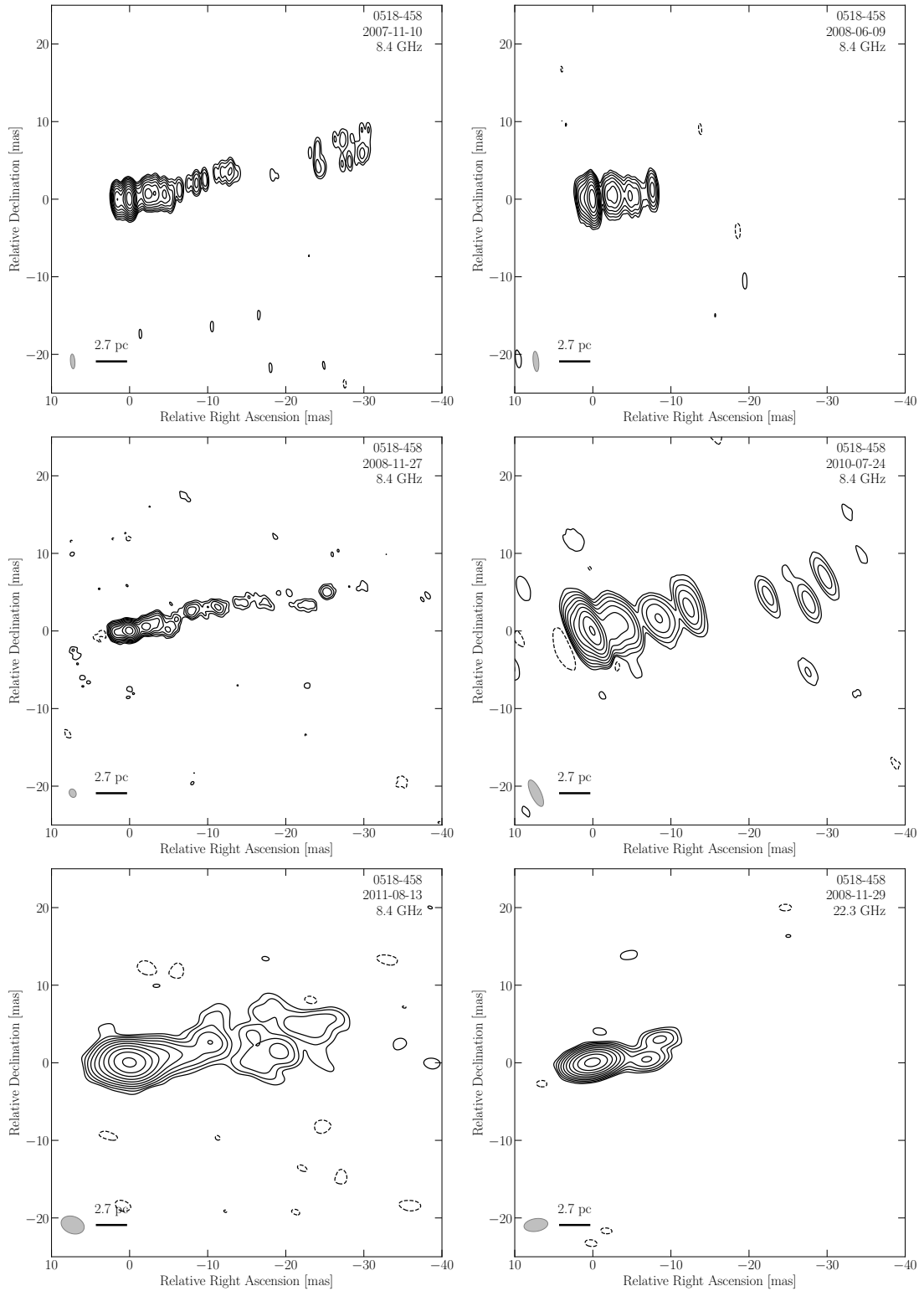


FIGURE A.1: Full-resolution images of Pictor A. The map parameters for each epoch can be found in Table A.1. The grey ellipse represents the beam size, while the black line indicates the linear scale at the source's redshift.

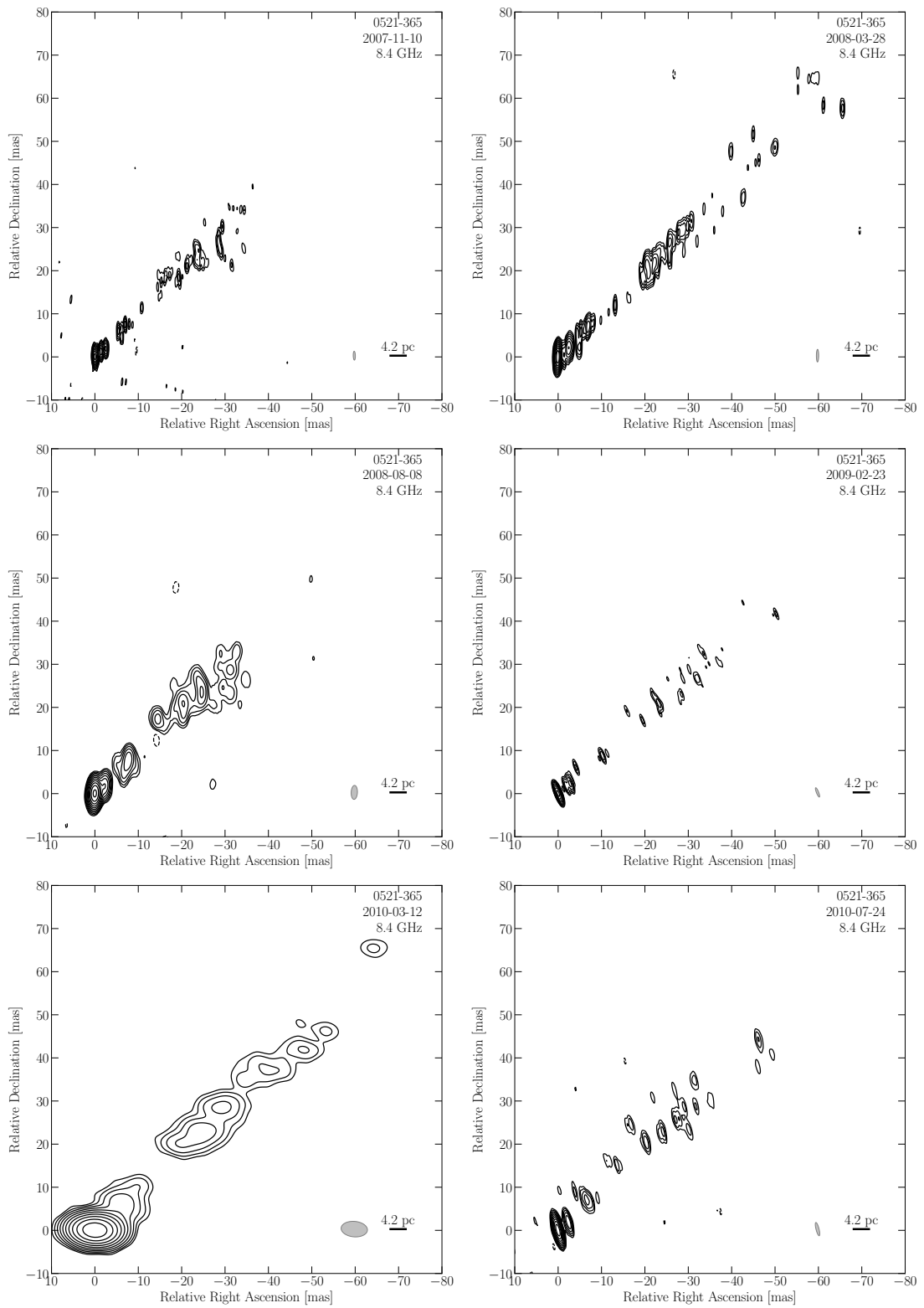


FIGURE A.2: Full-resolution images of PKS 0521–36. The map parameters for each epoch can be found in Table A.2. The grey ellipse represents the beam size, while the black line indicates the linear scale at the source’s redshift.

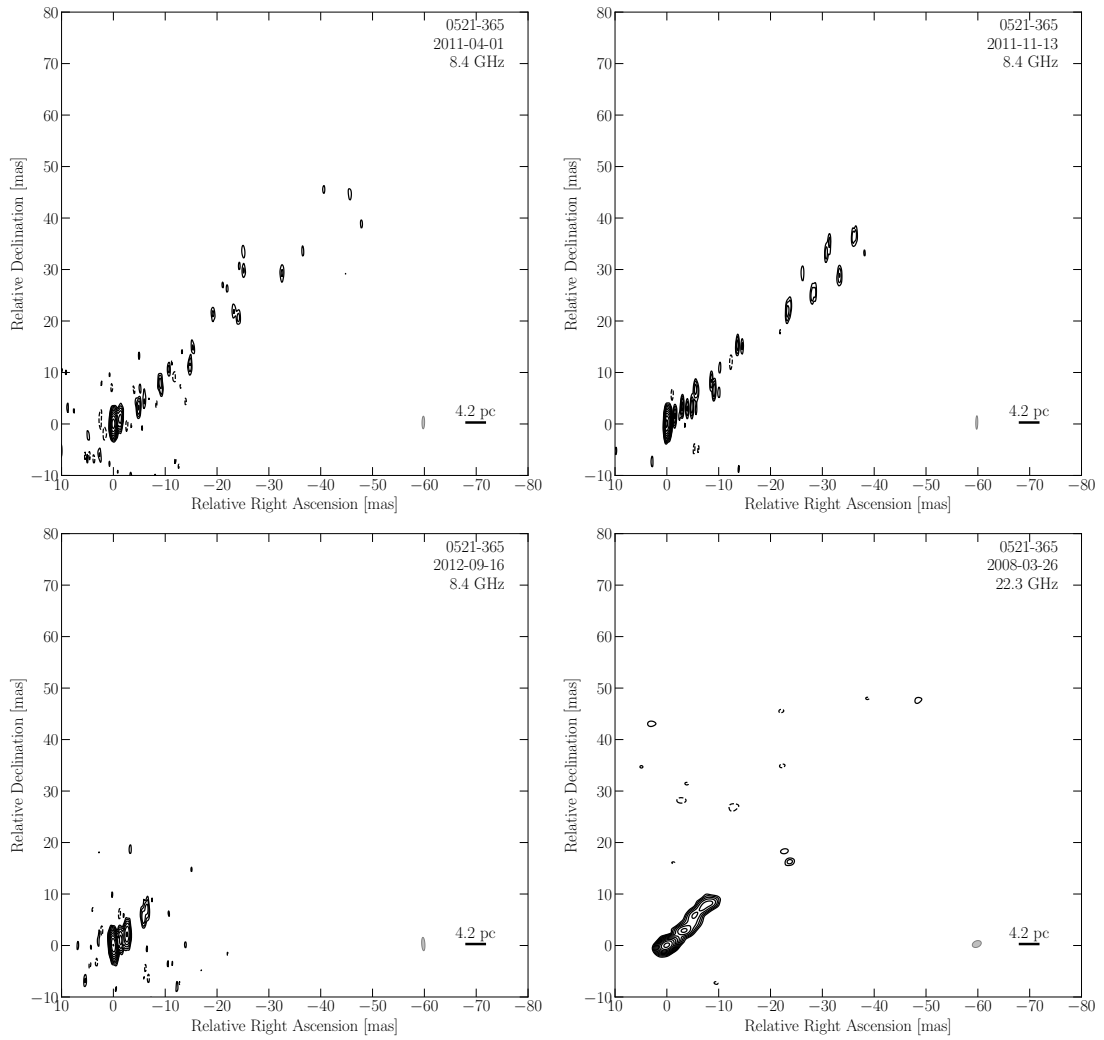


FIGURE A.3: Full-resolution images of PKS 0521–36 (continued). The map parameters for each epoch can be found in Table A.2. The grey ellipse represents the beam size, while the black line indicates the linear scale at the source’s redshift.

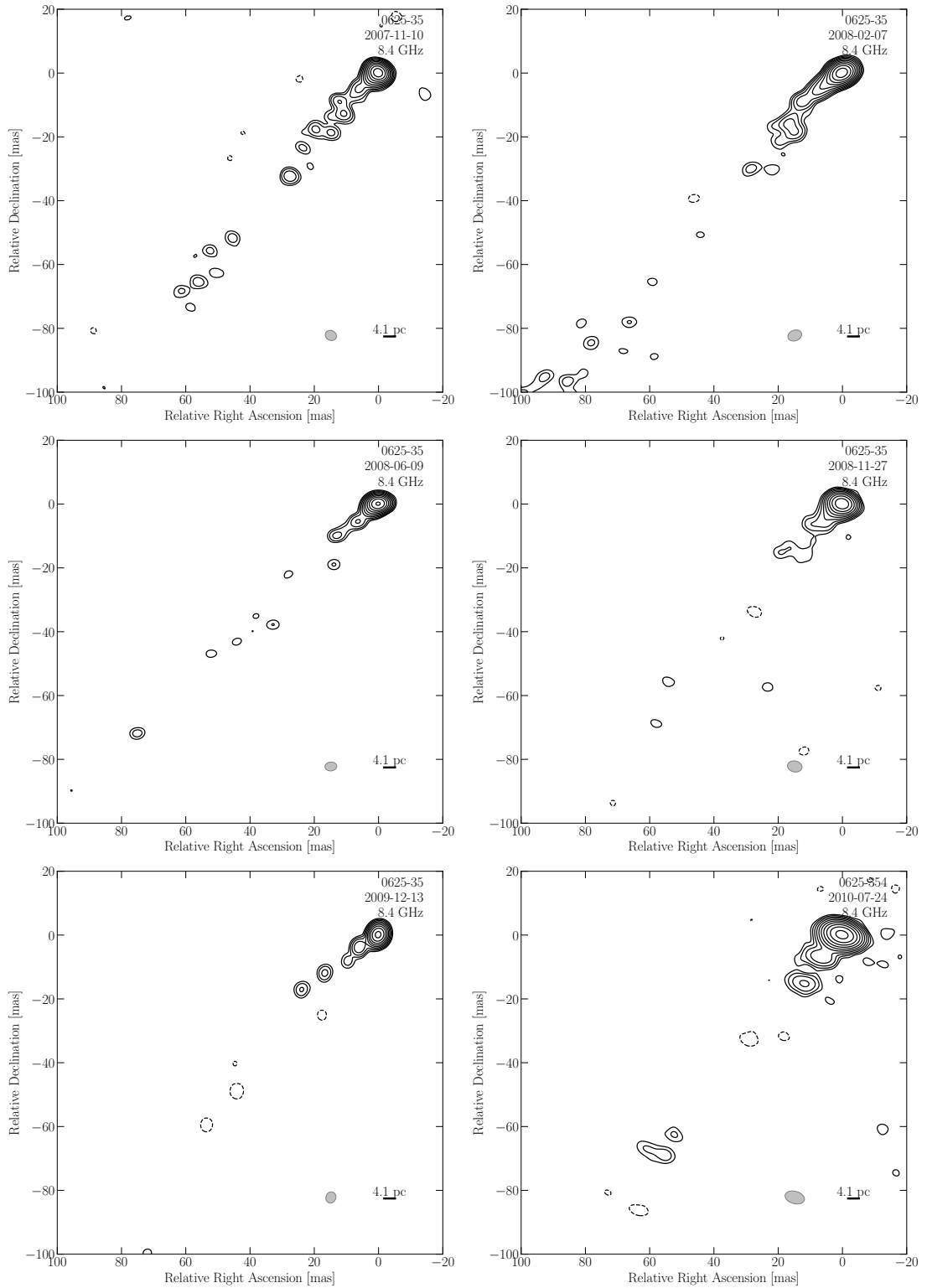


FIGURE A.4: Full-resolution images of PKS 0625–35. The map parameters for each epoch can be found in Table A.3. The grey ellipse represents the beam size, while the black line indicates the linear scale at the source’s redshift.

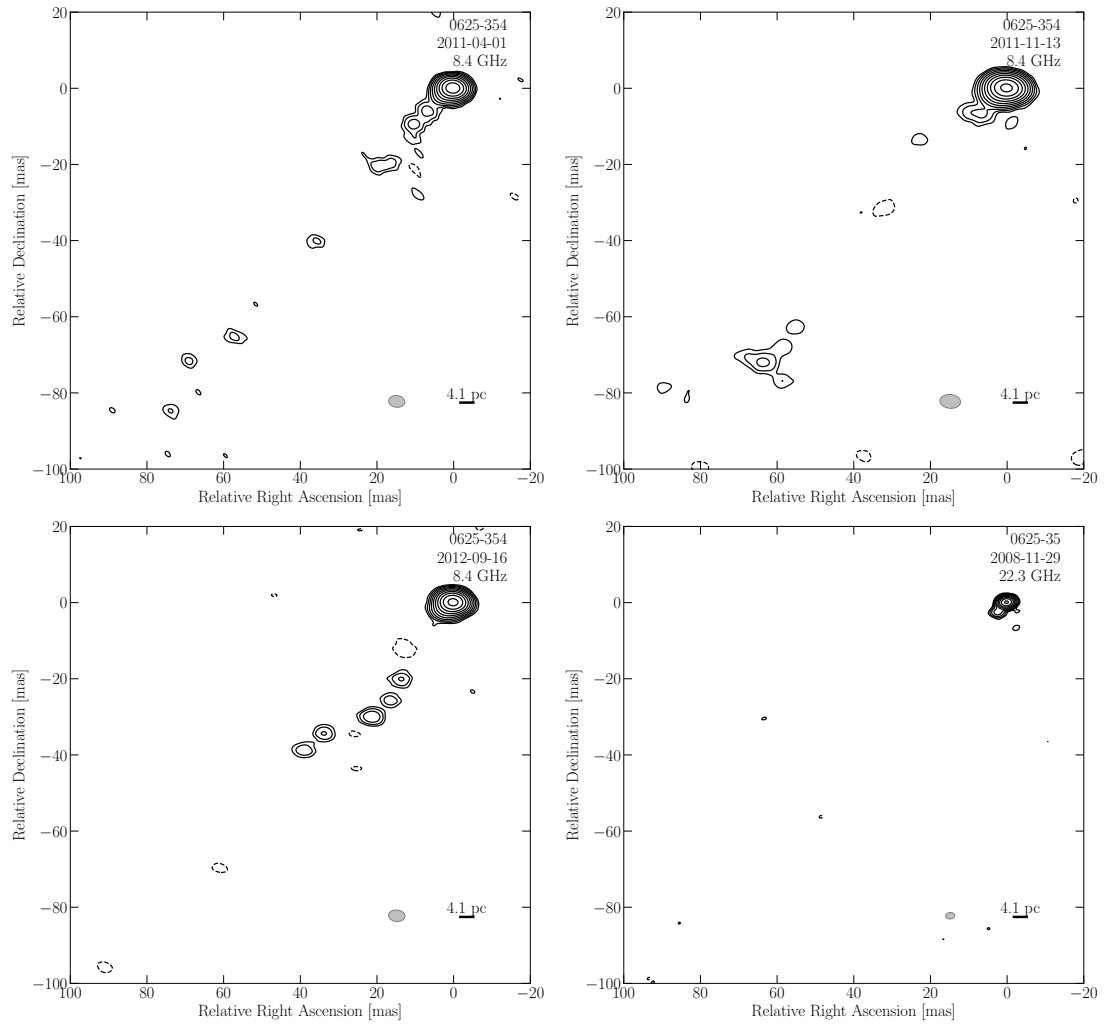


FIGURE A.5: Full-resolution images of PKS 0625–35 (continued). The map parameters for each epoch can be found in Table A.3. The grey ellipse represents the beam size, while the black line indicates the linear scale at the source’s redshift.

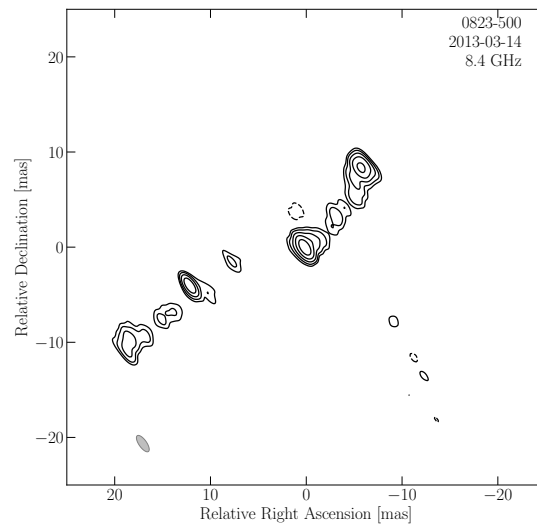


FIGURE A.6: Full-resolution images of PKS 0823–500. The map parameters for each epoch can be found in Table A.4. The grey ellipse represents the beam size, while the black line indicates the linear scale at the source’s redshift.

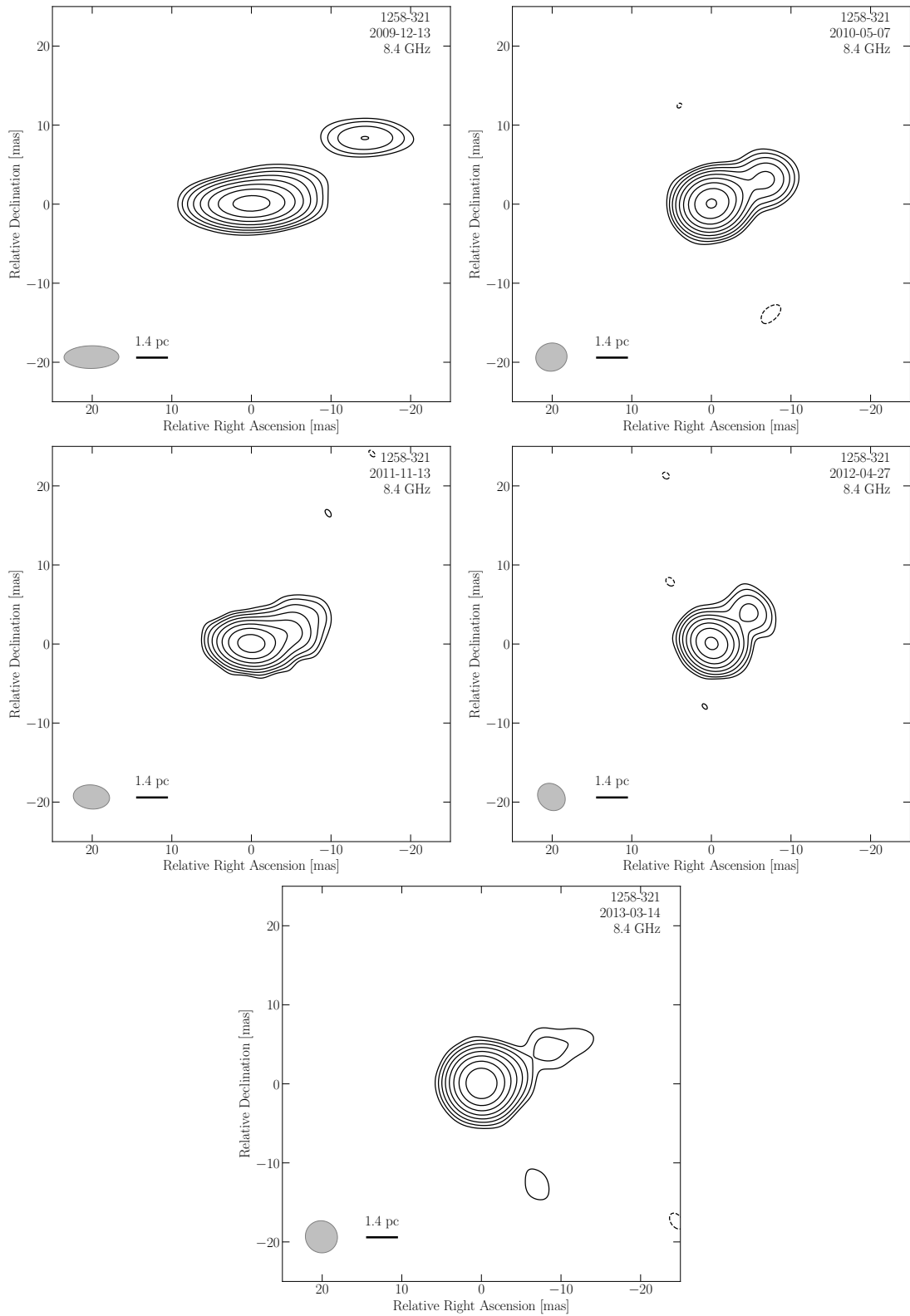


FIGURE A.7: Full-resolution images of PKS 1258–321. The map parameters for each epoch can be found in Table A.5. The grey ellipse represents the beam size, while the black line indicates the linear scale at the source’s redshift.

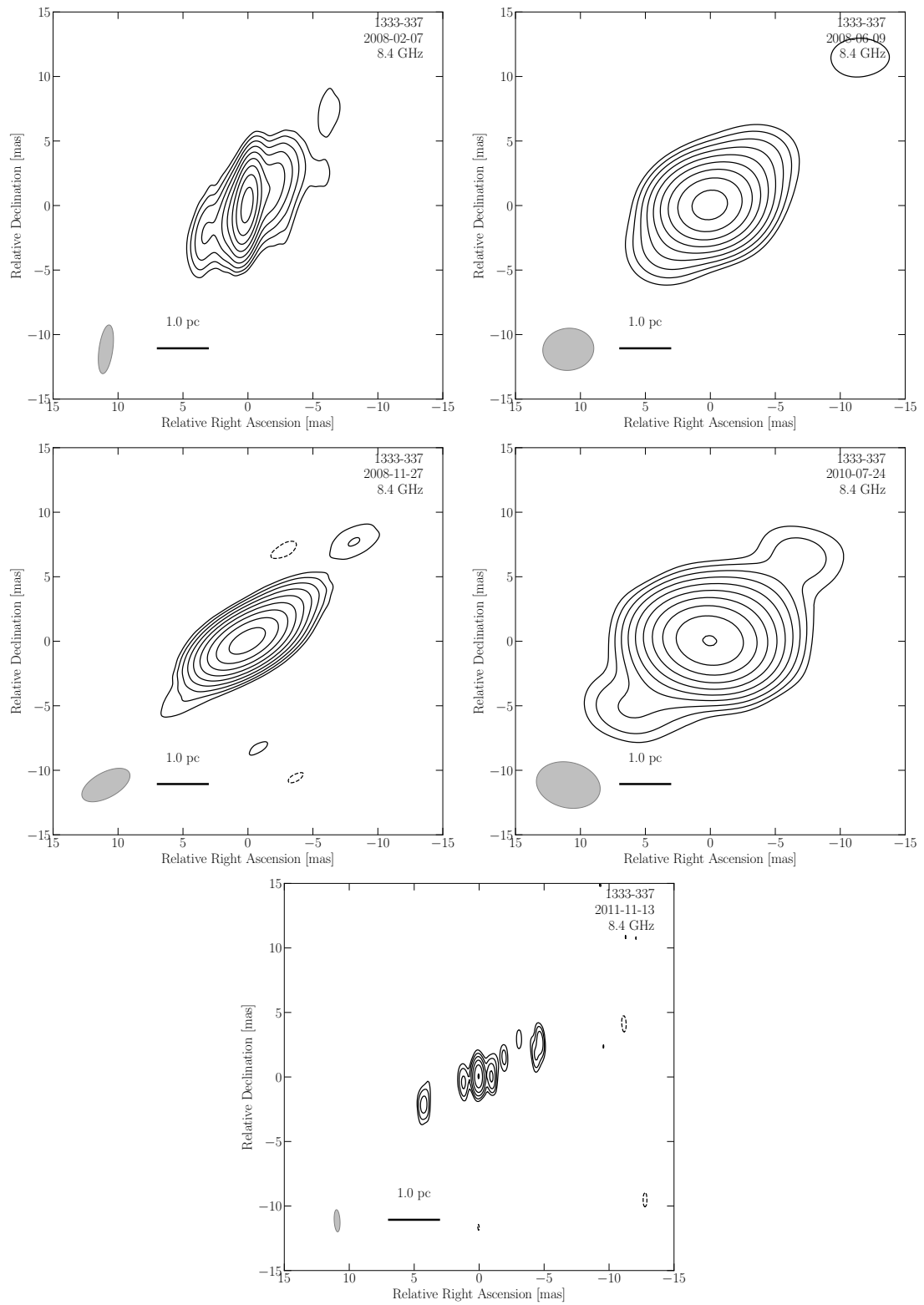


FIGURE A.8: Full-resolution images of IC 4296. The map parameters for each epoch can be found in Table A.6. The grey ellipse represents the beam size, while the black line indicates the linear scale at the source's redshift.

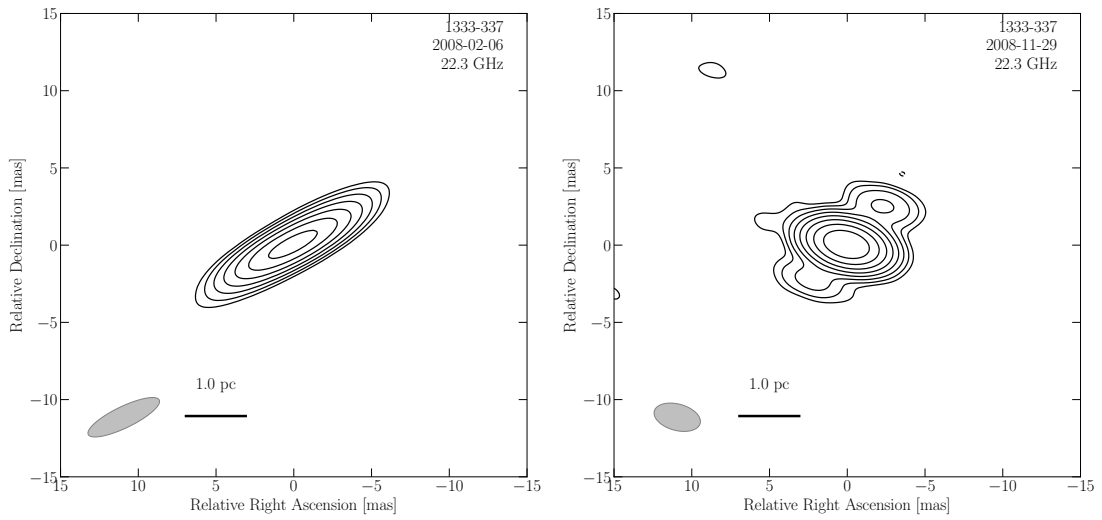


FIGURE A.9: Full-resolution images of IC 4296 (continued). The map parameters for each epoch can be found in Table A.6. The grey ellipse represents the beam size, while the black line indicates the linear scale at the source's redshift.

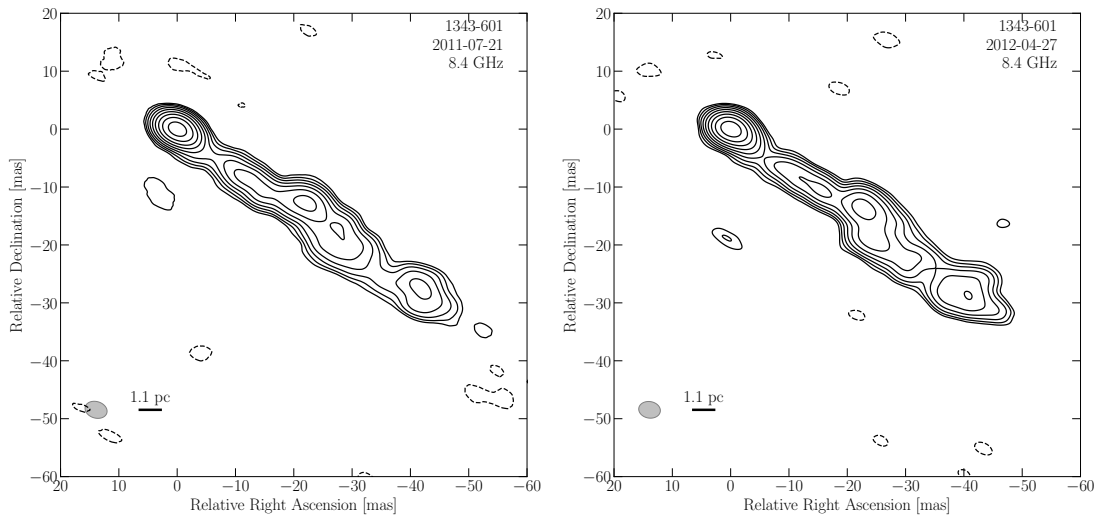


FIGURE A.10: Full-resolution images of Centaurus B. The map parameters for each epoch can be found in Table A.7. The grey ellipse represents the beam size, while the black line indicates the linear scale at the source's redshift.

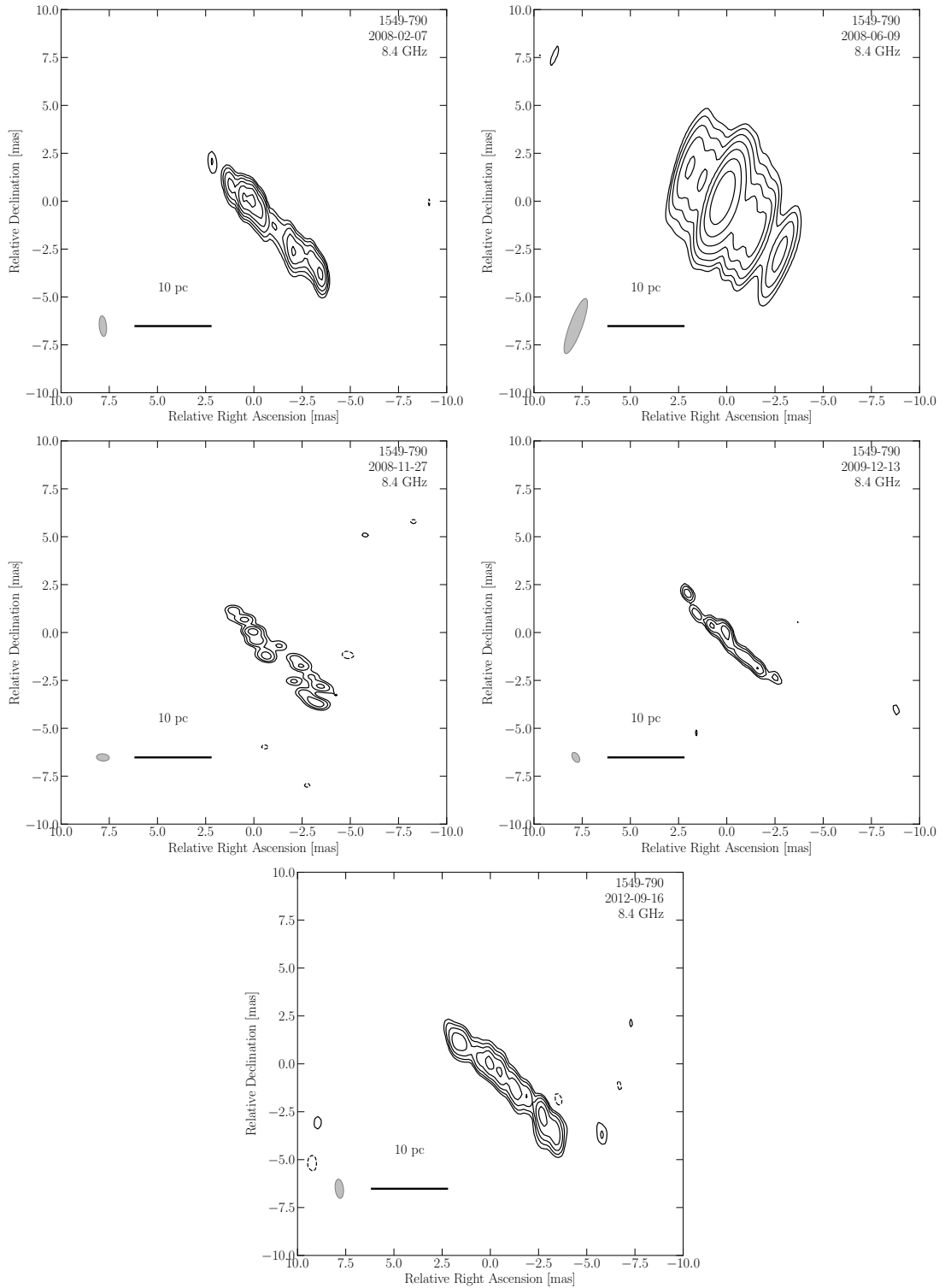


FIGURE A.11: Full-resolution images of PKS 1549–79. The map parameters for each epoch can be found in Table A.8. The grey ellipse represents the beam size, while the black line indicates the linear scale at the source’s redshift.

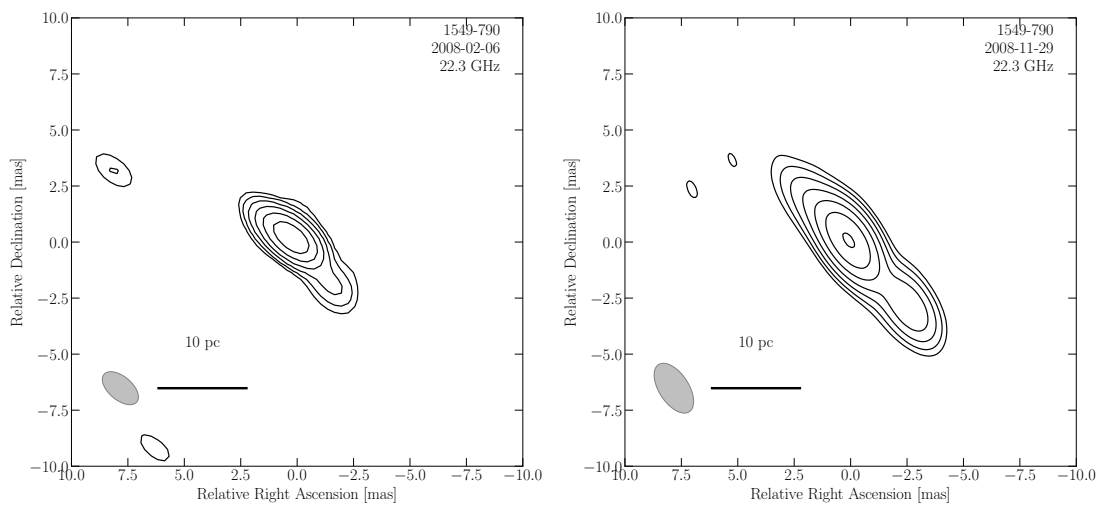


FIGURE A.12: Full-resolution images of PKS 1549-79 (continued). The map parameters for each epoch can be found in Table A.8. The grey ellipse represents the beam size, while the black line indicates the linear scale at the source's redshift.

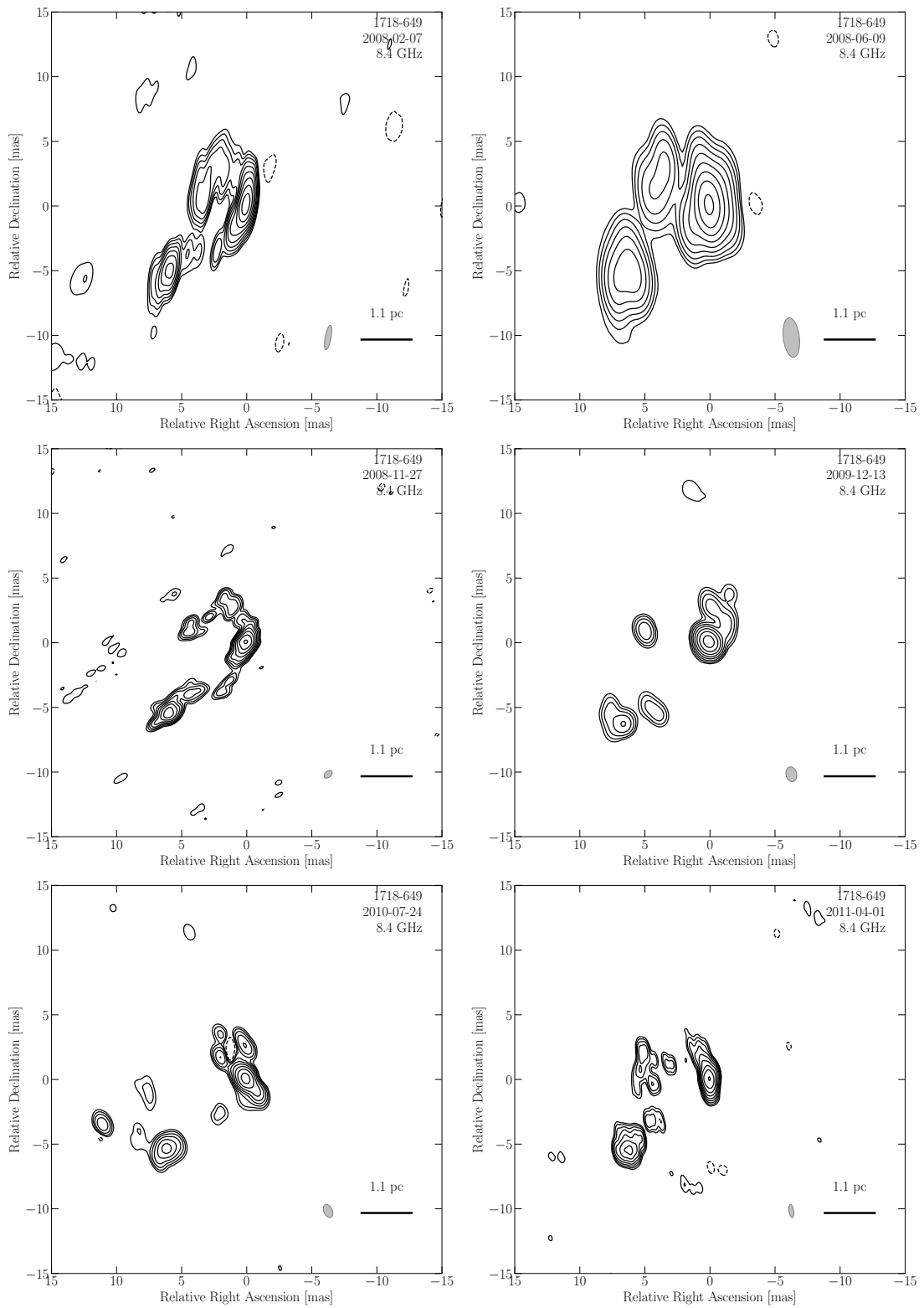


FIGURE A.13: Full-resolution images of PKS 1718–649. The map parameters for each epoch can be found in Table A.9. The grey ellipse represents the beam size, while the black line indicates the linear scale at the source’s redshift.

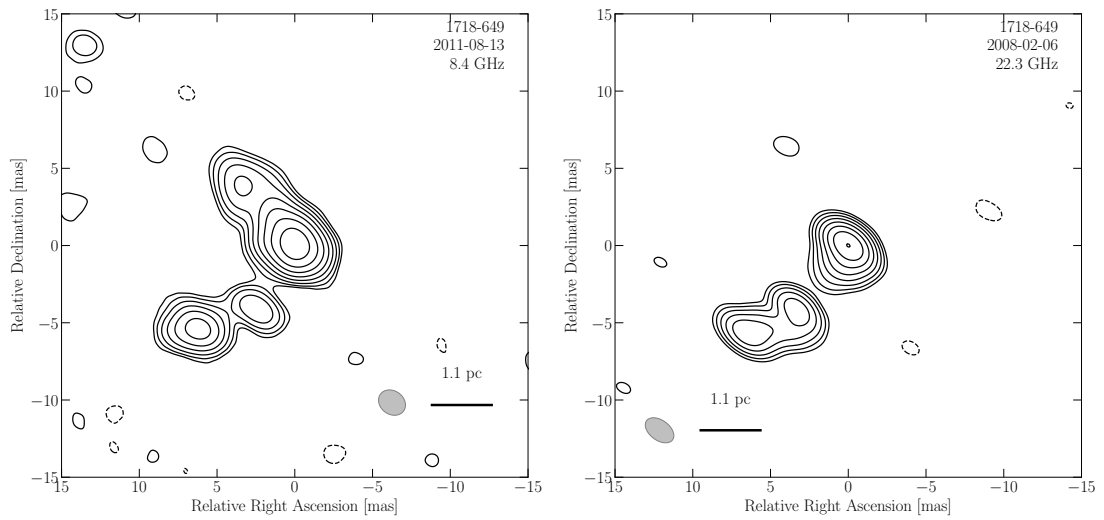


FIGURE A.14: Full-resolution images of PKS 1718–649 (continued). The map parameters for each epoch can be found in Table A.9. The grey ellipse represents the beam size, while the black line indicates the linear scale at the source’s redshift.

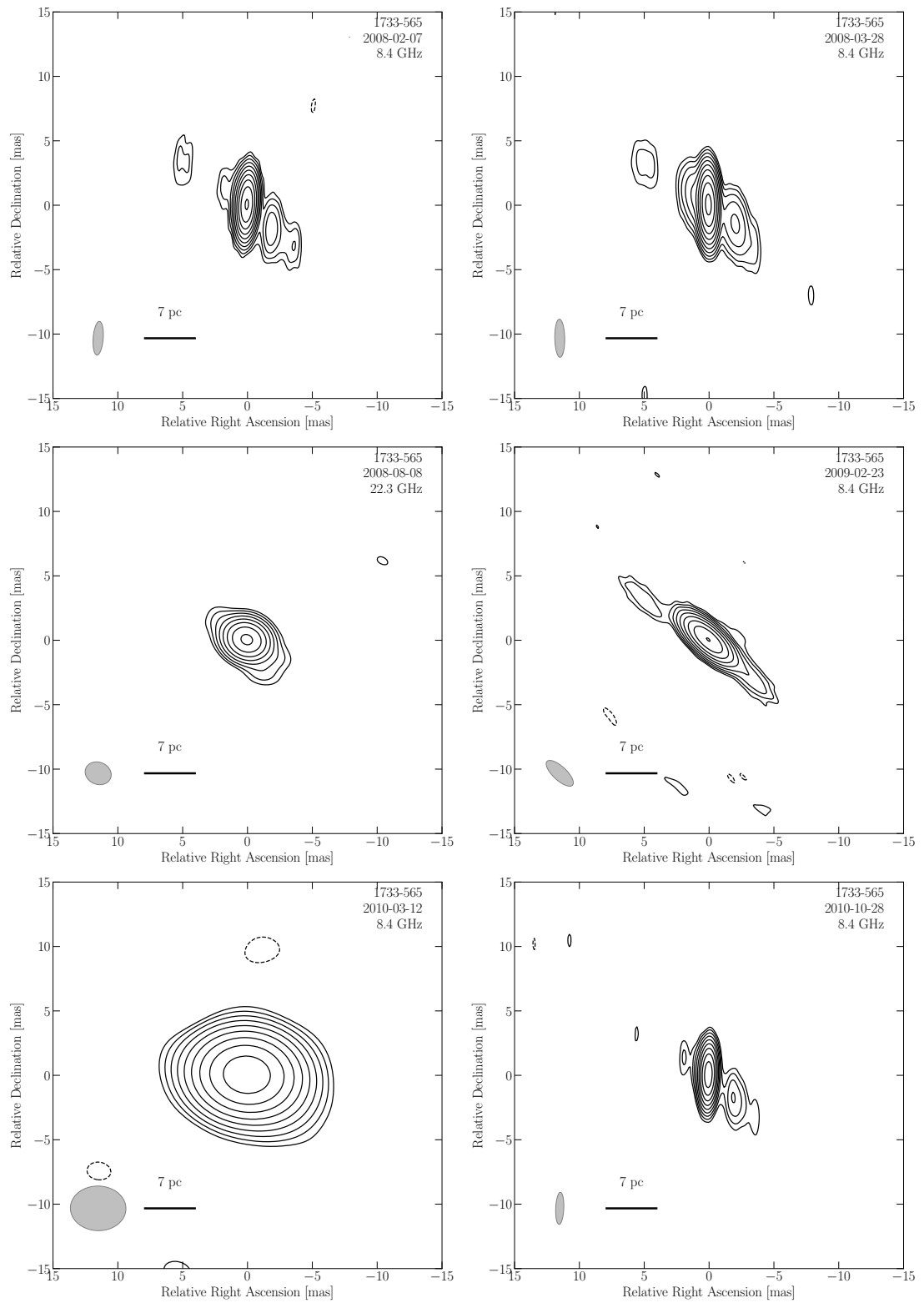


FIGURE A.15: Full-resolution images of PKS 1733–56. The map parameters for each epoch can be found in Table A.10. The grey ellipse represents the beam size, while the black line indicates the linear scale at the source’s redshift.

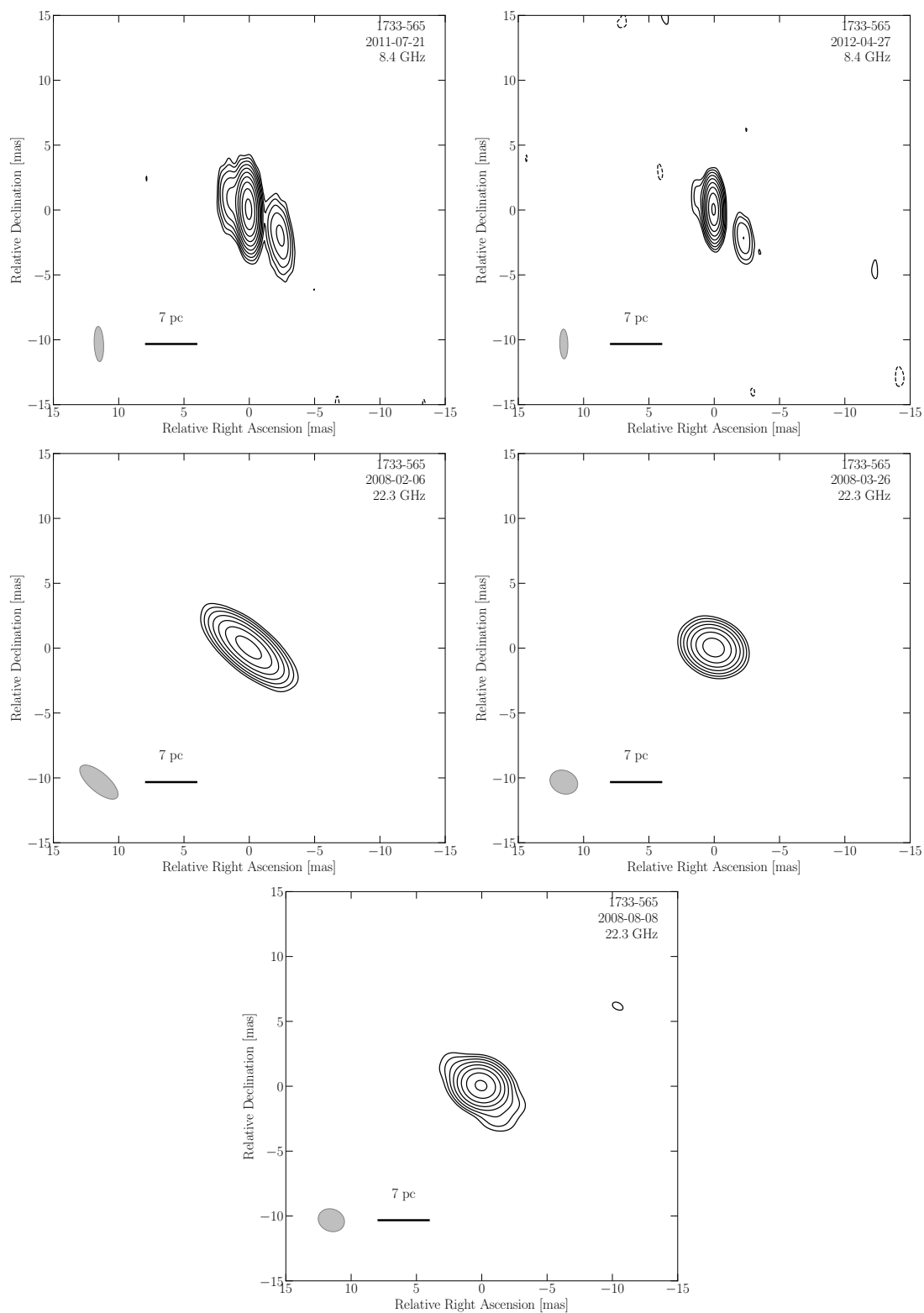


FIGURE A.16: Full-resolution images of PKS 1733–56 (continued). The map parameters for each epoch can be found in Table A.10. The grey ellipse represents the beam size, while the black line indicates the linear scale at the source’s redshift.

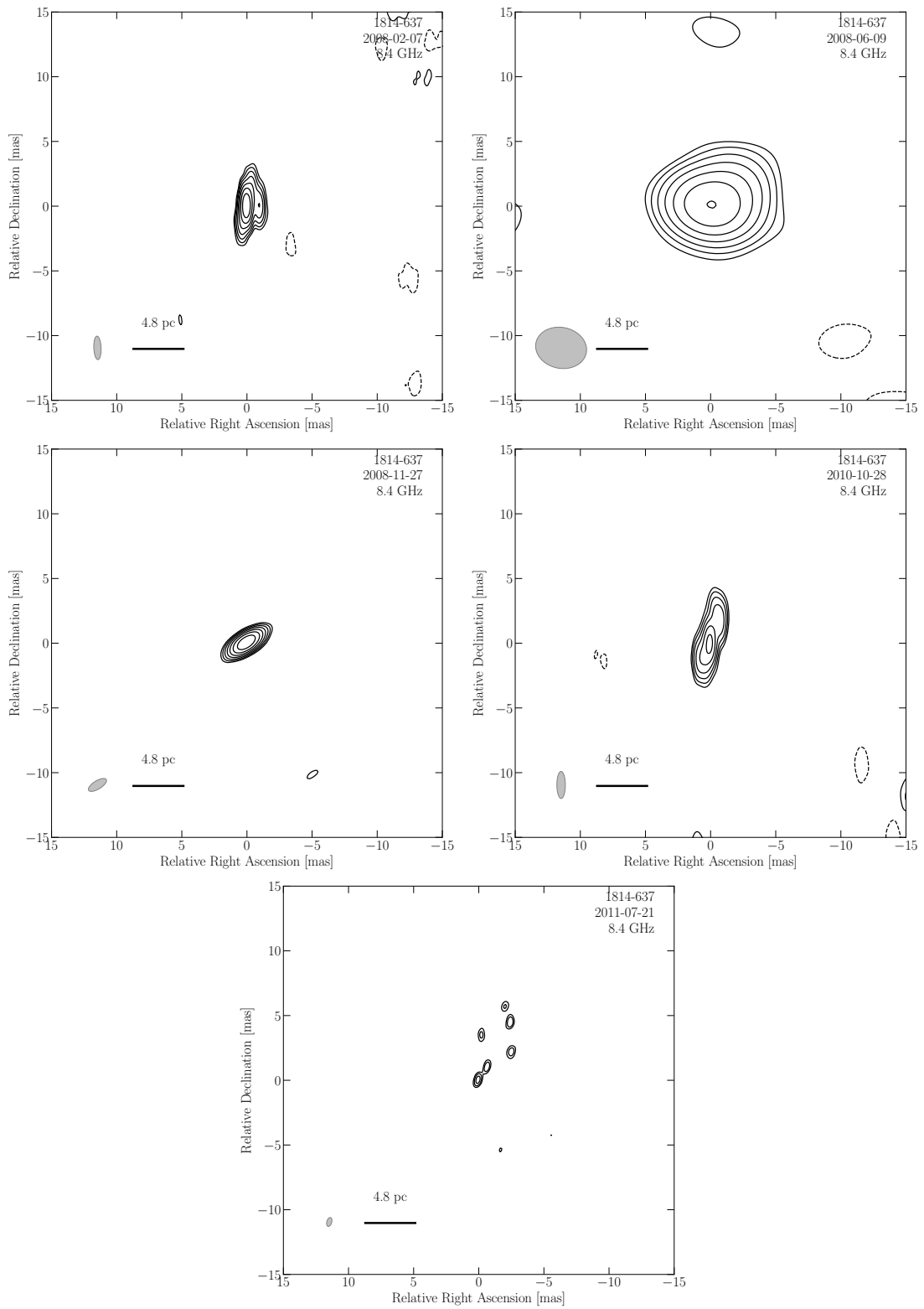


FIGURE A.17: Full-resolution images of PKS 1814–63. The map parameters for each epoch can be found in Table A.11. The grey ellipse represents the beam size, while the black line indicates the linear scale at the source’s redshift.

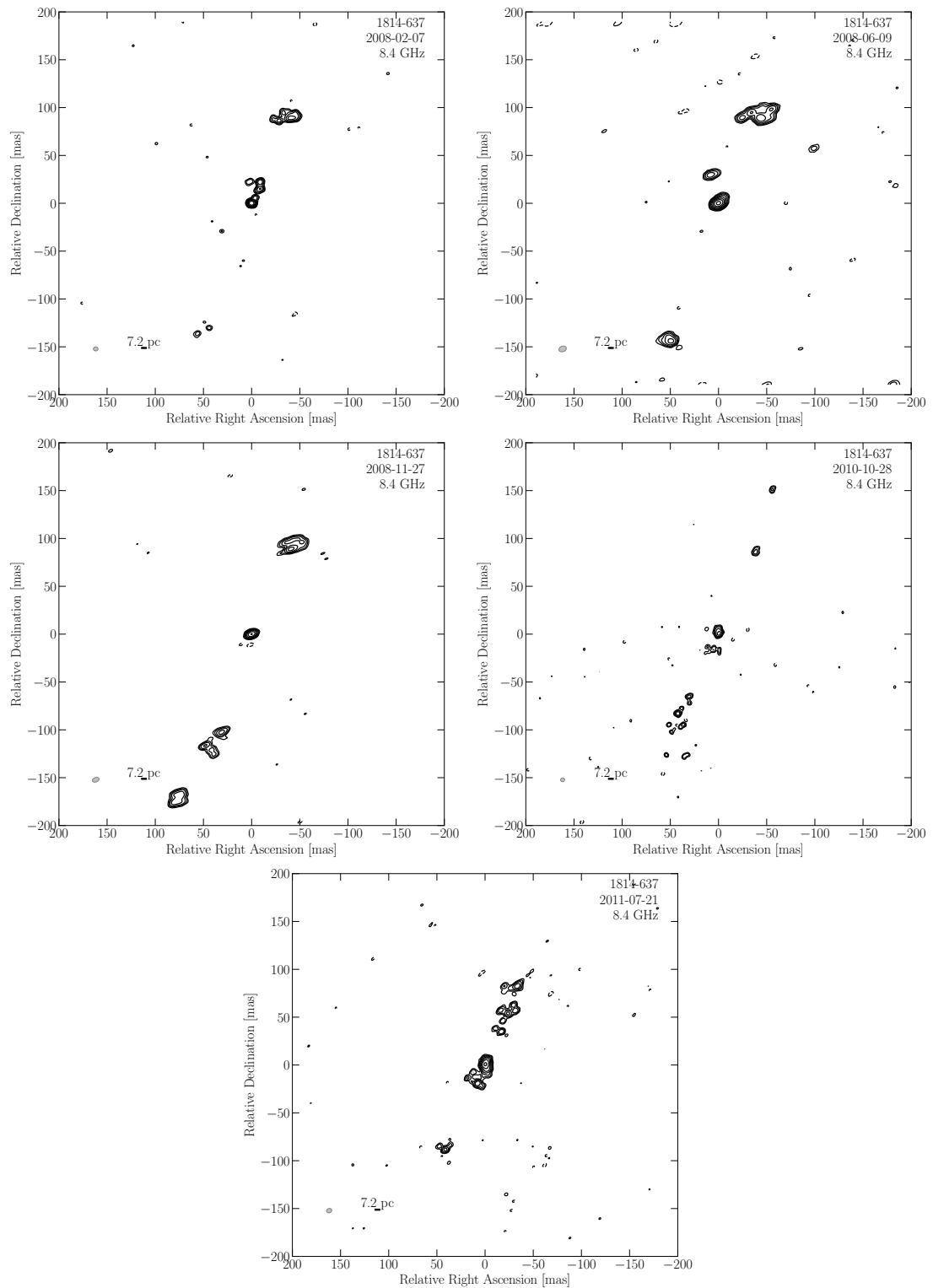


FIGURE A.18: Tapered images of PKS 1814–63. The grey ellipse represents the beam size, while the black line indicates the linear scale at the source’s redshift.

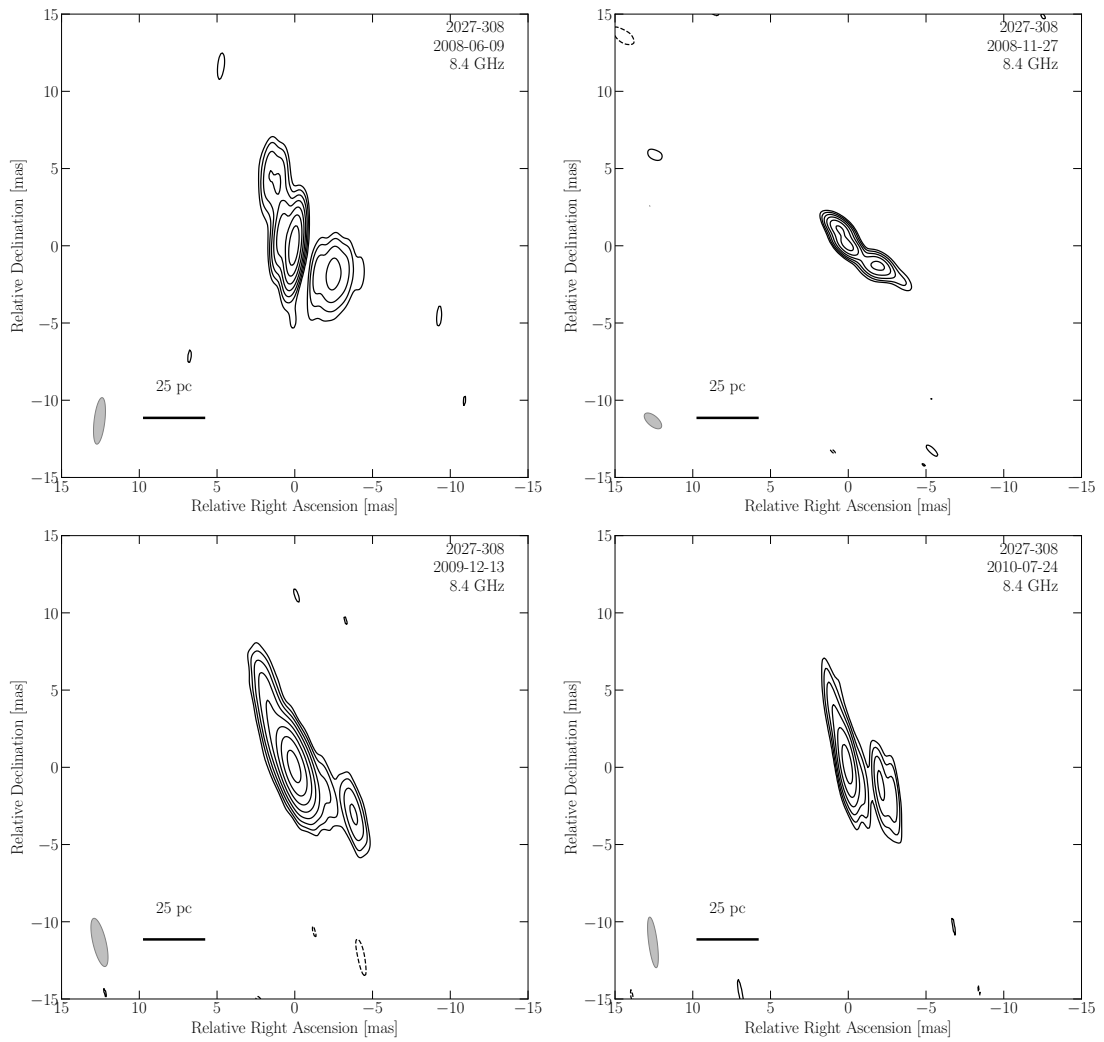


FIGURE A.19: Full-resolution images of PKS 2027–308. The map parameters for each epoch can be found in Table A.12. The grey ellipse represents the beam size, while the black line indicates the linear scale at the source’s redshift.

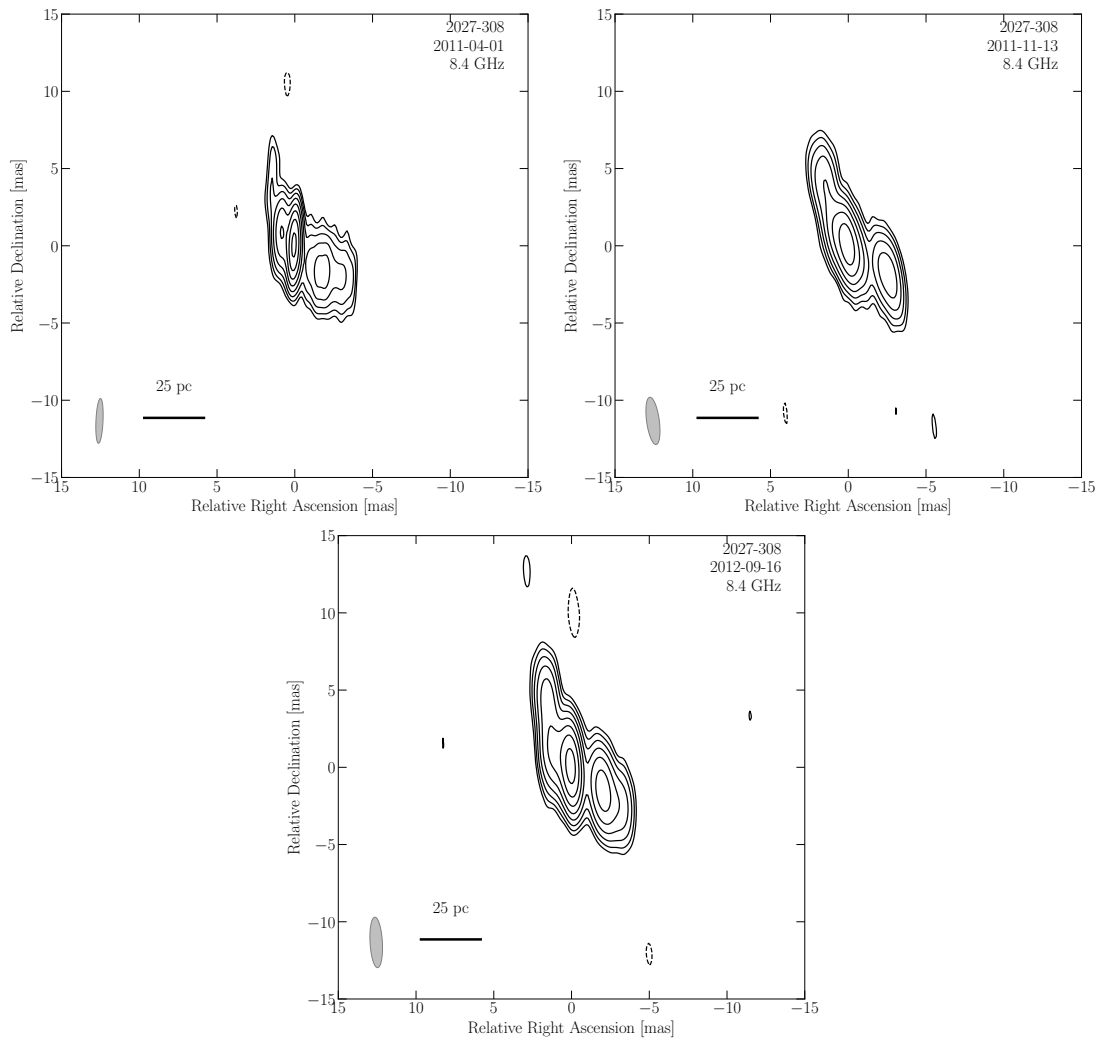


FIGURE A.20: Full-resolution images of PKS 207–308 (continued). The map parameters for each epoch can be found in Table A.12. The grey ellipse represents the beam size, while the black line indicates the linear scale at the source’s redshift.

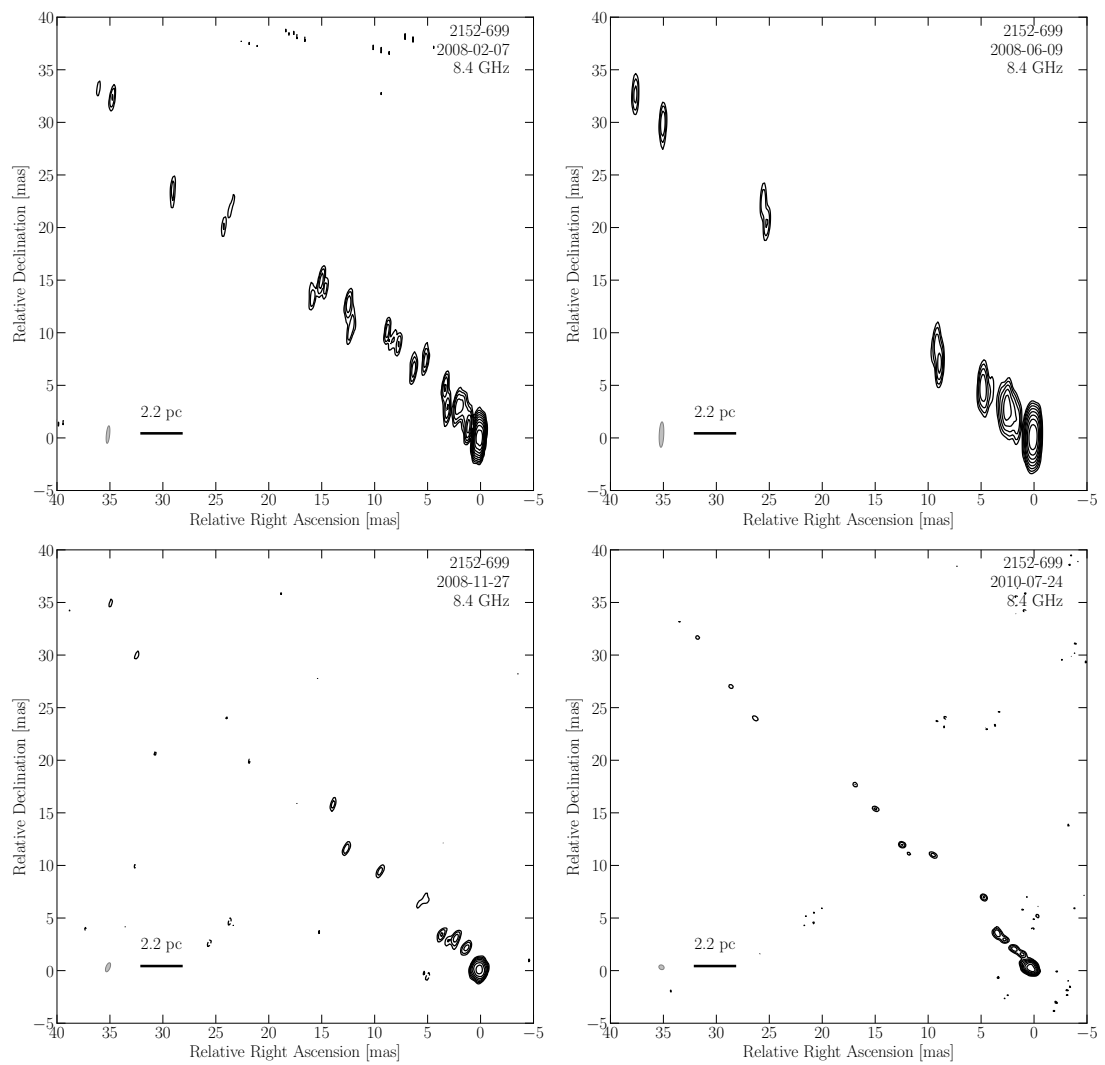


FIGURE A.21: Full-resolution images of PKS 2153–69. The map parameters for each epoch can be found in Table A.13. The grey ellipse represents the beam size, while the black line indicates the linear scale at the source’s redshift.

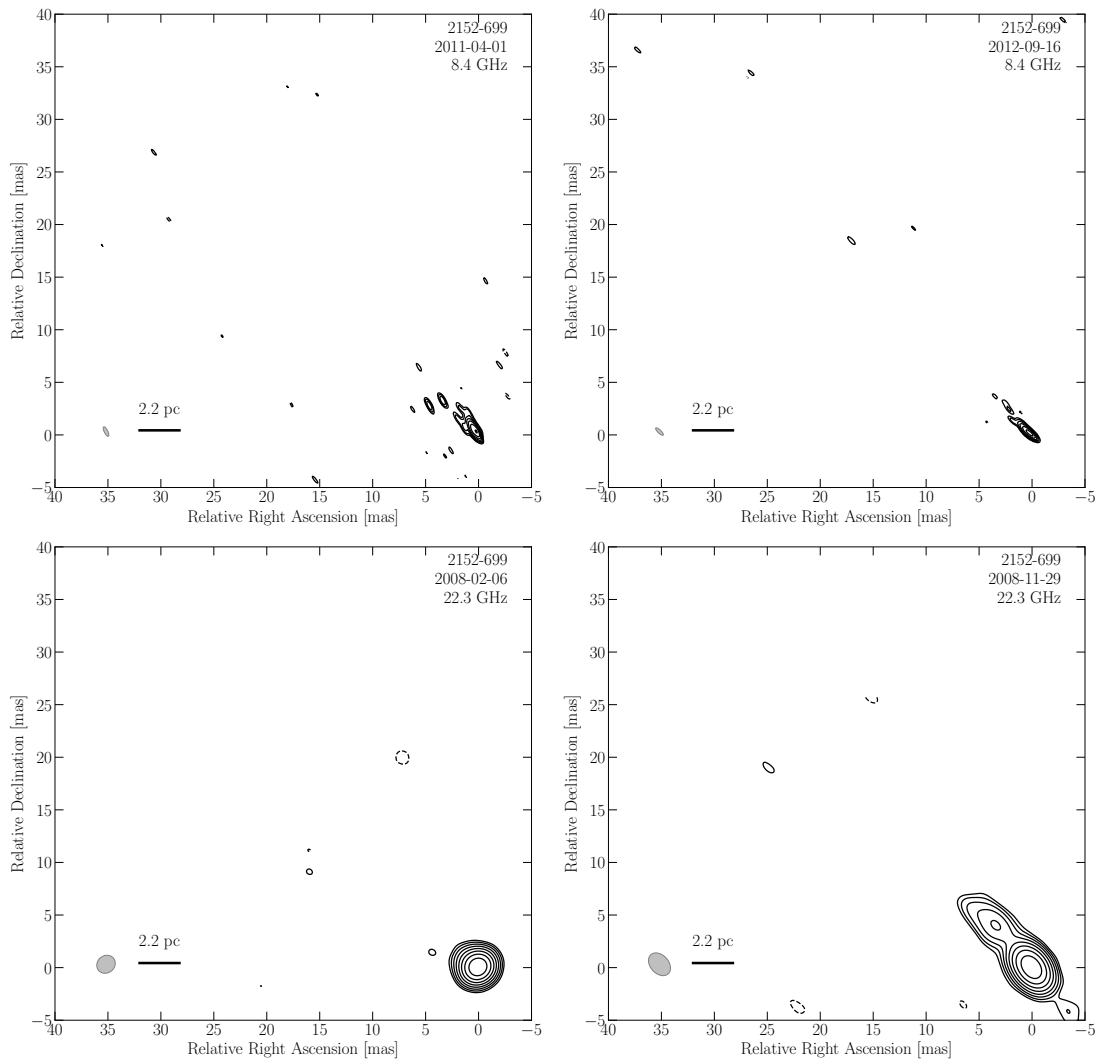


FIGURE A.22: Full-resolution images of PKS 2153–69 (continued). The map parameters for each epoch can be found in Table A.13. The grey ellipse represents the beam size, while the black line indicates the linear scale at the source’s redshift.

TABLE A.1: Details of the 8.4 GHz TANAMI observations of Pictor A

| Obs. date<br>(yyyy-mm-dd) | Array configuration <sup>a</sup> | $S_{\text{total}}^b$<br>(Jy) | $S_{\text{peak}}^b$<br>(Jy beam <sup>-1</sup> ) | RMS <sup>b</sup><br>(mJy beam <sup>-1</sup> ) | $b_{\text{maj}}^c$<br>(mas) | $b_{\text{min}}^c$<br>(mas) | P.A. <sup>c</sup><br>(°) |
|---------------------------|----------------------------------|------------------------------|---|---|-----------------------------|-----------------------------|--------------------------|
| 2007-11-10                | AT-MP-HO-HH-CD-PKS               | 0.77                         | 0.37  | 0.11  | 1.90                        | 0.57                        | 4.5                      |
| 2008-06-09                | AT-MP-HO-HH-CD-PKS               | 0.80                         | 0.48  | 0.24  | 2.62                        | 0.71                        | 5.4                      |
| 2008-11-27                | TC-OH-AT-MP-HO-CD-PKS-DSS43      | 0.75                         | 0.36  | 0.29  | 1.12                        | 0.86                        | 23.8                     |
| 2010-07-24                | TC-AT-MP-HO-CD-PKS               | 0.81                         | 0.49  | 0.30  | 3.71                        | 1.28                        | 25.2                     |
| 2011-08-14                | YG-TC-AT-MP-HO-HH-CD-PKS-DSS43   | 0.86                         | 0.58  | 0.31  | 3.13                        | 2.25                        | 68.1                     |

<sup>a</sup> AT: Australia Telescope Compact Array, CD: Ceduna, HH: Hartebeesthoek, HO: Hobart, MP: Mopra, OH: GARS/O'Higgins, PKS: Parkes, TC: TIGO, DSS43, DSS34 & DSS45: NASA's Deep Space Network Tidbinbilla (70 m, 34 m & 34 m), WW: Warkworth, YG: Yarragadee, KE: Katherine, AK : ASKAP

<sup>b</sup> Total flux density, peak flux density and RMS noise level in the CLEAN-image. An error of 15% is assumed (see Section 4)

<sup>c</sup> Major and minor axes and position angle of restoring beam.

TABLE A.2: Details of the 8.4 GHz TANAMI observations of PKS 0521–36

| Obs. date<br>(yyyy-mm-dd) | Array configuration <sup>a</sup>  | $S_{\text{total}}^b$<br>(Jy) | $S_{\text{peak}}^b$<br>(Jy beam <sup>-1</sup> ) | RMS <sup>b</sup><br>(mJy beam <sup>-1</sup> ) | $b_{\text{maj}}^c$<br>(mas) | $b_{\text{min}}^c$<br>(mas) | P.A. <sup>c</sup><br>(°) |
|---------------------------|-----------------------------------|------------------------------|---|---|-----------------------------|-----------------------------|--------------------------|
| 2007-11-10                | AT-MP-HO-HH-CD-PKS                | 1.65                         | 0.94  | 0.37  | 2.05                        | 0.488                       | 1.55                     |
| 2008-03-28                | AT-MP-HO-HH-CD-PKS-DSS43          | 1.66                         | 0.83  | 0.18  | 2.92                        | 0.526                       | -0.369                   |
| 2008-08-08                | AT-MP-HO-HH-CD-PKS-DSS45          | 1.88                         | 1.49  | 0.30  | 3.24                        | 1.43                        | -2.59                    |
| 2009-02-23                | AT-MP-HO-CD-PKS-TC-OH             | 1.59                         | 0.89  | 0.36  | 2.31                        | 0.515                       | 21.6                     |
| 2010-03-12                | AT-MP-HO-CD-PKS-DSS43             | 1.53                         | 1.32  | 0.28  | 6.07                        | 3.58                        | 84.9                     |
| 2010-07-24                | AT-MP-HO-CD-PKS-TC-DSS43          | 1.98                         | 1.34  | 0.34  | 3.16                        | 0.698                       | 14.2                     |
| 2011-04-01                | AT-MP-HO-HH-CD-PKS-DSS43-WW       | 3.07                         | 1.83  | 1.14  | 2.44                        | 0.502                       | 0.968                    |
| 2011-11-13                | AT-MP-HO-HH-CD-PKS-WW-DSS43-DSS45 | 2.77                         | 1.55  | 0.51  | 2.61                        | 0.387                       | -1.03                    |
| 2012-09-16                | AT-HO-HH-CD-PKS-DSS34-DSS45-KE-AK | 2.16                         | 1.55  | 0.88  | 2.59                        | 0.618                       | 3.63                     |

<sup>a</sup> AT: Australia Telescope Compact Array, CD: Ceduna, HH: Hartebeesthoek, HO: Hobart, MP: Mopra, OH: GARS/O'Higgins, PKS: Parkes, TC: TIGO, DSS43, DSS34 & DSS45: NASA's Deep Space Network Tidbinbilla (70 m, 34 m & 34 m), WW: Warkworth, YG: Yarragadee, KE: Katherine, AK : ASKAP

<sup>b</sup> Total flux density, peak flux density and RMS noise level in the CLEAN-image. An error of 15% is assumed (see Section 4).

<sup>c</sup> Major and minor axes and position angle of restoring beam.

TABLE A.3: Details of the 8.4 GHz TANAMI observations of PKS 0625–35

| Obs. date<br>(yyyy-mm-dd) | Array configuration <sup>a</sup>  | $S_{\text{total}}^b$<br>(Jy) | $S_{\text{peak}}^b$<br>(Jy beam <sup>-1</sup> ) | RMS <sup>b</sup><br>(mJy beam <sup>-1</sup> ) | $b_{\text{maj}}^c$<br>(mas) | $b_{\text{min}}^c$<br>(mas) | P.A. <sup>c</sup><br>(°) |
|---------------------------|-----------------------------------|------------------------------|---|---|-----------------------------|-----------------------------|--------------------------|
| 2007-11-10                | AT-MP-HO-HH-CD-PKS                | 0.35                         | 0.30  | 0.08  | 3.64                        | 3.08                        | 62.6                     |
| 2008-02-07                | AT-MP-HO-CD-PKS                   | 0.46                         | 0.37  | 0.07  | 4.41                        | 3.32                        | -68.4                    |
| 2008-06-09                | AT-MP-HO-HH-CD-PKS                | 0.35                         | 0.31  | 0.07  | 3.68                        | 2.77                        | -85.0                    |
| 2008-11-27                | TC-OH-AT-MP-HO-CD-PKS-DSS43       | 0.37                         | 0.34  | 0.15  | 4.55                        | 3.43                        | 77.0                     |
| 2009-12-14                | AT-MP-HO-CD-TC                    | 0.34                         | 0.31  | 0.10  | 3.56                        | 3.06                        | -19.8                    |
| 2010-07-24                | TC-AT-MP-HO-CD-PKS                | 0.34                         | 0.31  | 0.11  | 6.2                         | 3.86                        | 74.2                     |
| 2011-04-01                | AT-MP-HO-HH-CD-PKS-DSS43-WW       | 0.40                         | 0.34  | 0.16  | 4.22                        | 3.07                        | 82.5                     |
| 2011-11-13                | AT-MP-HO-HH-CD-PKS-WW-DSS43-DSS45 | 0.37                         | 0.34  | 0.12  | 5.39                        | 3.61                        | 84.6                     |
| 2012-09-16                | AT-HO-HH-CD-PKS-DSS34-DSS45-KE    | 0.38                         | 0.34  | 0.10  | 4.29                        | 3.02                        | 84.6                     |

<sup>a</sup> AT: Australia Telescope Compact Array, CD: Ceduna, HH: Hartebeesthoek, HO: Hobart, MP: Mopra, OH: GARS/O'Higgins, PKS: Parkes, TC: TIGO, DSS43, DSS34 & DSS45: NASA's Deep Space Network Tidbinbilla (70 m, 34 m & 34 m), WW: Warkworth, YG: Yarragadee, KE: Katherine, AK : ASKAP

<sup>b</sup> Total flux density, peak flux density and RMS noise level in the CLEAN-image. An error of 15% is assumed (see Section 4).

<sup>c</sup> Major and minor axes and position angle of restoring beam.

TABLE A.4: Details of the 8.4 GHz TANAMI observations of PKS 0823–500

| Obs. date<br>(yyyy-mm-dd) | Array configuration <sup>a</sup> | $S_{\text{total}}^b$<br>(Jy) | $S_{\text{peak}}^b$<br>(Jy beam <sup>-1</sup> ) | RMS <sup>b</sup><br>(mJy beam <sup>-1</sup> ) | $b_{\text{maj}}^c$<br>(mas) | $b_{\text{min}}^c$<br>(mas) | P.A. <sup>c</sup><br>(°) |
|---------------------------|----------------------------------|------------------------------|---|---|-----------------------------|-----------------------------|--------------------------|
| 2013-03-14                | AT-HO-CD-PKS-KE-WW-DSS34-DSS45   | 0.95                         | 0.18  | 1.3   | 2.03                        | 0.81                        | 35                       |

<sup>a</sup> AT: Australia Telescope Compact Array, CD: Ceduna, HH: Hartebeesthoek, HO: Hobart, MP: Mopra, OH: GARS/O’Higgins, PKS: Parkes, TC: TIGO, DSS43, DSS34 & DSS45: NASA’s Deep Space Network Tidbinbilla (70 m, 34 m & 34 m), WW: Warkworth, YG: Yarragadee, KE: Katherine, AK : ASKAP

<sup>b</sup> Total flux density, peak flux density and RMS noise level in the CLEAN-image. An error of 15% is assumed (see Section 4).

<sup>c</sup> Major and minor axes and position angle of restoring beam.

TABLE A.5: Details of the 8.4 GHz TANAMI observations of PKS 1258–321

| Obs. date<br>(yyyy-mm-dd) | Array configuration <sup>a</sup>  | $S_{\text{total}}^b$<br>(Jy) | $S_{\text{peak}}^b$<br>(Jy beam <sup>-1</sup> ) | RMS <sup>b</sup><br>(mJy beam <sup>-1</sup> ) | $b_{\text{maj}}^c$<br>(mas) | $b_{\text{min}}^c$<br>(mas) | P.A. <sup>c</sup><br>(°) |
|---------------------------|-----------------------------------|------------------------------|---|---|-----------------------------|-----------------------------|--------------------------|
| 2009-12-13                | AT-MP-HO-CD-TC                    | 0.13                         | 0.12  | 0.09  | 6.89                        | 2.87                        | –89.3                    |
| 2010-05-08                | AT-MP-HO-CD-PKS-TC-DSS43          | 0.10                         | 0.09  | 0.08  | 3.94                        | 3.55                        | –75.9                    |
| 2011-11-13                | AT-MP-HO-HH-CD-PKS-WW-DSS43-DSS45 | 0.13                         | 0.12  | 0.14  | 4.57                        | 3.04                        | 84                       |
| 2012-04-27                | AT-MP-HO-CD-PKS                   | 0.13                         | 0.12  | 0.18  | 3.73                        | 3.17                        | 46                       |
| 2013-03-14                | AT-HO-CD-PKS-KE-WW-DSS34-DSS45    | 0.15                         | 0.14  | 0.15  | 4.11                        | 3.98                        | 38                       |

<sup>a</sup> AT: Australia Telescope Compact Array, CD: Ceduna, HH: Hartebeesthoek, HO: Hobart, MP: Mopra, OH: GARS/O’Higgins, PKS: Parkes, TC: TIGO, DSS43, DSS34 & DSS45: NASA’s Deep Space Network Tidbinbilla (70 m, 34 m & 34 m), WW: Warkworth, YG: Yarragadee, KE: Katherine, AK : ASKAP

<sup>b</sup> Total flux density, peak flux density and RMS noise level in the CLEAN-image. An error of 15% is assumed (see Section 4)

<sup>c</sup> Major and minor axes and position angle of restoring beam.

TABLE A.6: Details of the 8.4 GHz TANAMI observations of IC 4296

| Obs. date<br>(yyyy-mm-dd) | Array configuration <sup>a</sup> | $S_{\text{total}}^b$<br>(Jy) | $S_{\text{peak}}^b$<br>(Jy beam <sup>-1</sup> ) | RMS <sup>b</sup><br>(mJy beam <sup>-1</sup> ) | $b_{\text{maj}}^c$<br>(mas) | $b_{\text{min}}^c$<br>(mas) | P.A. <sup>c</sup><br>(°) |
|---------------------------|----------------------------------|------------------------------|---|---|-----------------------------|-----------------------------|--------------------------|
| 2008-02-07                | AT-MP-HO-HH-CD-PKS               | 0.21                         | 0.15  | 0.044   | 3.81                        | 1.06                        | –7.8                     |
| 2008-06-09                | AT-MP-HO-CD-PKS                  | 0.22                         | 0.19  | 0.045   | 3.94                        | 3.26                        | –82.9                    |
| 2008-11-27                | OH-AT-MP-HO-CD-PKS-DSS43         | 0.23                         | 0.20  | 0.12  | 4.08                        | 1.96                        | –61.5                    |
| 2010-07-24                | AT-MP-HO-CD-PKS                  | 0.23                         | 0.20  | 0.051   | 4.98                        | 3.52                        | 76.6                     |
| 2011-11-13                | AT-MP-HO-HH-CD-PKS-WW-TC         | 0.12                         | 0.037   | 0.30  | 1.72                        | 0.448                       | 3.2                      |

<sup>a</sup> AT: Australia Telescope Compact Array, CD: Ceduna, HH: Hartebeesthoek, HO: Hobart, MP: Mopra, OH: GARS/O’Higgins, PKS: Parkes, TC: TIGO, DSS43, DSS34 & DSS45: NASA’s Deep Space Network Tidbinbilla (70 m, 34 m & 34 m), WW: Warkworth, YG: Yarragadee, KE: Katherine, AK : ASKAP

<sup>b</sup> Total flux density, peak flux density and RMS noise level in the CLEAN-image. An error of 15% is assumed (see Section 4)

<sup>c</sup> Major and minor axes and position angle of restoring beam.

TABLE A.7: Details of the 8.4 GHz TANAMI observations of Centaurus B.

| Obs. date<br>(yyyy-mm-dd) | Array configuration <sup>a</sup> | $S_{\text{total}}^b$<br>(Jy) | $S_{\text{peak}}^b$<br>(Jy beam <sup>-1</sup> ) | RMS <sup>b</sup><br>(mJy beam <sup>-1</sup> ) | $b_{\text{maj}}^c$<br>(mas) | $b_{\text{min}}^c$<br>(mas) | P.A. <sup>c</sup><br>(°) |
|---------------------------|----------------------------------|------------------------------|---|---|-----------------------------|-----------------------------|--------------------------|
| 2011-07-22                | AT-MP-HO-HH-CD-PKS-DSS43-DSS34   | 2.35                         | 0.96  | 0.73  | 3.85                        | 2.85                        | 72.9                     |
| 2012-04-27                | AT-MP-HO-CD-PKS                  | 2.09                         | 0.77  | 0.46  | 3.73                        | 2.85                        | 80.3                     |

<sup>a</sup> AT: Australia Telescope Compact Array, CD: Ceduna, HH: Hartebeesthoek, HO: Hobart, MP: Mopra, OH: GARS/O’Higgins, PKS: Parkes, TC: TIGO, DSS43, DSS34 & DSS45: NASA’s Deep Space Network Tidbinbilla (70 m, 34 m & 34 m), WW: Warkworth, YG: Yarragadee, KE: Katherine, AK : ASKAP

<sup>b</sup> Total flux density, peak flux density and RMS noise level in the CLEAN-image. An error of 15% is assumed (see Section 4).

<sup>c</sup> Major and minor axes and position angle of restoring beam.

TABLE A.8: Details of the 8.4 GHz TANAMI observations of PKS 1549–790.

| Obs. date<br>(yyyy-mm-dd) | Array configuration <sup>a</sup> | $S_{\text{total}}^b$<br>(Jy) | $S_{\text{peak}}^b$<br>(Jy beam <sup>-1</sup> ) | RMS <sup>b</sup><br>(mJy beam <sup>-1</sup> ) | $b_{\text{maj}}^c$<br>(mas) | $b_{\text{min}}^c$<br>(mas) | P.A. <sup>c</sup><br>(°) |
|---------------------------|----------------------------------|------------------------------|---|---|-----------------------------|-----------------------------|--------------------------|
| 2008-02-07                | AT-MP-HO-CD-PKS                  | 1.75                         | 0.15  | 0.90  | 1.07                        | 0.38                        | 5.6                      |
| 2008-06-09                | AT-MP-HO-HH-CD-PKS               | 1.00                         | 0.32  | 1.13  | 3.06                        | 0.65                        | -20.2                    |
| 2008-11-27                | TC-OH-AT-MP-HO-CD-PKS-DSS43      | 0.69                         | 0.12  | 1.15  | 0.67                        | 0.38                        | 85.1                     |
| 2009-12-13                | AT-MP-HO-CD-TC                   | 0.80                         | 0.12  | 2.35  | 0.57                        | 0.34                        | 31.6                     |
| 2012-09-17                | AT-HO-HH-CD-PKS-DSS34-DSS45-KE   | 0.60                         | 0.08  | 0.87  | 1.01                        | 0.43                        | 6.4                      |

<sup>a</sup> AT: Australia Telescope Compact Array, CD: Ceduna, HH: Hartebeesthoek, HO: Hobart, MP: Mopra, OH: GARS/O’Higgins, PKS: Parkes, TC: TIGO, DSS43, DSS34 & DSS45: NASA’s Deep Space Network Tidbinbilla (70 m, 34 m & 34 m), WW: Warkworth, YG: Yarragadee, KE: Katherine, AK : ASKAP

<sup>b</sup> Total flux density, peak flux density and RMS noise level in the CLEAN-image. An error of 15% is assumed (see Section 4).

<sup>c</sup> Major and minor axes and position angle of restoring beam.

TABLE A.9: Details of the 8.4 GHz TANAMI observations of PKS 1718–649

| Obs. date<br>(yyyy-mm-dd) | Array configuration <sup>a</sup> | $S_{\text{total}}^b$<br>(Jy) | $S_{\text{peak}}^b$<br>(Jy beam <sup>-1</sup> ) | RMS <sup>b</sup><br>(mJy beam <sup>-1</sup> ) | $b_{\text{maj}}^c$<br>(mas) | $b_{\text{min}}^c$<br>(mas) | P.A. <sup>c</sup><br>(°) |
|---------------------------|----------------------------------|------------------------------|---|---|-----------------------------|-----------------------------|--------------------------|
| 2008-02-07                | AT-MP-HO-CD-PKS                  | 3.9                          | 1.13  | 1.12  | 1.94                        | 0.45                        | -10.2                    |
| 2008-06-09                | AT-MP-HO-HH-CD-PKS               | 3.26                         | 1.64  | 1.80  | 3.08                        | 1.23                        | 6.8                      |
| 2008-11-27                | TC-OH-AT-MP-HO-CD-PKS-DSS43      | 2.67                         | 0.63  | 0.79  | 0.74                        | 0.46                        | -47.9                    |
| 2009-12-13                | AT-MP-HO-CD-TC                   | 3.08                         | 1.44  | 1.78  | 1.15                        | 0.82                        | 12.4                     |
| 2010-07-24                | TC-AT-MP-HO-CD-PKS               | 2.33                         | 1.03  | 1.11  | 1.07                        | 0.65                        | 23.4                     |
| 2011-04-01                | AT-MP-HO-HH-CD-PKS-DSS43-WW      | 3.00                         | 0.61  | 0.57  | 1.03                        | 0.36                        | 8.5                      |
| 2011-08-14                | AT-MP-HO-CD-PKS-TC-DSS43-YG      | 3.36                         | 1.31  | 1.70  | 1.85                        | 1.51                        | 52.6                     |

<sup>a</sup> AT: Australia Telescope Compact Array, CD: Ceduna, HH: Hartebeesthoek, HO: Hobart, MP: Mopra, OH: GARS/O’Higgins, PKS: Parkes, TC: TIGO, DSS43, DSS34 & DSS45: NASA’s Deep Space Network Tidbinbilla (70 m, 34 m & 34 m), WW: Warkworth, YG: Yarragadee, KE: Katherine, AK : ASKAP

<sup>b</sup> Total flux density, peak flux density and RMS noise level in the CLEAN-image. An error of 15% is assumed (see Section 4).

<sup>c</sup> Major and minor axes and position angle of restoring beam.

TABLE A.10: Details of the 8.4 GHz TANAMI observations of PKS 1733–565

| Obs. date<br>(yyyy-mm-dd) | Array configuration <sup>a</sup>  | $S_{\text{total}}^b$<br>(Jy) | $S_{\text{peak}}^b$<br>(Jy beam <sup>-1</sup> ) | RMS <sup>b</sup><br>(mJy beam <sup>-1</sup> ) | $b_{\text{maj}}^c$<br>(mas) | $b_{\text{min}}^c$<br>(mas) | P.A. <sup>c</sup><br>(°) |
|---------------------------|-----------------------------------|------------------------------|---|---|-----------------------------|-----------------------------|--------------------------|
| 2008-02-07                | AT-MP-HO-CD-PKS                   | 0.18                         | 0.16  | 0.06  | 2.62                        | 0.77                        | -4.3                     |
| 2008-03-28                | AT-MP-HO-HH-CD-PKS-DSS43          | 0.19                         | 0.16  | 0.04  | 2.95                        | 0.76                        | 1.1                      |
| 2008-08-08                | AT-MP-HO-HH-CD-PKS-DSS45          | 0.19                         | 0.17  | 0.08  | 3.64                        | 1.19                        | 13.3                     |
| 2009-02-23                | AT-MP-HO-CD-PKS-TC-OH             | 0.16                         | 0.12  | 0.12  | 2.7                         | 1.05                        | 46.8                     |
| 2010-03-12                | AT-MP-HO-CD-PKS-DSS43             | 0.10                         | 0.10  | 0.07  | 4.28                        | 3.46                        | 88.5                     |
| 2010-10-29                | AT-MP-HO-CD-PKS-DSS34-DSS45-TC-HH | 0.15                         | 0.12  | 0.05  | 2.49                        | 0.62                        | -2.4                     |
| 2011-07-22                | AT-MP-HO-HH-CD-PKS-DSS43-DSS34    | 0.12                         | 0.10  | 0.03  | 2.71                        | 0.72                        | 2.5                      |
| 2012-04-27                | AT-MP-HO-CD-PKS                   | 0.07                         | 0.07  | 0.06  | 2.29                        | 0.62                        | 1.2                      |

<sup>a</sup> AT: Australia Telescope Compact Array, CD: Ceduna, HH: Hartebeesthoek, HO: Hobart, MP: Mopra, OH: GARS/O’Higgins, PKS: Parkes, TC: TIGO, DSS43, DSS34 & DSS45: NASA’s Deep Space Network Tidbinbilla (70 m, 34 m & 34 m), WW: Warkworth, YG: Yarragadee, KE: Katherine, AK : ASKAP

<sup>b</sup> Total flux density, peak flux density and RMS noise level in the CLEAN-image. An error of 15% is assumed (see Section 4).

<sup>c</sup> Major and minor axes and position angle of restoring beam.

TABLE A.11: Details of the 8.4 GHz TANAMI observations of PKS 1814–63

| Obs. date<br>(yyyy-mm-dd) | Array configuration <sup>a</sup>  | $S_{\text{total}}^b$<br>(Jy) | $S_{\text{peak}}^b$<br>(Jy beam <sup>-1</sup> ) | RMS <sup>b</sup><br>(mJy beam <sup>-1</sup> ) | $b_{\text{maj}}^c$<br>(mas) | $b_{\text{min}}^c$<br>(mas) | P.A. <sup>c</sup><br>(°) |
|---------------------------|-----------------------------------|------------------------------|---|---|-----------------------------|-----------------------------|--------------------------|
| 2008-02-07                | AT-MP-HO-CD-PKS                   | 0.60                         | 0.41  | 2.07  | 1.84                        | 0.58                        | 2.8                      |
| 2008-06-09                | AT-MP-HO-HH-CD-PKS                | 0.63                         | 0.52  | 5.00  | 4.14                        | 3.18                        | 71.4                     |
| 2008-11-27                | TC-OH-AT-MP-HO-CD-PKS-DSS43       | 0.77                         | 0.25  | 1.85  | 1.44                        | 0.63                        | -55.2                    |
| 2010-10-29                | AT-MP-HO-CD-PKS-DSS34-DSS45-TC-HH | 0.44                         | 0.10  | 0.97  | 2.09                        | 0.65                        | 0.2                      |
| 2011-07-22                | AT-MP-HO-HH-CD-PKS-DSS43-DSS34    | 0.39                         | 0.12  | 4.92  | 1.99                        | 1.58                        | 78.9                     |

<sup>a</sup> AT: Australia Telescope Compact Array, CD: Ceduna, HH: Hartebeesthoek, HO: Hobart, MP: Mopra, OH: GARS/O’Higgins, PKS: Parkes, TC: TIGO, DSS43, DSS34 & DSS45: NASA’s Deep Space Network Tidbinbilla (70 m, 34 m & 34 m), WW: Warkworth, YG: Yarragadee, KE: Katherine, AK : ASKAP

<sup>b</sup> Total flux density, peak flux density and RMS noise level in the CLEAN-image. An error of 15% is assumed (see Section 4).

<sup>c</sup> Major and minor axes and position angle of restoring beam.

TABLE A.12: Details of the 8.4 GHz TANAMI observations of PKS 2027–308

| Obs. date<br>(yyyy-mm-dd) | Array configuration <sup>a</sup> | $S_{\text{total}}^b$<br>(Jy) | $S_{\text{peak}}^b$<br>(Jy beam <sup>-1</sup> ) | RMS <sup>b</sup><br>(mJy beam <sup>-1</sup> ) | $b_{\text{maj}}^c$<br>(mas) | $b_{\text{min}}^c$<br>(mas) | P.A. <sup>c</sup><br>(°) |
|---------------------------|----------------------------------|------------------------------|---|---|-----------------------------|-----------------------------|--------------------------|
| 2008-06-09                | AT-MP-HO-HH-CD-PKS               | 0.12                         | 0.08  | 0.15  | 3.03                        | 0.69                        | -6.6                     |
| 2008-11-28                | TC-OH-AT-MP-HO-CD-PKS-DSS43      | 0.10                         | 0.04  | 0.26  | 1.37                        | 0.67                        | 49.2                     |
| 2009-12-14                | AT-MP-HO-CD-TC                   | 0.11                         | 0.07  | 0.08  | 3.2                         | 0.84                        | 13.3                     |
| 2010-07-24                | TC-AT-MP-HO-CD-PKS               | 0.10                         | 0.05  | 0.23  | 3.3                         | 0.55                        | 7.4                      |
| 2011-04-01                | AT-MP-HO-HH-CD-PKS-DSS43-WW      | 0.12                         | 0.05  | 0.09  | 2.9                         | 0.45                        | -2.5                     |
| 2011-11-14                | AT-MP-HO-HH-CD-PKS-WW-TC         | 0.09                         | 0.05  | 0.09  | 3.09                        | 0.82                        | 7.62                     |
| 2012-09-17                | AT-HO-HH-CD-PKS-DSS34-DSS45-KE   | 0.10                         | 0.05  | 0.05  | 3.27                        | 0.79                        | 3.14                     |

<sup>a</sup> AT: Australia Telescope Compact Array, CD: Ceduna, HH: Hartebeesthoek, HO: Hobart, MP: Mopra, OH: GARS/O’Higgins, PKS: Parkes, TC: TIGO, DSS43, DSS34 & DSS45: NASA’s Deep Space Network Tidbinbilla (70 m, 34 m & 34 m), WW: Warkworth, YG: Yarragadee, KE: Katherine, AK : ASKAP

<sup>b</sup> Total flux density, peak flux density and RMS noise level in the CLEAN-image. An error of 15% is assumed (see Section 4).

<sup>c</sup> Major and minor axes and position angle of restoring beam.

TABLE A.13: Details of the 8.4 GHz TANAMI observations of PKS 2153–69

| Obs. date<br>(yyyy-mm-dd) | Array configuration <sup>a</sup> | $S_{\text{total}}^b$<br>(Jy) | $S_{\text{peak}}^b$<br>(Jy beam <sup>-1</sup> ) | RMS <sup>b</sup><br>(mJy beam <sup>-1</sup> ) | $b_{\text{maj}}^c$<br>(mas) | $b_{\text{min}}^c$<br>(mas) | P.A. <sup>c</sup><br>(°) |
|---------------------------|----------------------------------|------------------------------|---|---|-----------------------------|-----------------------------|--------------------------|
| 2008-02-08                | AT-MP-HO-CD-PKS                  | 0.48                         | 0.21  | 0.25  | 1.67                        | 0.31                        | -5.8                     |
| 2008-06-09                | AT-MP-HO-HH-CD-PKS               | 0.64                         | 0.27  | 0.25  | 2.42                        | 0.43                        | -2.5                     |
| 2008-11-27                | TC-OH-AT-MP-HO-CD-PKS-DSS43      | 0.42                         | 0.20  | 0.51  | 0.91                        | 0.38                        | -21.5                    |
| 2010-07-24                | TC-AT-MP-HO-CD-PKS               | 0.32                         | 0.20  | 0.63  | 0.518                       | 0.42                        | 59.0                     |
| 2011-04-01                | AT-MP-HO-HH-CD-PKS-DSS43-WW      | 0.54                         | 0.24  | 0.94  | 0.99                        | 0.33                        | 26.3                     |
| 2012-09-16                | AT-HO-HH-CD-PKS-DSS34-DSS45-KE   | 0.52                         | 0.25  | 1.20  | 0.97                        | 0.31                        | 45.7                     |

<sup>a</sup> AT: Australia Telescope Compact Array, CD: Ceduna, HH: Hartebeesthoek, HO: Hobart, MP: Mopra, OH: GARS/O’Higgins, PKS: Parkes, TC: TIGO, DSS43, DSS34 & DSS45: NASA’s Deep Space Network Tidbinbilla (70 m, 34 m & 34 m), WW: Warkworth, YG: Yarragadee, KE: Katherine, AK : ASKAP

<sup>b</sup> Total flux density, peak flux density and RMS noise level in the CLEAN-image. An error of 15% is assumed (see Section 4).

<sup>c</sup> Major and minor axes and position angle of restoring beam.

## Appendix B

# Modelfit component parameters

Here we report the `Modelfit` parameters of the Gaussian components used for the kinematic analysis presented in Section 5.4. Tables B.1 through B.11 list the flux density, radial distance, position angle and size for each component identified in each source during the kinematic analysis. The position angle is given in the range  $(\pi, -\pi)$ , with the zero in the N-S direction (in image coordinates) and positive values in the counter-clockwise direction. Components that were not identified (blue crossed circles in Figures 5.12 through 5.21) are not listed. Note that an apparent speed was fitted only for components detected in at least five epochs.

TABLE B.1: Difmap Modelfit parameters for the Gaussian components model of the TANAMI 8.4 GHz images of Pictor A.

| Epoch      | ID   | $S^a$ (Jy) | $d^b$ (mas) | $\phi^c$ (deg) | Size (mas) |
|------------|------|------------|-------------|----------------|------------|
| 2007-11-11 | Core | 0.538      | 0.00        | -56.87         | 0.24       |
|            | CJ1  | 0.085      | 1.50        | 96.06          | 0.27       |
|            | J1   | 0.122      | 3.17        | -78.93         | 0.48       |
|            | J2   | 0.006      | 6.30        | -86.63         | 0.66       |
|            | J3   | 0.004      | 8.95        | -77.84         | 0.03       |
|            | J4   | 0.012      | 12.52       | -73.40         | 0.20       |
| 2008-06-10 | Core | 0.588      | 0.00        | 145.94         | 0.09       |
|            | CJ1  | 0.052      | 1.61        | 96.84          | 0.05       |
|            | J1   | 0.115      | 3.13        | -76.97         | 0.52       |
|            | J2   | 0.021      | 8.12        | -74.94         | 0.06       |
|            | J3   | 0.018      | 11.26       | -66.96         | 0.13       |
|            | J4   | 0.013      | 15.64       | -72.87         | 0.09       |
| 2008-11-28 | Core | 0.557      | 0.00        | 51.34          | 0.24       |
|            | CJ1  | 0.080      | 1.75        | 98.34          | 0.45       |
|            | J1   | 0.097      | 3.04        | -70.88         | 0.24       |
|            | J2   | 0.030      | 7.83        | -66.70         | 0.11       |
|            | J3   | 0.021      | 11.39       | -72.74         | 0.21       |
|            | J4   | 0.013      | 15.64       | -72.87         | 0.09       |
| 2010-07-26 | Core | 0.579      | 0.00        | -64.70         | 0.34       |
|            | CJ1  | 0.072      | 1.62        | 90.37          | 0.26       |
|            | J1   | 0.091      | 3.30        | -76.47         | 0.45       |
|            | J2   | 0.031      | 8.54        | -79.30         | 0.41       |
|            | J3   | 0.027      | 12.65       | -75.67         | 0.65       |
|            | J4   | 0.025      | 19.43       | -85.40         | 0.56       |
| 2011-08-14 | Core | 0.478      | 0.00        | -16.23         | 0.10       |
|            | CJ1  | 0.083      | 1.95        | 98.73          | 0.51       |
|            | J1   | 0.051      | 4.24        | -77.55         | 0.45       |
|            | J2   | 0.036      | 10.48       | -77.11         | 1.85       |
|            | J3   | 0.027      | 12.65       | -75.67         | 0.65       |
|            | J4   | 0.025      | 19.43       | -85.40         | 0.56       |

<sup>a</sup> Flux density.

<sup>b</sup> Radial distance from the core.

<sup>c</sup> Position angle.

TABLE B.2: Difmap Modelfit parameters for the Gaussian components model of the TANAMI 8.4 GHz images of PKS 0521–36.

| Epoch      | ID         | $S^a$ (Jy) | $d^b$ (mas) | $\phi^c$ (deg) | Size (mas) |      |
|------------|------------|------------|-------------|----------------|------------|------|
| 2007-11-11 | Core       | 1.184      | 0.00        | 158.21         | 0.08       |      |
|            | J1         | 0.144      | 2.73        | -47.11         | 0.11       |      |
|            | J2         | 0.045      | 9.70        | -42.68         | 1.09       |      |
|            | J4         | 0.125      | 28.55       | -46.62         | 2.62       |      |
|            | J5         | 0.059      | 41.27       | -47.40         | 1.68       |      |
|            | J6         | 0.016      | 69.20       | -42.65         | 8.64       |      |
| 2008-03-30 | Core       | 1.096      | 0.00        | -53.33         | 0.06       |      |
|            | J1         | 0.181      | 3.52        | -51.41         | 1.27       |      |
|            | J2         | 0.027      | 9.53        | -45.37         | 0.15       |      |
|            | J3         | 0.036      | 19.40       | -47.81         | 1.04       |      |
|            | J4         | 0.171      | 31.03       | -45.71         | 1.89       |      |
|            | J5         | 0.024      | 45.04       | -45.01         | 1.16       |      |
| 2008-08-09 | J6         | 0.011      | 72.54       | -42.80         | 0.30       |      |
|            | Core       | 1.532      | 0.00        | 44.63          | 0.06       |      |
|            | J1         | 0.084      | 2.93        | -48.61         | 0.19       |      |
|            | J2         | 0.067      | 10.32       | -45.93         | 1.24       |      |
|            | J3         | 0.020      | 22.71       | -40.73         | 0.69       |      |
|            | J4         | 0.102      | 30.64       | -46.14         | 3.04       |      |
| 2008-08-09 | J5         | 0.031      | 42.60       | -45.89         | 3.25       |      |
|            | J6         | 0.003      | 66.73       | -43.93         | 4.70       |      |
|            | 2009-02-23 | Core       | 1.206       | 0.00           | -169.52    | 0.06 |
|            |            | J1         | 0.145       | 3.15           | -49.35     | 0.26 |
|            |            | J2         | 0.011       | 13.21          | -44.76     | 1.94 |
|            |            | J3         | 0.013       | 20.09          | -51.59     | 0.69 |
| J4         |            | 0.100      | 31.07       | -47.81         | 1.86       |      |
| J5         |            | 0.087      | 44.38       | -44.70         | 2.75       |      |
| 2009-02-23 | J6         | 0.016      | 66.46       | -46.96         | 7.81       |      |
|            | 2010-03-14 | Core       | 1.228       | 0.00           | -109.34    | 0.08 |
|            |            | J1         | 0.171       | 2.31           | -55.09     | 0.31 |
|            |            | J2         | 0.036       | 10.70          | -50.38     | 2.25 |
|            |            | J4         | 0.016       | 27.71          | -45.24     | 0.89 |
|            |            | J5         | 0.064       | 37.39          | -46.50     | 5.25 |
| J6         |            | 0.013      | 63.28       | -46.62         | 1.32       |      |
| 2010-03-14 | 2010-07-26 | Core       | 1.718       | 0.00           | 35.86      | 0.04 |
|            |            | J1         | 0.068       | 3.06           | -48.92     | 0.54 |
|            |            | J2         | 0.043       | 10.03          | -47.08     | 0.63 |
|            |            | J4         | 0.028       | 28.00          | -43.29     | 1.73 |
|            |            | J5         | 0.055       | 39.33          | -46.91     | 4.86 |
|            |            | J6         | 0.012       | 64.43          | -46.27     | 0.80 |

<sup>a</sup> Flux density.<sup>b</sup> Radial distance from the core.<sup>c</sup> Position angle.

TABLE B.3: Difmap Modelfit parameters for the Gaussian components model of the TANAMI 8.4 GHz images of PKS 0521–36 (continued).

| Epoch      | ID   | $S^a$ (Jy) | $d^b$ (mas) | $\phi^c$ (deg) | Size (mas) |
|------------|------|------------|-------------|----------------|------------|
| 2011-04-03 | Core | 2.470      | 0.00        | -60.52         | 0.06       |
|            | J1   | 0.226      | 1.51        | -37.52         | 0.15       |
|            | J2   | 0.027      | 8.56        | -55.91         | 0.45       |
|            | J3   | 0.028      | 18.39       | -51.54         | 0.12       |
|            | J4   | 0.070      | 29.23       | -47.04         | 1.59       |
|            | J5   | 0.080      | 45.05       | -44.73         | 2.72       |
|            | J6   | 0.033      | 65.63       | -43.96         | 4.02       |
| 2011-11-14 | Core | 2.418      | 0.00        | -83.00         | 0.06       |
|            | J1   | 0.114      | 2.38        | -60.16         | 0.16       |
|            | J2   | 0.066      | 10.88       | -49.97         | 0.21       |
|            | J3   | 0.036      | 21.31       | -43.67         | 0.48       |
|            | J4   | 0.040      | 31.74       | -47.21         | 1.57       |
|            | J5   | 0.067      | 45.78       | -44.74         | 3.72       |
|            | J6   | 0.057      | 69.94       | -46.66         | 3.86       |
| 2012-09-17 | Core | 1.879      | 0.00        | -102.43        | 0.05       |
|            | J1   | 0.135      | 3.21        | -49.55         | 0.31       |
|            | J2   | 0.041      | 9.27        | -43.29         | 0.38       |
|            | J3   | 0.001      | 20.85       | -46.15         | 0.38       |

<sup>a</sup> Flux density.

<sup>b</sup> Radial distance from the core.

<sup>c</sup> Position angle.

TABLE B.4: Difmap Modelfit parameters for the Gaussian components model of the TANAMI 8.4 GHz images of PKS 0625–35.

| Epoch      | ID   | $S^a$ (Jy) | $d^b$ (mas) | $\phi^c$ (deg) | Size (mas) |
|------------|------|------------|-------------|----------------|------------|
| 2007-11-11 | Core | 0.301      | 0.00        | 124.15         | 0.12       |
|            | J1   | 0.027      | 2.87        | 141.47         | 0.61       |
|            | J2   | 0.007      | 8.54        | 140.98         | 1.22       |
|            | J3   | 0.013      | 17.55       | 145.39         | 2.53       |
| 2008-02-07 | Core | 0.367      | 0.00        | -97.56         | 0.04       |
|            | J1   | 0.047      | 2.50        | 133.55         | 0.50       |
|            | J2   | 0.014      | 5.62        | 132.94         | 0.77       |
|            | J3   | 0.008      | 17.56       | 142.27         | 1.00       |
|            | J4   | 0.011      | 22.81       | 136.83         | 2.38       |
| 2008-06-10 | Core | 0.309      | 0.00        | -65.20         | 0.02       |
|            | J1   | 0.021      | 2.93        | 140.90         | 0.23       |
|            | J2   | 0.007      | 8.06        | 137.90         | 0.81       |
|            | J3   | 0.011      | 15.36       | 146.91         | 1.39       |
|            | J4   | 0.003      | 23.11       | 144.02         | 1.20       |
| 2008-11-28 | Core | 0.348      | 0.00        | 112.20         | 0.15       |
|            | J1   | 0.025      | 3.14        | 142.40         | 0.39       |
|            | J2   | 0.011      | 7.71        | 141.29         | 1.51       |
|            | J3   | 0.001      | 13.29       | 140.87         | 3.40       |
|            | J4   | 0.006      | 20.31       | 144.18         | 1.51       |
| 2009-12-14 | Core | 0.325      | 0.00        | -104.25        | 0.07       |
|            | J1   | 0.025      | 2.87        | 149.51         | 0.19       |
|            | J2   | 0.004      | 9.34        | 148.14         | 0.54       |
|            | J3   | 0.013      | 17.14       | 142.98         | 2.76       |
|            | J4   | 0.002      | 22.05       | 139.62         | 0.34       |
| 2010-07-26 | Core | 0.312      | 0.00        | 15.51          | 0.09       |
|            | J1   | 0.020      | 3.22        | 139.97         | 0.22       |
|            | J2   | 0.012      | 9.07        | 143.04         | 1.40       |
|            | J3   | 0.008      | 19.44       | 144.56         | 1.09       |
| 2011-04-03 | Core | 0.325      | 0.00        | 126.16         | 0.09       |
|            | J1   | 0.050      | 2.23        | 134.81         | 0.80       |
|            | J2   | 0.001      | 9.37        | 144.95         | 1.04       |
|            | J3   | 0.013      | 17.62       | 147.02         | 1.88       |
| 2011-11-14 | Core | 0.344      | 0.00        | -58.08         | 0.22       |
|            | J1   | 0.032      | 3.02        | 132.83         | 0.23       |
|            | J2   | 0.015      | 9.71        | 143.93         | 2.38       |
|            | J3   | 0.006      | 20.39       | 140.74         | 2.05       |
|            | J4   | 0.001      | 25.02       | 141.50         | 1.15       |
| 2012-09-17 | Core | 0.344      | 0.00        | -34.11         | 0.06       |
|            | J1   | 0.027      | 2.85        | 143.47         | 0.27       |
|            | J2   | 0.008      | 8.31        | 140.43         | 0.80       |
|            | J3   | 0.005      | 19.90       | 148.02         | 0.56       |

<sup>a</sup> Flux density.

<sup>b</sup> Radial distance from the core.

<sup>c</sup> Position angle.

TABLE B.5: Difmap `Modelfit` parameters for the Gaussian components model of the TANAMI 8.4 GHz images of PKS 1258–321.

| Epoch      | ID   | $S^a$ (Jy) | $d^b$ (mas) | $\phi^c$ (deg) | Size (mas) |
|------------|------|------------|-------------|----------------|------------|
| 2009-12-14 | Core | 0.115      | 0.00        | -166.72        | 0.22       |
|            | J2   | 0.009      | 4.63        | -58.07         | 0.28       |
| 2010-05-09 | Core | 0.088      | 0.00        | 156.29         | 0.10       |
|            | J1   | 0.009      | 2.68        | -62.67         | 0.44       |
|            | J2   | 0.007      | 7.49        | -65.24         | 0.64       |
| 2011-11-14 | Core | 0.113      | 0.00        | -41.25         | 0.16       |
|            | J2   | 0.017      | 4.54        | -70.20         | 0.80       |
| 2012-04-28 | Core | 0.112      | 0.00        | -62.62         | 0.03       |
|            | J1   | 0.014      | 2.08        | -68.12         | 0.61       |
|            | J2   | 0.008      | 6.20        | -50.87         | 0.45       |
| 2013-03-16 | Core | 0.135      | 0.00        | -152.52        | 0.01       |
|            | J1   | 0.009      | 2.87        | -68.31         | 0.50       |
|            | J2   | 0.002      | 10.05       | -62.22         | 1.37       |

<sup>a</sup> Flux density.

<sup>b</sup> Radial distance from the core.

<sup>c</sup> Position angle.

TABLE B.6: Difmap `Modelfit` parameters for the Gaussian components model of the TANAMI 8.4 GHz images of IC 4296.

| Epoch      | ID   | $S^a$ (Jy) | $d^b$ (mas) | $\phi^c$ (deg) | Size (mas) |
|------------|------|------------|-------------|----------------|------------|
| 2008-02-07 | Core | 0.176      | 0.00        | -39.24         | 0.20       |
|            | J1   | 0.024      | 2.69        | -52.59         | 0.69       |
|            | CJ1  | 0.012      | 2.77        | 125.33         | 0.08       |
| 2008-06-10 | Core | 0.190      | 0.00        | -81.58         | 0.29       |
|            | CJ1  | 0.017      | 2.18        | 133.03         | 0.13       |
|            | J1   | 0.010      | 3.78        | -52.72         | 0.19       |
| 2008-11-28 | Core | 0.192      | 0.00        | 36.26          | 0.03       |
|            | CJ1  | 0.017      | 2.05        | 130.03         | 0.17       |
|            | J1   | 0.015      | 3.22        | -48.98         | 0.08       |
| 2010-07-26 | Core | 0.195      | 0.00        | 2.22           | 0.14       |
|            | J1   | 0.018      | 2.62        | -45.52         | 0.35       |
|            | CJ1  | 0.008      | 2.63        | 132.57         | 0.30       |
| 2011-11-14 | Core | 0.088      | 0.00        | -140.43        | 0.06       |
|            | J1   | 0.014      | 4.11        | -57.20         | 0.52       |
|            | CJ1  | 0.012      | 4.56        | 121.68         | 0.47       |

<sup>a</sup> Flux density.

<sup>b</sup> Radial distance from the core.

<sup>c</sup> Position angle.

TABLE B.7: Difmap `Modelfit` parameters for the Gaussian components model of the TANAMI 8.4 GHz images of PKS 1549–79.

| Epoch      | ID   | $S^a$ (Jy) | $d^b$ (mas) | $\phi^c$ (deg) | Size (mas) |
|------------|------|------------|-------------|----------------|------------|
| 2008-02-07 | Core | 0.582      | 0.00        | -56.41         | 0.45       |
|            | CJ1  | 0.131      | 3.02        | 48.06          | 0.23       |
|            | J1   | 0.322      | 3.89        | -135.08        | 0.28       |
| 2008-06-10 | Core | 0.696      | 0.00        | 26.97          | 0.34       |
|            | CJ1  | 0.140      | 3.10        | 47.35          | 0.28       |
|            | J1   | 0.170      | 3.18        | -130.89        | 0.19       |
| 2008-11-28 | Core | 0.438      | 0.00        | -28.46         | 0.33       |
|            | CJ1  | 0.174      | 2.85        | 50.63          | 0.79       |
|            | J1   | 0.292      | 3.89        | -138.32        | 0.45       |
| 2009-12-14 | Core | 0.738      | 0.00        | 64.25          | 0.25       |
|            | CJ1  | 0.087      | 4.46        | 37.68          | 0.10       |
|            | J1   | 0.109      | 5.54        | -140.60        | 0.01       |
| 2012-09-17 | Core | 0.244      | 0.00        | -24.03         | 0.24       |
|            | CJ1  | 0.137      | 3.07        | 54.07          | 0.59       |
|            | J1   | 0.199      | 3.71        | -131.91        | 0.72       |

<sup>a</sup> Flux density.<sup>b</sup> Radial distance from the core.<sup>c</sup> Position angle.TABLE B.8: Difmap `Modelfit` parameters for the Gaussian components model of the TANAMI 8.4 GHz images of PKS 1718–649.

| Epoch      | ID | $S^a$ (Jy) | $d^b$ (mas) | $\phi^c$ (deg) | Size (mas) |
|------------|----|------------|-------------|----------------|------------|
| 2008-02-07 | C1 | 2.967      | 0.00        | -25.16         | 1.17       |
|            | C2 | 0.189      | 7.86        | 133.24         | 0.29       |
| 2008-06-10 | C1 | 2.684      | 0.00        | -36.00         | 0.99       |
|            | C2 | 0.419      | 8.50        | 127.48         | 0.31       |
| 2008-11-28 | C1 | 1.965      | 0.00        | -77.07         | 0.85       |
|            | C2 | 0.646      | 8.00        | 133.06         | 0.44       |
| 2009-12-14 | C1 | 2.549      | 0.00        | -150.40        | 1.01       |
|            | C2 | 0.341      | 8.79        | 130.54         | 0.73       |
| 2010-07-26 | C1 | 2.180      | 0.00        | 172.80         | 0.95       |
|            | C2 | 0.638      | 7.89        | 130.27         | 0.75       |
| 2011-04-03 | C1 | 1.699      | 0.00        | -26.43         | 0.54       |
|            | C2 | 0.957      | 8.20        | 130.70         | 0.77       |
| 2011-08-14 | C1 | 2.504      | 0.00        | 35.25          | 0.85       |
|            | C2 | 0.535      | 8.23        | 130.07         | 1.08       |

<sup>a</sup> Flux density.<sup>b</sup> Radial distance from the core.<sup>c</sup> Position angle.

TABLE B.9: Difmap Modelfit parameters for the Gaussian components model of the TANAMI 8.4 GHz images of PKS 1733–565.

| Epoch      | ID   | $S^a$ (Jy) | $d^b$ (mas) | $\phi^c$ (deg) | Size (mas) |
|------------|------|------------|-------------|----------------|------------|
| 2008-02-07 | Core | 0.171      | 0.00        | 48.16          | 0.15       |
|            | CJ1  | 0.002      | 2.08        | 61.63          | 0.05       |
|            | J1   | 0.006      | 3.24        | -135.13        | 0.17       |
|            | CJ2  | 0.001      | 5.71        | 56.00          | 0.49       |
| 2008-03-30 | Core | 0.165      | 0.00        | 128.94         | 0.14       |
|            | CJ1  | 0.005      | 1.92        | 68.29          | 0.03       |
|            | J1   | 0.008      | 2.98        | -121.55        | 0.22       |
|            | CJ2  | 0.001      | 6.45        | 58.60          | 0.33       |
| 2008-08-09 | Core | 0.182      | 0.00        | 95.43          | 0.26       |
|            | CJ1  | 0.001      | 2.18        | 63.11          | 0.13       |
|            | J1   | 0.004      | 3.85        | -132.29        | 0.26       |
| 2009-02-23 | Core | 0.134      | 0.00        | 154.40         | 0.19       |
|            | CJ1  | 0.001      | 3.67        | 55.31          | 0.10       |
|            | J1   | 0.005      | 4.01        | -130.93        | 0.66       |
|            | CJ2  | 0.002      | 6.58        | 58.26          | 0.08       |
| 2010-03-14 | Core | 0.102      | 0.00        | 47.57          | 0.43       |
|            | CJ1  | 0.001      | 2.61        | 68.87          | 0.08       |
|            | J1   | 0.002      | 2.90        | -125.16        | 0.04       |
| 2010-10-29 | Core | 0.137      | 0.00        | -29.71         | 0.18       |
|            | CJ1  | 0.002      | 2.76        | 69.52          | 0.04       |
|            | J1   | 0.004      | 3.10        | -134.81        | 0.17       |
| 2011-07-23 | Core | 0.107      | 0.00        | 178.79         | 0.19       |
|            | CJ1  | 0.007      | 1.21        | 58.89          | 0.03       |
|            | J1   | 0.005      | 3.03        | -130.44        | 0.59       |
| 2012-04-28 | Core | 0.073      | 0.00        | 91.32          | 0.17       |
|            | CJ1  | 0.001      | 2.01        | 63.43          | 0.01       |
|            | J1   | 0.003      | 3.27        | -135.75        | 0.14       |

<sup>a</sup> Flux density.

<sup>b</sup> Radial distance from the core.

<sup>c</sup> Position angle.

TABLE B.10: Difmap Modelfit parameters for the Gaussian components model of the TANAMI 8.4 GHz images of PKS 2027–308.

| Epoch      | ID   | $S^a$ (Jy) | $d^b$ (mas) | $\phi^c$ (deg) | Size (mas) |
|------------|------|------------|-------------|----------------|------------|
| 2008-06-10 | Core | 0.061      | 0.00        | -114.51        | 0.08       |
|            | CJ1  | 0.029      | 0.93        | 38.51          | 0.04       |
|            | J1   | 0.025      | 2.90        | -126.30        | 0.64       |
|            | CJ2  | 0.013      | 4.85        | 16.47          | 0.34       |
| 2008-11-28 | Core | 0.031      | 0.00        | -42.65         | 0.38       |
|            | CJ1  | 0.043      | 0.71        | 37.81          | 0.54       |
|            | J1   | 0.018      | 2.85        | -126.22        | 0.14       |
|            | CJ2  | 0.008      | 4.48        | 17.34          | 0.44       |
| 2009-12-14 | Core | 0.090      | 0.00        | -84.95         | 0.25       |
|            | CJ1  | 0.008      | 2.14        | 2.65           | 1.21       |
|            | J1   | 0.008      | 2.24        | -131.26        | 0.45       |
|            | CJ2  | 0.003      | 5.03        | 21.30          | 0.12       |
| 2010-07-26 | Core | 0.041      | 0.00        | -40.67         | 0.13       |
|            | CJ1  | 0.030      | 0.78        | 30.47          | 0.09       |
|            | J1   | 0.022      | 2.79        | -125.51        | 0.45       |
|            | CJ2  | 0.009      | 4.34        | 15.32          | 0.20       |
| 2011-04-03 | Core | 0.063      | 0.00        | 56.16          | 0.15       |
|            | CJ1  | 0.022      | 1.20        | 44.99          | 0.18       |
|            | J1   | 0.024      | 2.70        | -127.68        | 0.32       |
|            | CJ2  | 0.006      | 4.39        | 24.93          | 1.39       |
| 2011-11-14 | Core | 0.058      | 0.00        | -44.63         | 0.15       |
|            | CJ1  | 0.007      | 1.84        | 54.85          | 0.17       |
|            | J1   | 0.017      | 3.12        | -129.34        | 0.62       |
|            | CJ2  | 0.009      | 4.21        | 17.89          | 0.22       |
| 2012-09-17 | Core | 0.050      | 0.00        | -27.36         | 0.12       |
|            | CJ1  | 0.020      | 1.25        | 45.02          | 0.12       |
|            | J1   | 0.018      | 2.84        | -130.86        | 0.28       |
|            | CJ2  | 0.009      | 4.34        | 19.06          | 0.34       |

<sup>a</sup> Flux density.

<sup>b</sup> Radial distance from the core.

<sup>c</sup> Position angle.

TABLE B.11: Difmap Modelfit parameters for the Gaussian components model of the TANAMI 8.4 GHz images of PKS 2153–69.

| Epoch      | ID   | $S^a$ (Jy) | $d^b$ (mas) | $\phi^c$ (deg) | Size (mas) |
|------------|------|------------|-------------|----------------|------------|
| 2008-02-07 | Core | 0.435      | 0.00        | 35.39          | 0.18       |
|            | J1   | 0.023      | 1.91        | 73.49          | 0.04       |
|            | J2   | 0.028      | 4.21        | 32.82          | 0.40       |
|            | J3   | 0.008      | 8.55        | 45.65          | 0.32       |
|            | J4   | 0.008      | 12.44       | 39.21          | 0.60       |
|            | J5   | 0.013      | 17.02       | 43.30          | 0.28       |
|            | J6   | 0.005      | 21.56       | 48.95          | 1.16       |
| 2008-06-10 | Core | 0.467      | 0.00        | -143.96        | 0.04       |
|            | J1   | 0.005      | 1.67        | 46.58          | 0.69       |
|            | J2   | 0.077      | 3.59        | 41.63          | 0.37       |
|            | J3   | 0.040      | 6.71        | 45.80          | 0.10       |
|            | J4   | 0.029      | 11.62       | 49.38          | 0.44       |
| 2008-11-28 | Core | 0.416      | 0.00        | -104.97        | 0.29       |
|            | J1   | 0.043      | 2.88        | 46.22          | 0.59       |
|            | J2   | 0.015      | 4.87        | 41.53          | 0.12       |
|            | J3   | 0.003      | 9.84        | 41.26          | 2.73       |
|            | J4   | 0.008      | 16.57       | 47.45          | 0.45       |
|            | J5   | 0.004      | 19.51       | 45.30          | 0.26       |
|            | J6   | 0.002      | 23.10       | 46.03          | 0.48       |
| 2010-07-26 | Core | 0.501      | 0.00        | 78.52          | 0.11       |
|            | J1   | 0.047      | 3.64        | 40.67          | 0.45       |
|            | J2   | 0.006      | 6.75        | 41.61          | 1.07       |
|            | J3   | 0.006      | 12.12       | 41.28          | 0.66       |
|            | J4   | 0.006      | 16.99       | 44.73          | 1.05       |
|            | J5   | 0.005      | 21.70       | 45.62          | 0.38       |
|            | J6   | 0.005      | 28.42       | 43.58          | 2.29       |
| 2011-04-03 | Core | 0.359      | 0.00        | 63.90          | 0.13       |
|            | J1   | 0.029      | 3.23        | 36.72          | 0.87       |
| 2012-09-17 | Core | 0.402      | 0.00        | 42.75          | 0.11       |
|            | J1   | 0.044      | 3.69        | 43.33          | 0.38       |
|            | J2   | 0.014      | 7.21        | 43.79          | 0.06       |
|            | J3   | 0.008      | 12.49       | 44.61          | 0.11       |
|            | J4   | 0.007      | 20.42       | 44.56          | 0.35       |
|            | J5   | 0.020      | 24.49       | 42.57          | 0.28       |

<sup>a</sup> Flux density.<sup>b</sup> Radial distance from the core.<sup>c</sup> Position angle.

## Appendix C

# *Fermi*-LAT results on full MOJAVE and TANAMI samples

Here we report the full results of the *Fermi*-LAT analysis on the combined MOJAVE-TANAMI AGN sample. Since the analysis was performed in an iterative fashion on the full sample, this means the radio galaxies listed in Table 7.1 are also included. The LAT results for galaxies listed in Tables C.1 through C.11 are consistent with those in Table 7.1.

TABLE C.1: Results of *Fermi*-LAT analysis in the range 0.1-100 GeV for the complete MOJAVE and TANAMI combined sample.

| B1950 name | Common name       | Redshift | Class | Flux <sup>a</sup> | Spectral index <sup>b</sup> | Curvature <sup>c</sup> | TS    |
|------------|-------------------|----------|-------|-------------------|-----------------------------|------------------------|-------|
| 0003+380   | S4 0003+38        | 0.23     | Q     | 23.0±1.6          | 2.72±0.06                   | -                      | 337   |
| 0003-066   | NRAO 005          | 0.35     | B     | 2.4±0.9           | 2.15±0.14                   | -                      | 34    |
| 0006+061   | CRATES J0009+0628 | -        | B     | 6.7±1.2           | 2.12±0.08                   | -                      | 193   |
| 0007+106   | III Zw 2          | 0.09     | G     | <4.56             | -                           | -                      | 2     |
| 0010+405   | 4C +40.01         | 0.26     | Q     | 4.8±1.3           | 2.43±0.14                   | -                      | 43    |
| 0015-054   | PMN J0017-0512    | 0.23     | Q     | 27.6±1.7          | 2.52±0.04                   | -                      | 688   |
| 0016+731   | S5 0016+73        | 1.78     | Q     | 43±2              | 2.52±0.03                   | -                      | 672   |
| 0026+346   | B2 0026+34        | 0.52     | G     | <2.93             | -                           | -                      | 7     |
| 0027+056   | PKS 0027+056      | 1.32     | Q     | 7.2±1.7           | 2.57±0.13                   | -                      | 33    |
| 0035+413   | B3 0035+413       | 1.35     | Q     | <3.03             | -                           | -                      | 18    |
| 0047-579   | [HB89] 0047-579   | 1.80     | Q     | 9.8±1.3           | 2.49±0.08                   | -                      | 189   |
| 0048-071   | OB -082           | 1.98     | Q     | 10.1±1.4          | 2.03±0.08                   | 0.21±0.05              | 459   |
| 0048-097   | PKS 0048-09       | 0.63     | B     | 37.7±1.3          | 2.008±0.019                 | -                      | 4796  |
| 0055+300   | NGC 315           | 0.02     | G     | 5.4±1.2           | 2.28±0.11                   | -                      | 76    |
| 0055-328   | PKS 0055-328      | 1.37     | B     | 17.0±1.1          | 2.11±0.03                   | -                      | 1326  |
| 0059+581   | TXS 0059+581      | 0.64     | Q     | 76±2              | 2.11±0.02                   | 0.082±0.012            | 5086  |
| 0106+013   | 4C +01.02         | 2.10     | Q     | 236±2             | 2.196±0.012                 | 0.101±0.007            | 41092 |
| 0106+612   | TXS 0106+612      | 0.78     | Q     | 83±3              | 2.36±0.04                   | 0.11±0.02              | 2061  |
| 0106+678   | 4C +67.04         | 0.29     | B     | 17.0±1.6          | 1.9±0.04                    | -                      | 1170  |
| 0108+388   | CGRABS J0111+3906 | 0.67     | G     | <4.94             | -                           | -                      | 3     |
| 0109+224   | S2 0109+22        | 0.26     | B     | 76.1±1.8          | 1.974±0.016                 | 0.047±0.008            | 14439 |
| 0109+351   | B2 0109+35        | 0.45     | Q     | <3.50             | -                           | -                      | 0     |
| 0110+318   | 4C +31.03         | 0.60     | Q     | 53.8±1.6          | 2.34±0.02                   | -                      | 3681  |
| 0111+021   | UGC 00773         | 0.05     | B     | 5.7±1.7           | 2.38±0.13                   | -                      | 46    |
| 0112-017   | UM 310            | 1.37     | Q     | 8.4±1.6           | 2.53±0.11                   | -                      | 78    |
| 0113-118   | PKS 0113-118      | 0.67     | Q     | 21.6±1.4          | 2.36±0.04                   | -                      | 784   |
| 0116-219   | OC -228           | 1.16     | Q     | 49.9±1.7          | 2.27±0.02                   | 0.077±0.015            | 4815  |
| 0118-272   | OC -230.4         | -        | B     | 26.8±1.0          | 1.875±0.019                 | -                      | 5230  |
| 0119+041   | PKS 0119+041      | 0.64     | Q     | <1.56             | -                           | -                      | 0     |
| 0119+115   | PKS 0119+11       | 0.57     | Q     | <0.75             | -                           | -                      | 7     |
| 0122-003   | UM 321            | 1.08     | Q     | 9.0±1.8           | 2.84±0.16                   | -                      | 50    |
| 0130-171   | OC -150           | 1.02     | Q     | 41.0±1.5          | 2.39±0.03                   | -                      | 2476  |
| 0133+388   | B3 0133+388       | -        | B     | 19.9±0.8          | 1.639±0.018                 | -                      | 6717  |
| 0133+476   | DA 55             | 0.86     | Q     | 65.6±1.8          | 2.09±0.02                   | 0.115±0.013            | 7197  |
| 0136+176   | PKS 0136+176      | 2.72     | Q     | <11.53            | -                           | -                      | 24    |
| 0141+268   | TXS 0141+268      | -        | B     | 63.6±1.8          | 1.98±0.02                   | 0.072±0.010            | 9443  |
| 0142-278   | OC -270           | 1.15     | Q     | 27.6±1.4          | 2.57±0.04                   | -                      | 907   |
| 0149+218   | PKS 0149+21       | 1.32     | Q     | 16.6±1.7          | 2.68±0.07                   | -                      | 179   |
| 0153+744   | S5 0153+744       | 2.34     | Q     | <6.12             | -                           | -                      | 2     |
| 0201+113   | PKS 0201+113      | 3.64     | Q     | <2.84             | -                           | -                      | 19    |
| 0202+149   | 4C +15.05         | 0.41     | Q     | 16.9±1.5          | 2.31±0.05                   | -                      | 488   |
| 0202+319   | B2 0202+31        | 1.47     | Q     | 33.4±1.7          | 2.67±0.04                   | -                      | 753   |
| 0202-172   | PKS 0202-17       | 1.74     | Q     | 37.4±1.6          | 2.64±0.03                   | -                      | 1281  |
| 0208+106   | MG1 J021114+1051  | 0.20     | B     | 66±2              | 2.069±0.019                 | 0.039±0.010            | 7745  |
| 0208-512   | [HB89] 0208-512   | 1.00     | Q     | 89.8±1.7          | 2.189±0.019                 | 0.095±0.011            | 12521 |

<sup>a</sup> *Fermi*-LAT flux between 0.1-100 GeV in photons cm<sup>-2</sup> s<sup>-1</sup>.<sup>b</sup> *Fermi*-LAT spectral index  $\Gamma$ , in case of power-law spectrum  $dN/dE = N_0 \times (E/E_0)^{-\Gamma}$ , or  $\alpha$  in case of logParabola spectrum  $dN/dE = N_0 \times (E/E_b)^{-[\alpha+\beta \log(E/E_b)]}$ .<sup>c</sup> Curvature parameter of logParabola spectrum  $\beta$ .

TABLE C.2: Results of *Fermi*-LAT analysis in the range 0.1-100 GeV for the complete MOJAVE and TANAMI combined sample (continued).

| B1950 name | Common name     | Redshift | Class | Flux <sup>a</sup> | Spectral index <sup>b</sup> | Curvature <sup>c</sup> | TS    |
|------------|-----------------|----------|-------|-------------------|-----------------------------|------------------------|-------|
| 0212+735   | S5 0212+73      | 2.37     | Q     | 50±2              | 2.95±0.05                   | -                      | 672   |
| 0215+015   | OD 026          | 1.72     | Q     | 46.3±1.5          | 2.19±0.02                   | -                      | 4012  |
| 0219+428   | 3C 66A          | -        | B     | 116.2±1.9         | 1.866±0.009                 | 0.037±0.005            | 34179 |
| 0221+067   | 4C +06.11       | 0.51     | Q     | 4.4±1.4           | 2.34±0.14                   | -                      | 38    |
| 0224+671   | 4C +67.05       | 0.52     | Q     | 13±2              | 2.45±0.08                   | -                      | 78    |
| 0226-559   | PKS 0226-559    | -        | U     | 49.2±1.4          | 2.254±0.019                 | -                      | 4659  |
| 0227-369   | PKS 0227-369    | 2.12     | Q     | 32.0±1.4          | 2.57±0.03                   | -                      | 1219  |
| 0229+131   | 4C +13.14       | 2.06     | Q     | 22.3±1.9          | 2.61±0.06                   | -                      | 280   |
| 0234+285   | 4C +28.07       | 1.21     | Q     | 160±2             | 2.197±0.016                 | 0.089±0.008            | 20468 |
| 0235+164   | AO 0235+164     | 0.94     | Q     | 126±2             | 1.945±0.015                 | 0.092±0.007            | 22859 |
| 0235-618   | PKS 0235-618    | 0.47     | Q     | 23.3±1.3          | 2.35±0.04                   | -                      | 1090  |
| 0238-084   | NGC 1052        | 0.005    | G     | <0.41             | -                           | -                      | 0     |
| 0241+622   | 7C 0241+6215    | 0.05     | Q     | <13.73            | -                           | -                      | 6     |
| 0244-470   | PKS 0244-470    | 1.39     | Q     | 69.5±1.6          | 2.24±0.03                   | 0.095±0.014            | 7357  |
| 0248+430   | B3 0248+430     | 1.31     | Q     | <0.53             | -                           | -                      | 0     |
| 0250-225   | OD -283         | 1.42     | Q     | 83.3±1.8          | 2.17±0.02                   | 0.096±0.012            | 10386 |
| 0300+470   | 4C +47.08       | -        | B     | 38.1±1.7          | 2.21±0.02                   | -                      | 1983  |
| 0301-243   | PKS 0301-243    | 0.27     | B     | 41.5±1.1          | 1.871±0.015                 | -                      | 9727  |
| 0302-623   | PKS 0302-623    | 1.35     | Q     | 17.7±1.3          | 2.34±0.04                   | -                      | 630   |
| 0305+039   | 3C 78           | 0.03     | G     | 5.5±0.9           | 1.88±0.06                   | -                      | 332   |
| 0308-611   | PKS 0308-611    | 1.48     | Q     | 60.4±1.6          | 2.44±0.02                   | -                      | 4397  |
| 0309+411   | NRAO 128        | 0.14     | G     | 5.1±1.6           | 2.25±0.12                   | -                      | 51    |
| 0313+088   | BZB J0316+0904  | -        | B     | 13.5±1.3          | 1.91±0.04                   | -                      | 983   |
| 0316+162   | CTA21           | 0.91     | Q     | <3.90             | -                           | -                      | 0     |
| 0316+413   | 3C 84           | 0.02     | G     | 333±3             | 2.010±0.006                 | 0.055±0.003            | 97469 |
| 0321+340   | 1H 0323+342     | 0.06     | G     | 65±2              | 2.69±0.05                   | 0.11±0.03              | 1437  |
| 0332-376   | PMN J0334-3725  | -        | B     | 30.3±1.1          | 2.02±0.02                   | -                      | 4102  |
| 0332-403   | [HB89] 0332-403 | 1.45     | B     | 40.0±1.4          | 1.97±0.03                   | 0.096±0.014            | 6288  |
| 0333+321   | NRAO 140        | 1.26     | Q     | 55±2              | 2.95±0.05                   | -                      | 644   |
| 0336-019   | CTA 26          | 0.85     | Q     | 106±2             | 2.23±0.02                   | 0.063±0.010            | 10010 |
| 0346+800   | S5 0346+80      | -        | B     | 4.3±0.9           | 2.11±0.08                   | -                      | 124   |
| 0347-211   | OE -280         | 2.94     | Q     | 28.3±1.6          | 2.24±0.05                   | 0.20±0.03              | 1262  |
| 0355+508   | NRAO 150        | 1.52     | Q     | 94±3              | 2.63±0.03                   | -                      | 1487  |
| 0400+258   | CTD 026         | 2.11     | Q     | <5.40             | -                           | -                      | 12    |
| 0402-362   | PKS 0402-362    | 1.42     | Q     | 188±2             | 2.305±0.015                 | 0.143±0.010            | 30345 |
| 0403-132   | PKS 0403-13     | 0.57     | Q     | 18.3±1.5          | 2.54±0.06                   | -                      | 358   |
| 0405-385   | [HB89] 0405-385 | 1.28     | Q     | 47.9±1.6          | 2.33±0.02                   | -                      | 3590  |
| 0414-189   | PKS 0414-189    | 1.54     | Q     | 17.7±1.3          | 2.38±0.05                   | -                      | 571   |
| 0415+379   | 3C 111          | 0.05     | G     | 29±3              | 2.77±0.08                   | -                      | 170   |
| 0420+022   | PKS 0420+022    | 2.28     | Q     | 13±2              | 2.94±0.15                   | -                      | 48    |
| 0420-014   | PKS 0420-01     | 0.92     | Q     | 58±2              | 2.15±0.03                   | 0.091±0.014            | 4739  |
| 0422+004   | PKS 0422+00     | 0.27     | B     | 30.4±1.8          | 2.25±0.03                   | -                      | 1364  |
| 0426-380   | PKS 0426-380    | 1.11     | B     | 248±2             | 1.989±0.006                 | 0.076±0.004            | 89229 |
| 0429+415   | 3C 119          | 1.02     | Q     | <0.45             | -                           | -                      | 0     |
| 0430+052   | 3C 120          | 0.03     | G     | 32±2              | 2.71±0.05                   | -                      | 368   |

<sup>a</sup> *Fermi*-LAT flux between 0.1-100 GeV in photons cm<sup>-2</sup> s<sup>-1</sup>.<sup>b</sup> *Fermi*-LAT spectral index  $\Gamma$ , in case of power-law spectrum  $dN/dE = N_0 \times (E/E_0)^{-\Gamma}$ , or  $\alpha$  in case of logParabola spectrum  $dN/dE = N_0 \times (E/E_b)^{-[\alpha+\beta \log(E/E_b)]}$ .<sup>c</sup> Curvature parameter of logParabola spectrum  $\beta$ .

TABLE C.3: Results of *Fermi*-LAT analysis in the range 0.1-100 GeV for the complete MOJAVE and TANAMI combined sample (continued).

| B1950 name | Common name       | Redshift | Class | Flux <sup>a</sup> | Spectral index <sup>b</sup> | Curvature <sup>c</sup> | TS    |
|------------|-------------------|----------|-------|-------------------|-----------------------------|------------------------|-------|
| 0430+289   | BZB J0433+2905    | -        | B     | 30.8±1.8          | 2.02±0.03                   | -                      | 1694  |
| 0438-436   | [HB89] 0438-436   | 2.86     | Q     | 9.3±1.3           | 2.49±0.08                   | -                      | 132   |
| 0440-003   | NRAO 190          | 0.85     | Q     | 98±2              | 2.428±0.016                 | -                      | 7183  |
| 0446+112   | PKS 0446+11       | 2.15     | Q     | 76±2              | 2.30±0.04                   | 0.11±0.02              | 2688  |
| 0447-439   | PKS 0447-439      | 0.11     | B     | 73.0±1.3          | 1.822±0.010                 | -                      | 25597 |
| 0451-282   | OF -285           | 2.56     | Q     | 58.7±1.7          | 2.64±0.03                   | -                      | 2724  |
| 0454+844   | S5 0454+84        | -        | B     | <3.23             | -                           | -                      | 18    |
| 0454-234   | PKS 0454-234      | 1.00     | Q     | 275±2             | 2.037±0.009                 | 0.078±0.005            | 77019 |
| 0454-463   | [HB89] 0454-463   | 0.85     | Q     | 36.7±1.5          | 2.53±0.03                   | -                      | 1499  |
| 0458-020   | S3 0458-02        | 2.29     | Q     | 88.1±1.9          | 2.374±0.016                 | -                      | 6291  |
| 0502+675   | 1ES 0502+675      | 0.34     | B     | 6.2±0.5           | 1.53±0.03                   | -                      | 2307  |
| 0506+056   | TXS 0506+056      | -        | B     | 68.7±1.9          | 2.052±0.015                 | -                      | 7270  |
| 0506-612   | [HB89] 0506-612   | 1.09     | Q     | 25.9±1.5          | 2.56±0.04                   | -                      | 738   |
| 0514-459   | PKS 0514-459      | -        | U     | 18.1±1.5          | 2.46±0.05                   | -                      | 474   |
| 0516-621   | PKS 0516-621      | 1.30     | B     | 32.8±1.4          | 2.17±0.02                   | -                      | 2737  |
| 0518-458   | PICTOR A          | 0.04     | G     | 12.3±1.5          | 2.53±0.08                   | -                      | 172   |
| 0521-365   | ESO 362- G 021    | 0.06     | B     | 109.3±1.9         | 2.28±0.02                   | 0.085±0.011            | 12290 |
| 0524-485   | PKS 0524-485      | 1.30     | Q     | 46.5±1.5          | 2.23±0.02                   | -                      | 3593  |
| 0528+134   | PKS 0528+134      | 2.07     | Q     | 51±3              | 2.12±0.06                   | 0.25±0.03              | 1202  |
| 0529+075   | OG 050            | 1.25     | Q     | 99±3              | 2.21±0.02                   | 0.075±0.012            | 6409  |
| 0529+483   | TXS 0529+483      | 1.16     | Q     | 74±2              | 2.44±0.02                   | -                      | 3073  |
| 0530-485   | PMN J0531-4827    | -        | U     | 46.5±1.6          | 2.01±0.02                   | 0.093±0.012            | 6939  |
| 0534-340   | PKS 0534-340      | -        | U     | 11.1±1.6          | 2.67±0.12                   | -                      | 61    |
| 0536+145   | TXS 0536+145      | 2.69     | Q     | 21±2              | 2.44±0.06                   | -                      | 188   |
| 0537-441   | [HB89] 0537-441   | 0.89     | B     | 217±2             | 1.975±0.009                 | 0.058±0.004            | 67454 |
| 0539-057   | PKS 0539-057      | 0.84     | Q     | <5.06             | -                           | -                      | 5     |
| 0552+398   | DA 193            | 2.36     | Q     | 40±2              | 2.83±0.05                   | -                      | 447   |
| 0602+673   | CGRABS J0607+6720 | 1.97     | Q     | 6.6±1.0           | 2.26±0.08                   | -                      | 135   |
| 0605-085   | OC -010           | 0.87     | Q     | 34±2              | 2.35±0.04                   | -                      | 637   |
| 0605-153   | PMN J0608-1520    | 1.09     | Q     | 38±2              | 2.41±0.06                   | 0.09±0.03              | 787   |
| 0607-157   | PKS 0607-15       | 0.32     | Q     | <4.52             | -                           | -                      | 0     |
| 0609+413   | B3 0609+413       | -        | B     | 41.2±1.4          | 1.954±0.017                 | -                      | 5446  |
| 0615+820   | S5 0615+82        | 0.71     | Q     | <4.02             | -                           | -                      | 3     |
| 0619+334   | B2 0619+33        | 1.06     | Q     | 58±2              | 2.12±0.03                   | 0.046±0.012            | 3811  |
| 0625-354   | PKS 0625-35, OH-3 | 0.05     | G     | 10.8±1.0          | 1.89±0.04                   | -                      | 1065  |
| 0627-199   | PKS 0627-199      | 1.72     | B     | 34.7±1.8          | 2.22±0.03                   | -                      | 1430  |
| 0628-240   | TXS 0628-240      | 1.60     | B     | 24.8±1.1          | 1.756±0.019                 | -                      | 5381  |
| 0637-752   | PKS 0637-752      | 0.65     | Q     | 30.1±1.8          | 2.65±0.05                   | -                      | 552   |
| 0640+090   | PMN J0643+0857    | 0.88     | Q     | 47±3              | 2.46±0.04                   | 0.24±0.04              | 841   |
| 0642+449   | OH 471            | 3.40     | Q     | <5.99             | -                           | -                      | 21    |
| 0646+600   | S4 0646+60        | 0.46     | Q     | <6.98             | -                           | -                      | 14    |
| 0646-306   | PKS 0646-306      | 0.46     | Q     | 28.6±1.7          | 2.43±0.04                   | -                      | 696   |
| 0648-165   | PKS 0648-16       | -        | U     | 22±2              | 2.51±0.06                   | -                      | 170   |
| 0650+453   | B3 0650+453       | 0.93     | Q     | 26.2±1.3          | 2.21±0.03                   | -                      | 1562  |
| 0650+507   | GB6 J0654+5042    | 1.25     | Q     | 16.5±1.4          | 2.09±0.04                   | 0.08±0.02              | 1231  |

<sup>a</sup> *Fermi*-LAT flux between 0.1-100 GeV in photons cm<sup>-2</sup> s<sup>-1</sup>.<sup>b</sup> *Fermi*-LAT spectral index  $\Gamma$ , in case of power-law spectrum  $dN/dE = N_0 \times (E/E_0)^{-\Gamma}$ , or  $\alpha$  in case of logParabola spectrum  $dN/dE = N_0 \times (E/E_b)^{-[\alpha+\beta \log(E/E_b)]}$ .<sup>c</sup> Curvature parameter of logParabola spectrum  $\beta$ .

TABLE C.4: Results of *Fermi*-LAT analysis in the range 0.1-100 GeV for the complete MOJAVE and TANAMI combined sample (continued).

| B1950 name | Common name       | Redshift | Class | Flux <sup>a</sup> | Spectral index <sup>b</sup> | Curvature <sup>c</sup> | TS    |
|------------|-------------------|----------|-------|-------------------|-----------------------------|------------------------|-------|
| 0700-661   | PKS 0700-661      | -        | B     | 48.5±1.5          | 2.033±0.017                 | -                      | 5674  |
| 0707+476   | S4 0707+47        | 1.29     | Q     | 12.3±1.4          | 2.62±0.08                   | -                      | 153   |
| 0710+196   | WB92 0711+1940    | 0.54     | Q     | 30.2±1.9          | 2.23±0.04                   | 0.10±0.03              | 1287  |
| 0710+439   | B3 0710+439       | 0.52     | G     | <0.51             | -                           | -                      | 0     |
| 0716+332   | B2 0716+33        | 0.78     | Q     | 51.2±1.6          | 2.06±0.02                   | 0.080±0.012            | 6359  |
| 0716+714   | S5 0716+71        | -        | B     | 218.9±1.8         | 1.955±0.008                 | 0.042±0.003            | 97564 |
| 0723-008   | PKS 0723-008      | 0.13     | B     | 10.7±1.3          | 2.05±0.05                   | -                      | 433   |
| 0727-115   | PKS 0727-11       | 1.59     | Q     | 225±3             | 2.17±0.014                  | 0.062±0.006            | 21799 |
| 0730+504   | TXS 0730+504      | 0.72     | Q     | 12.4±1.3          | 2.54±0.07                   | -                      | 210   |
| 0735+178   | OI 158            | 0.45     | B     | 64.9±1.5          | 2.017±0.013                 | -                      | 10418 |
| 0736+017   | OI 061            | 0.19     | Q     | 122±2             | 2.25±0.02                   | 0.086±0.011            | 10643 |
| 0736-770   | PKS 0736-770      | -        | U     | 22.1±1.6          | 2.3±0.04                    | -                      | 536   |
| 0738+313   | OI 363            | 0.63     | Q     | <3.59             | -                           | -                      | 8     |
| 0738+548   | VIPS 0027         | 0.72     | Q     | 41.6±1.4          | 2.15±0.03                   | 0.09±0.015             | 4366  |
| 0742+103   | PKS B0742+103     | 2.62     | Q     | <3.61             | -                           | -                      | 3     |
| 0743-006   | OI -072           | 1.00     | Q     | <6.97             | -                           | -                      | 20    |
| 0745+241   | PKS 0745+241      | 0.41     | Q     | 10.9±1.2          | 2.21±0.06                   | -                      | 324   |
| 0745-330   | PKS 0745-330      | -        | U     | 46±3              | 2.33±0.03                   | -                      | 715   |
| 0748+126   | OI 280            | 0.89     | Q     | 18.7±1.6          | 2.46±0.05                   | -                      | 417   |
| 0754+100   | PKS 0754+100      | 0.27     | B     | 21.3±1.3          | 2.11±0.03                   | -                      | 1445  |
| 0804+499   | BZQ J0808+4950    | 1.44     | Q     | 14.9±1.4          | 2.83±0.08                   | -                      | 182   |
| 0805-077   | PKS 0805-07       | 1.84     | Q     | 87±2              | 2.04±0.018                  | 0.091±0.010            | 10691 |
| 0808+019   | OJ 014            | 1.15     | B     | 40.4±1.4          | 2.052±0.019                 | -                      | 4468  |
| 0814+425   | OJ 425            | -        | B     | 52.6±1.5          | 1.918±0.02                  | 0.093±0.010            | 10642 |
| 0821+394   | 4C +39.23         | 1.22     | Q     | 15.3±1.3          | 2.38±0.05                   | -                      | 462   |
| 0823+033   | PKS 0823+033      | 0.50     | B     | 7.9±1.2           | 2.09±0.07                   | -                      | 311   |
| 0823-223   | PKS 0823-223      | -        | B     | 38.1±1.4          | 1.945±0.018                 | -                      | 4908  |
| 0823-500   | PKS 0823-500      | -        | G     | <0.69             | -                           | -                      | 0     |
| 0827+243   | OJ 248            | 0.94     | Q     | 54.0±1.7          | 2.53±0.02                   | -                      | 2612  |
| 0829+046   | OJ 049            | 0.17     | B     | 47.0±1.8          | 2.15±0.03                   | 0.079±0.015            | 4222  |
| 0831+557   | 4C +55.16         | 0.24     | G     | <0.23             | -                           | -                      | 2     |
| 0834-201   | PKS 0834-20       | 2.75     | Q     | 21.5±1.9          | 2.99±0.09                   | -                      | 178   |
| 0836+710   | 4C +71.07         | 2.22     | Q     | 143.6±1.7         | 2.64±0.02                   | 0.17±0.016             | 15825 |
| 0837+012   | PKS 0837+012      | 1.12     | Q     | 14.6±1.4          | 2.36±0.05                   | -                      | 333   |
| 0838+133   | 3C 207            | 0.68     | Q     | 10.7±1.5          | 2.60±0.09                   | -                      | 107   |
| 0846+513   | SBS 0846+513      | 0.58     | G     | 34.3±1.2          | 2.23±0.02                   | -                      | 3154  |
| 0847-120   | BZQ J0850-1213    | 0.57     | Q     | 30.3±1.7          | 2.09±0.04                   | 0.1±0.02               | 2302  |
| 0850+581   | 4C +58.17         | 1.32     | Q     | <5.60             | -                           | -                      | 8     |
| 0851+202   | OJ 287            | 0.31     | B     | 81.4±1.8          | 2.13±0.015                  | 0.072±0.009            | 12032 |
| 0859+470   | 4C +47.29         | 1.46     | Q     | 10.5±1.2          | 2.43±0.07                   | -                      | 261   |
| 0859-140   | PKS B0859-140     | 1.34     | Q     | <1.60             | -                           | -                      | 0     |
| 0902-350   | 1FGL J0904.7-3514 | -        | U     | 35±2              | 2.66±0.05                   | -                      | 408   |
| 0903-573   | PKS 0903-57       | 0.69     | U     | 70±2              | 2.306±0.02                  | -                      | 3146  |
| 0906+015   | 4C +01.24         | 1.03     | Q     | 55±2              | 2.47±0.03                   | 0.092±0.019            | 2921  |
| 0907+336   | Ton 1015          | 0.35     | B     | 12.3±0.9          | 1.9±0.03                    | -                      | 1504  |

<sup>a</sup> *Fermi*-LAT flux between 0.1-100 GeV in photons cm<sup>-2</sup> s<sup>-1</sup>.<sup>b</sup> *Fermi*-LAT spectral index  $\Gamma$ , in case of power-law spectrum  $dN/dE = N_0 \times (E/E_0)^{-\Gamma}$ , or  $\alpha$  in case of logParabola spectrum  $dN/dE = N_0 \times (E/E_b)^{-[\alpha+\beta \log(E/E_b)]}$ .<sup>c</sup> Curvature parameter of logParabola spectrum  $\beta$ .

TABLE C.5: Results of *Fermi*-LAT analysis in the range 0.1-100 GeV for the complete MOJAVE and TANAMI combined sample (continued).

| BI950 name | Common name     | Redshift | Class | Flux <sup>a</sup> | Spectral index <sup>b</sup> | Curvature <sup>c</sup> | TS     |
|------------|-----------------|----------|-------|-------------------|-----------------------------|------------------------|--------|
| 0917+449   | S4 0917+44      | 2.19     | Q     | 76.6±1.6          | 2.19±0.02                   | 0.087±0.011            | 10718  |
| 0917+624   | OK 630          | 1.45     | Q     | 43.1±1.3          | 2.47±0.02                   | -                      | 2848   |
| 0920-397   | [HB89] 0920-397 | 0.59     | Q     | 33±2              | 2.76±0.06                   | -                      | 322    |
| 0923+392   | 4C +39.25       | 0.69     | Q     | <1.13             | -                           | -                      | 0      |
| 0938-133   | BZQ J0941-1335  | 0.55     | Q     | 17.0±1.4          | 2.39±0.05                   | -                      | 413    |
| 0945+408   | 4C +40.24       | 1.25     | Q     | 4.5±1.0           | 2.35±0.11                   | -                      | 73     |
| 0946+006   | PMN J0948+0022  | 0.58     | G     | 113±2             | 2.40±0.03                   | 0.162±0.018            | 7172   |
| 0953+254   | OK 290          | 0.71     | Q     | 25.5±1.5          | 2.51±0.04                   | -                      | 749    |
| 0954+556   | 4C +55.17       | 0.90     | Q     | 80.3±1.4          | 1.836±0.014                 | 0.072±0.006            | 30593  |
| 0954+658   | S4 0954+65      | 0.37     | B     | 56.2±1.3          | 2.21±0.015                  | -                      | 7180   |
| 0955+476   | OK 492          | 1.88     | Q     | 21.2±1.2          | 2.62±0.05                   | -                      | 614    |
| 1009+249   | GB6 J1012+2439  | 1.80     | Q     | 35.1±1.6          | 2.12±0.04                   | 0.11±0.02              | 2944   |
| 1011+496   | 1ES 1011+496    | 0.21     | B     | 53.1±1.0          | 1.791±0.010                 | -                      | 21392  |
| 1012+232   | 4C +23.24       | 0.56     | Q     | 6.8±1.4           | 2.60±0.13                   | -                      | 48     |
| 1013+054   | TXS 1013+054    | 1.71     | Q     | 17.7±1.4          | 2.13±0.04                   | -                      | 964    |
| 1015+359   | B2 1015+35B     | 1.23     | Q     | 14.7±1.3          | 2.57±0.06                   | -                      | 319    |
| 1030+415   | S4 1030+41      | 1.12     | Q     | 23.0±1.2          | 2.35±0.03                   | -                      | 1267   |
| 1030+611   | S4 1030+61      | 1.40     | Q     | 57.4±1.4          | 2.14±0.015                  | 0.084±0.010            | 10565  |
| 1032-199   | PKS 1032-199    | 2.20     | Q     | <7.49             | -                           | -                      | 9      |
| 1034+574   | GB6 J1037+5711  | -        | B     | 17.3±0.9          | 1.70±0.03                   | 0.085±0.014            | 6180   |
| 1034-293   | PKS 1034-293    | 0.31     | Q     | 8.3±1.5           | 2.45±0.1                    | -                      | 94     |
| 1036+054   | PKS 1036+054    | 0.47     | Q     | <1.99             | -                           | -                      | 0      |
| 1038+064   | 4C +06.41       | 1.26     | Q     | 30.8±1.6          | 2.29±0.03                   | -                      | 1402   |
| 1044+719   | S5 1044+71      | 1.15     | Q     | 147.6±1.6         | 2.235±0.008                 | -                      | 31433  |
| 1045-188   | PKS 1045-18     | 0.60     | Q     | <3.13             | -                           | -                      | 14     |
| 1049+215   | 4C +21.28       | 1.30     | Q     | 6.2±1.4           | 2.58±0.14                   | -                      | 44     |
| 1055+018   | 4C +01.28       | 0.89     | Q     | 96±2              | 2.186±0.014                 | 0.044±0.009            | 11140  |
| 1055+201   | 4C +20.24       | 1.11     | Q     | <0.68             | -                           | -                      | 0      |
| 1055+567   | 7C 1055+5644    | 0.14     | B     | 25.9±0.9          | 1.923±0.019                 | -                      | 5601   |
| 1057-797   | PKS 1057-79     | 0.58     | B     | 30±2              | 2.07±0.05                   | 0.08±0.02              | 1690   |
| 1101+384   | Mrk 421         | 0.03     | B     | 209.9±1.6         | 1.75±0.004                  | -                      | 131490 |
| 1101-536   | PKS 1101-536    | -        | U     | 24±2              | 1.94±0.05                   | 0.10±0.02              | 1438   |
| 1104-445   | [HB89] 1104-445 | 1.60     | Q     | 41±2              | 2.75±0.04                   | -                      | 770    |
| 1114-483   | PMN J1117-4838  | -        | U     | 11±2              | 2.46±0.13                   | -                      | 35     |
| 1116-462   | PKS 1116-46     | -        | U     | 9.5±1.5           | 2.37±0.08                   | -                      | 101    |
| 1118-056   | PKS 1118-05     | 1.30     | Q     | 40.5±1.7          | 2.38±0.03                   | -                      | 1660   |
| 1121-640   | PMN J1123-6417  | -        | U     | 52±4              | 2.74±0.11                   | 0.48±0.17              | 257    |
| 1124-186   | PKS 1124-186    | 1.05     | Q     | 112±2             | 2.064±0.017                 | 0.068±0.008            | 17050  |
| 1127-145   | PKS 1127-14     | 1.18     | Q     | 30.6±1.8          | 2.74±0.05                   | -                      | 543    |
| 1128+385   | B2 1128+38      | 1.73     | Q     | 27.0±1.5          | 2.57±0.04                   | -                      | 730    |
| 1128-047   | PKS 1128-047    | 0.27     | G     | 6.9±1.4           | 2.40±0.10                   | -                      | 61     |
| 1144+402   | S4 1144+40      | 1.09     | Q     | 85.9±1.6          | 2.329±0.014                 | -                      | 10191  |
| 1144-379   | [HB89] 1144-379 | 1.05     | Q     | 37.6±1.6          | 2.25±0.03                   | -                      | 2062   |
| 1145-071   | PKS 1145-071    | 1.34     | Q     | 20.4±1.5          | 2.35±0.04                   | -                      | 547    |
| 1148-001   | 4C -00.47       | 1.98     | Q     | <3.75             | -                           | -                      | 1      |

<sup>a</sup> *Fermi*-LAT flux between 0.1-100 GeV in photons cm<sup>-2</sup> s<sup>-1</sup>.<sup>b</sup> *Fermi*-LAT spectral index  $\Gamma$ , in case of power-law spectrum  $dN/dE = N_0 \times (E/E_0)^{-\Gamma}$ , or  $\alpha$  in case of logParabola spectrum  $dN/dE = N_0 \times (E/E_b)^{-[\alpha+\beta \log(E/E_b)]}$ .<sup>c</sup> Curvature parameter of logParabola spectrum  $\beta$ .

TABLE C.6: Results of *Fermi*-LAT analysis in the range 0.1-100 GeV for the complete MOJAVE and TANAMI combined sample (continued).

| B1950 name | Common name       | Redshift | Class | Flux <sup>a</sup> | Spectral index <sup>b</sup> | Curvature <sup>c</sup> | TS     |
|------------|-------------------|----------|-------|-------------------|-----------------------------|------------------------|--------|
| 1149-084   | PKS B1149-084     | 2.37     | Q     | 20.7±1.7          | 2.40±0.05                   | -                      | 480    |
| 1150+497   | 4C +49.22         | 0.33     | Q     | 32.4±1.3          | 2.38±0.03                   | -                      | 2083   |
| 1150+812   | S5 1150+81        | 1.25     | Q     | <2.71             | -                           | -                      | 19     |
| 1156+295   | 4C +29.45         | 0.73     | Q     | 115.9±1.9         | 2.123±0.015                 | 0.078±0.008            | 20572  |
| 1157-215   | CGRABS J1159-2148 | 0.93     | Q     | <1.34             | -                           | -                      | 0      |
| 1202-262   | PKS 1203-26       | 0.79     | Q     | 27.6±1.8          | 2.65±0.05                   | -                      | 481    |
| 1213-172   | PKS 1213-17       | -        | U     | 9.7±1.8           | 2.63±0.12                   | -                      | 70     |
| 1215+303   | ON 325            | 0.13     | B     | 74.8±1.4          | 1.912±0.011                 | -                      | 17131  |
| 1218+304   | B2 1218+30        | 0.18     | B     | 15.5±0.9          | 1.66±0.02                   | -                      | 3318   |
| 1219+044   | 4C +04.42         | 0.97     | Q     | 74±3              | 2.81±0.05                   | 0.04±0.03              | 1878   |
| 1219+285   | W Comae           | 0.10     | B     | 45.1±1.4          | 2.103±0.018                 | -                      | 5183   |
| 1222+216   | 4C +21.35         | 0.43     | Q     | 385±3             | 2.24±0.009                  | 0.045±0.004            | 94468  |
| 1226+023   | 3C 273            | 0.16     | Q     | 339±3             | 2.609±0.014                 | 0.085±0.009            | 35935  |
| 1228+126   | M87               | 0.00     | G     | 15.9±1.1          | 2.0±0.03                    | -                      | 1264   |
| 1236+049   | BZQ J1239+0443    | 1.76     | Q     | 128±2             | 2.218±0.017                 | 0.109±0.011            | 14267  |
| 1243-072   | PKS 1243-072      | 1.29     | Q     | <8.02             | -                           | -                      | 19     |
| 1244-255   | PKS 1244-255      | 0.63     | Q     | 128±2             | 2.113±0.018                 | 0.1±0.009              | 15715  |
| 1246+586   | PG 1246+586       | -        | B     | 34.2±0.9          | 1.837±0.014                 | -                      | 10412  |
| 1251-713   | PKS 1251-71       | -        | U     | 7.5±1.8           | 2.29±0.1                    | -                      | 68     |
| 1253-055   | 3C 279            | 0.54     | Q     | 499±3             | 2.216±0.007                 | 0.071±0.004            | 115636 |
| 1257-326   | PKS 1257-326      | 1.26     | Q     | <0.93             | -                           | -                      | 0      |
| 1258-321   | ESO 443- G 024    | 0.02     | G     | <3.95             | -                           | -                      | 2      |
| 1300+248   | VIPS 0623         | 0.99     | B     | 24.8±1.2          | 2.14±0.03                   | -                      | 2025   |
| 1302-102   | PG 1302-102       | 0.28     | Q     | <11.00            | -                           | -                      | 16     |
| 1308+326   | OP 313            | 1.00     | Q     | 45.4±1.6          | 2.11±0.03                   | 0.085±0.014            | 4201   |
| 1313-333   | [HB89] 1313-333   | 1.21     | Q     | 50.2±1.8          | 2.28±0.02                   | -                      | 2632   |
| 1322-428   | Cen A, NGC 5128   | 0.0018   | G     | 169±3             | 2.670±0.015                 | -                      | 8855   |
| 1323+321   | 4C +32.44         | 0.37     | G     | <1.15             | -                           | -                      | 11     |
| 1323-526   | PMN J1326-5256    | -        | B     | 42±2              | 2.25±0.03                   | -                      | 1323   |
| 1324+224   | B2 1324+22        | 1.40     | Q     | 29.0±1.7          | 2.26±0.04                   | 0.15±0.03              | 1579   |
| 1325-558   | PMN J1329-5608    | -        | U     | 88±3              | 2.28±0.02                   | 0.106±0.015            | 3499   |
| 1328+254   | 3C 287            | 1.05     | Q     | <6.14             | -                           | -                      | 5      |
| 1328+307   | 3C 286            | 0.85     | Q     | 4.3±1.2           | 2.43±0.14                   | -                      | 43     |
| 1329-049   | OP -050           | 2.15     | Q     | 99±2              | 2.486±0.019                 | 0.113±0.016            | 6664   |
| 1329-126   | PMN J1332-1256    | 1.49     | Q     | 78±2              | 2.424±0.019                 | -                      | 3936   |
| 1331+170   | OP 151            | 2.08     | Q     | <7.39             | -                           | -                      | 8      |
| 1333-337   | IC 4296           | 0.01     | G     | <9.41             | -                           | -                      | 13     |
| 1334-127   | PKS 1335-127      | 0.54     | Q     | 34±2              | 2.29±0.04                   | 0.17±0.03              | 1543   |
| 1341-171   | PMN J1344-1723    | 2.51     | Q     | 26.2±1.8          | 2.13±0.04                   | 0.08±0.02              | 1380   |
| 1343+451   | VIPS 0700         | 2.53     | Q     | 144.2±1.8         | 2.125±0.013                 | 0.071±0.007            | 33103  |
| 1343-601   | Centaurus B       | 0.01     | G     | 59±4              | 2.44±0.04                   | -                      | 424    |
| 1344-376   | PMN J1347-3750    | 1.30     | Q     | 11.8±1.5          | 2.33±0.07                   | -                      | 206    |
| 1345+125   | 4C +12.50         | 0.12     | G     | <1.15             | -                           | -                      | 0      |
| 1348+308   | B2 1348+30B       | 0.71     | Q     | 17.5±1.3          | 2.47±0.05                   | -                      | 529    |
| 1354+195   | 4C +19.44         | 0.72     | Q     | 10.5±1.7          | 2.80±0.16                   | -                      | 72     |

<sup>a</sup> *Fermi*-LAT flux between 0.1-100 GeV in photons cm<sup>-2</sup> s<sup>-1</sup>.<sup>b</sup> *Fermi*-LAT spectral index  $\Gamma$ , in case of power-law spectrum  $dN/dE = N_0 \times (E/E_0)^{-\Gamma}$ , or  $\alpha$  in case of logParabola spectrum  $dN/dE = N_0 \times (E/E_b)^{-[\alpha+\beta \log(E/E_b)]}$ .<sup>c</sup> Curvature parameter of logParabola spectrum  $\beta$ .

TABLE C.7: Results of *Fermi*-LAT analysis in the range 0.1-100 GeV for the complete MOJAVE and TANAMI combined sample (continued).

| B1950 name | Common name     | Redshift | Class | Flux <sup>a</sup> | Spectral index <sup>b</sup> | Curvature <sup>c</sup> | TS     |
|------------|-----------------|----------|-------|-------------------|-----------------------------|------------------------|--------|
| 1354–152   | PKS 1354–152    | 1.89     | Q     | <5.06             | -                           | -                      | 2      |
| 1406–076   | PKS B1406–076   | 1.49     | Q     | 40.9±1.7          | 2.38±0.03                   | -                      | 1753   |
| 1409–651   | Circinus Galaxy | -        | U     | 3.8±1.5           | 1.97±0.13                   | -                      | 46     |
| 1413+135   | PKS B1413+135   | 0.25     | B     | 10.1±1.4          | 2.35±0.07                   | -                      | 191    |
| 1417+385   | B3 1417+385     | 1.83     | Q     | 13.0±1.3          | 2.49±0.06                   | -                      | 297    |
| 1418+546   | OQ 530          | 0.15     | B     | 28.2±1.2          | 2.35±0.03                   | -                      | 1877   |
| 1424+240   | OQ 240          | -        | B     | 68.6±1.6          | 1.72±0.014                  | 0.036±0.006            | 26243  |
| 1424+366   | B2 1424+36      | 1.09     | Q     | 3.4±1.0           | 2.29±0.13                   | -                      | 36     |
| 1424–418   | [HB89] 1424–418 | 1.52     | Q     | 493±3             | 2.028±0.006                 | 0.077±0.003            | 140128 |
| 1435+638   | VIPS 0792       | 2.07     | Q     | <6.71             | -                           | -                      | 18     |
| 1440–389   | PKS 1440–389    | 0.07     | B     | 21.0±1.1          | 1.75±0.02                   | -                      | 3936   |
| 1451–375   | [HB89] 1451–375 | 0.31     | U     | 27±2              | 2.76±0.06                   | -                      | 303    |
| 1454–354   | PKS 1454–354    | 1.42     | Q     | 61±2              | 2.12±0.03                   | 0.117±0.015            | 4940   |
| 1458+718   | 3C 309.1        | 0.90     | Q     | 9.1±1.1           | 2.56±0.08                   | -                      | 181    |
| 1502+036   | PKS 1502+036    | 0.41     | G     | 48.7±1.9          | 2.63±0.03                   | -                      | 1364   |
| 1502+106   | OR 103          | 1.84     | Q     | 303±2             | 2.052±0.009                 | 0.095±0.005            | 76751  |
| 1504+377   | B2 1504+37      | 0.67     | Q     | 61.6±1.5          | 2.468±0.019                 | -                      | 4715   |
| 1504–166   | PKS 1504–167    | 0.88     | Q     | <3.01             | -                           | -                      | 10     |
| 1505–496   | PMN J1508–4953  | 0.78     | U     | 57±3              | 2.87±0.05                   | -                      | 515    |
| 1508–055   | PKS 1508–05     | 1.19     | Q     | 44±2              | 2.49±0.03                   | -                      | 1057   |
| 1509+054   | PMN J1511+0518  | 0.08     | G     | <2.37             | -                           | -                      | 0      |
| 1510–089   | PKS 1510–08     | 0.36     | Q     | 850±4             | 2.299±0.004                 | 0.060±0.003            | 213032 |
| 1510–324   | PKS 1510–324    | 1.15     | Q     | 29±2              | 2.57±0.05                   | -                      | 406    |
| 1511–100   | PKS 1511–100    | 1.51     | Q     | 24±3              | 3.2±0.2                     | -                      | 62     |
| 1514+004   | CGCG 021-063    | 0.05     | G     | 8.7±1.6           | 2.45±0.1                    | -                      | 81     |
| 1514+197   | PKS 1514+197    | -        | B     | <8.45             | -                           | -                      | 11     |
| 1514–241   | AP Librae       | 0.05     | B     | 85.5±1.9          | 2.128±0.013                 | -                      | 8899   |
| 1519–273   | PKS 1519–273    | 1.30     | B     | 32.3±1.7          | 2.15±0.03                   | -                      | 1574   |
| 1520+319   | B2 1520+31      | 1.48     | Q     | 298±2             | 2.271±0.010                 | 0.074±0.005            | 69633  |
| 1529–131   | PMN J1532–1319  | -        | U     | 66.8±1.8          | 2.161±0.016                 | -                      | 5233   |
| 1532+016   | PKS 1532+01     | 1.43     | Q     | 26.0±1.8          | 2.46±0.04                   | -                      | 588    |
| 1538+149   | 4C +14.60       | 0.61     | B     | 4.4±1.2           | 2.13±0.11                   | -                      | 102    |
| 1542+616   | GB6 J1542+6129  | -        | B     | 44.5±1.2          | 1.863±0.017                 | 0.051±0.008            | 13499  |
| 1546+027   | PKS 1546+027    | 0.41     | Q     | 34.0±1.9          | 2.47±0.04                   | -                      | 850    |
| 1548+056   | 4C +05.64       | 1.42     | Q     | 24.2±1.7          | 2.42±0.04                   | -                      | 576    |
| 1549–790   | PKS 1549–79     | 0.15     | G     | <3.31             | -                           | -                      | 0      |
| 1551+130   | OR 186          | 1.31     | Q     | 38±2              | 2.35±0.04                   | 0.07±0.02              | 1520   |
| 1553+113   | PG 1553+113     | -        | B     | 61.5±1.6          | 1.615±0.012                 | 0.022±0.005            | 31029  |
| 1555+001   | PKS 1555+001    | 1.77     | Q     | <4.96             | -                           | -                      | 24     |
| 1600–445   | PMN J1604–4441  | -        | U     | 53±3              | 2.47±0.04                   | -                      | 623    |
| 1600–489   | PMN J1603–4904  | 0.18     | U     | 63±4              | 2.02±0.02                   | -                      | 2450   |
| 1604+159   | 4C +15.54       | 0.50     | Q     | 40.5±1.6          | 2.28±0.02                   | -                      | 2435   |
| 1606+106   | 4C +10.45       | 1.23     | Q     | 45.5±1.9          | 2.67±0.03                   | -                      | 1144   |
| 1607+268   | CTD 93          | 0.47     | G     | <6.54             | -                           | -                      | 7      |
| 1610–771   | [HB89] 1610–771 | 1.71     | Q     | 58±2              | 2.49±0.03                   | 0.07±0.02              | 2021   |

<sup>a</sup> *Fermi*-LAT flux between 0.1-100 GeV in photons cm<sup>-2</sup> s<sup>-1</sup>.<sup>b</sup> *Fermi*-LAT spectral index  $\Gamma$ , in case of power-law spectrum  $dN/dE = N_0 \times (E/E_0)^{-\Gamma}$ , or  $\alpha$  in case of logParabola spectrum  $dN/dE = N_0 \times (E/E_b)^{-[\alpha+\beta \log(E/E_b)]}$ .<sup>c</sup> Curvature parameter of logParabola spectrum  $\beta$ .

TABLE C.8: Results of *Fermi*-LAT analysis in the range 0.1-100 GeV for the complete MOJAVE and TANAMI combined sample (continued).

| B1950 name | Common name       | Redshift | Class | Flux <sup>a</sup> | Spectral index <sup>b</sup> | Curvature <sup>c</sup> | TS    |
|------------|-------------------|----------|-------|-------------------|-----------------------------|------------------------|-------|
| 1611+343   | DA 406            | 1.40     | Q     | 21.9±1.3          | 2.37±0.04                   | -                      | 973   |
| 1613-586   | PMN J1617-5848    | -        | U     | 30±3              | 2.55±0.06                   | -                      | 262   |
| 1617+229   | CGRABS J1619+2247 | 1.99     | Q     | <4.47             | -                           | -                      | 12    |
| 1622-253   | PKS 1622-253      | 0.79     | Q     | 86±3              | 2.154±0.02                  | 0.169±0.014            | 4644  |
| 1622-297   | PKS 1622-29       | 0.81     | Q     | 99±3              | 2.59±0.03                   | 0.105±0.018            | 3425  |
| 1633+382   | 4C +38.41         | 1.81     | Q     | 312±2             | 2.398±0.007                 | 0.125±0.006            | 72132 |
| 1636+473   | 4C +47.44         | 0.74     | Q     | 34.9±1.4          | 2.45±0.03                   | -                      | 1889  |
| 1637+574   | OS 562            | 0.75     | Q     | 16.7±1.3          | 2.88±0.07                   | -                      | 265   |
| 1637+826   | NGC 6251          | 0.02     | G     | 18.4±1.3          | 2.22±0.04                   | 0.12±0.03              | 1281  |
| 1638+398   | NRAO 512          | 1.67     | Q     | 35±2              | 2.29±0.03                   | 0.11±0.02              | 2083  |
| 1641+399   | 3C 345            | 0.59     | Q     | 61.0±1.9          | 2.46±0.02                   | -                      | 2747  |
| 1642+690   | 4C +69.21         | 0.75     | Q     | <1.41             | -                           | -                      | 4     |
| 1646-506   | PMN J1650-5044    | -        | U     | 68±4              | 2.33±0.03                   | -                      | 1309  |
| 1652+398   | Mrk 501           | 0.03     | B     | 61.3±1.1          | 1.719±0.009                 | -                      | 27289 |
| 1653-329   | Swift J1656.3-330 | 2.40     | Q     | 42±3              | 2.76±0.06                   | -                      | 267   |
| 1655+077   | PKS 1655+077      | 0.62     | Q     | <4.85             | -                           | -                      | 7     |
| 1656+053   | PKS 1656+053      | 0.88     | Q     | <10.63            | -                           | -                      | 17    |
| 1656+477   | S4 1656+47        | 1.62     | Q     | <2.87             | -                           | -                      | 1     |
| 1656+482   | 4C +48.41         | 1.67     | B     | 39.4±1.4          | 2.41±0.02                   | -                      | 2385  |
| 1700+685   | TXS 1700+685      | 0.30     | Q     | 60.6±1.4          | 2.349±0.016                 | -                      | 6067  |
| 1708+433   | B3 1708+433       | 1.03     | Q     | 51.9±1.6          | 2.21±0.03                   | 0.065±0.014            | 5197  |
| 1713-518   | PMN J1717-5155    | -        | U     | 31±3              | 2.68±0.06                   | -                      | 227   |
| 1714-336   | PMN J1717-3342    | -        | B     | 86±5              | 2.45±0.03                   | -                      | 788   |
| 1716-771   | PKS 1716-771      | -        | U     | 53.9±1.9          | 2.29±0.02                   | -                      | 2681  |
| 1717+178   | OT 129            | 0.14     | B     | 25.0±1.3          | 2.02±0.03                   | -                      | 2332  |
| 1718-649   | NGC 6328          | 0.01     | G     | 5.2±1.9           | 2.43±0.18                   | -                      | 29    |
| 1722+119   | 1H 1720+117       | -        | B     | 25.3±1.3          | 1.81±0.02                   | -                      | 3823  |
| 1722+401   | VIPS 1080         | 1.05     | Q     | 22.6±1.4          | 2.42±0.04                   | -                      | 783   |
| 1725+044   | PKS 1725+044      | 0.29     | Q     | 32±2              | 2.81±0.06                   | -                      | 301   |
| 1726+455   | S4 1726+45        | 0.72     | Q     | 53.4±1.7          | 2.36±0.03                   | 0.078±0.017            | 3762  |
| 1730-130   | NRAO 530          | 0.90     | Q     | 116±3             | 2.21±0.02                   | 0.087±0.011            | 6059  |
| 1732+389   | OT 355            | 0.98     | Q     | 43.7±1.5          | 2.40±0.02                   | -                      | 2546  |
| 1733-565   | PKS 1733-56       | 0.10     | G     | <0.50             | -                           | -                      | 0     |
| 1738+499   | OT 463            | 1.54     | Q     | 20.7±1.2          | 2.29±0.03                   | -                      | 980   |
| 1739+522   | 4C +51.37         | 1.38     | Q     | 43.2±1.5          | 2.43±0.02                   | -                      | 2533  |
| 1741-038   | PKS 1741-03       | 1.05     | Q     | 10±3              | 2.47±0.14                   | -                      | 38    |
| 1749+096   | 4C +09.57         | 0.32     | B     | 71±2              | 2.17±0.02                   | 0.066±0.012            | 5399  |
| 1749+701   | S4 1749+70        | 0.77     | B     | 45.2±1.2          | 1.977±0.014                 | -                      | 9334  |
| 1751+288   | B2 1751+28        | 1.12     | Q     | 3.0±1.2           | 2.30±0.17                   | -                      | 25    |
| 1758+388   | B3 1758+388B      | 2.09     | Q     | <6.84             | -                           | -                      | 8     |
| 1759-396   | PMN J1802-3940    | 1.32     | Q     | 82±3              | 2.18±0.02                   | 0.09±0.013             | 4920  |
| 1800+440   | S4 1800+44        | 0.66     | Q     | 38.1±1.4          | 2.34±0.02                   | -                      | 2291  |
| 1803+784   | S5 1803+784       | 0.68     | B     | 82.3±1.4          | 2.198±0.011                 | -                      | 14300 |
| 1807+698   | 3C 371            | 0.05     | B     | 58.0±1.4          | 2.229±0.015                 | -                      | 6687  |
| 1814-637   | PKS 1814-63       | 0.06     | G     | <0.03             | -                           | -                      | 1     |

<sup>a</sup> *Fermi*-LAT flux between 0.1-100 GeV in photons cm<sup>-2</sup> s<sup>-1</sup>.<sup>b</sup> *Fermi*-LAT spectral index  $\Gamma$ , in case of power-law spectrum  $dN/dE = N_0 \times (E/E_0)^{-\Gamma}$ , or  $\alpha$  in case of logParabola spectrum  $dN/dE = N_0 \times (E/E_b)^{-[\alpha+\beta \log(E/E_b)]}$ .<sup>c</sup> Curvature parameter of logParabola spectrum  $\beta$ .

TABLE C.9: Results of *Fermi*-LAT analysis in the range 0.1-100 GeV for the complete MOJAVE and TANAMI combined sample (continued).

| B1950 name | Common name      | Redshift | Class | Flux <sup>a</sup> | Spectral index <sup>b</sup> | Curvature <sup>c</sup> | TS    |
|------------|------------------|----------|-------|-------------------|-----------------------------|------------------------|-------|
| 1823+568   | 4C +56.27        | 0.66     | B     | 44.1±1.6          | 2.35±0.02                   | -                      | 2587  |
| 1824-582   | PKS 1824-582     | -        | U     | 101±2             | 2.586±0.018                 | -                      | 5172  |
| 1827+062   | TXS 1827+062     | 0.75     | Q     | 18±3              | 2.29±0.06                   | -                      | 201   |
| 1828+487   | 3C 380           | 0.69     | Q     | 34.2±1.5          | 2.40±0.03                   | -                      | 1578  |
| 1842+681   | GB6 J1842+6809   | 0.47     | Q     | 9.4±1.6           | 2.67±0.11                   | -                      | 77    |
| 1845+797   | 3C 390.3         | 0.06     | G     | <1.34             | -                           | -                      | 5     |
| 1846+322   | B2 1846+32A      | 0.80     | Q     | 55±2              | 2.42±0.02                   | -                      | 1744  |
| 1849+670   | S4 1849+67       | 0.66     | Q     | 80.6±1.7          | 2.172±0.015                 | 0.085±0.010            | 12413 |
| 1851+488   | S4 1851+48       | 1.25     | Q     | 22.6±1.3          | 2.20±0.03                   | -                      | 1350  |
| 1901+319   | 3C 395           | 0.63     | Q     | <4.83             | -                           | -                      | 16    |
| 1902+556   | TXS 1902+556     | -        | B     | 22.9±1.2          | 1.78±0.02                   | 0.086±0.013            | 6150  |
| 1908-201   | PKS B1908-201    | 1.12     | Q     | 113±2             | 2.439±0.016                 | -                      | 5640  |
| 1915-458   | PKS 1915-458     | 2.47     | Q     | <7.38             | -                           | -                      | 7     |
| 1920-211   | OV -235          | 0.87     | Q     | 32±2              | 2.09±0.04                   | 0.12±0.02              | 2090  |
| 1921-293   | [HB89] 1921-293  | -        | U     | 37.9±1.9          | 2.35±0.03                   | -                      | 1256  |
| 1921-293   | PKS B1921-293    | 0.35     | Q     | 37.9±1.9          | 2.35±0.03                   | -                      | 1256  |
| 1923+210   | PKS B1923+210    | -        | B     | <14.60            | -                           | -                      | 10    |
| 1928+738   | 4C +73.18        | 0.30     | Q     | <6.72             | -                           | -                      | 9     |
| 1933-400   | PKS 1933-400     | 0.96     | Q     | 28.8±1.8          | 2.58±0.05                   | -                      | 489   |
| 1934-638   | PKS 1934-63      | 0.18     | G     | <5.56             | -                           | -                      | 2     |
| 1936-155   | PKS 1936-15      | 1.66     | Q     | 5.7±1.6           | 2.33±0.12                   | -                      | 44    |
| 1936-623   | PKS 1936-623     | -        | U     | 66.7±1.8          | 2.47±0.02                   | -                      | 3598  |
| 1951-115   | TXS 1951-115     | 0.68     | Q     | 20.1±1.8          | 2.30±0.05                   | -                      | 426   |
| 1954-388   | [HB89] 1954-388  | 0.63     | Q     | 60±2              | 2.17±0.03                   | 0.114±0.016            | 4124  |
| 1957+405   | Cygnus A         | 0.06     | G     | <7.40             | -                           | -                      | 20    |
| 1958-179   | PKS 1958-179     | 0.65     | Q     | 30.3±1.8          | 2.30±0.03                   | -                      | 980   |
| 1959+437   | MG4 J200112+4352 | -        | B     | 44±2              | 1.96±0.02                   | -                      | 3609  |
| 1959+650   | 1ES 1959+650     | 0.05     | B     | 54.0±1.2          | 1.786±0.011                 | -                      | 16040 |
| 2004-447   | PKS 2004-447     | 0.24     | G     | 24.3±1.6          | 2.55±0.05                   | -                      | 519   |
| 2005+403   | TXS 2005+403     | 1.74     | Q     | <13.18            | -                           | -                      | 24    |
| 2005-489   | [HB89] 2005-489  | 0.07     | B     | 17.7±1.0          | 1.80±0.02                   | -                      | 2980  |
| 2007+777   | S5 2007+77       | 0.34     | B     | 42.5±1.4          | 2.191±0.019                 | -                      | 3813  |
| 2008-159   | PKS 2008-159     | 1.18     | Q     | 12.3±1.9          | 2.62±0.1                    | -                      | 79    |
| 2013+370   | MG2 J201534+3710 | 0.86     | Q     | 161±5             | 2.49±0.02                   | 0.176±0.014            | 4519  |
| 2021+317   | 4C +31.56        | 0.36     | U     | 8±2               | 2.04±0.08                   | -                      | 115   |
| 2021+614   | OW 637           | 0.23     | G     | <10.88            | -                           | -                      | 20    |
| 2022-077   | PKS 2023-07      | 1.39     | Q     | 142±2             | 2.199±0.013                 | 0.087±0.008            | 18300 |
| 2023+335   | B2 2023+33       | 0.22     | Q     | 83±4              | 2.73±0.05                   | 0.13±0.03              | 852   |
| 2027-308   | PKS 2027-308     | 0.54     | G     | <0.97             | -                           | -                      | 4     |
| 2029+121   | PKS 2029+121     | 1.21     | Q     | 14.1±1.9          | 2.40±0.07                   | -                      | 183   |
| 2032+107   | OW 154.9         | 0.60     | Q     | 127±2             | 2.392±0.013                 | -                      | 8924  |
| 2037+511   | 3C 418           | 1.69     | Q     | 50±3              | 2.71±0.05                   | -                      | 388   |
| 2047+098   | PKS 2047+098     | -        | U     | 23.4±1.8          | 2.46±0.05                   | -                      | 436   |
| 2052-474   | [HB89] 2052-474  | 1.49     | Q     | 127±2             | 2.294±0.017                 | 0.101±0.011            | 14492 |
| 2106-413   | [HB89] 2106-413  | 1.06     | Q     | 5.0±1.2           | 2.38±0.12                   | -                      | 41    |

<sup>a</sup> *Fermi*-LAT flux between 0.1-100 GeV in photons cm<sup>-2</sup> s<sup>-1</sup>.<sup>b</sup> *Fermi*-LAT spectral index  $\Gamma$ , in case of power-law spectrum  $dN/dE = N_0 \times (E/E_0)^{-\Gamma}$ , or  $\alpha$  in case of logParabola spectrum  $dN/dE = N_0 \times (E/E_0)^{-[\alpha+\beta \log(E/E_b)]}$ .<sup>c</sup> Curvature parameter of logParabola spectrum  $\beta$ .

TABLE C.10: Results of *Fermi*-LAT analysis in the range 0.1-100 GeV for the complete MOJAVE and TANAMI combined sample (continued).

| BI950 name | Common name     | Redshift | Class | Flux <sup>a</sup> | Spectral index <sup>b</sup> | Curvature <sup>c</sup> | TS     |
|------------|-----------------|----------|-------|-------------------|-----------------------------|------------------------|--------|
| 2113+293   | B2 2113+29      | 1.51     | Q     | 52.9±1.9          | 2.33±0.02                   | -                      | 2386   |
| 2121+053   | PKS 2121+053    | 1.94     | Q     | 8.3±1.4           | 2.30±0.08                   | -                      | 129    |
| 2123-463   | PKS 2123-463    | 1.67     | Q     | 33.3±1.6          | 2.53±0.04                   | -                      | 1055   |
| 2126-158   | PKS 2126-158    | 3.27     | Q     | <8.65             | -                           | -                      | 22     |
| 2128+048   | PKS 2127+04     | 0.99     | G     | <1.91             | -                           | -                      | 0      |
| 2128-123   | PKS 2128-12     | 0.50     | Q     | <1.76             | -                           | -                      | 0      |
| 2131-021   | 4C -02.81       | 1.28     | Q     | 16.8±1.4          | 2.24±0.04                   | -                      | 625    |
| 2134+004   | PKS 2134+004    | 1.93     | Q     | 10.9±1.8          | 2.82±0.15                   | -                      | 64     |
| 2136+141   | OX 161          | 2.43     | Q     | <11.83            | -                           | -                      | 18     |
| 2136-428   | PMN J2139-4235  | -        | B     | 43.6±1.5          | 1.93±0.02                   | 0.056±0.011            | 6978   |
| 2141+175   | OX 169          | 0.21     | Q     | 155±2             | 2.426±0.018                 | 0.033±0.009            | 12677  |
| 2142-758   | PKS 2142-75     | 1.14     | Q     | 146±2             | 2.423±0.019                 | 0.025±0.009            | 13033  |
| 2144+092   | PKS 2144+092    | 1.11     | Q     | 41±2              | 2.19±0.05                   | 0.17±0.03              | 2015   |
| 2145+067   | 4C +06.69       | 1.00     | Q     | 11.5±1.7          | 2.69±0.10                   | -                      | 77     |
| 2149-306   | PKS 2149-306    | 2.35     | Q     | 101±2             | 2.58±0.04                   | 0.21±0.03              | 4611   |
| 2152-699   | ESO 075- G 041  | 0.03     | G     | <6.40             | -                           | -                      | 15     |
| 2154-838   | PKS 2155-83     | -        | Q     | 52±2              | 2.55±0.03                   | 0.13±0.03              | 1880   |
| 2155+312   | B2 2155+31      | 1.49     | Q     | 50±2              | 2.09±0.03                   | 0.144±0.017            | 4468   |
| 2155-152   | PKS 2155-152    | 0.67     | Q     | 16.4±1.3          | 2.21±0.04                   | -                      | 625    |
| 2155-304   | [HB89] 2155-304 | 0.12     | B     | 122.1±1.8         | 1.764±0.009                 | 0.033±0.004            | 51911  |
| 2200+420   | BL Lac          | 0.07     | B     | 298±3             | 2.094±0.010                 | 0.051±0.004            | 54949  |
| 2201+171   | PKS 2201+171    | 1.08     | Q     | 48.3±1.9          | 2.10±0.03                   | 0.095±0.016            | 4006   |
| 2201+315   | 4C +31.63       | 0.29     | Q     | 28±2              | 3.56±0.17                   | -                      | 203    |
| 2204-540   | [HB89] 2204-540 | 1.21     | Q     | 19.8±1.4          | 2.52±0.05                   | -                      | 529    |
| 2209+236   | PKS 2209+236    | 1.12     | Q     | 16.8±1.3          | 2.17±0.04                   | -                      | 692    |
| 2216-038   | PKS 2216-03     | 0.90     | Q     | <3.21             | -                           | -                      | 16     |
| 2223+210   | DA 580          | 1.96     | Q     | 9.0±1.6           | 2.66±0.12                   | -                      | 60     |
| 2223-052   | 3C 446          | 1.40     | Q     | 34.3±1.8          | 2.48±0.04                   | -                      | 958    |
| 2227-088   | PHL 5225        | 1.56     | Q     | 110±2             | 2.33±0.03                   | 0.171±0.017            | 7167   |
| 2230+114   | CTA 102         | 1.04     | Q     | 683±3             | 2.092±0.006                 | 0.078±0.003            | 212281 |
| 2233-148   | OY -156         | -        | B     | 76.1±1.9          | 2.018±0.018                 | 0.077±0.010            | 11423  |
| 2234+282   | CTD 135         | 0.79     | B     | 65.9±1.9          | 2.11±0.03                   | 0.089±0.013            | 6974   |
| 2241+200   | RGB J2243+203   | -        | B     | 25.6±1.1          | 1.79±0.02                   | -                      | 4991   |
| 2241+406   | TXS 2241+406    | 1.17     | Q     | 86.0±1.8          | 2.124±0.012                 | -                      | 9649   |
| 2243-123   | PKS 2243-123    | 0.63     | Q     | <3.35             | -                           | -                      | 17     |
| 2247-283   | PMN J2250-2806  | 0.52     | Q     | 41.8±1.5          | 2.16±0.02                   | -                      | 3716   |
| 2251+158   | 3C 454.3        | 0.86     | Q     | 2015±5            | 1.648±0.014                 | -                      | 875325 |
| 2254+074   | PKS 2254+074    | 0.19     | B     | <3.00             | -                           | -                      | 15     |
| 2255-282   | PKS 2255-282    | 0.93     | Q     | 68.3±1.9          | 2.29±0.03                   | 0.125±0.017            | 5191   |
| 2308+341   | B2 2308+34      | 1.82     | Q     | 82±2              | 2.20±0.02                   | 0.086±0.012            | 7721   |
| 2318+049   | PKS 2318+049    | 0.62     | Q     | <2.48             | -                           | -                      | 0      |
| 2319+317   | B2 2319+31      | 1.49     | Q     | 44.8±1.8          | 2.07±0.03                   | 0.113±0.016            | 4134   |
| 2320-035   | PKS 2320-035    | 1.41     | Q     | 63.0±1.9          | 2.02±0.03                   | 0.125±0.014            | 6760   |
| 2325+093   | OZ 042          | 1.84     | Q     | 57±2              | 2.72±0.03                   | -                      | 1571   |
| 2326-477   | [HB89] 2326-477 | 1.30     | Q     | 11.0±1.6          | 2.57±0.09                   | -                      | 146    |

<sup>a</sup> *Fermi*-LAT flux between 0.1-100 GeV in photons cm<sup>-2</sup> s<sup>-1</sup>.<sup>b</sup> *Fermi*-LAT spectral index  $\Gamma$ , in case of power-law spectrum  $dN/dE = N_0 \times (E/E_0)^{-\Gamma}$ , or  $\alpha$  in case of logParabola spectrum  $dN/dE = N_0 \times (E/E_b)^{-[\alpha+\beta \log(E/E_b)]}$ .<sup>c</sup> Curvature parameter of logParabola spectrum  $\beta$ .

TABLE C.11: Results of *Fermi*-LAT analysis in the range 0.1-100 GeV for the complete MOJAVE and TANAMI combined sample (continued).

| B1950 name | Common name     | Redshift | Class | Flux <sup>a</sup> | Spectral index <sup>b</sup> | Curvature <sup>c</sup> | TS    |
|------------|-----------------|----------|-------|-------------------|-----------------------------|------------------------|-------|
| 2326-502   | PKS 2326-502    | 0.52     | Q     | 224±2             | 2.079±0.010                 | 0.11±0.006             | 57035 |
| 2328-220   | PMN J2331-2148  | 0.56     | Q     | 18.6±1.5          | 2.13±0.07                   | 0.18±0.04              | 818   |
| 2331+073   | TXS 2331+073    | 0.40     | Q     | 10.0±1.6          | 2.41±0.08                   | -                      | 124   |
| 2342-161   | PMN J2345-1555  | 0.62     | Q     | 113.8±1.9         | 2.024±0.011                 | 0.100±0.007            | 24166 |
| 2344+514   | 1ES 2344+514    | 0.04     | B     | 18.0±1.0          | 1.81±0.02                   | -                      | 2689  |
| 2345-167   | PKS 2345-16     | 0.58     | Q     | 45.5±1.8          | 2.32±0.02                   | -                      | 1984  |
| 2351+456   | 4C +45.51       | 1.99     | Q     | 7.1±1.5           | 2.51±0.12                   | -                      | 62    |
| 2353+816   | S5 2353+81      | 1.34     | B     | 7.1±1.6           | 2.57±0.14                   | -                      | 50    |
| 2355-534   | [HB89] 2355-534 | 1.01     | Q     | 15.9±1.4          | 2.55±0.06                   | -                      | 344   |
| 2356+196   | PKS 2356+196    | 1.07     | Q     | <5.84             | -                           | -                      | 3     |

<sup>a</sup> *Fermi*-LAT flux between 0.1-100 GeV in photons cm<sup>-2</sup> s<sup>-1</sup>.

<sup>b</sup> *Fermi*-LAT spectral index  $\Gamma$ , in case of power-law spectrum  $dN/dE = N_0 \times (E/E_0)^{-\Gamma}$ , or  $\alpha$  in case of logParabola spectrum  $dN/dE = N_0 \times (E/E_b)^{-[\alpha + \beta \log(E/E_b)]}$ .

<sup>c</sup> Curvature parameter of logParabola spectrum  $\beta$ .

# Bibliography

- Aartsen, M. G., Abbasi, R., Abdou, Y., et al. 2013, *Physical Review Letters*, 111, 021103
- Aartsen, M. G., Abraham, K., Ackermann, M., et al. 2016, *Physical Review Letters*, 117, 241101
- Aartsen, M. G., Ackermann, M., Adams, J., et al. 2014, *Physical Review Letters*, 113, 101101
- Abbott, B. P., Abbott, R., Abbott, T. D., et al. 2017, *Phys. Rev. Lett.*, 119, 161101
- Abbott, B. P., Abbott, R., Abbott, T. D., et al. 2017a, *ApJ*, 848, L13
- Abbott, B. P., Abbott, R., Abbott, T. D., et al. 2017b, *ApJ*, 848, L12
- Abdalla, H., Abramowski, A., Aharonian, F., et al. 2018, *MNRAS*, 476, 4187
- Abdo, A. A., Ackermann, M., Ajello, M., et al. 2010a, *ApJS*, 188, 405
- Abdo, A. A., Ackermann, M., Ajello, M., et al. 2009a, *ApJ*, 699, 31
- Abdo, A. A., Ackermann, M., Ajello, M., et al. 2009b, *ApJ*, 707, 55
- Abdo, A. A., Ackermann, M., Ajello, M., et al. 2010b, *ApJ*, 719, 1433
- Abdo, A. A., Ackermann, M., Ajello, M., et al. 2010c, *Science*, 328, 725
- Abdo, A. A., Ackermann, M., Ajello, M., et al. 2010d, *ApJ*, 720, 912
- Acero, F., Ackermann, M., Ajello, M., et al. 2015, *ApJS*, 218, 23
- Ackermann, M., Ajello, M., Allafort, A., et al. 2011, *ApJ*, 741, 30
- Ackermann, M., Ajello, M., Baldini, L., et al. 2016, *ApJ*, 826, 1
- Aharonian, F., Akhperjanian, A., Beilicke, M., et al. 2003, *A&A*, 403, L1
- Aharonian, F., Akhperjanian, A. G., Bazer-Bachi, A. R., et al. 2006, *Science*, 314, 1424
- Akritas, M. G. & Siebert, J. 1996, *MNRAS*, 278, 919
- Aleksić, J., Ansoldi, S., Antonelli, L. A., et al. 2014, *Science*, 346, 1080
- Angioni, R., Grandi, P., Torresi, E., Vignali, C., & Knödlseher, J. 2017, *Astroparticle Physics*, 92, 42
- Antonucci, R. 1993, *ARA&A*, 31, 473

- Antonucci, R. R. J. & Miller, J. S. 1985, *ApJ*, 297, 621
- Atwood, W. B., Abdo, A. A., Ackermann, M., et al. 2009, *ApJ*, 697, 1071
- Baade, W. & Minkowski, R. 1954, *ApJ*, 119, 206
- Baczko, A.-K., Schulz, R., Kadler, M., et al. 2016, *A&A*, 593, A47
- Barvainis, R. 1987, *ApJ*, 320, 537
- Beckmann, V. & Shrader, C. R. 2012, *Active Galactic Nuclei*
- Begelman, M. C. 1979, *MNRAS*, 187, 237
- Bennett, A. S. 1962, *MmRAS*, 68, 163
- Bignami, G. F., Boella, G., Burger, J. J., et al. 1975, *Space Science Instrumentation*, 1, 245
- Boccardi, B., Krichbaum, T. P., Ros, E., & Zensus, J. A. 2017, *A&A Rev.*, 25, 4
- Böck, M., Kadler, M., Müller, C., et al. 2016, *A&A*, 590, A40
- Bridle, A. H., Hough, D. H., Lonsdale, C. J., Burns, J. O., & Laing, R. A. 1994, *AJ*, 108, 766
- Brown, A. M. & Adams, J. 2012, *MNRAS*, 421, 2303
- Casadio, C., Gómez, J. L., Grandi, P., et al. 2015, *ApJ*, 808, 162
- Cerruti, M., Zech, A., Boisson, C., & Inoue, S. 2015, *MNRAS*, 448, 910
- Chatterjee, R., Marscher, A. P., Jorstad, S. G., et al. 2011, *ApJ*, 734, 43
- Cohen, M. H., Lister, M. L., Homan, D. C., et al. 2007, *ApJ*, 658, 232
- D'Abrusco, R., Massaro, F., Paggi, A., et al. 2014, *ApJS*, 215, 14
- D'Ammando, F., Orienti, M., Tavecchio, F., et al. 2015, *MNRAS*, 450, 3975
- Doeleman, S. S., Fish, V. L., Schenck, D. E., et al. 2012, *Science*, 338, 355
- Edge, D. O., Shakeshaft, J. R., McAdam, W. B., Baldwin, J. E., & Archer, S. 1959, *MmRAS*, 68, 37
- Fabian, A. C., Zoghbi, A., Ross, R. R., et al. 2009, *Nature*, 459, 540
- Fanaroff, B. L. & Riley, J. M. 1974, *MNRAS*, 167, 31P
- Fey, A. L., Ojha, R., Reynolds, J. E., et al. 2004, *AJ*, 128, 2593
- Fromm, C. M., Ros, E., Perucho, M., et al. 2013, *A&A*, 557, A105
- Ghisellini, G., ed. 2013, *Lecture Notes in Physics*, Berlin Springer Verlag, Vol. 873, *Radiative Processes in High Energy Astrophysics*
- Ghisellini, G. & Celotti, A. 2001, *A&A*, 379, L1
- Ghisellini, G., Righi, C., Costamante, L., & Tavecchio, F. 2017, *MNRAS*, 469, 255

- Ghisellini, G., Tavecchio, F., Foschini, L., & Ghirlanda, G. 2011, *MNRAS*, 414, 2674
- Ghisellini, G., Tavecchio, F., Maraschi, L., Celotti, A., & Sbarrato, T. 2014, *Nature*, 515, 376
- Giroletti, M., Giovannini, G., Taylor, G. B., & Falomo, R. 2004, *ApJ*, 613, 752
- Giroletti, M. & Polatidis, A. 2009, *Astronomische Nachrichten*, 330, 193
- Goldoni, P., Pita, S., Boisson, C., et al. 2016, *A&A*, 586, L2
- Grandi, P., Capetti, A., & Baldi, R. D. 2016, *MNRAS*, 457, 2
- Grandi, P., Torresi, E., De Rosa, A., Rainó, S., & Malaguti, G. 2013, in *European Physical Journal Web of Conferences*, Vol. 61, *European Physical Journal Web of Conferences*, 04007
- Grandi, P., Torresi, E., & on behalf of the FERMI-LAT collaboration. 2012a, *ArXiv e-prints* [[arXiv]1205.1686]
- Grandi, P., Torresi, E., & Stanghellini, C. 2012b, *ApJ*, 751, L3
- Gubbay, J., Legg, A. J., Robertson, D. S., et al. 1969, *Nature*, 224, 1094
- Haardt, F. & Maraschi, L. 1991, *ApJ*, 380, L51
- Hancock, P. J., Tingay, S. J., Sadler, E. M., Phillips, C., & Deller, A. T. 2009, *MNRAS*, 397, 2030
- Hardcastle, M. J., Lenc, E., Birkinshaw, M., et al. 2016, *MNRAS*, 455, 3526
- Harrison, C. 2014, PhD thesis, Durham University
- Hartman, R. C., Bertsch, D. L., Bloom, S. D., et al. 1999, *ApJS*, 123, 79
- Hervet, O., Boisson, C., & Sol, H. 2016, *A&A*, 592, A22
- Ho, L. C., Filippenko, A. V., & Sargent, W. L. 1995, *ApJS*, 98, 477
- Högbom, J. A. 1974, *A&AS*, 15, 417
- IceCube Collaboration, Aartsen, M. G., Ackermann, M., et al. 2018, *Science*, 361, eaat1378
- Ichikawa, K. & Inayoshi, K. 2017, *ApJ*, 840, L9
- Janiak, M., Sikora, M., & Moderski, R. 2016, *MNRAS*, 458, 2360
- Kadler, M., Krauß, F., Mannheim, K., et al. 2016, *Nature Physics*, 12, 807
- Kadler, M., Ojha, R., & TANAMI Collaboration. 2015, *Astronomische Nachrichten*, 336, 499
- Kadler, M., Ojha, R., Tingay, S., Lovell, J., & TANAMI Collaboration. 2007, in *Bulletin of the American Astronomical Society*, Vol. 39, *American Astronomical Society Meeting Abstracts*, 732
- Kellermann, K. I., Sramek, R., Schmidt, M., Shaffer, D. B., & Green, R. 1989, *AJ*, 98, 1195
- Kotera, K. & Olinto, A. V. 2011, *ARA&A*, 49, 119

- Kovalev, Y. Y., Aller, H. D., Aller, M. F., et al. 2009, *ApJ*, 696, L17
- Kovalev, Y. Y., Kellermann, K. I., Lister, M. L., et al. 2005, *AJ*, 130, 2473
- Kraushaar, W., Clark, G. W., Garmire, G., et al. 1965, *ApJ*, 141, 845
- Krauß, F., Kadler, M., Mannheim, K., et al. 2014, *A&A*, 566, L7
- Krauß, F., Wilms, J., Kadler, M., et al. 2016, *A&A*, 591, A130
- Kuehr, H., Witzel, A., Pauliny-Toth, I. I. K., & Nauber, U. 1981, *A&AS*, 45, 367
- Lawrence, A. 1991, *MNRAS*, 252, 586
- Leon, S., Cortes, P. C., Guerard, M., et al. 2016, *A&A*, 586, A70
- Lico, R., Giroletti, M., Orienti, M., et al. 2017, *A&A*, 606, A138
- Lico, R., Giroletti, M., Orienti, M., et al. 2012, *A&A*, 545, A117
- Liska, M., Hesp, C., Tchekhovskoy, A., et al. 2018, *MNRAS*, 474, L81
- Lister, M. L., Aller, M. F., Aller, H. D., et al. 2013, *AJ*, 146, 120
- Lister, M. L., Aller, M. F., Aller, H. D., et al. 2016, *AJ*, 152, 12
- Lister, M. L., Cohen, M. H., Homan, D. C., et al. 2009a, *AJ*, 138, 1874
- Lister, M. L., Homan, D. C., Kadler, M., et al. 2009b, *ApJ*, 696, L22
- Mahony, E. K., Sadler, E. M., Croom, S. M., et al. 2011, *MNRAS*, 417, 2651
- Markowitz, A. G., Krumpe, M., & Nikutta, R. 2014, *MNRAS*, 439, 1403
- Marshall, H. L., Schwartz, D. A., Lovell, J. E. J., et al. 2005, *ApJS*, 156, 13
- Mattox, J. R., Bertsch, D. L., Chiang, J., et al. 1996, *ApJ*, 461, 396
- Meegan, C., Lichti, G., Bhat, P. N., et al. 2009, *ApJ*, 702, 791
- Mezcua, M. 2017, *International Journal of Modern Physics D*, 26, 1730021
- Migliori, G., Siemiginowska, A., Sobolewska, M., et al. 2016, *ApJ*, 821, L31
- Mueller, C., Krauss, F., Kadler, M., et al. 2012, in *Proceedings of the 11th European VLBI Network Symposium Users Meeting. 9-12 October, 2012. Bordeaux (France)*. Online at <http://pos.sissa.it/cgi-bin/reader/conf.cgi?confid=178>, 20
- Mukherjee, R., Halpern, J., Mirabal, N., & Gotthelf, E. V. 2002, *ApJ*, 574, 693
- Müller, C., Burd, P. R., Schulz, R., et al. 2016, *A&A*, 593, L19
- Müller, C., Kadler, M., Ojha, R., et al. 2014a, *A&A*, 562, A4
- Müller, C., Kadler, M., Ojha, R., et al. 2014b, *A&A*, 569, A115
- Müller, C., Kadler, M., Ojha, R., et al. 2018, *A&A*, 610, A1

- Müller, C., Krauß, F., Dauser, T., et al. 2015, *A&A*, 574, A117
- Nandra, K., George, I. M., Mushotzky, R. F., Turner, T. J., & Yaqoob, T. 1997, *ApJ*, 477, 602
- Nolan, P. L., Abdo, A. A., Ackermann, M., et al. 2012, *ApJS*, 199, 31
- O’Dea, C. P. 1998, *PASP*, 110, 493
- Ojha, R., Kadler, M., Böck, M., et al. 2010, *A&A*, 519, A45
- Orienti, M. & Dallacasa, D. 2014, *MNRAS*, 438, 463
- Padovani, P. 2011, *MNRAS*, 411, 1547
- Padovani, P. 2017, *Nature Astronomy*, 1, 0194
- Padovani, P., Alexander, D. M., Assef, R. J., et al. 2017, *A&A Rev.*, 25, 2
- Perley, R. A., Chandler, C. J., Butler, B. J., & Wrobel, J. M. 2011, *ApJ*, 739, L1
- Perley, R. A., Willis, A. G., & Scott, J. S. 1979, *Nature*, 281, 437
- Peterson, B. M. 1997, *An Introduction to Active Galactic Nuclei*
- Petrov, L., Kovalev, Y. Y., Fomalont, E., & Gordon, D. 2005, *AJ*, 129, 1163
- Pian, E., Falomo, R., Ghisellini, G., et al. 1996, *ApJ*, 459, 169
- Piner, B. G. & Edwards, P. G. 2018, *ApJ*, 853, 68
- Rees, M. J. 1966, *Nature*, 211, 468
- Rybicki, G. B. & Lightman, A. P. 1979, *Radiative processes in astrophysics*
- Salpeter, E. E. 1964, *ApJ*, 140, 796
- Salvetti, D., Chiaro, G., La Mura, G., & Thompson, D. J. 2017, *MNRAS*, 470, 1291
- Schmidt, M. 1963, *Nature*, 197, 1040
- Schulz, R. F. 2016, PhD thesis, Julius-Maximilians-Universität Würzburg
- Seyfert, C. K. 1943, *ApJ*, 97, 28
- Shakura, N. I. & Sunyaev, R. A. 1973, *A&A*, 24, 337
- Shepherd, M. C., Pearson, T. J., & Taylor, G. B. 1994, in *BAAS*, Vol. 26, *Bulletin of the American Astronomical Society*, 987–989
- Soltan, A. 1982, *MNRAS*, 200, 115
- Sreekumar, P., Bertsch, D. L., Hartman, R. C., Nolan, P. L., & Thompson, D. J. 1999, *Astroparticle Physics*, 11, 221
- Stalevski, M., Ricci, C., Ueda, Y., et al. 2016, *MNRAS*, 458, 2288
- Stickel, M., Meisenheimer, K., & Kuehr, H. 1994, *A&AS*, 105

- Swanenburg, B. N., Bennett, K., Bignami, G. F., et al. 1981, *ApJ*, 243, L69
- Tanaka, Y., Nandra, K., Fabian, A. C., et al. 1995, *Nature*, 375, 659
- Taylor, G. B., Healey, S. E., Helmboldt, J. F., et al. 2007, *ApJ*, 671, 1355
- Tchekhovskoy, A., Narayan, R., & McKinney, J. C. 2011, *MNRAS*, 418, L79
- Terashima, Y. & Wilson, A. S. 2003, *ApJ*, 583, 145
- Thompson, A. R., Moran, J. M., & Swenson, G. W. 1986, *Interferometry and synthesis in radio astronomy*
- Thompson, D. J., Bertsch, D. L., Fichtel, C. E., et al. 1993, *ApJS*, 86, 629
- Tingay, S. J. & Edwards, P. G. 2002, *AJ*, 124, 652
- Tingay, S. J., Jauncey, D. L., Reynolds, J. E., et al. 1997, *AJ*, 113, 2025
- Tingay, S. J., Jauncey, D. L., Reynolds, J. E., et al. 2000, *AJ*, 119, 1695
- Torresi, E. 2012, *ArXiv e-prints* [[arXiv]1205.1691]
- Trussoni, E., Vagnetti, F., Massaglia, S., et al. 1999, *A&A*, 348, 437
- Urry, C. M. & Padovani, P. 1995, *PASP*, 107, 803
- Venturi, T., Morganti, R., Tzioumis, T., & Reynolds, J. 2000, *A&A*, 363, 84
- Véron-Cetty, M.-P. & Véron, P. 2010, *A&A*, 518, A10
- Walker, R. C., Benson, J. M., & Unwin, S. C. 1987, *ApJ*, 316, 546
- Wills, K. A., Morganti, R., Tadhunter, C. N., Robinson, T. G., & Villar-Martin, M. 2004, *MNRAS*, 347, 771
- Wood, M., Caputo, R., Charles, E., et al. 2017, *ArXiv e-prints* [[arXiv]1707.09551]
- Wright, A. & Otrupcek, R. 1990, in *PKS Catalog (1990)*
- Zamaninasab, M., Clausen-Brown, E., Savolainen, T., & Tchekhovskoy, A. 2014, *Nature*, 510, 126
- Zensus, J. A. 1997, *ARA&A*, 35, 607

# Acknowledgements

The completion of this thesis work would not have been possible without the help and support of many others.

I would like to thank the director Prof. Zensus, as well as the IMPRS, for the opportunity to carry out my doctoral research in a prestigious context such as the VLBI group of the MPIfR, and for following the progress of my thesis work during these three years, together with Prof. Eckart, as doctoral referee.

I would also like to deeply thank my advisor at the MPIfR, Prof. Eduardo Ros, for his dedication, for always making the time in his schedule to fulfill the role at his best, no matter how busy, and his guidance. I am also grateful to my co-advisor at the Universität Würzburg, Prof. Matthias Kadler, for providing an ideal context for my project, for always providing useful feedback on its science, and for including me as a guest member of his research group, an experience which I have valued very much during these three years. Additionally, I would like to thank Dr. Cornelia Müller and Dr. Nicholas McDonald for participating in my Thesis Advisory Committee, providing a fresh perspective and useful feedback on the project. My thanks go also to Dr. Roopesh Ojha, for hosting me during my work visit at NASA Goddard, and to the *Fermi*-LAT collaboration for providing excellent networking opportunities and a competent environment to share feedback and exchange ideas.

I am also grateful to my fellow PhD students and all the young researchers in the group, and especially Laura, Jae-Young and Anne, with whom I have shared this journey since its very beginning. An additional thanks goes to Laura for developing and making available GUI-based Python codes for kinematic and spectral analysis.

Infine, il ringraziamento più sentito va alla mia famiglia, il mio porto sicuro, le mie radici più solide, senza le quali non avrei potuto raggiungere nessuno dei miei traguardi.

Bonn, 22.08.2018

# Erklärung

Ich versichere, dass ich die von mir vorgelegte Dissertation selbständig angefertigt, die benutzten Quellen und Hilfsmittel vollständig angegeben und die Stellen der Arbeit, einschließlich Tabellen, Karten und Abbildungen, die anderen Werken im Wortlaut oder dem Sinn nach entnommen sind, in jedem Einzelfall als Entlehnung kenntlich gemacht habe; dass diese Dissertation noch keiner anderen Fakultät oder Universität zur Prüfung vorgelegen hat; dass sie, abgesehen von unten angegebenen Teilpublikationen noch nicht veröffentlicht worden ist sowie, dass ich eine solche Veröffentlichung vor Abschluss des Promotionsverfahrens nicht vornehmen werde. Die Bestimmungen der Promotionsordnung sind mir bekannt. Die von mir vorgelegte Dissertation ist von Prof. Dr. Andreas Eckart und Prof. Dr. J. Anton Zensus betreut worden.

Köln, den 25.02.2019

# Publication/Teilpublikationen

- Radio galaxies with the Cherenkov Telescope Array”, **R. Angioni**, P. Grandi, E. Torresi, C. Vignali, J. Knödseder, 2017, *Astroparticle Physics* 92, 42
- ”Gamma-ray emission in radio galaxies under the VLBI scope: I. Parsec-scale jet kinematics and high-energy properties of  $\gamma$ -ray-detected TANAMI radio galaxies”, **R. Angioni**, E. Ros, M. Kadler, R. Ojha et al., to be submitted to *Astronomy & Astrophysics* in August-September 2018
- ”Gamma-ray emission in radio galaxies under the VLBI scope: II. The relationship between  $\gamma$ -ray emission and parsec-scale jet in radio galaxies”, **R. Angioni**, E. Ros, M. Kadler, R. Ojha et al., to be submitted to *Astronomy & Astrophysics* by the end of 2018
- ”TANAMI: Tracking Active Galactic Nuclei with Austral Milliarcsecond Interferometry: II. Additional sources”, C. Müller, M. Kadler, R. Ojha, R. Schulz, J. Trstedt, P. G. Edwards, E. Ros, B. Carpenter, **R. Angioni**, J. Blanchard, M. Böck, P. R. Burd, M. Dörr, M. S. Dutka, T. Eberl, S. Gulyaev, H. Hase, S. Horiuchi, U. Katz, F. Krauss, J. E. J. Lovell, T. Natusch, R. Nesci, C. Phillips, C. Plötz, T. Pursimo, J. F. H. Quick, J. Stevens, D. J. Thompson, S. J. Tingay, A. K. Tzioumis, S. Weston, J. Wilms and J. A. Zensus, *Astronomy & Astrophysics* 610, 1
- ”Extended X-ray emission in PKS 1718–649”, T. Beuchert, A. Rodríguez-Ardila, V. A. Moss, R. Schulz, M. Kadler, J. Wilms, **R. Angioni**, J. R. Callingham, C. Gräfe, F. Krauss, A. Kreikenbohm, M. Langejahn, K. Leiter, F. M. Maccagni, C. Müller, R. Ojha, E. Ros and S. J. Tingay, 2018, *Astronomy & Astrophysics* 612, 4
- ”Multimessenger observations of a flaring blazar coincident with high-energy neutrino IceCube-170922A”, The IceCube Collaboration, **Fermi-LAT**, MAGIC, AGILE, ASAS-SN, HAWC, H.E.S.S., INTEGRAL, Kanata, Kiso, Kapteyn, Liverpool Telescope, Subaru, Swift/NuSTAR, VERITAS, VLA/17B-403 teams, 2018, *Science* 361, 6398
- ”VLBI studies of TANAMI radio galaxies”, **R. Angioni**, F. Rösch, E. Ros, M. Kadler, R. Ojha, C. Müller for the TANAMI collaboration, 2016, Proceedings of the 13<sup>th</sup> European VLBI Network Symposium and Users Meeting
- ”Radio galaxies from Fermi to the CTA”, **R. Angioni**, P. Grandi, E. Torresi, C. Vignali, J. Knödseder, 2017, Proceedings of the 6th International Symposium on High-Energy Gamma-Ray Astronomy
- 11 Astronomer’s Telegrams as first author, on behalf of the *Fermi-LAT* collaboration (ATels #11854, #11706, #11251, #11249, #11227, #11141, #11137, #11064, #11056, #11039, #10696)

# Lebenslauf

## Personliche Daten

Roberto Angioni  
Geburtsdatum: 21. November 1990  
Geburtsort: Carbonia, Italien  
Staatsangehörigkeit: Italienisch

## Anschrift

Max-Planck-Institut für Radioastronomie  
Auf dem Hügel 69  
53121 Bonn  
Deutschland  
email: [angioni@mpifr-bonn.mpg.de](mailto:angioni@mpifr-bonn.mpg.de)

## Ausbildung

2015–2018 Doktorand an der Universität zu Köln und dem  
Max-Planck-Institut für Radioastronomie  
Gruppe Prof. Dr. J. A. Zensus  
wiss. Betreuer Prof. Dr. Eduardo Ros (MPIFR-U. València) und  
Prof. Dr. Matthias Kadler (U. Würzburg)  
Titel: “*VLBI and  $\gamma$ -ray studies of radio galaxies in the TANAMI  
monitoring program*”

- 2012–2015 Master an der Università di Bologna  
MSc Astrophysik und Cosmologie  
wiss. Betreuer Prof. Dr. Cristian Vignali, Dr. Paola Grandi und  
Dr. Eleonora Torresi  
Titel: ” *High-energy view of radio galaxies:  
prospects for the new generation of Cherenkov telescopes*”
- 2009–2012 Bachelor an der Università di Cagliari  
BSc Physik  
wiss. Betreuer Prof. Dr. Luciano Burderi, Dr. Andrea Tarchi und  
Dr. Paola Castangia  
Titel: ” *Radio observations with the JVLA of water masers  
in the galaxy Mrk 766*”
- 2004–2009 Allgemeine Hochschulreife am Liceo Scientifico E. Amaldi  
Carbonia, Italien